

Titre: Analytical and Numerical Studies on the Stresses in Backfilled
Stopes and the Stability of Side-Exposed Backfill in Inclined Stopes

Auteur: Shupeng Chai
Author:

Date: 2020

Type: Mémoire ou thèse / Dissertation or Thesis

Référence: Chai, S. (2020). Analytical and Numerical Studies on the Stresses in Backfilled
Stopes and the Stability of Side-Exposed Backfill in Inclined Stopes [Mémoire de
maîtrise, Polytechnique Montréal]. PolyPublie.
Citation: <https://publications.polymtl.ca/5222/>

 **Document en libre accès dans PolyPublie**
Open Access document in PolyPublie

URL de PolyPublie: <https://publications.polymtl.ca/5222/>
PolyPublie URL:

**Directeurs de
recherche:** Li Li
Advisors:

Programme: Génie minéral
Program:

POLYTECHNIQUE MONTRÉAL

affiliée à l'Université de Montréal

**ANALYTICAL AND NUMERICAL STUDIES ON THE STRESSES IN
BACKFILLED STOPES AND THE STABILITY OF SIDE-EXPOSED
BACKFILL IN INCLINED STOPES**

SHUPENG CHAI

Département des génies civil, géologique et des mines

Mémoire présenté en vue de l'obtention du diplôme de *Maîtrise ès sciences appliquées*

(Génie minéral)

Avril 2020

POLYTECHNIQUE MONTRÉAL

affiliée à l'Université de Montréal

Ce mémoire intitulé:

**ANALYTICAL AND NUMERICAL STUDIES ON THE STRESSES IN
BACKFILLED STOPEs AND THE STABILITY OF SIDE-EXPOSED
BACKFILL IN INCLINED STOPEs**

Présenté par **Shupeng CHAI**

en vue de l'obtention du diplôme de *Maîtrise ès sciences appliquées*

a été dûment accepté par le jury d'examen constitué de :

Richard SIMON, président

Li LI, membre et directeur de recherche

Carlos OVALLE, membre

DEDICATION

To my family

致我的家人

ACKNOWLEDGEMENTS

First, I am very grateful to my research supervisor Prof. Li Li for offering me the opportunity to carry out my master's study in Montreal, and also for his kind support and guidance throughout the project. Thank him very much for spending lots of time sharing his ideas and knowledge, discussing my projects, and giving me much valuable advice.

I would also like to express my gratitude to Prof. Robert Chapuis, Prof. Samuel Yniesta, and Prof. Biao Li for their courses. I have benefited a lot from these courses. Many thanks also go to Prof. Richard Simon and Prof. Carlos Ovalle for being the committee members.

I would like to acknowledge the financial support from the Natural Sciences and Engineering Research Council of Canada (NSERC), Fonds de recherche du Québec—Nature et Technologies (FRQNT), and industrial partners of the Research Institute on Mines and the Environment (RIME UQAT-Polytechnique; <http://rime-irme.ca/>).

I would also express my thanks to my friends and colleagues who have ever helped me during my courses and research. Special thanks go to Dr. Feitao Zeng and Dr. Jian Zheng for their reading of the preliminary version of my thesis.

Finally, I strongly appreciate my family for their kind support and unconditional love during my life and study. They are always standing by me and encouraging me mentally. I owe them special gratitude. Having stayed here for almost two years, now I am looking forward to going back and getting together with them.

RÉSUMÉ

L'exploitation minière est une industrie importante dans de nombreux pays, comme le Canada, la Chine, l'Australie, etc. Dans les méthodes d'extraction souterraine, de grands vides minés (appelés chantiers) peuvent être créés après l'extraction du minerai. Entre-temps, de grandes quantités de déchets solides comme les résidus et les stériles sont également produites comme produits secondaires. Traditionnellement, ces déchets miniers sont entreposés à la surface sous forme d'installations de stockage de résidus ou de tas de stériles. Au fil des ans, le remblayage des chantiers avec des déchets solides miniers a été de plus en plus utilisé dans les mines souterraines. Le remblayage peut améliorer les conditions de stabilité du sol, augmenter la récupération du minerai et réduire la dilution du minerai. Il peut également aider à réduire les déchets solides entreposés en surface et à minimiser les impacts environnementaux associés.

L'application réussie du remblai nécessite une bonne compréhension de l'état de contrainte dans les chantiers de remblayage, ce qui est nécessaire pour la conception de barricades, de tapis de seuil et de remblais exposés latéralement. À cette fin, un certain nombre de solutions analytiques et numériques ont été publiées. Dans la plupart des cas, les contraintes verticales et horizontales sont surveillées le long de la profondeur du remblai à la fin de l'opération de remblayage. Les courbes résultantes sont alors une description de la variation des contraintes en fonction de leurs positions pour un remblai donné. Parfois, on ne peut s'intéresser qu'aux contraintes à la base du remblai. Dans ce cas, on peut obtenir une courbe qui décrit la variation des contraintes à la base du remblai en fonction de l'épaisseur du remblai. On obtient un profil contrainte-profondeur dans le premier cas et un profil contrainte-épaisseur dans le second cas. Même si les significations physiques des deux types de courbes sont différentes, l'utilisation des solutions analytiques existantes donnera les mêmes résultats entre elles. Les contraintes verticales et horizontales augmentent presque linéairement avec la profondeur ou l'épaisseur lorsque la profondeur ou l'épaisseur est très faible. Lorsque la profondeur ou l'épaisseur devient importante, les contraintes verticales et horizontales ont alors tendance à devenir constantes. Cela ne correspond pas aux résultats obtenus par des simulations numériques, qui montraient parfois une augmentation soudaine des contraintes près du fond sur le profil profondeur-contrainte. Ce phénomène a été appelé effets kink par Sivakugan et ses collaborateurs en 2014. Jusqu'à présent, il n'y a pas de solution analytique qui prend en compte l'effet kink pour évaluer les contraintes dans les chantiers remblayés. Le mécanisme de l'effet de

pli reste également inconnu. Dans cette thèse, le mécanisme de l'effet kink est d'abord analysé. Une solution analytique est ensuite proposée après avoir pris en compte le mécanisme de l'effet de pli pour estimer les contraintes verticales et horizontales dans les paliers remblayés. Le mécanisme d'apparition de l'effet de pli et la solution analytique proposée sont validés par les résultats numériques obtenus avec FLAC. Les résultats montrent que l'apparition d'un effet de coude est étroitement liée à l'état du remblai, qui est déterminé par la relation entre le coefficient de Poisson μ et l'angle de frottement interne φ du remblai. Le pli peut se produire lorsque $\mu > (1 - \sin \varphi)/2$ alors qu'il ne se produit pas lorsque $\mu \leq (1 - \sin \varphi)/2$.

Un autre problème critique pour la conception d'un chantier remblayé est d'évaluer la stabilité ou de déterminer la résistance requise du remblai dans le chantier principal afin que le remblai reste stable lors de l'exposition du remblai d'un côté en raison de l'excavation d'un chantier secondaire. Au fil des ans, un certain nombre de solutions analytiques ont été proposées pour évaluer la stabilité et la résistance requise du remblai exposé latéralement dans les chantiers verticaux. Seules quelques études ont été menées pour évaluer la stabilité du remblai exposé latéralement dans les chantiers inclinés. Les quelques solutions disponibles contiennent plusieurs limitations. Dans cette thèse, une solution analytique améliorée a été développée pour évaluer la stabilité et la cohésion requise du remblai exposé latéralement dans les chantiers inclinés. La solution analytique proposée est validée par des simulations numériques réalisées avec FLAC3D. Les résultats montrent qu'il existe un angle d'inclinaison critique de la paroi du chantier, auquel la cohésion minimale requise du remblai exposé latéralement dans les chantiers inclinés atteint une valeur maximale, à partir de laquelle la cohésion minimale requise diminue quel que soit l'angle d'inclinaison de la paroi du chantier augmente ou diminue.

ABSTRACT

Mining is an important industry in many countries, such as Canada, China, Australia, etc. In underground mining methods, large mined-out voids (called stopes) can be created after ore extraction. In the meantime, large quantities of solid wastes like tailings and waste rocks are also produced as secondary products. Traditionally, these mining wastes are disposed of on the surface in forms of tailings storage facilities or waste rock piles. Over the years, stope backfilling with mine solid wastes has been increasingly used in underground mines. The backfilling can improve the ground stability conditions, increase ore recovery, and reduce ore dilution. It can also help reduce surface disposal of mine solid wastes and minimize the associated environmental impacts.

The successful application of backfill requires a good understanding of the stress state in backfilled stopes, which is necessary for the design of barricade, sill mat, and side-exposed backfill. To this end, a number of analytical and numerical solutions have been published. In most cases, the vertical and horizontal stresses are monitored along the depth of the backfill at the end of the backfilling operation. The resulting curves are then a description of the variation of the stresses as a function of their positions for a given backfill. Sometimes, one can be only interested in the stresses at the base of the backfill. In this case, one can obtain a curve that describes the variation of the stresses at the base of the backfill as a function of backfill thickness. One obtains a stress-depth profile in the former case and a stress-thickness profile in the latter case. Even though the physical meanings of the two types of curves are different, the use of existing analytical solutions will result in the same results between them. The vertical and horizontal stresses increase almost linearly with the depth or thickness when the depth or thickness is very small. When the depth or thickness becomes large, the vertical and horizontal stresses then tend to become constant. This does not correspond to the results obtained by numerical simulations, which sometimes showed a sudden increase of the stresses near the bottom of the stress-depth profile. This phenomenon was called kink effects by Sivakugan and coworkers in 2014. Until now, there is no analytical solution that takes into account the kink effect to evaluate the stresses in backfilled stopes. The mechanism of the kink effect also remains unknown. In this thesis, the mechanism of kink effects is first analyzed. An analytical solution is then proposed after taking into account the mechanism of kink effect to estimate the vertical and horizontal stresses in backfilled stopes. The mechanism for the occurrence of kink effects and the proposed analytical solution are validated by numerical results obtained

with FLAC. The results show that the occurrence of kink effect is closely related to the state of the backfill, which is determined by the relationship between the Poisson's ratio μ and internal friction angle φ of the backfill. The kink can occur when $\mu > (1 - \sin \varphi)/2$ while not occur when $\mu \leq (1 - \sin \varphi)/2$.

Another critical issue for backfilled slope design is to evaluate the stability or determine the required strength of the backfill in primary slope in order for the backfill to remain stable upon the exposure of the backfill on one side due to the excavation of a secondary slope. Over the years, a number of analytical solutions have been proposed to evaluate the stability and required strength of side-exposed backfill in vertical slopes. Only a few studies have been conducted to evaluate the stability of side-exposed backfill in inclined slopes. The few available solutions contain several limitations. In this thesis, an improved analytical solution has been developed to evaluate the stability and the required cohesion of side-exposed backfill in inclined slopes. The proposed analytical solution is validated by numerical simulations conducted with FLAC3D. The results show that a critical slope wall inclination angle exists, at which the minimum required cohesion of side-exposed backfill in inclined slopes reaches a peak value, from which the minimum required cohesion decreases whatever the slope wall inclination angle increases or decreases.

TABLE OF CONTENTS

DEDICATION	III
ACKNOWLEDGEMENTS	IV
RÉSUMÉ.....	V
ABSTRACT.....	VII
TABLE OF CONTENTS	IX
LIST OF TABLES	XII
LIST OF FIGURES.....	XIII
LIST OF SYMBOLS AND ABBREVIATIONS.....	XXIII
LIST OF APPENDICES	XXVIII
CHAPTER 1 INTRODUCTION.....	1
1.1 Background and problems.....	1
1.2 Objectives and methodology.....	2
1.3 Contributions.....	3
1.4 Contents.....	3
CHAPTER 2 LITERATURE REVIEW.....	5
2.1 Stress state in backfilled stopes.....	5
2.1.1 Analytical solutions.....	5
2.1.2 Numerical simulations.....	23
2.1.3 Relevant experimental tests.....	38
2.2 Lateral earth pressure coefficient	48
2.2.1 Theory	48
2.2.2 Numerical simulations.....	53
2.2.3 Experiments.....	55

2.3	The stability of side-exposed backfill	57
2.3.1	Analytical solutions.....	57
2.3.2	Numerical simulations.....	70
2.3.3	Experimental tests	74
2.4	Final remarks.....	79
CHAPTER 3 ARTICLE 1: NUMERICAL AND ANALYTICAL INVESTIGATIONS OF STRESS DISTRIBUTION IN BACKFILLED STOPEs CONSIDERING THE KINK EFFECT NEAR THE BOTTOM		80
3.1	Introduction	81
3.2	Mechanism of kink effects	82
3.3	Analytical solution	84
3.4	Numerical simulations and comparisons.....	87
3.4.1	Numerical models	87
3.4.2	Validation of the proposed mechanism.....	89
3.4.3	Calibration of the proposed analytical solution.....	90
3.4.4	Tests of the ability of prediction of the proposed and calibrated analytical solution.....	92
3.5	Discussion	94
3.6	Conclusions	95
3.7	References	96
CHAPTER 4 ARTICLE 2: A NEW SOLUTION TO EVALUATE THE STABILITY OF SIDE-EXPOSED BACKFILL IN INCLINED STOPEs.....		100
4.1	Introduction	101
4.2	Proposed solutions.....	104
4.3	Numerical modeling.....	107

4.3.1	Numerical models	107
4.3.2	Criterion of instability	110
4.3.3	Comparison between numerical modeling and analytical solution.....	112
4.4	Comparison with experimental results	116
4.5	Discussion	119
4.6	Conclusions	121
4.7	Appendix I: Formulation for deducing the normal stresses at the hanging wall and footwall in an inclined backfilled stope	122
4.8	References	126
CHAPTER 5	DISCUSSION	132
CHAPTER 6	CONCLUSIONS AND RECOMMENDATIONS.....	136
6.1	Conclusions	136
6.2	Recommendations	137
REFERENCES	139
APPENDICES	150

LIST OF TABLES

Table 2-1: Definition of K_i and α_i (adapted from Li et al. 2005; Li and Aubertin 2009d)	9
Table 2-2: Summary of the analytical solutions for the stress state in backfilled stopes.....	22
Table 2-3: Summary of the numerical simulations for the stress state in backfilled stopes	36
Table 2-4: K used in analytical solutions	53
Table 3-1: A summary of previous numerical results regarding the occurrence of kink effects ...	85
Table 3-2: Program of additional numerical simulations.....	89
Table 4-1: Program of numerical simulations (with $\gamma_R = 27 \text{ kN/m}^3$, $E_R = 30 \text{ GPa}$, and $\mu_R = 0.3$ for the rock mass and $\gamma = 18 \text{ kN/m}^3$, $E = 300 \text{ MPa}$ and $\mu = 0.2$ for the cemented backfill)	109
Table 4-2: Combined indicators to evaluate the instability of exposed backfill	110
Table 4-3: Model tests of backfill stability (data taken or calculated from Mitchell 1989)	117
Table 4-4: Parameters used in the proposed solution and prediction errors of analytical solutions	119
Table A-1: The properties of the elastic model.....	153
Table A-2: The properties of the Mohr-Coulomb model.....	155
Table B-1: Summary of the analytical solution for the stress in the backfill.....	174
Table C-1: The minimum required cohesion for the cases in Table 4-1	185

LIST OF FIGURES

Figure 2-1: A schematic presentation of a 2D vertical stope and a layer element with its acting forces (taken from Aubertin et al. 2003)	7
Figure 2-2: A 3D vertical backfilled stope with acting forces on an isolated layer element (taken from Li et al. 2005)	8
Figure 2-3: A schematic view of a partly submerged 3D stope with a layer element and its acting forces (taken from Li and Aubertin 2009d)	10
Figure 2-4: Comparisons between the analytical solutions and field measurements in (a) 3FC4 stope and (b) 3FF4 stope (taken from Knutsson 1981)	13
Figure 2-5: (a) A schematic diagram of a vertical backfilled stope; (b) Distribution of the horizontal and vertical total stresses with different c_v (taken from Zheng et al. 2019)	14
Figure 2-6: Pascal's triangle (taken from Ting et al. 2012)	15
Figure 2-7: A schematic view of a 2D inclined stope (taken from Ting et al. 2011)	18
Figure 2-8: A schematic view of a 3D inclined stope and a layer element with forces on it (taken from Jahanbakhshzadeh et al. 2018b)	20
Figure 2-9: Stress contours in the backfill: (a) the vertical stress and (b) the horizontal stress; comparisons of the analytical and numerical results: (c) the vertical stress and (d) the horizontal stress (taken from Li et al. 2003)	24
Figure 2-10: Vertical stress along the central line of the backfill (taken from Pirapakaran 2008)	25
Figure 2-11: Vertical and horizontal stresses for a plain-strain (PS) stope and an axisymmetric (AX) stope (taken from Fahey et al. 2009)	25
Figure 2-12: (a) Total stress at the end of filling (EOF), consolidation (EOC) and drawdown (EOD) in undrained filling process and (b) at the end of filling in partially drained filling process (taken from Fahey et al. 2009)	26
Figure 2-13: Vertical stress along the central line of the backfilled stope with different widths (taken from Sivakugan et al. 2014)	27

Figure 2-14: (a) A model of the slope with nonplanar interfaces and (b) the stresses along the height of the slope with different values of saw-teeth angle ($\theta = 180^\circ$ is the condition with a planar interface) (taken from Liu et al. 2016)	28
Figure 2-15: Numerical simulations of stresses in backfilled slopes by considering adjacent slopes: (a) a model with two slopes; numerical results of the (b) horizontal and (c) vertical stresses at the end of the filling process of the second slope (taken from Falaknaz et al. 2015a)	29
Figure 2-16: The stress distributions within the backfill of the first slope (Slope A) along the VCL due to the excavation and backfilling of the second slope (Slope B) (taken from Newman and Agioutantis 2018).....	31
Figure 2-17: (a) Comparisons of the normalized vertical stress between the numerical and the experimental results; (b) contact point ratio across the width (taken from Hasan et al. 2017)	31
Figure 2-18: Horizontal and vertical stresses along the VCL with time: (a) half day, and (b) 3 days (taken from Qi and Fourie 2019).....	32
Figure 2-19: (a) Stress contours for inclined backfill with $\beta = 70^\circ$ and (b) the stress distribution across the width with different inclination angles (taken from Caceres 2005).....	34
Figure 2-20: Stress variation for various inclination angles: (a) along the central line; (b) along hanging wall and (c) along footwall (taken from Li et al. 2009b)	34
Figure 2-21: Comparisons of numerical results with (a) experimental results of Take and Valsangkar (2001) and analytical solution results with (b) $\beta = 80^\circ$ and (c) $\beta = 70^\circ$ ($B = 184$ mm, taken from Yan et al. 2019).	36
Figure 2-22: (a) Positions of measuring systems in the slope and (b) the stresses in the three directions at the base of the slope (taken from Belem et al. 2004)	39
Figure 2-23: Measurements in the 715 slope: (a) measuring points and (b) long-term total earth pressures (TEP), pore pressures (Pore P) and temperature (Temp) for Cages 3 and 4 (taken from Thompson et al. 2012).....	39

Figure 2-24: Field experiments: (a) The position of the stress boxes; (b) vertical stress of 1# stress box; (c) vertical stress of 2# stress box (adapted from Wang et al. 2019)	40
Figure 2-25: Laboratory tests measuring the vertical stress in inclined stopes: (a) a side view of the experimental apparatus and (b) the average vertical stress at the base with different inclination angles (taken from Ting et al. 2012)	41
Figure 2-26: The horizontal pressure in a coal silo with 20 m in diameter and 54 m high (taken from Blight 1986).....	43
Figure 2-27: (a) Locations of pressure sensors in the backfilled silo; vertical (b) and horizontal (c) stresses measured and calculated with the analytical solutions (adapted from Li et al. 2014)	44
Figure 2-28: (a) a schematic diagram and (b) a photo of the laboratory model and (c) the variation of μ with the ratio z/D (z is the depth and D is the silo diameter) (adapted from Han et al. 2018)	45
Figure 2-29: Experimental model and results: (a) a schematic model and (b) the failure surface of the backfill with translation mode (taken from Yang and Tang, 2017)	46
Figure 2-30: (a) Comparison between Marston solution and experimental results with loose sand and (b) variations of $K \tan \delta$ with the relative height (adapted from Hong et al. 2016)	47
Figure 2-31: The earth pressure coefficient obtained from FLAC and curve-fitting derived for the rock friction angle range (taken from Caceres 2005).....	50
Figure 2-32: Comparisons between measured wall pressures and calculated pressures by applying analytical formulas for (a) deep silos and (b) squat silos (taken from Sun et al. 2018).....	52
Figure 2-33: The earth pressure coefficient for (a) different dilation angles in dry stopes and (b) different hydraulic conductivities in partially drained stopes (taken from Fahey et al. 2009)	54
Figure 2-34: The lateral earth pressure coefficient along the CL of backfilled stopes with different (a) friction angles and (b) inclination angles (taken from Sobhi et al. 2017)	54

Figure 2-35: (a) The state of the backfill for different relationships between μ and φ and (b) the earth pressure coefficient along the VCL as a function of μ (taken from Yang et al. 2018) .55	.55
Figure 2-36: K measured in laboratory tests: (a) pressures near the central and corner of the wall (taken from Jarrett et al. 1995); (b) K at different fill heights h (taken from Li et al. 2014); (c) K at different depths z (D is the silo diameter, taken from Han et al. 2018).....56	56
Figure 2-37: K calculated from field measurement at different positions in the 715 stope (adapted from Thompson et al. 2012).....56	56
Figure 2-38: The wedge model of Mitchell et al. (1982) solution (taken from Mitchell et al. 1982)58	58
Figure 2-39: Forces and geometry for 3D wedge analysis: (a) a general view of half of the wedge, (b) side view and (c) plan view (taken from Dight and Coulthard 1980)59	59
Figure 2-40: Geometry of the Smith et al. (1983) model for side-exposed backfill in an inclined stope (taken from Smith et al. 1983)60	60
Figure 2-41: A schematic model for side-exposed backfill in inclined stopes (adapted from Dirige and De Souza 2008)61	61
Figure 2-42: The backfill with a low aspect ratio (taken from Li and Aubertin 2012).....63	63
Figure 2-43: Backfilled containing a plug with the sliding plane (a) in the plug and (b) intersecting with the top surface of the plug (taken from Li 2014a)64	64
Figure 2-44: Forces on the two parts of the model: (a) the upper block and (b) the lower wedge (taken from Li and Aubertin 2014)67	67
Figure 2-45: Side-exposed backfill with tension crack (taken from Yang et al. 2017a).....68	68
Figure 2-46: Mechanical model of a cemented backfill (taken from Wang et al. 2019)69	69
Figure 2-47: Failure zones with an exposure height of 20, 30, 40, 50, 60 and 70 m (taken from Dight and Coulthard 1980).....71	71
Figure 2-48: Vertical stresses in backfill after the excavation of the secondary stope: (a) static analysis; (b) dynamic analysis (taken from Emad et al. 2014)72	72

Figure 2-49: Comparisons of the numerical results with the analytical solution and experimental data of Mitchell et al. (1982) (taken from Liu et al. 2016b)	73
Figure 2-50: Experimental tests for the side-exposed stability of backfill: (a) model construction and (b) comparisons with the analytical solution (taken from Mitchell et al. 1982)	74
Figure 2-51: Tension crack during the failure of the model: (a) test 1a and (b) test 2a (taken from Mitchell 1986) and (c) test No. 1a (taken from Zhao et al. 2019)	75
Figure 2-52: A schematic view of (a) the retaining wall model and (b) laboratory model (taken from Antonov 2005).....	76
Figure 2-53: (a) The positions of the measuring systems and (b) the side-exposed backfill (taken from Yang et al. 2015)	76
Figure 2-54: Experimental tests for the side-exposed stability of inclined backfill: (a) model construction and (b) comparisons with the analytical solution (taken from Smith et al. 1983)	77
Figure 2-55: (a) Model 3 (with 10% UCS wall closure stress and a wall inclination angle of 75°) after failure and (b) comparisons of the analytical solution and experimental data (taken from Mitchell 1989).....	78
Figure 2-56: Tension cracks and failure surface development in Model 4 (taken from Dirige and De Souza 2008)	78
Figure 3-1: Possible stress states in the backfilled stope (adapted from Yang et al. 2018)	83
Figure 3-2: A backfilled stope and possible stress distribution with kink effects.....	86
Figure 3-3: (a) A physical model and (b) a numerical model built with FLAC of a vertical backfilled stope	88
Figure 3-4: Variation of the vertical (a) and horizontal (b) stresses along the VCL of the backfilled stope for a given Poisson's ratio with different internal friction angles (details given in Table 2, Cases 0 and 1)	89

Figure 3-5: Variation of the vertical (a) and horizontal (b) stresses along the VCL of the backfilled stope for a given internal friction angle with different Poisson's ratios (details given in Table 2, Cases 0 and 2)	90
Figure 3-6: Vertical and horizontal stresses obtained by numerical modeling and predicted by applying the proposed solution (Eqs. 3-6 to 3-13 with $a = 1/10$ and $b = 1/20$) for (a) Case 0, (b) Case 1c and (c) Case 2b.....	91
Figure 3-7: Vertical and horizontal stresses obtained by numerical modeling and predicted by the proposed solution (Eqs. 3-6 to 3-13 with $a = 1/10$ and $b = 1/20$) with different parameters for (a) Case 3 with $B = 12$ m, (b) Case 4 with $H = 35$ m, (c) Case 5 with $E = 30$ MPa and (d) Case 6 with $\delta = 20^\circ$	92
Figure 3-8: Vertical and horizontal stresses obtained by numerical modeling and predicted with the proposed solution (Eqs. 3-6 to 3-13 with $a = 1/10$ and $b = 1/20$). Comparisons with numerical results taken from (a) Sivakugan et al. (2014) with $\gamma = 17.65$ kN/m ³ , $E = 50$ MPa, $\mu = 0.25$, $\varphi = 36^\circ$, $\delta = 36^\circ$, $H = 100$ or 150 m, $B = 25$ m; (b) Yang (2016) with $\gamma = 18$ kN/m ³ , $E = 300$ MPa, $\mu = 0.3$, $\varphi = 30^\circ$, $\delta = 30^\circ$, $H = 40$ m, $B = 8$ m; (c) Liu et al. (2017) with $\gamma = 18$ kN/m ³ , $E = 300$ MPa, $\mu = 0.3$, $\varphi = 35^\circ$, $\delta = 28^\circ$, $H = 40$ m, $B = 10$ m.....	93
Figure 4-1: Open stoping with a primary and a secondary stope: β ($^\circ$) is the wall inclination angle; B (m), L (m) and H (m) are the width, length, and height of the backfill in the primary stope, respectively.....	101
Figure 4-2: Wedge model of side-exposed backfill in an inclined stope (adapted from Dirige and De Sousa 2008)	103
Figure 4-3: The geometry of (a) a physical model and (b) the FLAC3D numerical model of a side-exposed backfill in an inclined stope	108
Figure 4-4: The variation of the total displacement of the open face as the iteration steps increase for Case 0 (Table 4-1) with (a) $c = 70$ kPa and (b) $c = 69$ kPa	111
Figure 4-5: Variation of the total displacement at $z = 10$ m on the central line C_1C_2 of the open face as a function of backfill cohesion for Case 0 (Table 4-1)	111

Figure 4-6: Strength-stress ratio iso-contours of the side-exposed backfill for Case 0 (Table 4-1) with (a) $c = 70$ kPa and (b) $c = 69$ kPa.....	112
Figure 4-7: Variation of the minimum required cohesion c as a function of slope wall inclination angles β , obtained by numerical modeling and predicted by applying the proposed solution; predictive results obtained by applying existing analytical solutions are also plotted on the figure for (a) Case 1 in Table 4-1 and (b) Case 2 in Table 4-1	113
Figure 4-8: Variation of the minimum required cohesion c as a function of (a) backfill height H (Case 3, Table 4-1), (b) slope length L (Case 4, Table 4-1) and (c) slope width B (Case 5, Table 4-1), obtained by numerical modeling and predicted by the proposed and existing solutions	115
Figure 4-9: Variation of the minimum required cohesion c as a function of the backfill internal friction angles φ (Case 6 in Table 4-1), obtained by numerical modeling and predicted by the proposed and existing solutions.	116
Figure 4-10: Comparison of the required cohesion obtained from experimental results of Mitchell (1989) and predicted by the proposed analytical solution (Eq. 4-30) and the Mitchell (1989) solution (Eq. 4-2) for tests with (a) 10% UCS wall closure stress and (b) 50% UCS wall closure stress, and (c) for all the tests.....	118
Figure 4-11: An inclined narrow backfilled slope with an isolated differential layer element....	122
Figure 4-12: Shear stress iso-contours along fill-rock wall interfaces upon exposure of the backfill in a slope with wall inclination angle $\beta = 60^\circ$ (Case 1 in Table 4-1)	125
Figure A-1: A schematic view of the cylindrical hole problem	150
Figure A-2: (a) Boundary conditions (adapted from Itasca 2011) and (b) numerical model of the cylindrical hole problem in FLAC	152
Figure A-3: Sensitivity analysis of the domain in an elastic model: (a) the variation of radial stress, (b) tangential stress and (c) radial displacement with domain size R	153
Figure A-4. Sensitivity analysis of the mesh size in an elastic model: (a) the variation of radial stress, (b) tangential stress and (c) radial displacement with the mesh size.....	154

Figure A-5. Comparisons between analytical results and numerical results in an elastic model: (a) the variation of radial and tangential stresses and (b) the variation of radial displacement	154
Figure A-6: Sensitivity analysis of the domain in Mohr-Coulomb model with $\psi = 0^\circ$: (a) the variation of radial stress, (b) tangential stress and (a) radial displacement with Radius155
Figure A-7: Sensitivity analysis of the domain in Mohr-Coulomb model with $\psi = 30^\circ$: (a) the variation of radial stress, (b) tangential stress and (a) radial displacement with Radius156
Figure A-8. Sensitivity analysis of the mesh size in the Mohr-Coulomb model with $\psi = 0^\circ$: (a) the variation of radial stress, (b) tangential stress and (a) radial displacement with mesh size.	156
Figure A-9. Sensitivity analysis of the mesh size in the Mohr-Coulomb model with $\psi = 30^\circ$: (a) the variation of radial stress, (b) tangential stress and (a) radial displacement with mesh size.	157
Figure A-10: Comparisons between analytical results and numerical results in the Mohr-Coulomb model with $\psi = 0^\circ$: (a) the variation of radial and tangential stresses and (b) radial displacement.....	157
Figure A-11: Comparisons between analytical results and numerical results in the Mohr-Coulomb model with $\psi = 30^\circ$: (a) the variation of radial and tangential stresses and (b) radial displacement.....	158
Figure A-12: (a) Boundary conditions (adapted from Itasca 2013) and (b) numerical model of the cylindrical hole problem in FLAC3D 158
Figure A-13: Sensitivity analysis of the domain in an elastic model: (a) the variation of radial stress, (b) tangential stress and (a) radial displacement with domain size R 159
Figure A-14: Sensitivity analysis of the mesh size in an elastic model: (a) the variation of radial stress, (b) tangential stress and (a) radial displacement with mesh size 160
Figure A-15: Comparisons between analytical results and FLAC3D results in an elastic model: (a) the variation of radial and tangential stresses; and (b) the variation of radial displacement	160
Figure A-16: Sensitivity analysis of the domain in Mohr-Coulomb model with $\psi = 0^\circ$: (a) the variation of radial stress, (b) tangential stress and (a) radial displacement with domain size R 161

Figure A-17: Sensitivity analysis of the domain in Mohr-Coulomb model with $\psi = 30^\circ$: (a) the variation of radial stress, (b) tangential stress and (a) radial displacement with domain size R	161
Figure A-18: Sensitivity analysis of the mesh size in Mohr-Coulomb model with $\psi = 0^\circ$: (a) the variation of radial stress, (b) tangential stress and (a) radial displacement with mesh size.	162
Figure A-19: Sensitivity analysis of the mesh size in Mohr-Coulomb model with $\psi = 30^\circ$: (a) the variation of radial stress, (b) tangential stress and (a) radial displacement with mesh size.	162
Figure A-20: Comparisons between analytical results and numerical results in the Mohr-Coulomb model with $\psi = 0^\circ$: (a) the variation of radial and tangential stresses and (b) radial displacement.....	163
Figure A-21: Comparisons between analytical results and numerical results in the Mohr-Coulomb model with $\psi = 30^\circ$: (a) the variation of radial and tangential stresses and (b) radial displacement.....	163
Figure B-1: Positions of the monitoring points for the sensitivity analyses of the backfill model	164
Figure B-2: Variation of the (a) vertical and (b) horizontal stresses at the four monitoring points with different element sizes.....	165
Figure B-3: Variation of the (a) vertical and (b) horizontal stresses at the four monitoring points with different domain sizes	165
Figure B-4: The variations of (a) VSD, VSB and (b) HSD, HSB for the reference case	169
Figure B-5: The variations of (a) VSD, VSB and (b) HSD, HSB with different internal friction angles of the backfill	170
Figure B-6: The variations of (a) VSD, VSB and (b) HSD, HSB with different Poisson's ratios of the backfill.....	170
Figure B-7: The variations of (a) VSD, VSB and (b) HSD, HSB with different backfill widths	171
Figure B-8: The variations of (a) VSD, VSB and (b) HSD, HSB with different backfill heights	171

Figure B-9: The variations of (a) VSD, VSB and (b) HSD, HSB with different Young's modulus of the backfill	172
Figure B-10: The variations of (a) VSD, VSB and (b) HSD, HSB with different internal friction angles of the fill-rock interface	172
Figure B-11: Comparisons between analytical solutions and numerical simulations when no kink occurs: (a) Case 1 when $\varphi = 20^\circ$ and (b) Case 2 when $\mu = 0.2$	173
Figure B-12: Comparisons between the proposed analytical solutions and numerical simulations for different backfill properties when the kink occurs: (a) Case 0; (b) Case 3 when $B = 12$ m (c) Case 4 when $H = 35$ m and (d) Case 6 when $\delta=20^\circ$	174
Figure C-1: A schematic view of the side-exposed backfill in inclined stopes with two monitoring lines C_1C_2 and H_1H_2	175
Figure C-2: Results for the sensitivity analyses of the domain size: the total displacement along the line (a) C_1C_2 and (b) H_1H_2 , the stress in the z -direction along the line (c) C_1C_2 and (d) H_1H_2 and the stress in the x -direction along the line (e) C_1C_2 and (f) H_1H_2	176
Figure C-3: Results for the sensitivity analyses of the mesh size: the total displacement along the line (a) C_1C_2 and (b) H_1H_2 , the stress in the z -direction along the line (c) C_1C_2 and (d) H_1H_2 and the stress in the x -direction along the line (e) C_1C_2 and (f) H_1H_2	177
Figure C-4: Results for the sensitivity analyses of the filling layer thickness: the total displacement along the line (a) C_1C_2 and (b) H_1H_2 , the stress in the z -direction along the line (c) C_1C_2 and (d) H_1H_2 and the stress in the x -direction along the line (e) C_1C_2 and (f) H_1H_2	178

LIST OF SYMBOLS AND ABBREVIATIONS

Symbols

B	width of the backfill or slope (m)
B_t	equivalent width of the sliding wedge considering a tension crack (m)
c	cohesion of backfill (kPa)
c'	effective cohesion of backfill (kPa)
c_f	cohesion of the fill-footwall interface (kPa)
c_h	cohesion of the fill-hanging wall interface (kPa)
c_i	cohesion of the fill-wall interface (kPa)
c_m	cohesion of wet backfill (kPa)
c_p	cohesion of the backfill plug pour (kPa)
c_v	consolidation coefficient of backfill (m ² /s)
D	diameter of a circle slope (m)
e	Euler's number
E	the Young's modulus of backfilled materials (kPa)
E_R	the Young's modulus of rock mass (kPa)
F_b	force on the back wall (kN)
F_f	normal force on the footwall (kN)
F_{fL}	normal force on footwall of layer element (kN)
F_h	normal force on the hanging wall (kN)
F_{hL}	normal force on hanging wall of layer element (kN)
H	total height of the backfill or slope (m)
h	height of the study point from backfill bottom (m)
H'	height of the wedge model at the back wall (m)
H^*	equivalent height of the wedge block (m)

H_f	failing height of backfill (m)
H_i	initial height of backfill (m)
h_{kh}	critical height from the bottom of the horizontal stress profile (m)
h_{kv}	critical height from the bottom of the vertical stress profile (m)
H_t	depth of tension crack (m)
H_w	height of the lower wedge used in the backfill design (m)
K	lateral earth pressure coefficient
$K_{0\mu}$	at-rest earth pressure coefficient obtained by Poisson's ratio
$K_{0\phi}$	at-rest earth pressure coefficient obtained by internal friction angle
K_a	Rankine's active earth pressure coefficient
K_b	earth pressure coefficient at the central line used in Xu et al. (2018)
K_c	earth pressure coefficient obtained by Caceres (2005)
K_H	earth pressure coefficient obtained by Handy (1985)
K_J	a parameter related to earth pressure coefficient in Janssen (1895)
K_K	earth pressure coefficient obtained by Krynine (1945)
K_M	earth pressure coefficient obtained by Jaouhar et al. (2018)
K_p	Rankine's passive earth pressure coefficient
K_S	earth pressure coefficient obtained by Sobhi et al. (2017)
K_T	earth pressure coefficient obtained by Ting et al. (2012)
K_x	earth pressure coefficient at a distance x_w from the wall in Xu et al. (2018)
K_β	earth pressure coefficient obtained by Jahanbakhshzadeh et al. (2017, 2018b)
L	length of the backfill or slope (m)
p_0	surcharge at the top of backfill in the backfill design (kPa)
p_w	pore water pressure (kPa)
q	surcharge at the top of backfill in the stress estimation (kPa)
r_b	adherence ratio of the cohesion of the interface c_i to the backfill cohesion c

r_f	adherence ratio of the footwall (kPa)
r_h	adherence ratio of the hanging wall (kPa)
r_p	ratio of the plug pour cohesion c_p to the final pour cohesion c
r_β	coefficient applied to adjust the shear stress along the fill-hanging wall interface
S_f	shear force on the footwall (kN)
S_{fL}	shear force on the footwall of layer element (kN)
S_h	shear force on the hanging wall (kN)
S_{hL}	shear force on the hanging wall of layer element (kN)
t	filling time (s)
v	backfilling rate (m/s)
V	vertical force on the top of layer element (kN)
W	weight of the sliding wedge model (kN)
w	initial water content of backfill
W_L	weight of layer element (kN)
W_n	net weight of the sliding wedge model (kN)
W_v	vertical load on buried conduits (kN)
x	horizontal distance from the central line of a 2D backfilled stope (m)
z	depth from the backfill surface to the study point (m)
z_m	distance from the water table to the backfill surface (m)
α	sliding angle between the assumed sliding plane and the horizontal in a side-exposed stope ($^\circ$)
β	wall inclination angle of the inclined backfill (or stope) ($^\circ$)
γ	unit weight of backfill (kN/m^3)
γ'	effective unit weight of saturated backfill (kN/m^3)
γ_m	unit weight of wet backfill (kN/m^3)
γ_R	unit weight of surrounding rock (kN/m^3)

δ	internal friction angle of the fill-wall interface ($^{\circ}$)
δ_f	internal friction angle of the fill-footwall interface ($^{\circ}$)
δ_h	internal friction angle of the fill-hanging wall interface ($^{\circ}$)
θ	angle made between the two lines of intersection formed by the side (hanging or foot) wall, sliding plane and the horizontal base ($^{\circ}$)
μ	Poisson's ratio of backfill
μ_c	critical Poisson's ratio of backfill when $K_a = K_{0\mu}$
μ_f	friction coefficient of the fill-wall interface
μ_R	Poisson's ratio of rock mass
σ'_h	effective horizontal stress at a depth of z in the backfill (kPa)
σ'_v	effective vertical stress at a depth of z in the backfill (kPa)
σ_1	major principal stress (kPa)
σ_3	minor principal stress (kPa)
σ_{av}	average vertical stress across the width of the stope (kPa)
σ_f	normal stress at the footwall (kPa)
σ_h	total horizontal stress (kPa)
σ_{hL}	transversal horizontal stress (kPa)
σ_{hT}	longitude horizontal stress (kPa)
σ_{hw}	normal stress at the hanging wall (kPa)
σ_n	normal stress perpendicular to the wall (kPa)
σ_v	total vertical stress (kPa)
σ_{vx}	vertical stress at a horizontal distance of x from the central line (kPa)
τ	shear stress at the wall (kPa)
τ_f	shear stress at the footwall (kPa)
τ_h	shear stress at the hanging wall (kPa)
τ_{vh}	shear stress related to σ_h and σ_v (kPa)

φ	internal friction angle of backfill ($^{\circ}$)
φ'	effective internal friction angle of backfill ($^{\circ}$)
ψ	dilation angle of the backfill ($^{\circ}$)
ψ_x	angle between σ_l and vertical direction at x from the central line ($^{\circ}$)

Abbreviations

2D	two-dimensional
3D	three-dimensional
CL	central line
DF	distribution factor
FS	factor of safety
HF	hydraulic fill
HSB	horizontal stress at the bottom (with different filling heights)
HSD	horizontal stress along depth
PF	paste fill
RF	rock fill
SB	stress at the bottom (with different filling heights)
SD	stress along depth
UCS	unconfined compressive strength
VCL	vertical central line
VSb	vertical stress at the bottom (with different filling heights)
VSD	vertical stress along depth

LIST OF APPENDICES

Appendix A	Validation of used numerical codes.....	150
Appendix B	Additional results related to Chapter 3	164
Appendix C	Additional results related to Chapter 4	175

CHAPTER 1 INTRODUCTION

1.1 Background and problems

The mining industry is an important part of the national economy in many countries, such as Canada, Australia, China. The mining industry not only produces valuable minerals but also generates a high amount of mine wastes (i.e., tailings and waste rocks). Traditionally, the mining wastes are disposed of on the surface. For example, the tailings can be deposited and confined in tailings ponds while the waste rocks are disposed of as waste rock piles. The surface disposal of mining wastes can result in several geotechnical and environmental problems, such as the failure of tailings dams and acid mine drainage.

In recent decades, backfilling has been increasingly used in underground mine stopes as it can help to improve ground stability, increase ore recovery, reduce ore dilution and provide a safe workplace (Potvin et al. 2005; Darling 2011; Li 2014a, 2014b; Yang et al. 2017a). Using mine wastes to fill the underground mine stopes can also reduce the surface disposal of mining wastes and minimize the associated environmental impacts (Bussi re 2007; Yang et al 2015; Liu et al. 2018). The commonly used backfill can be classified as rock fill (RF), hydraulic fill (HF), and paste fill (PF). Backfill can be mixed with or without cement to fill mine stopes, depending on the purpose of the used backfill and the underground mining methods.

The use of backfill in underground mines requires a good understanding of the stress distribution in backfilled stopes. To this end, a number of analytical and numerical solutions have been published. In most cases, the vertical and horizontal stresses are monitored along the depth of the backfill at the end of the backfilling operation. The resulting curves are then a description of the variation of the stresses as a function of their positions for a given backfill. Sometimes, one can be only interested in the stresses at the base of the backfill. In this case, one can obtain a curve that describes the variation of the stresses at the base of the backfill as a function of backfill thickness. One obtains a stress-depth profile in the former case and a stress-thickness profile in the latter case. Even though the physical meanings of the two types of curves are different, the use of existing analytical solutions will result in the same results between them. The vertical and horizontal stresses increase almost linearly with the depth or thickness when the depth or thickness is very small. When the depth or thickness becomes large, the vertical and horizontal stresses then tend to

become constant. This does not correspond to the results obtained by numerical simulations, which sometimes showed a sudden increase in the stresses near the bottom on the stress-depth profile (Sivakugan et al. 2014; Yang 2016). This phenomenon was called kink effects by Sivakugan et al. (2014). Until now, there is no analytical solution that takes into account the kink effect to evaluate the stresses in backfilled stopes. The mechanism of kink effects also remains unknown. More work is necessary to understand the mechanism of kink effects and to develop a solution that can be used to evaluate the stresses in backfilled stopes after taking into account the kink effect.

Another critical concern for backfilled stope design is to evaluate the stability or determine the required strength of side-exposed backfill. In open stoping methods, the ore body in the primary stope will be first excavated and then filled with cemented backfill. Then, the backfill in the primary stope will be exposed on one side during the excavation of the ore body in the secondary stope. The backfill in the primary stope must be strong enough to at least remain self-standing during the excavation of the secondary stope. The minimum required strength of the side-exposed backfill in the primary stope needs to be determined to ensure a safe and economic backfill design. Over the years, a number of analytical solutions have been proposed to evaluate the stability and required strength of side-exposed backfill in vertical stopes (Mitchell et al. 1982; Li et al. 2014a, 2014b). Only a few studies have been conducted to evaluate the stability of side-exposed backfill in inclined stopes. The few available solutions contain several limitations. New solutions are necessary to better evaluate the stability or required strength of side-exposed backfill in inclined stopes.

1.2 Objectives and methodology

The main objective of the thesis is to investigate the stress distribution in backfilled stopes and the stability of side-exposed backfill in an inclined stope. This objective can be realized through the addressing of the following sub-objectives:

- (1) Investigate the stress distribution in backfilled stopes by considering the kink effect
 - Analyze the mechanism of kink effect;
 - Develop an analytical solution to estimate the stress distribution along the depth of backfilled stopes by incorporating the kink effect;

- Validate the proposed mechanism and analytical solution by numerical results available in the literature and obtained with FLAC.
- (2) Investigate the stability of side-exposed backfill in inclined stopes
- Develop an analytical solution to evaluate the stability and required cohesion of side-exposed backfill in inclined stopes;
 - Conduct numerical simulations with FLAC3D to estimate the minimum required cohesion of side-exposed backfill in inclined stopes;
 - Validate the proposed analytical solution with the numerical results obtained with FLAC3D.

1.3 Contributions

The realization of the thesis leads to the submission of two articles in peer-reviewed journals:

Article 1: Chai S., Zheng J., and Li L. (2020). Numerical and analytical investigations of stress distribution in backfilled stopes considering the kink effect near the bottom. *International Journal of Geomechanics*. Submitted in January 2020. This article is presented in Chapter 3.

Article 2: Chai S., Wang R., and Li L. (2020). A new solution to evaluate the stability of side-exposed backfill in inclined stopes. *International Journal of Geomechanics*. Submitted in March 2020. This article is presented in Chapter 4.

The project contributes to a better understanding of the geotechnical behavior of the backfill placed in mine stopes. The analytical and numerical solutions presented in this thesis can be used to estimate the stress state in vertical backfilled stopes incorporating the kink effect and evaluate the stability of side-exposed backfill in inclined stopes. These analytical solutions can provide simple and useful tools for mining engineers in the preliminary design of backfilled stopes.

1.4 Contents

The thesis is organized in an article-based format shown as follows:

Chapter 1 presents a general introduction, including the background and problems, the objectives of the thesis, and the contents of the thesis.

Chapter 2 gives a detailed literature review of the state of knowledge, including the estimation of stress state in backfilled stopes, the lateral pressure coefficients used in the analytical solutions for the stress state in underground mine stopes, and investigations of the stability of side-exposed backfill.

Chapter 3 (Article 1) presents a study on the estimation of the stress distribution in backfilled stopes. The mechanism of the kink effect is first analyzed. An analytical solution considering the kink effect is proposed to evaluate the vertical and horizontal stresses along the backfill depth. The proposed analytical solution is also validated by numerical results available in the literature and obtained by newly performed numerical modeling with FLAC.

Chapter 4 (Article 2) presents the development of a new analytical solution to evaluate the stability and minimum required strength of side-exposed backfill in inclined stopes. The proposed analytical solution is verified by numerical results obtained with FALC3D.

Chapter 5 discusses the main limitations of the thesis.

Chapter 6 summarizes the main conclusions of this thesis and gives future recommendations.

Finally, appendices are given at the end of the thesis. Appendix A presents the validation of the numerical software FLAC and FLAC3D against analytical solutions. Appendix B shows the sensitivity analyses of the numerical model and additional numerical results pertaining to Chapter 3. Appendix C contains the additional results related to Chapter 4, including the sensitivity analyses of the numerical model and the minimum required cohesions obtained by the proposed analytical solution and numerical simulations.

CHAPTER 2 LITERATURE REVIEW

In this chapter, a literature review is first given on the stress estimation in backfilled stopes, followed by a brief review on the lateral earth pressure coefficient closely associated with stress estimation in backfilled stopes. Previous studies for analyzing the stability and required strength of side-exposed backfill are presented.

2.1 Stress state in backfilled stopes

A good understanding of the stress state in backfilled stopes is critical for the designs of backfill and barricades. In the following subsections, the analytical solutions and numerical simulations for estimating the stress state in backfilled stopes will first be presented. Stress measurements in backfilled stopes are then reviewed.

2.1.1 Analytical solutions

Analytical solutions are very useful to provide economical and rapid information, especially during the preliminary stage of design.

2.1.1.1 Backfilled stopes with vertical walls

2.1.1.1.1 Overburden solution

In geotechnical engineering, the stresses based on overburden solution (Terzaghi 1943) are given as below:

$$\sigma_v = \gamma z \quad (2-1)$$

$$\sigma_h = K \sigma_v \quad (2-2)$$

where σ_v (kPa) and σ_h (kPa) are the vertical and horizontal stresses at a depth of z (m) in the backfill; γ (kN/m³) is the unit weight of the backfill; K is the lateral earth pressure coefficient.

2.1.1.1.2 Arching solutions

When a backfill is placed into a stope, it tends to settle down under the gravity. The surrounding rock walls tend to hold the backfill by shear forces, leading to smaller stresses in the backfill than

those based on the overburden solution. This stress redistribution in the backfilled stope is a well-known phenomenon, called the arching effect.

Janssen (1895) proposed an analytical solution for estimating the vertical and horizontal stresses in a square silo filled with corn by considering the arching effect (Sperl 2005). The proposed solution is given as follows:

$$\sigma_v = \frac{\gamma s}{4K_J} \left(1 - e^{-4K_J \frac{z}{s}}\right) \quad (2-3)$$

where σ_v (kPa) is the vertical stress at a depth of z (m); γ (kN/m³) is the unit weight of the filling material; s (m) is the side length of the square silo; K_J is related to the lateral earth pressure coefficient K as follows:

$$K_J = \frac{\sigma_h \mu_f}{\sigma_v} = \frac{\mu_f}{K} \quad (2-4)$$

where σ_h (kPa) is the horizontal stress at the depth z ; μ_f is the friction coefficient of the interface between the backfill and silo wall.

An important assumption in Janssen's arching theory is the uniform vertical stress across the width of the silo. Nevertheless, Janssen's analytical solution was proved to provide a good stress estimation in backfilled silos compared with experimental results.

Later, Marston (1930) made use of Janssen's arching theory to estimate the vertical external loads on conduits buried in ditches. The vertical load is expressed as follows:

$$W_v = \frac{\gamma B^2}{2K\mu} \left(1 - e^{-2K\mu \frac{z}{B}}\right) \quad (2-5)$$

where W_v (kN) is the vertical load at a depth of z (m); K is the lateral earth pressure coefficient, taken as the Rankine's active earth pressure coefficient K_a ; B (m) is the width of the backfilled openings; μ is internal friction coefficient of the fill materials.

Terzaghi (1943) calculated the vertical stress in tunnels and took into consideration the cohesion of materials and the surcharge. For tunnels through the sand with a surcharge q (kPa) on the top surface, the vertical stress is given as:

$$\sigma_v = \frac{\gamma B}{2K \tan \varphi} \left(1 - e^{-2K \frac{z}{B} \tan \varphi}\right) + q e^{-2K \frac{z}{B} \tan \varphi} \quad (2-6)$$

where φ ($^\circ$) is the internal friction angle of the soil. For tunnels going through a cohesive soil, the vertical stress is calculated as follows:

$$\sigma_v = \frac{\gamma B - 2c}{2K \tan \varphi} \left(1 - e^{-2K \frac{z}{B} \tan \varphi} \right) \quad (2-7)$$

where c (kPa) is the cohesion of the filling material.

Askew et al. (1978) proposed a solution to calculate the stress in the backfill after exposure based on Terzaghi (1943)'s solution (Eq. 2-7). The vertical stress is expressed as:

$$\sigma_v = \frac{\gamma B - 2c_i}{K \tan \varphi} \left(1 - e^{-K \frac{z}{B} \tan \delta} \right) \quad (2-8)$$

where c_i (kPa) is the fill-wall interface cohesion; δ ($^\circ$) is the internal friction angle of the interface between the backfill and rock walls.

Aubertin et al. (2003) considered the equilibrium of a differential layer element (shown in Figure 2-1) in a two-dimensional (2D) stope. The vertical and horizontal stresses at the bottom of the backfilled stope are given as:

$$\sigma_v = \frac{\gamma B}{2K \tan \delta} \left(1 - e^{-2K \frac{H}{B} \tan \delta} \right) \quad (2-9)$$

$$\sigma_h = \frac{\gamma B}{2 \tan \delta} \left(1 - e^{-2K \frac{H}{B} \tan \delta} \right) \quad (2-10)$$

where H (m) is the total height of the backfill.

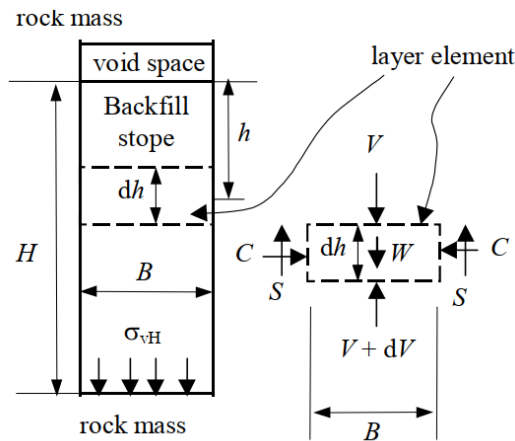


Figure 2-1: A schematic presentation of a 2D vertical stope and a layer element with its acting forces (taken from Aubertin et al. 2003)

The analytical solution was compared with the experimental results conducted by Take and Valsangkar (2001). A good agreement was observed, indicating the validity of the analytical solution.

Table 2-1: Definition of K_i and α_i (adapted from Li et al. 2005; Li and Aubertin 2009d)

Fill Condition	Dry backfill		Wet backfill		Saturated backfill	
	K_i	α_i	K_{im}	α_{im}	K_i'	α_i'
At-rest (K_0)	$1 - \sin \varphi$	0°	$1 - \sin \varphi_m$	0°	$1 - \sin \varphi'$	0°
Active (K_a)	$\frac{1 - \sin \varphi}{1 + \sin \varphi}$	$\frac{\varphi}{2} - 45^\circ$	$\frac{1 - \sin \varphi_m}{1 + \sin \varphi_m}$	$\frac{\varphi_m}{2} - 45^\circ$	$\frac{1 - \sin \varphi'}{1 + \sin \varphi'}$	$\frac{\varphi'}{2} - 45^\circ$
Passive (K_p)	$\frac{1 + \sin \varphi}{1 - \sin \varphi}$	$\frac{\varphi}{2} + 45^\circ$	$\frac{1 + \sin \varphi_m}{1 - \sin \varphi_m}$	$\frac{\varphi_m}{2} + 45^\circ$	$\frac{1 + \sin \varphi'}{1 - \sin \varphi'}$	$\frac{\varphi'}{2} + 45^\circ$

Pirapakaran and Sivakugan (2007a) proposed a similar formula for the vertical stress in a 3D vertical backfill as follows:

$$\sigma_v = \frac{\gamma B}{2K \tan \delta} \left(\frac{L}{L+B} \right) \left[1 - e^{-2 \left(\frac{L+B}{LB} \right) K z \tan \delta} \right] \quad (2-17)$$

Good agreements were observed between 2D numerical results for plane strain and axisymmetric condition, obtained by numerical simulations with FLAC and analytical results obtained with the analytical solution by using $\delta = 2/3\varphi$ and $K = K_0$ (K_0 is the at-rest earth pressure coefficient).

2.1.1.1.4 Considering the pore water pressure

Li and Aubertin (2009c) took into consideration the pore water pressure in the stress estimation in 2D vertical stopes. In partly submerged stopes, the effective vertical stress σ'_v (kPa) is expressed as:

$$\sigma'_v = \begin{cases} \frac{\gamma B}{2K \tan \varphi} \left(1 - e^{-2K \tan \varphi \frac{z}{B}} \right), & z < z_m \\ \frac{\gamma' B}{2K \tan \varphi'} \left(1 - e^{-2K \tan \varphi' \frac{z-z_m}{B}} \right) + \frac{\gamma B}{2K \tan \varphi} \left(1 - e^{-2K \tan \varphi \frac{z_m}{B}} \right) \cdot e^{-2K \tan \varphi' \frac{z-z_m}{B}}, & z > z_m \end{cases} \quad (2-18)$$

where z_m is the distance from the water table to the backfill surface; γ' (kN/m³) is the effective unit weight of the backfill; φ' (°) is the effective friction angle of the backfill.

For fully saturated stopes ($z_m = 0$), the effective vertical stress is given as:

$$\sigma'_v = \frac{\gamma' B}{2K \tan \varphi'} \left(1 - e^{-2K \frac{z}{B} \tan \varphi'}\right) \quad (2-19)$$

Numerical simulations were also conducted to verify the analytical solutions. Although the analytical method seemed to overestimate the stress a little bit near the wall and underestimate the stress along the central line, the analytical solutions worked well as a preliminary tool for the stress estimation in backfilled stopes.

Li and Aubertin (2009d) also gave a solution for the stress in a 3D stope by considering the pore water pressure and cohesion. For a partly submerged stope shown in Figure 2-3, the vertical stress at a point above the water table ($z < z_m$) is calculated as follows:

$$\sigma_v = \sigma'_v = \frac{\gamma_m - 2c_m(\lambda_{1m}B^{-1} + \lambda_{2m}L^{-1})}{M_m} (1 - e^{-M_m z}) + p_0 e^{-z M_m} \quad (2-20)$$

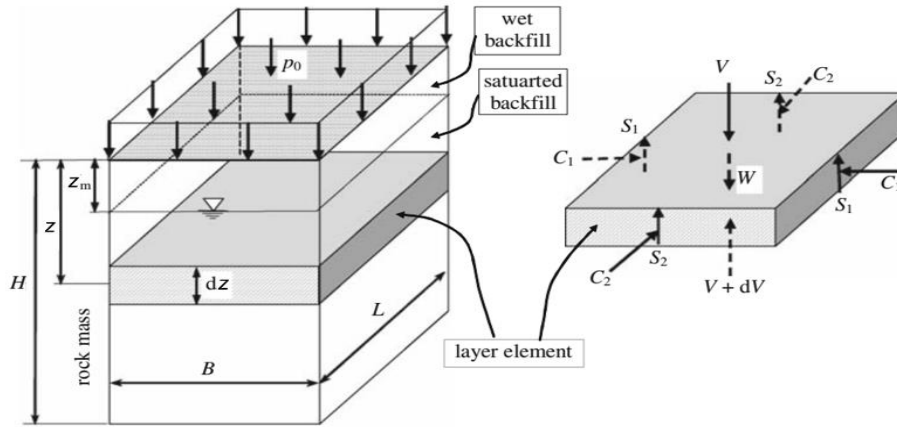


Figure 2-3: A schematic view of a partly submerged 3D stope with a layer element and its acting forces (taken from Li and Aubertin 2009d)

The effective and total vertical stresses at a point below the water table ($z > z_m$) are given by:

$$\sigma'_v = \frac{\gamma_m - 2c_m(\lambda_{1m}B^{-1} + \lambda_{2m}L^{-1})}{M_m} (1 - e^{-M_m z_m}) e^{-M'(z_m - z)} + \frac{\gamma' - 2c'(\lambda'_1 B^{-1} + \lambda'_2 L^{-1})}{M'} (1 - e^{(z_m - z)M'}) + p_0 e^{(z_m - z)M' - z_m M_m} \quad (2-21)$$

$$\sigma_v = \sigma'_v + \gamma_w(z - z_m) \quad (2-22)$$

with

$$M_m = 2(K_{1m}B^{-1} + K_{2m}L^{-1}) \tan \delta_m \quad (2-23)$$

$$\lambda_{1m} = 1 + 2 \tan \alpha_{1m} \tan \delta_m \quad (2-24)$$

$$\lambda_{2m} = 1 + 2 \tan \alpha_{2m} \tan \delta_m \quad (2-25)$$

$$M' = 2(K'_1 B^{-1} + K'_2 L^{-1}) \tan \delta' \quad (2-26)$$

$$\lambda'_1 = 1 + 2 \tan \alpha'_1 \tan \delta' \quad (2-27)$$

$$\lambda'_2 = 1 + 2 \tan \alpha'_2 \tan \delta' \quad (2-28)$$

where γ_m (kN/m³) and c_m (kPa) are the unit weight and cohesion of the wet backfill; c' (kPa) is the effective cohesion of the saturated backfill and the values of K_{im} , α_{im} , K' and α' are shown in Table 2-1.

2.1.1.1.5 Considering the nonuniform distribution of vertical stress across the width

Li and Aubertin (2008) modified the Marston solution by considering a nonuniform distribution of vertical stress across the width of a 2D vertical backfilled slope. The vertical and horizontal stresses are then expressed as follows:

$$\sigma_{vx} = \frac{\gamma B}{2K \tan \delta} \left[1 - e^{-\frac{2K' \tan \delta}{B(1-DF)z}} \right] \times \left[1 - a \left(\frac{|x|}{B} \right)^b \right] \quad (2-29)$$

$$\sigma_h = \frac{\gamma B}{2 \tan \delta} \left(1 - e^{-2K \frac{z}{B} \tan \delta} \right) \quad (2-30)$$

with

$$DF = \frac{a}{2^b(b+1)} = \frac{2^{\left(1-\frac{\lambda_1 H}{B}\right)} \tan^{-\lambda_2}(\varphi_0 + \varphi)}{2^3(3+1)} = 2^{\left(-4-\frac{0.02H}{B}\right)} \tan^{-0.1}(50^\circ + \varphi) \quad (2-31)$$

where σ_{vx} (kPa) is the vertical stress at a distance of x (m) from the vertical central line; a , b , λ_1 , λ_2 , φ_0 are some intermediate parameters in the distribution factor (DF) and they were obtained by calibration with some numerical results obtained with FLAC. The calibrated analytical solution was then further validated against additional numerical results.

Jaouhar et al. (2018) also considered nonuniform vertical stress across the width of a vertical slope by considering an arc layer element. The vertical and horizontal stresses are expressed as follows:

$$\sigma_v = \sigma_1 \left[1 - (1 - K_a) \left(\frac{x}{\xi_x B \kappa} \right)^2 \right] \quad (2-32)$$

$$\sigma_h = \sigma_1 \left[K_a - (1 - K_a) \left(\frac{x}{\xi_x B \kappa} \right)^2 \right] \quad (2-33)$$

With

$$\sigma_1 = \frac{\gamma \xi_x B \kappa \omega_w \cos \omega_w}{\tan \delta (\sin^2 \omega_w + K_a \cos^2 \omega_w)} \left(1 - e^{-\frac{\tan \delta (\sin^2 \omega_w + K_a \cos^2 \omega_w)}{\xi_x B \kappa \cos \omega_w} (z - [\xi_x B \kappa - \sqrt{(\xi_x B \kappa)^2 - x^2}])} \right) \quad (2-34)$$

$$\xi_x = \left\{ 1.5 + 0.25 \left(\frac{H}{B} \right)^{0.25} \tan \varphi + \left[0.75 - 0.25 \left(\frac{H}{B} \right)^{0.25} \tan \varphi \right] \sqrt{1 - \left(\frac{x}{B} \right)^2} \right\} \tan^{0.25} \varphi \quad (2-35)$$

where ξ_x is a correction factor for the radius $R (= \kappa B, \text{m})$; $\omega_w (= 45^\circ - \varphi/2)$ is the angle between the major principal stress σ_1 (kPa) along the walls and the vertical axis; $\kappa (= 1/\sin \omega_w)$ is a parameter related to the internal friction angle of the backfill.

To note that Eq. 2-36 was obtained by calibration against some numerical results. The calibrated solution was then further validated with additional numerical results.

Xu et al. (2018) assumed uniform horizontal stress across the width of the slope. The stress rotation was considered in their analytical solution and the trajectory of the minor principal stress σ_3 (kPa) was regarded as a circular arc, a parabola, and a catenary, respectively in a differential flat element. For the case of a circular-arc shape, the vertical stress in the backfilled slope is given by:

$$\sigma_{vx} = \frac{K_b}{K_x} \frac{\gamma B}{2K_b \tan \varphi} \left(1 - e^{-\frac{2zK_b \tan \varphi}{mB}} \right) + q e^{-\frac{2zK_b \tan \varphi}{mB}} \quad (2-36)$$

with

$$m = K_b \left[\frac{(1 + K_a) \cdot \arctan(\cos \theta_w \sqrt{(1 - K_a)/K_a})}{\cos \theta_w \sqrt{K_a(1 - K_a)}} - 1 \right] \quad (2-37)$$

$$K_x = \frac{\sigma_h}{\sigma_{vx}} = \frac{\cos^2 \psi_x + K_a \sin^2 \psi_x}{\sin^2 \psi_x + K_a \cos^2 \psi_x} \quad (2-38)$$

$$\theta_w = \arctan \left[\frac{1 - K_a + \sqrt{(1 - K_a)^2 - 4 \tan^2 \delta K_a}}{2 \tan \delta K_a} \right] \quad (2-39)$$

$$\cos \psi_x = \frac{B - x}{B} \cos \theta_w \quad (2-40)$$

where K_x is the earth pressure coefficient at a distance x_w (m) from the wall; ψ_x ($^\circ$) is the angle between the minor principal stress and vertical direction at a distance of x from the vertical central line; K_b is the earth pressure coefficient along the vertical central line of the backfilled stope ($x_w = B/2$) and θ_w is the angle between the minor principal stress and vertical direction at the fill-wall interface ($x = 0$). The solution was compared with numerical simulations conducted by ABAQUS and it was proved to predict well the stress distribution in some cases.

2.1.1.1.6 Considering wall convergence

Knutsson (1981) proposed an analytical solution to calculate the stress perpendicular to the rock wall (or horizontal stress) considering the wall convergence:

$$\sigma_h = \sigma_j \left[\eta_1 \eta_2 \Delta \varepsilon + \left(\frac{\sigma_0}{\sigma_j} \right)^{\eta_2} \right]^{\frac{1}{\eta_2}} \quad (2-41)$$

where σ_j (kPa) is relative stress which is usually 100 kPa; η_1 and η_2 are the modulus number and the stress exponent, respectively, which are determined by compressometer tests; $\Delta \varepsilon$ is the compressive strain of the backfill induced by wall convergence; σ_0 (kPa) is the initial stress level. The solution was compared with the classical silo solution and field experimental results measured in the Näsleden mine as shown in Figure 2-4. It is found that, on average, the stress component induced by the weight of backfill accounted for 70 ~ 80% of the total value of the stress while the wall convergence was responsible for 20 ~ 30% of the total value of the stress.

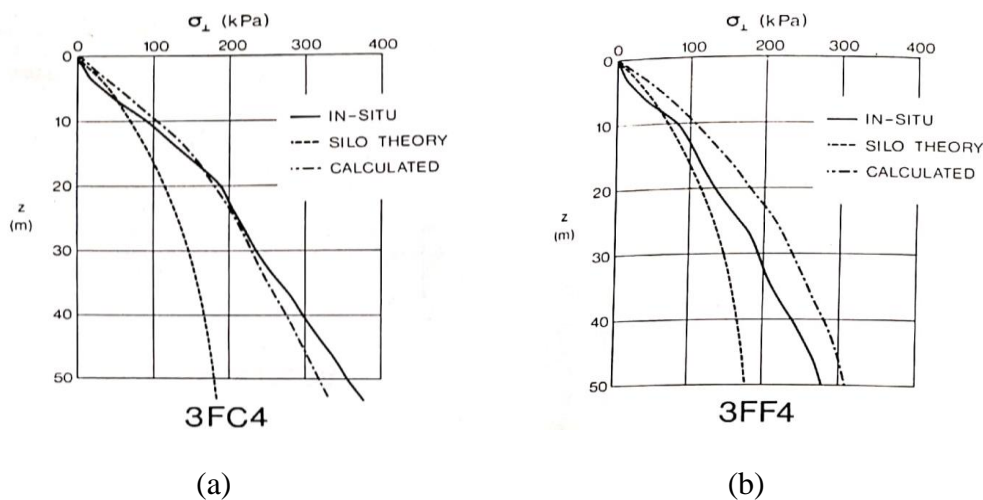


Figure 2-4: Comparisons between the analytical solutions and field measurements in (a) 3FC4 stope and (b) 3FF4 stope (taken from Knutsson 1981)

2.1.1.1.7 Considering the consolidation effect

Zheng et al. (2019) considered the consolidation and arching effects and proposed the following formulas for the total and effective stresses in backfilled stopes:

$$\sigma'_v = e^{-\frac{2K \tan \phi' z}{B}} \int_0^z \left(\gamma + \frac{dp_w}{dh} \right) \times e^{-\frac{2K \tan \phi' z}{B}} dz \quad (2-42)$$

$$\sigma'_h = K e^{-\frac{2K \tan \phi' z}{B}} \int_0^z \left(\gamma + \frac{dp_w}{dh} \right) \times e^{-\frac{2K \tan \phi' z}{B}} dz \quad (2-43)$$

$$\sigma_v = e^{-\frac{2K \tan \phi' z}{B}} \int_0^z \left(\gamma + \frac{dp_w}{dh} \right) \times e^{-\frac{2K \tan \phi' z}{B}} dz + p_w \quad (2-44)$$

$$\sigma_h = K e^{-\frac{2K \tan \phi' z}{B}} \int_0^z \left(\gamma + \frac{dp_w}{dh} \right) \times e^{-\frac{2K \tan \phi' z}{B}} dz + p_w \quad (2-45)$$

with

$$\frac{dp_w}{dh} = -\left(\gamma + \frac{v\gamma h}{c_v} \right) + \frac{v\gamma(\pi c_v t)^{-\frac{1}{2}}}{2c_v} e^{-\frac{h^2}{4c_v t}} \left[-\frac{h}{2c_v t} \sum_{n=-\infty}^{\infty} 8(c_v t)^{\frac{3}{2}} (n_0 h_0)^2 \coth \left(\frac{v n_0 h_0 \sqrt{t}}{\sqrt{c_v}} \right) \sinh \left(\frac{h n_0 h_0}{\sqrt{c_v t}} \right) e^{-(n_0 h_0)^2} \right. \\ \left. + \frac{h_0}{2} \sum_{n=-\infty}^{\infty} 8(c_v t)^{\frac{3}{2}} (n_0 h_0)^2 \coth \left(\frac{v n_0 h_0 \sqrt{t}}{\sqrt{c_v}} \right) \frac{n_0 h_0}{\sqrt{c_v t}} \cosh \left(\frac{h n_0 h_0}{\sqrt{c_v t}} \right) e^{-(n_0 h_0)^2} \right] \quad (2-46)$$

where h (m) is the height of the studied point; z (m) is the depth from the top of the stope; v is the filling rate (m/h); p_w (kPa) is water pressure; h_0 is the step length; n_0 is the series number in the range of $-\infty$ to ∞ , t (h) is the filling time and c_v (m^2/h) is consolidation coefficient of the backfill.

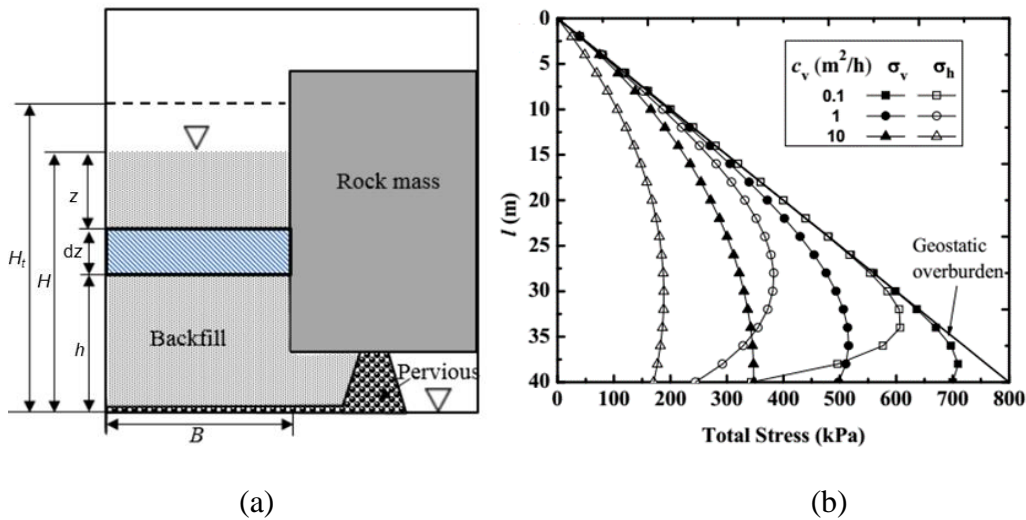


Figure 2-5: (a) A schematic diagram of a vertical backfilled stope; (b) Distribution of the horizontal and vertical total stresses with different c_v (taken from Zheng et al. 2019)

The analytical solution was compared with the numerical results obtained by Fahey et al. (2009). A good agreement was observed except some small difference which is due to the relatively thick layers used in the numerical models. Additional numerical results obtained by numerical simulations conducted by Zheng et al. (2019) corresponded well with the analytical results. According to their analytical solution, the total stress increases with filling rate and stope width but decreases with the consolidation coefficient and effective friction angle.

2.1.1.1.8 A solution by applying the Pascal's triangle

Ting et al. (2012) proposed an analytical solution based on Pascal's triangle to calculate the vertical stress at the base of a 2D vertical column. The granular materials stored in the vertical prism was divided into m layers with a thickness of n (m) and a self-weight of V_0 (kN) for each layer. The part of the vertical load in every layer transferred to the wall F_m (kN) and the bottom of the layer V_m (kN) is x and $1-x$, respectively, for example, in the layer m ,

$$F_m = (V_0 + V_{m-1})x \quad (2-47)$$

$$V_m = (V_0 + V_{m-1})(1 - x) \quad (2-48)$$

The equation of V_m can be expanded as

$$V_m = V_0(1 - x)(a_1 + a_2x + a_3x^2 + \dots + a_{m-1}x^{m-2} + a_mx^{m-1}) \quad (2-49)$$

with

$$a_i = (-1)^{i+1} \binom{m}{i} = (-1)^{i+1} \frac{m!}{i!(m-i)!} \quad (2-50)$$

where $\binom{m}{i}$ is the number in the m^{th} line and i^{th} row of Pascal's triangle.

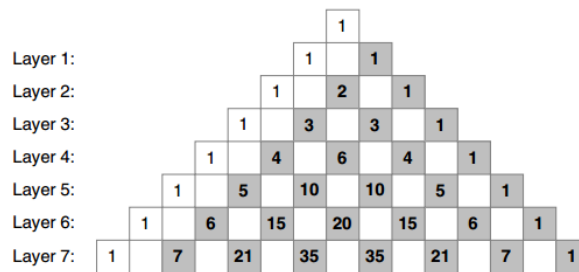


Figure 2-6: Pascal's triangle (taken from Ting et al. 2012)

The equation of V_m can be transferred as

$$V_m = V_0(1-x) \sum_{i=1}^m [(-1)^{i+1} \binom{m}{i} x^{i-1}] = \frac{V_0(1-x)}{x} [1 - (1-x)^m] \quad (2-51)$$

Then the average vertical stress at the bottom of the m^{th} layer is

$$\sigma_v = \frac{V_m}{B} = \frac{\gamma B n (1-x)}{B x} [1 - (1-x)^m] = \gamma n \frac{(1-x)}{x} [1 - (1-x)^m] \quad (2-52)$$

The shear stress τ (kPa) at the wall can be expressed as

$$\tau = K \sigma_v \tan \delta = \frac{F_m}{2n} \quad (2-53)$$

Submitting Eqs. 2-47 and 2-52 into Eq. 2-53, the parameter x can be obtained by

$$x = \frac{(2Kn \tan \delta)/B}{1 + (2Kn \tan \delta)/B} \quad (2-54)$$

The stress in the backfill with a given geometry was calculated using Eq. 2-52 for different values of m . It was observed that the stress obtained from the proposed method agreed well with the Marston solution once m is large sufficiently or n is small enough.

Actually, when Eq. 2-54 is submitted into Eq. 2-52, the vertical stress at the bottom becomes:

$$\sigma_v = \gamma n \frac{(1-x)}{x} [1 - (1-x)^m] = \frac{\gamma B}{2K \tan \delta} \left[1 - \left(\frac{1}{1 + (2Kn \tan \delta)/B} \right)^{\frac{z}{n}} \right] \quad (2-55)$$

Considering $n \rightarrow 0$, the vertical stress can be calculated as:

$$\sigma_v = \lim_{n \rightarrow 0} \frac{\gamma B}{2K \tan \delta} \left[1 - \left(\frac{1}{1 + (2Kn \tan \delta)/B} \right)^{\frac{z}{n}} \right] = \frac{\gamma B}{2K \tan \delta} \left(1 - e^{-\frac{2Kz \tan \delta}{B}} \right) \quad (2-56)$$

The solution of Ting et al. (2012) reduces to the Marston solution when the layer thickness tends to zero.

2.1.1.1.9 Empirical analytical solutions

In the experimental results conducted by Sivakugan and Widisinghe (2013), it was found that the vertical stress at the bottom increased steadily as the filling heights increased. Then, Rajeev et al. (2016) modified the Marston solution by adding several parameters calibrated from the

experimental results. However, no general analytical solutions were proposed. It was suggested that laboratory tests should be conducted first to determine relevant parameters for a certain backfilling material before calculating the stress in the backfill.

According to the numerical simulations conducted by Singh et al. (2009), the product of earth pressure coefficient K and interface friction coefficient $\tan \delta$ was almost a constant. Hong et al. (2016) then performed some laboratory tests to measure the stress in a trench. From their experimental data, the value of $K \cdot \tan \delta$ was constant at around 0.125. Thus, a semi-empirical analytical solution for the vertical stress modified from Marston solution is given as follows:

$$\sigma_v = 4\gamma B \left(1 - e^{-\frac{z}{4B}} \right) \quad (2-57)$$

The analytical equation was compared with the results obtained from two other field experiments and it predicated well the measured stress.

2.1.1.2 Backfilled stopes with inclined walls

2.1.1.2.1 Modified solutions based on the Marston model

Caceres (2005) assumed that the stresses at the hanging wall and footwall were identical in a 2D inclined stope. Based on the Marston solution, the vertical stress in the backfill was expressed as follows (Caceres 2005):

$$\sigma_v = \frac{\gamma B \sin^2 \beta}{2K_C \tan \varphi} \left(1 - e^{-\frac{2Kz \tan \varphi}{B \sin^2 \beta}} \right) \quad (2-58)$$

with

$$K_C = 1.4 \sin^2 \varphi - 2 \sin \varphi + 1 \quad (2-59)$$

where β ($^\circ$) is the inclination angle of the wall and K_C is the pressure coefficient obtained by curve fitting with numerical simulations.

However, some limitations exist in their analytical solution. For example, the shear stress at the hanging wall may be less than that at the footwall due to the wall inclination. In the derivation of the normal stress σ_n (kPa) perpendicular to the wall, the expression of $\sigma_n = \sigma_h / \sin^2 \beta$ is inaccurate.

Besides, the vertical component of the shear force at the walls should be $2\sigma_t dy$ instead of $2\sigma_t dy/\sin\beta$ in their analyses, where σ_t (kPa) is the shear stress at the walls.

2.1.1.2.2 Considering cohesion and surcharge

Ting et al. (2011) used the expression as follows to obtain the normal stress σ_n at the sidewalls in a 2D inclined stope (shown in Figure 2-7):

$$\sigma_n = \frac{\sigma_v + \sigma_h}{2} + \frac{\sigma_v - \sigma_h}{2} \cos 2\beta + \tau_{vh} \sin 2\beta \quad (2-60)$$

where τ_{vh} (kPa) is shear stress.

The vertical stress is given by the following equation after taking into account the backfill cohesion c and surcharge q :

$$\sigma_v = \frac{\gamma B - 2c(1 + \sin 2\beta \tan \delta)}{2K_T \tan \delta} \left(1 - e^{-2K_T \frac{z}{B} \tan \delta}\right) + q e^{-2K_T \frac{z}{B} \tan \delta} \quad (2-61)$$

with

$$K_T = \frac{1 + K_0}{2} + \frac{1 - K_0}{2} \cos 2\beta + K_0 \sin 2\beta \tan \delta \quad (2-62)$$

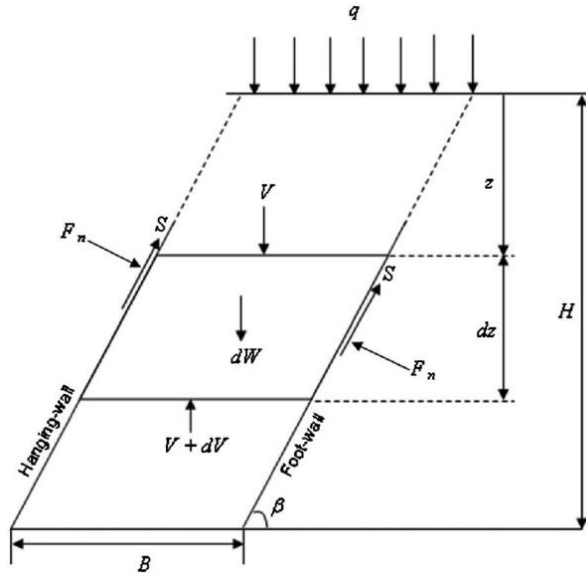


Figure 2-7: A schematic view of a 2D inclined stope (taken from Ting et al. 2011)

The stress calculated by the proposed analytical solution was found to compare well with that obtained from numerical simulations conducted by Li and Aubertin (2009e). However, it is unreasonable to calculate both τ_{vh} and τ with the Mohr-Coulomb yield criterion at the same time because yield should not simultaneously take place at a given point in two directions.

2.1.1.2.3 Considering nonuniform vertical stress across the width

By making use of the theory of Harrop-Williams (1989) who assumed that the trajectory of the major principal stress σ_1 in backfilled stopes was a circle arch, Singh et al. (2011) proposed the following equation for the major principal stress σ_1 :

$$\sigma_1 = \frac{\gamma B \delta \sin^2 \beta \operatorname{cosec} \delta - 2c}{2(\sin^2 \delta + K \cos^2 \delta) \tan \delta} \left(1 - e^{-\frac{8z(\sin^2 \delta + K \cos^2 \delta) \tan \delta \sin \delta}{B(2(1+K)\delta - (1-K) \sin 2\delta \cos 2\beta) \sin^3 \beta}} \right) + q e^{-\frac{8z(\sin^2 \delta + K \cos^2 \delta) \tan \delta \sin \delta}{B(2(1+K)\delta - (1-K) \sin 2\delta \cos 2\beta) \sin^3 \beta}} \quad (2-63)$$

However, it is difficult to apply the equation to calculate the vertical and horizontal stresses in inclined backfilled stopes. Nonetheless, Eq. 2-63 can be used to calculate the vertical stress in a vertical stope by submitting $\beta = 90^\circ$ into it.

Jahanbakhshzadeh et al. (2017, 2018a) compared the previous analytical solutions and proposed a 2D solution for inclined stopes with a modified coefficient K_β obtained by curve-fitting with numerical simulations. The proposed solution was given as follows for the vertical stress:

$$\sigma_v = \frac{\gamma B \sin \beta}{2K_\beta \tan \varphi} \left(1 - e^{-\frac{2K_\beta \tan \varphi}{B \sin \beta} z} \right) \quad (2-64)$$

with

$$K_\beta = K_a \times f_h \times f_w \quad (2-65)$$

$$f_h = (1 + \cos \beta) - \left(\frac{z}{H} \tan \varphi \cos^2 \beta \right) \quad (2-66)$$

$$f_w = 1 + 3 \left(1 - \frac{x_h}{B} \right)^4 \tan \varphi \cos(\beta - 10^\circ) \quad (2-67)$$

where x_h (m) is the distance from the hanging wall; f_h and f_w are the effects of geometrical factors. The horizontal stress can be calculated by K_β multiplying the vertical stress. The variation of the earth pressure coefficient across the width and along the height of the backfilled stope was taken

into consideration through the coefficient K_β . The calibrated analytical solution was further validated by additional numerical results. It has been shown that the proposed solution captured well the effect of inclination angle, stope width, and internal friction angle on the stress distribution in inclined stopes.

2.1.1.2.4 Three-dimensional (3D) situation

Jahanbakhshzadeh et al. (2018b) extended their 2D arching solution to a 3D situation (shown in Figure 2-8) with K_β :

$$\sigma_v = \frac{\gamma \sin \beta}{2(B^{-1} + L^{-1})K_\beta \tan \varphi} \left(1 - e^{-\frac{2(B^{-1} + L^{-1})K_\beta \tan \varphi}{\sin \beta} z} \right) \quad (2-68)$$

Similarly, the horizontal stress can be calculated by K_β multiplying the vertical stress. The analytical solution was validated by numerical and experimental results (Ting et al. 2012).

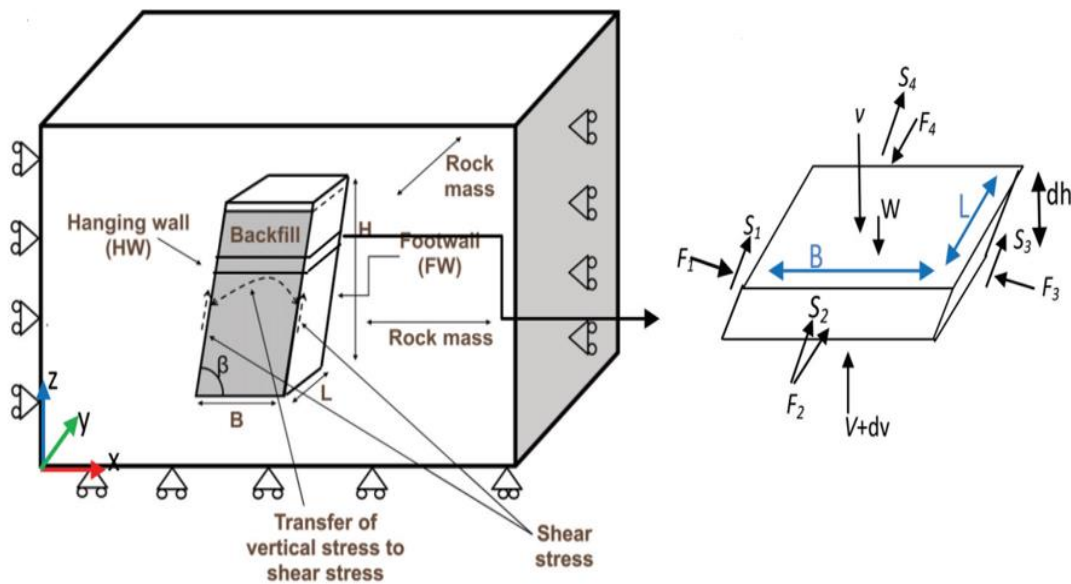


Figure 2-8: A schematic view of a 3D inclined stope and a layer element with forces on it (taken from Jahanbakhshzadeh et al. 2018b)

Yan et al. (2019) proposed a 3D analytical solution for the stress in backfilled stopes by applying the stress state at a point in the plane:

$$\sigma_{av} = \frac{\gamma B - 2c'}{2\mu'} \left(1 - e^{-\frac{2\mu'}{B} z} \right) + q e^{-\frac{2\mu'}{B} z} \quad (2-69)$$

$$\sigma_{hT} = K_{Yan}\sigma_{av} \quad (2-70)$$

$$\sigma_{hL} = K_L\sigma_{av} \quad (2-71)$$

with

$$c' = \frac{c \sin 2\beta \frac{\tan \delta_1 + \tan \delta_2}{2} + \frac{c_1 + c_2}{2} + \frac{c_3 + c_4}{2} \frac{B}{L} \sin \beta}{\sin \beta (\sin \beta - \cos \beta \tan \delta_2)} \quad (2-72)$$

$$\mu' = \frac{K_{Yan} \frac{\tan \delta_1 + \tan \delta_2}{2} + \frac{B \sin \beta \tan \delta_3 + \tan \delta_4}{L} K_L}{\sin \beta (\sin \beta - \cos \beta \tan \delta_2)} \quad (2-73)$$

$$K_{Yan} = K_0 \sin^2 \beta + \cos^2 \beta + K_0 \tan \varphi \sin 2\beta \quad (2-74)$$

where σ_{av} (kPa) is the average vertical stress across the width; σ_{hL} (kPa) and σ_{hT} (kPa) are the longitude and transversal horizontal stress, respectively; K_{Yan} is the backfill pressure coefficient used in their solution; K_L the ratio between the σ_{hL} and σ_{av} .

Their analytical solution was validated against the experimental results obtained by Take and Valsangkar (2001). However, the same limitation as the solution of Ting et al. (2011) existed in the proposed solution as it is impossible for a given point simultaneously yielding in two directions.

2.1.1.3 Summary

Table 2-2 shows a summary of the above-mentioned analytical solutions. Although more and more factors have been taken into account in the previous analytical solutions, more improvements can be made by accounting for the backfilling sequence, backfill inhomogeneity, and dynamic response of the backfill due to blasting.

Although cohesion is considered in several analytical solutions (Terzaghi 1943; Askew et al. 1978; Li et al. 2005, 2006; Ting et al. 2011; Xu et al. 2018), their applicability and reliability remain uncertain. When the backfill cohesion reaches a certain value, the stress calculated by these equations can become zero and even negative. This does not correspond to the numerical results shown by Li and Aubertin (2009e). Besides, these factors are usually considered separately in the existing analytical solutions. Further efforts are still needed to overcome these overly simplifying assumptions.

Table 2-2: Summary of the analytical solutions for the stress state in backfilled stopes

Analytical solutions	β^1	δ^2	c^3	q^4	$3D^5$	$D-\sigma_v^6$	W^7	c_v^8	Others ⁹
Askew et al. (1978)			√						
Knutsson (1981)									√
Aubertin et al. (2003)		√							
Li et al. (2005, 2006)		√	√		√				
Caceres (2005)	√								
Pirapakaran and Sivakugan (2007a)		√			√				
Li and Aubertin (2008)		√				√			
Li and Aubertin (2009c)							√		
Li and Aubertin (2009d)		√	√		√		√		
Ting et al. (2011)	√	√	√	√					
Singh et al. (2011)	√	√				√			
Ting et al. (2012)									√
Sivakugan and Widisinghe (2013)		√			√				
Rajeev et al. (2016)		√			√				
Hong et al. (2016)									
Jahanbakhshzadeh et al. (2017)	√	√				√			
Jahanbakhshzadeh et al. (2018b)	√	√			√	√			
Jaouhar et al. (2018)		√				√			
Xu et al. (2018)		√	√	√		√			
Zheng et al. (2019)								√	
Yan et al. (2019)	√	√			√				

Notes: 1. for inclined stopes; 2. interface friction angle considered; 3. cohesion considered; 4. surcharge considered; 5. three-dimensional situation; 6. nonuniform distribution of vertical stress across the width considered; 7. pore water pressure considered; 8. consolidation effect of the backfill considered; 9. other factors, for example, confining stress of the rock and other methods used.

2.1.2 Numerical simulations

Compared to analytical solutions, numerical simulations are more efficient to analyze the stress state in backfilled stopes as many influencing factors can be considered, including stope geometry, inhomogeneity of the backfill and filling sequence, etc.

2.1.2.1 Backfilled stopes with vertical walls

2.1.2.1.1 Modeling using TNJTEP and NONSAP

Barrett et al. (1978) performed numerical modeling using TNJTEP, a 2D finite-element program, and later using NONSAP, a 3D finite-element program, to assess the stress state in the backfill of primary stopes. Arching effects occurred in all the numerical models. In the 2D numerical models, the backfill was firstly considered as linearly elastic and secondly as elastoplastic, respectively. It is found the vertical stress was almost the same in the two conditions, while the horizontal stress was oscillating when the nonlinearity of backfill is not considered. Compared to the 2D linearly elastic models, the numerical simulations with the 3D linearly elastic models showed smaller vertical stress.

2.1.2.1.2 Modeling arching effects using PHASE²

Aubertin et al. (2003) conducted numerical simulations with PHASE² (RocScience 2002) to evaluate the stress state in backfilled stopes. The arching effect was confirmed in the backfilled stope. The numerical results were compared with the analytical solution based on the Marston theory using the at-rest, active, and passive earth pressure coefficients, respectively. A relatively large difference was observed. Both the vertical and horizontal stresses around the mid-height of the backfilled stope were much higher than the overburden stress, which was due to the confining effects caused by the inward displacement of the sidewalls in the numerical modeling.

2.1.2.1.3 Modeling arching effects using FLAC

Li et al. (2003) applied FLAC to estimate the stresses in delayed backfilled stopes using the same geometry and material properties as Aubertin et al. (2003). In the numerical simulations, the stope was first excavated instantaneously in one step and then filled in one step after resetting the wall

displacement induced by excavation to zero. With this mining sequence, the wall closure will not be considered.

Figures 2-9a and 2-9b show both the vertical and horizontal stresses are higher in the center than those near the wall at a given depth, indicating the occurrence of arching effects. Figures 2-9c and 2-9d show that the Marston theory underestimates the stresses in backfilled stopes. Li et al. (2003) also presented that the horizontal stress was uniform across the width while the vertical stress distributed nonuniformly.

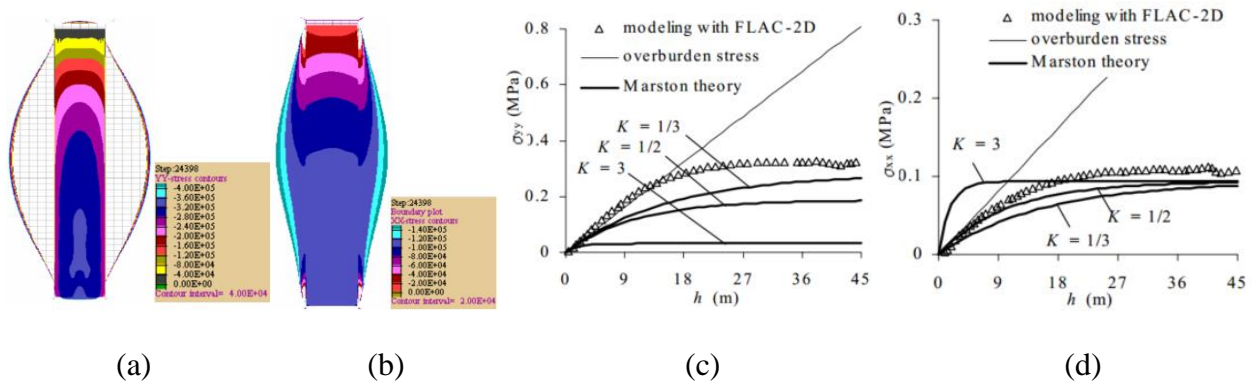


Figure 2-9: Stress contours in the backfill: (a) the vertical stress and (b) the horizontal stress; comparisons of the analytical and numerical results: (c) the vertical stress and (d) the horizontal stress (taken from Li et al. 2003)

Pirapakaran and Sivakugan (2007a) investigated the influence of filling layers on the stresses in backfilled stopes using FLAC. Their results show that numerical models with several filling layers would induce more realistic results compared to the numerical models with one filling layer. Good agreements were obtained between the numerical results and the analytical results by considering $\delta = (2/3) \varphi$ and $K = K_0$.

2.1.2.1.4 Three-dimensional models with FLAC3D

Pirapakaran and Sivakugan (2007b) analyzed by 3D numerical modeling with FLAC3D their laboratory tests performed with a square stope model. A good agreement was observed between the numerical and experimental results.

FLAC3D was further applied by Pirapakaran (2008) to model a square stope 10 m wide, 10 m long and 60 m high while FLAC was used to model a narrow 2D stope 10 m wide and 60 m high and a

circular slope with 10 m in diameter and 60 m in height. As shown in Figure 2-10, the vertical stresses of the circle slope obtained by numerical modeling with FLAC and those of the square slope obtained by numerical modeling with FLAC3D agree well, but much smaller than the vertical stresses of the narrow 2D slope obtained by numerical modeling with FLAC. These results indicate the importance of taking into account the 3D geometry of backfilled slopes when the third dimension is not significantly larger than the two other dimensions.

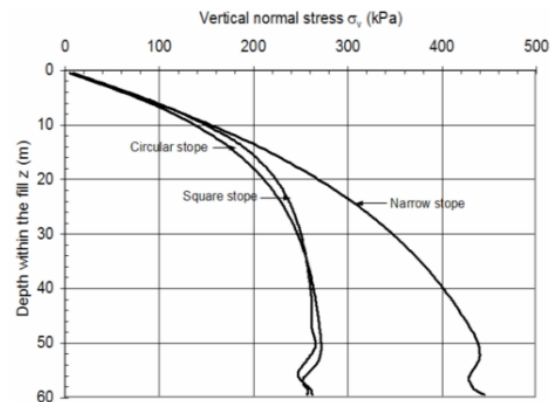


Figure 2-10: Vertical stress along the central line of the backfill (taken from Pirapakaran 2008)

2.1.2.1.5 Plain-strain and axisymmetric models with PLAXIS 2D

Fahey et al. (2009) used PLAXIS 2D to model a plain-strain slope 20 m wide and 50 m high and an axisymmetric slope 20 m in diameter and 50 m in height. Their numerical results show that the stresses under plain-strain conditions are much larger than those in axisymmetric conditions, as shown in Figure 2-11.

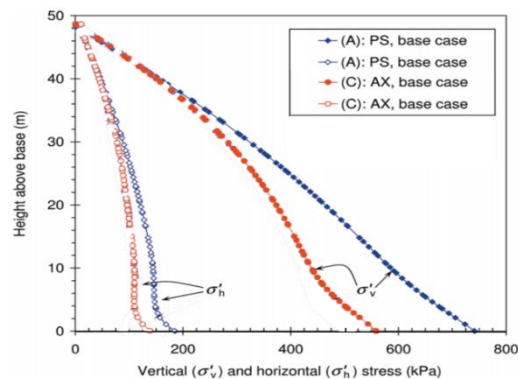


Figure 2-11: Vertical and horizontal stresses for a plain-strain (PS) slope and an axisymmetric (AX) slope (taken from Fahey et al. 2009)

2.1.2.1.6 Drainage and consolidation

Fahey et al. (2009) also investigated the stress state in backfilled stopes by considering the drainage and consolidation during and after backfilling. According to whether there are drainage and consolidation during the filling, three filling types, namely undrained filling, drained filling, and partially drained filling, were considered. Figure 2-12a shows that the total horizontal and vertical stresses at the end of filling were almost equal to the overburden stress in undrained filling conditions. Then the stresses decreased during the consolidation procedure due to the drainage and arching effect. In partially drained filling conditions, a larger value of hydraulic conductivity of the backfill could cause a decrease in the vertical stress at the base (shown in Figure 2-12b) and a more significant decrease in the horizontal stress. Besides, the final stress state of the backfill (after drainage and consolidation) was almost the same regardless of the filling type.

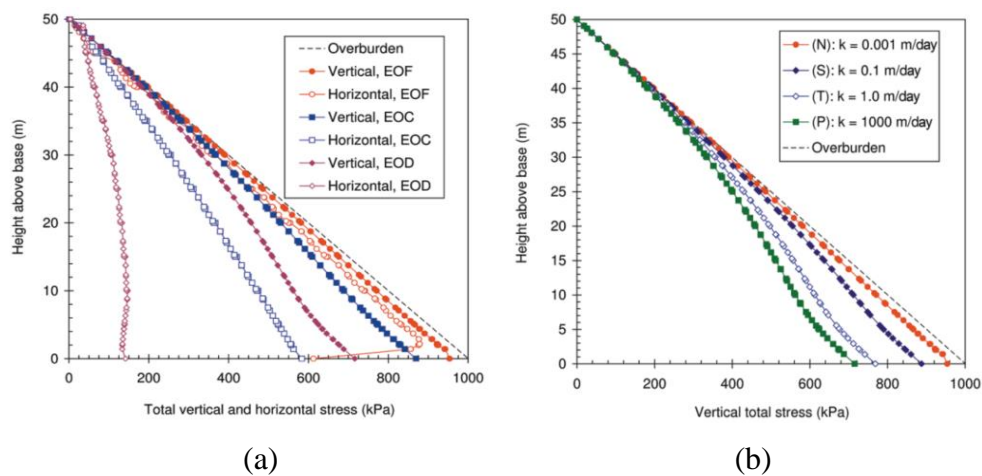


Figure 2-12: (a) Total stress at the end of filling (EOF), consolidation (EOC) and drawdown (EOD) in undrained filling process and (b) at the end of filling in partially drained filling process (taken from Fahey et al. 2009)

2.1.2.1.7 Pore water pressure

Li and Aubertin (2009c) performed numerical simulations with FLAC to evaluate the influence of hydrostatic water pressure on the effective and total stresses in backfilled stopes. Three conditions, namely partly submerged, submerged and overly submerged backfill, were taken into account. The numerical results showed that a transition of the stresses occurred at the phreatic surface in partly

submerged backfill. In submerged and overly submerged backfill, the effective stresses were found to correlate well with those predicted by the Marston solution using effective backfill properties.

2.1.2.1.8 Kink effects observed with FLAC

Sivakugan et al. (2014) analyzed by numerical modeling the vertical stresses at the bottom as a function of fill thickness (Method 1, stress-thickness profile) and at different positions as a function of depth (Method 2, stress-depth profile) along the vertical central line of backfilled stopes. As shown in Figure 2-13, their numerical results show that the stress-depth profile (Method 2) is lower than the stress-thickness profile (Method 1), except near the top and base where the vertical stresses obtained by the two methods are identical. In the stress-depth profile, a sudden increase in the stress occurred near the bottom. This phenomenon was called kink effects by Sivakugan et al. (2014), which was due to the not fully mobilized friction caused by the fixed boundary condition at the bottom in the numerical modeling.

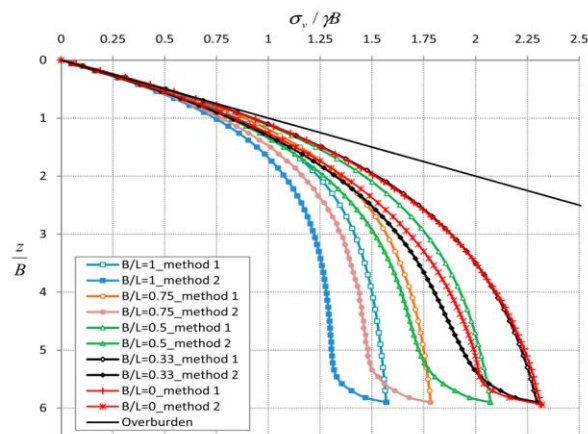


Figure 2-13: Vertical stress along the central line of the backfilled stope with different widths (taken from Sivakugan et al. 2014)

2.1.2.1.9 Fill-wall interface elements

In numerical modeling of the stresses in backfilled stopes, the use of interface elements between backfill and rock walls was subjective. Liu et al. (2017) investigated the influence of interface elements on the stress state in backfilled stopes using numerical models with FLAC. Their numerical results indicated that the vertical and horizontal stresses decreased with the increase of the interface friction angle. Both the vertical and horizontal stresses decreased as the interface

cohesion increased from 0 to 25 kPa but became almost constant when the cohesion exceeded 25 kPa and further increased. In addition, the stress state was found to be more associated with the interface properties other than fill properties. When the interface friction angle was equal to the fill friction angle, the use of interface elements did not change significantly the stress state in backfilled stopes.

Liu et al. (2016) also investigated the influence of nonplanar interfaces in the form of saw teeth on the stress distribution in backfilled stopes, as shown in Figure 2-14a. Figure 2-14b indicated that the obtained stresses were lower than those obtained by numerical modeling with planar ($\theta = 180^\circ$) interfaces. Besides, their numerical results also showed that it was unnecessary to consider interface elements if the nonplanar interfaces were rough enough.

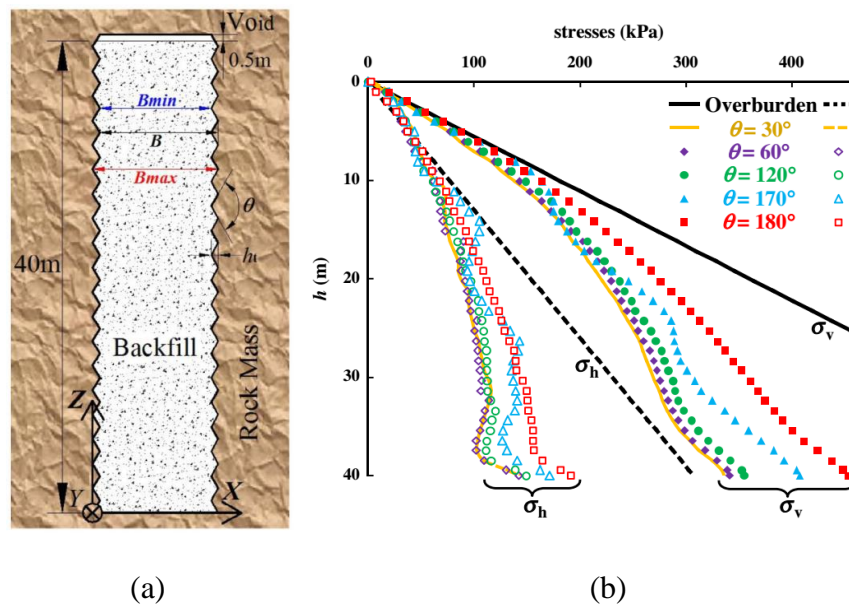


Figure 2-14: (a) A model of the stope with nonplanar interfaces and (b) the stresses along the height of the stope with different values of saw-teeth angle ($\theta = 180^\circ$ is the condition with a planar interface) (taken from Liu et al. 2016)

2.1.2.1.10 Effects of adjacent excavation and backfilling

Falakhnaz et al. (2015a) conducted numerical simulations with FLAC to investigate the stress state in two adjoining stopes sequentially excavated and backfilled. The obtained stress iso-contours are shown in Figure 2-15. The numerical results indicated that after the second stope was backfilled,

the horizontal stress in the backfill of the first stope was higher than that of a single stope while the vertical stress was almost the same. Besides, their results showed that the effects of stope width, friction angle, cohesion, and dilation angle on the stress state in the first backfilled stope followed the same trend as those in a single stope presented by Li and Aubertin (2009e). As the depth of the stopes increased, the horizontal stress in the first stope increased below the midheight of the stope while the vertical stress only increased slightly near the bottom of the stope. It was also reported that the stresses in the backfill of the second stope were similar to those in the backfill of a single stope.

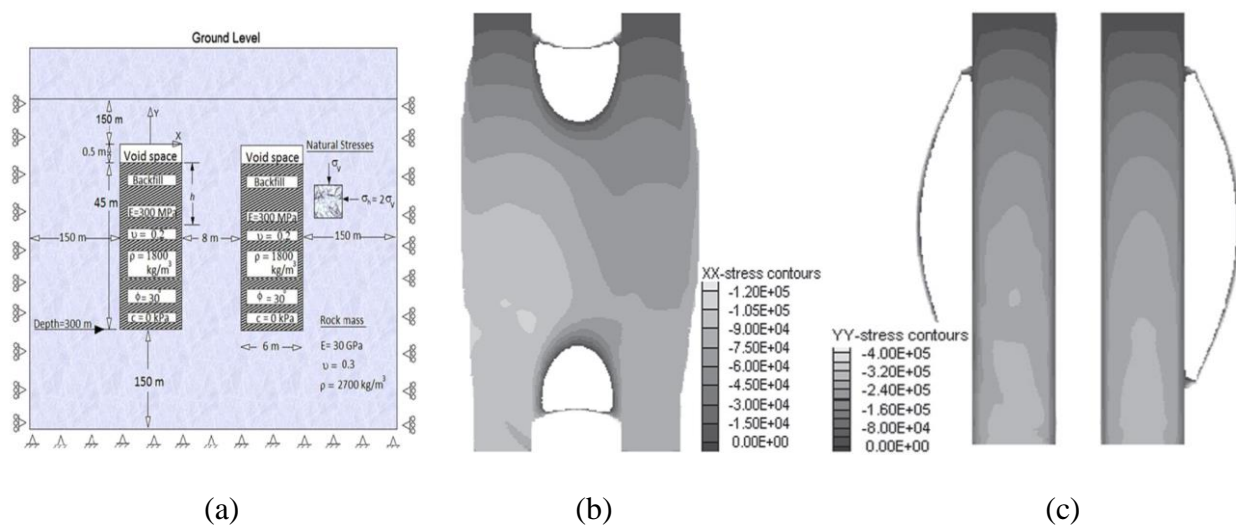


Figure 2-15: Numerical simulations of stresses in backfilled stopes by considering adjacent stopes: (a) a model with two stopes; numerical results of the (b) horizontal and (c) vertical stresses at the end of the filling process of the second stope (taken from Falaknaz et al. 2015a)

Falaknaz et al. (2015b) also performed numerical simulations by considering the effect of relating the internal friction angle and Poisson's ratio through the at-rest earth pressure coefficient. Their numerical results showed that increasing pillar width between the two neighboring stopes led to a decrease in the stresses in the first stope during the excavation and backfilling of the second stope. The effect was more significant for cohesive backfill material. In addition, when the elastic modulus of the rock mass diminished, the stresses in the first stope increased, especially at larger depth. The stress path along the vertical central line indicated that the fill material in the first stope yielded at some stages due to the loading and unloading process during the excavation and backfilling operations of the second stope.

By considering the rock mass as elastoplastic, Falaknaz et al. (2015c) further evaluated the influence of the rock mass properties on the stress distribution in two sequential-created adjacent stopes. Their numerical results indicated that the stresses in the first stope with an elastoplastic rock mass were different from those with an elastic model. However, the influences of the stope width and depth, the pillar width, and the rock mass modulus on the stresses in the first stope showed the same trends as those in the first stope with elastic rock mass. An increase of the natural stress ratio resulted in an increase of the stresses in the first stope after the filling of the second stope.

Newman et al. (2018) conducted numerical simulations with RS2 (RocScience, 2018) to investigate the stress distribution in the adjacent rock mass as well as in the fill material. The stopes were filled in 5 layers. Their numerical results indicated that both the vertical and horizontal stresses in the rock mass after excavation will return to far-field stress at a large distance from the stope wall. The distance was dependent on the in-situ stress ratio. It was also seen that tensile stress occurred near the walls. They also reported that the increase in vertical stress near the bottom of the backfilled stope was induced by the stress continuity in the numerical modeling, which caused the stress to transfer from the surrounding rock mass to the fill material.

Newman and Agioutantis (2018) used RS2 to evaluate the stress distribution in the fill material and surrounding rock mass for the case of two adjacent stopes which were sequentially excavated and backfilled. After the excavation and backfill processes of the second stope (Stope B), the vertical stress along the vertical central line (VCL) of the first stope (Stope A) increased slightly while the horizontal stress increased significantly, as shown in Figure 2-16. For the second stope, the stress distribution was similar to that in a single backfilled stope. Besides, a nonlinear compressive state was found in the stress distribution in the rock pillar, which was induced by the tensile stress developed near the pillar back and floor.

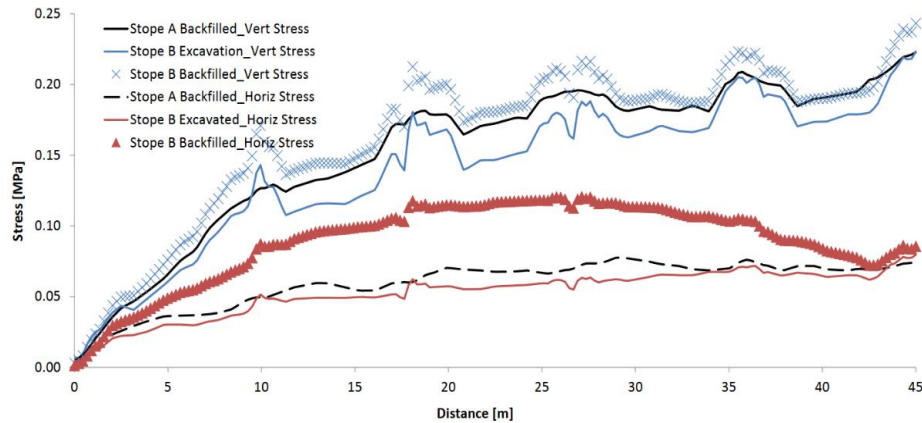


Figure 2-16: The stress distributions within the backfill of the first stope (Stope A) along the VCL due to the excavation and backfilling of the second stope (Stope B) (taken from Newman and Agioutantis 2018)

2.1.2.1.11 Modeling the backfill using DEM program

Hasan et al. (2017) used a numerical code, called YADE based on the discrete element method (DEM) to investigate the stress distribution in backfilled stopes and the influence of wall friction. As shown in Figure 2-17a, the vertical stress reached its maximum at about a quarter of the total backfill height, which corresponded well with the experimental results of Knutsson (1981). In Figure 2-17b, the decrease in contact point ratio is significant (about 6%) at the wall compared with that in the center for frictional walls. Besides, their numerical results also showed that the change in the shear force direction was more obvious for the backfilled stopes with frictional walls.

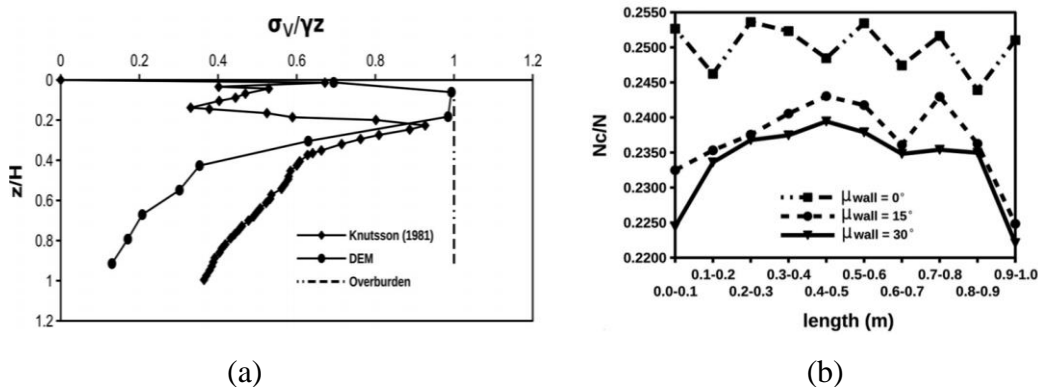


Figure 2-17: (a) Comparisons of the normalized vertical stress between the numerical and the experimental results; (b) contact point ratio across the width (taken from Hasan et al. 2017)

2.1.2.1.12 Modeling the backfilling procedure with ABAQUS

Xu et al. (2018) conducted numerical simulations using ABAQUS to verify their proposed analytical solution. The arching effect was observed according to the stress state contours. Moreover, it is indicated that a relatively good agreement was observed between the stresses obtained in numerical simulations and those calculated with Eq. 2-36.

2.1.2.1.13 Creep behavior of the rock mass

Qi and Fourie (2019) performed numerical simulations with FLAC by considering the creep behavior of rock mass (CBRM) to study the abnormal increase of the stresses in backfilled stopes after completion of backfilling. They used the Burger creep visco-plastic model (CVISC) to simulate the creep behavior of rock mass and the Mohr-Coulomb elastoplastic model (MC) to represent the mechanical behavior of backfill. The variations of the backfill stiffness and cohesion were also taken into account based on the curve-fitting expressions proposed by Helinski (2007). As shown in Figure 2-18a, both the vertical and horizontal stresses were smaller than the overburden stress and the vertical stress is higher than the horizontal stress at half-day after the filling process. In this stage, the stresses are mainly dependent on the self-weight of backfill and arching effects. Figure 2-18b shows that, at 3 days after the backfilling, both the stresses were much higher than the overburden stress and the horizontal stress become larger than the vertical stress. It can be attributed to the confining effects caused by rock displacement.

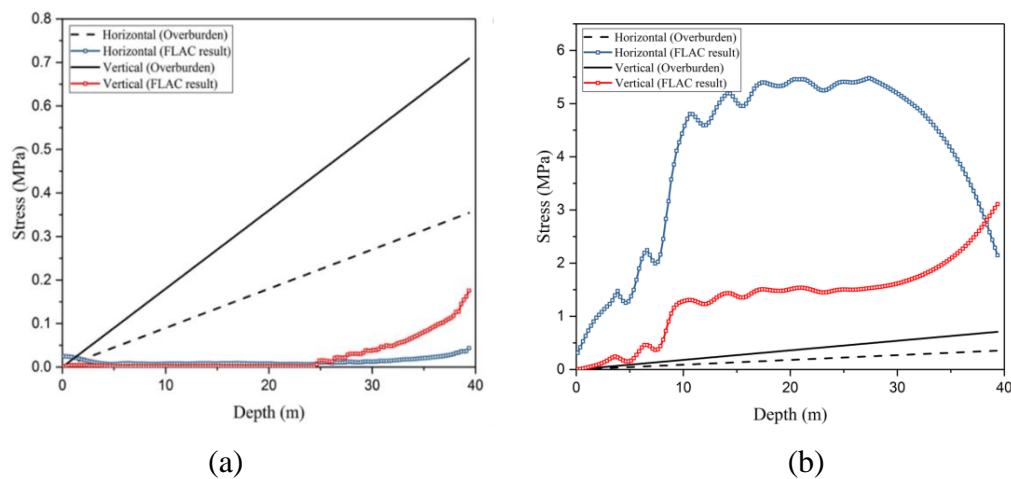


Figure 2-18: Horizontal and vertical stresses along the VCL with time: (a) half day, and (b) 3 days (taken from Qi and Fourie 2019)

Their proposed modeling framework was applied in Baixiangshan Iron Mine. A good agreement was obtained between the field measurement and numerical results. The stresses increased significantly with an increase in the backfill stiffness but were relatively insensitive to the variation of the backfill cohesion. A gap at the top of the backfill caused a decrease in the stress in the upper part of the stope but had an insignificant influence on the stresses near the lower part of the stope. The backfill placement delay could result in a larger horizontal displacement of the rock mass and lower stress in the backfilled stope.

2.1.2.2 Backfilled stopes with inclined walls

2.1.2.2.1 Modeling arching effects

Aubertin et al. (2003) also conducted some numerical simulations using PHASE² for stopes with a wall inclination angle of 45°. The obtained stress distribution was different from that in vertical stopes. The vertical stress was found to vary significantly across the width of the backfilled stope. The maximum vertical and horizontal stresses along the depth occurred at the mid-height of the backfill. The results were similar to those in vertical stopes they obtained.

Li et al. (2003) carried out numerical simulations for inclined stopes using FLAC. The results showed that the horizontal stress along the central line was predicted well by the Marston (1930) solution while the vertical stress was underestimated by the Marston (1930) solution.

2.1.2.2.2 Investigating the factors of influence using FLAC

Caceres (2005) evaluated the stress state in inclined backfilled stopes with FLAC. Figure 2-19a indicates the occurrence of arching effects in inclined backfilled stopes. It is also seen from Figure 2-19b that the vertical stress decreases as the wall inclination angle decreases and the maximum stress occurs near the footwall of the stope. Their numerical results also illustrated that the vertical stress would decrease as the backfill height increased. The vertical stress was found to increase proportionally with the increase in the backfill density. A higher internal friction angle could cause a decrease in vertical stress.

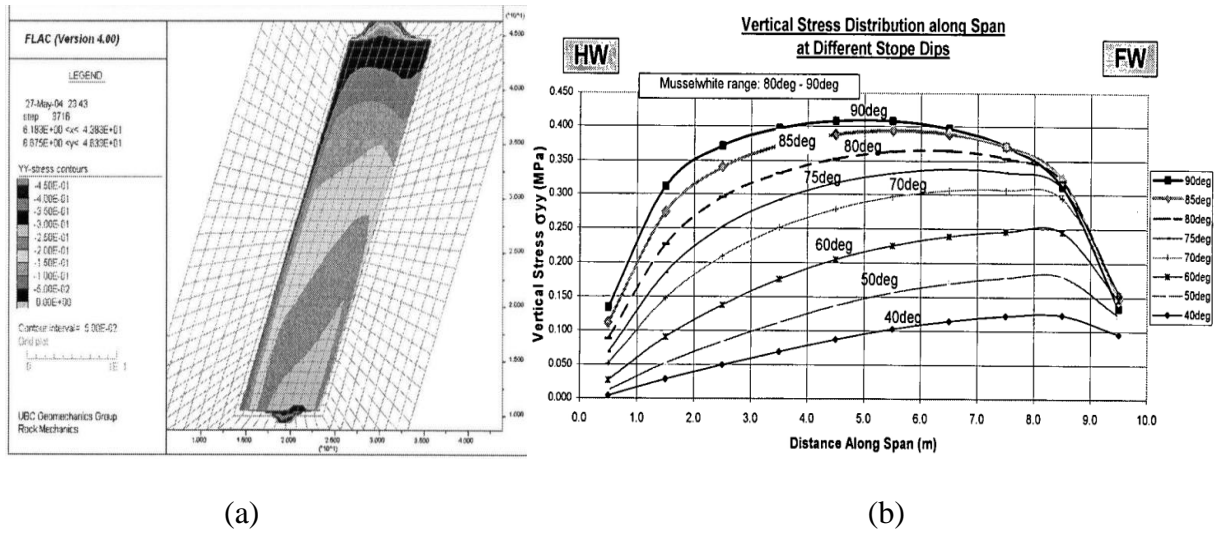


Figure 2-19: (a) Stress contours for inclined backfill with $\beta = 70^\circ$ and (b) the stress distribution across the width with different inclination angles (taken from Caceres 2005)

Li and Aubertin (2009e) performed many numerical simulations to investigate the influence of stope geometry and fill properties on the stress state along the hanging wall, footwall, and the central line. As shown in Figure 2-20, the horizontal stress seems to be insensitive to the variation of the wall inclination angle while the vertical stresses along the center line and hanging wall decrease as the wall inclination angle decreases from 90° to 60° . Along the footwall, the change of stress was irregular.

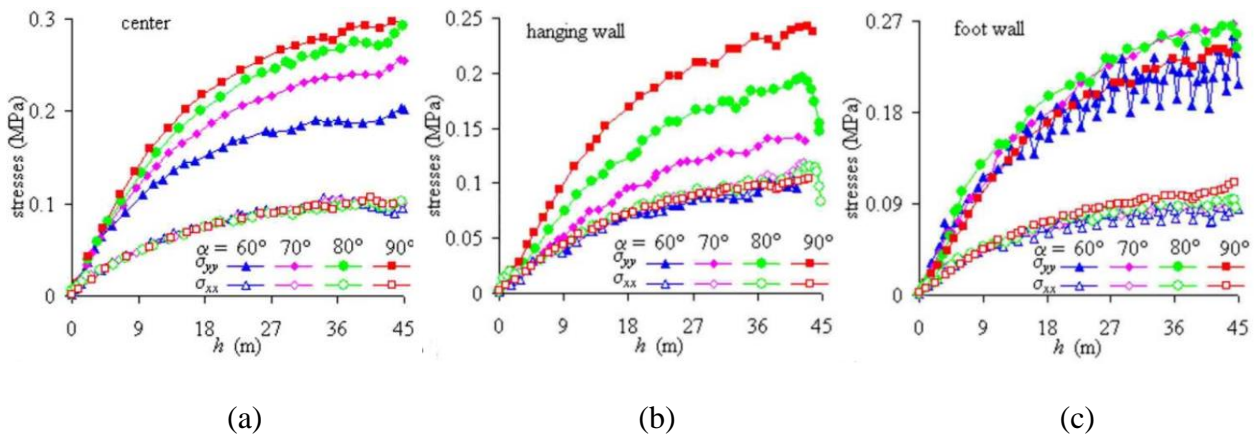


Figure 2-20: Stress variation for various inclination angles: (a) along the central line; (b) along hanging wall and (c) along footwall (taken from Li et al. 2009b)

The numerical results of Li and Aubertin (2009e) also showed that both the vertical and horizontal stresses decreased as the slope width decreased. Besides, both the vertical and horizontal stresses remained unchanged when the backfill Young's Modulus E changed, but below a value of about 300 MPa. The stresses became oscillatory as E increased to 3 GPa. When the Poisson's ratio μ increased, the horizontal stress tended to increase slightly whereas the vertical stress reduced significantly. As the internal friction angle φ increased from 10° to 40° , the horizontal stress decreased while the vertical stress became insensitive to the variation of the friction angle as long as its value exceeded 20° . As the cohesion c was small and increased, the stresses tended to decrease. When the cohesion was below 10 kPa, both the vertical and horizontal stresses increased linearly with the depth. However, the stresses became wavy when the cohesion was higher than 10 kPa and less than 50 kPa, indicating a change of mechanical behavior of the backfill from granular material to a beam-like material. Their results further showed that an increase of dilatation angle resulted in a decrease in both the vertical and horizontal stresses. The stresses became oscillatory once the dilatation angle was higher than 5° .

2.1.2.2.3 Three-dimensional models

Jahanbakhshzadeh et al. (2018b) applied FLAC3D to verify their proposed analytical solutions by considering related ν (Poisson's ratio) and φ (internal friction angle) through the at-rest earth pressure coefficient. The influences of slope width and length were evaluated. They concluded that the stress would decrease as the backfill length or width reduced. These results corresponded well with those reported by Li and Aubertin (2009e).

Yan et al. (2019) conducted numerical simulations with FLAC3D to verify their proposed analytical solutions. As shown in Figure 2-21a, their numerical results were first compared with experimental data of Take and Valsangkar (2001). The numerical simulations were then performed to validate their analytical solution for slopes with different wall inclination angles (shown in Figures 2-21b and 2-21c).

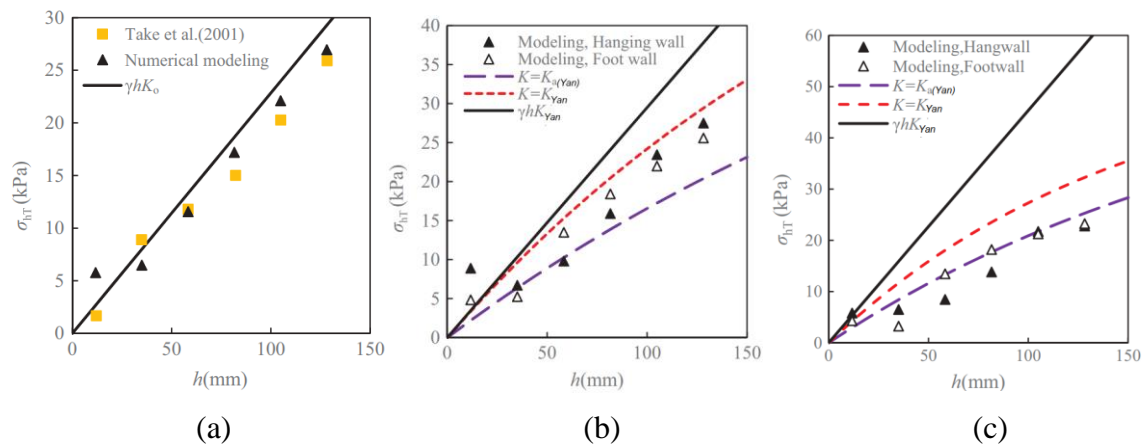


Figure 2-21: Comparisons of numerical results with (a) experimental results of Take and Valsangkar (2001) and analytical solution results with (b) $\beta = 80^\circ$ and (c) $\beta = 70^\circ$ ($B = 184$ mm, taken from Yan et al. 2019).

2.1.2.3 Summary

Table 2-3 shows a summary of the numerical modeling performed by different researchers to analyze the stress state in backfilled stopes.

Table 2-3: Summary of the numerical simulations for the stress state in backfilled stopes

References	Software	2D/ 3D	Vertical/ Inclined	Main work
Barrett et al. (1978)	TNJTEP/N ONSAP	2D/ 3D	Vertical	Evaluating the stress state in the backfill
Aubertin et al. (2003)	PHASE ²	2D	Both	Estimating the stress state in vertical and inclined stopes and comparing with Marston solution
Li et al. (2003)	FLAC	2D	Both	Considering the mining sequence and comparing with Marston solution
Caceres (2005)	FLAC	2D	Inclined	Investigating the factors influencing the vertical stress
Pirapakaran and Sivakugan (2007b)	FLAC	2D	Vertical	Comparing with their experimental data
Pirapakaran and Sivakugan (2007a)	FLAC	2D	Vertical	Backfilling in layers and comparison with the analytical solution they proposed
Li and Aubertin (2008)	FLAC	2D	Vertical	Used to calibrate and verify their analytical solution

Li and Aubertin (2009c)	FLAC	2D	Vertical	Considering pore water pressure and comparing with their analytical solution
Li and Aubertin (2009e)	FLAC	2D	Inclined	Investigating factors that influencing the stress state in inclined backfilled stopes
Fahey et al. (2009)	PLAXIS 2D	2D	Vertical	Investigating some aspects of mechanics of arching in backfilled stopes, for example, the difference between plain-strain and axisymmetric conditions and the effect of consolidation
Falaknaz et al. (2015a)	FLAC	2D	Vertical	Investigating the effect of adjacent excavation and backfilling on the stress in the backfill
Falaknaz et al. (2015b)	FLAC	2D	Vertical	Investigating the effect of adjacent excavation and backfilling considering a dependent relationship between the internal friction angle and Poisson's ratio
Falaknaz et al. (2015c)	FLAC	2D	Vertical	Investigating the effect of adjacent excavation and backfilling considering elastoplastic rock mass
Liu et al. (2016a)	FLAC3D	3D	Vertical	Investigating the effect of nonplanar interface elements on stress state in backfilled stopes
Liu et al. (2017)	FLAC3D	3D	Vertical	Investigating the effect of planar interface elements on stress state in backfilled stopes
Jahanbakhshzadeh et al. (2017)	FLAC	2D	Inclined	Verifying their analytical solution
Jahanbakhshzadeh et al. (2018b)	FLAC3D	3D	Both	Verifying their analytical solution for the stress state in 3D inclined stopes
Hasan et al. (2017)	YADE	2D	Vertical	Using DEM to model the arching effect in the backfill
Jaouhar et al. (2018)	FLAC	2D	Vertical	Verifying their analytical solution
Newman and Agioutantis (2018)	RocScience 2D (RS2)	2D	Vertical	Investigating the effect of adjacent excavation and backfilling on the stress in the backfill and rock pillar
Newman et al. (2018)	RocScience 2D (RS2)	2D	Vertical	Investigating the effect of adjacent excavation and backfilling on the stress in the backfill and rock pillar
Xu et al. (2019)	ABAQUS	2D	Vertical	Verifying their analytical solution
Qi and Fourie (2019)	FLAC	2D	Vertical	Considering the creep behavior of rock mass
Yan et al. (2019)	FLAC3D	3D	Inclined	Verifying their analytical solutions

It is worth noting that most previous numerical simulations were conducted mainly to verify some analytical solutions or compare them with experimental results. Only a few studies were devoted to purely numerical simulations. Although many factors have already been considered in numerical simulations, some other factors, such as the more complicated geometries and more realistic conditions, should also be considered in the future.

2.1.3 Relevant experimental tests

Experiments are usually believed to be the most appropriate way in research. However, experiments, especially field measurements in mining engineering can be complicated due to a number of uncertainties that can be involved. As existing experiments for investigating the stress state in backfilled stopes are quite rare, similar tests including backfilled silos, backfill behind retaining walls, backfill on trap doors, and backfilled trenches will also be presented. The reliability of the experiments will be discussed.

2.1.3.1 Backfilled stopes

2.1.3.1.1 In-situ experiments

Belem et al. (2004) carried out field experiments in two inclined stopes at Doyon Gold Mine with the measurements of the vertical and horizontal stresses in the center and horizontal stress at the footwall and the barricade, as shown in Figure 2-22a (see also Harvey 2004). The stope was filled in three layers and the measurement lasted for 320 days after the end of backfilling. The evolution of stress with the elapsed time and filling heights were assessed. The maximum stress at the base of the stope occurred at about the 10th day (shown in Figure 2-22b) during the filling of the second layer. The stresses as a function of the filling heights (stress-thickness profile) were also shown to be below the overburden stress, suggesting the occurrence of arching effects.

It is worth noting that when placing the pressure cell, the deviation from the ideal position was illustrated but neglected in their interpretation. The mentioned mining activities in the vicinity of the stope may also influence the measurement.

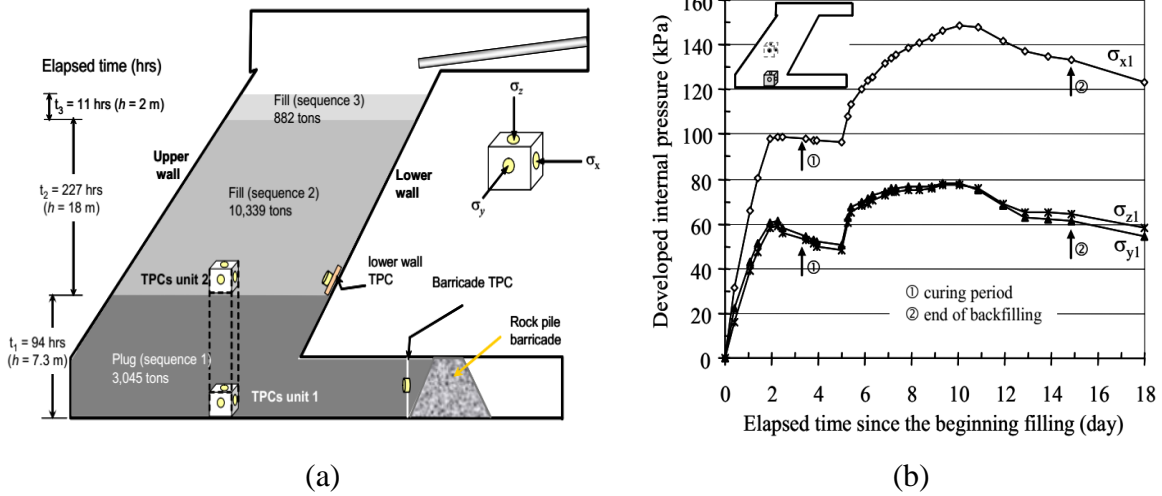


Figure 2-22: (a) Positions of measuring systems in the stope and (b) the stresses in the three directions at the base of the stope (taken from Belem et al. 2004)

Thompson et al. (2012) measured the vertical and horizontal stresses in two stopes (685 stope and 715 stope) at the Cayeli Mine. Figure 2-23a shows the measuring cages in stope 715. Both the total earth pressure (TEP) and the pore pressure (Pore P) were measured for 140 days. The degree of cement hydration was illustrated by recording the temperature in the fill material, which contributed a large part to the generation of effective stress. Comparisons of the stresses measured in the two stopes suggested that a high deposition rate and lower binder content would result in a higher pressure on the barricade.

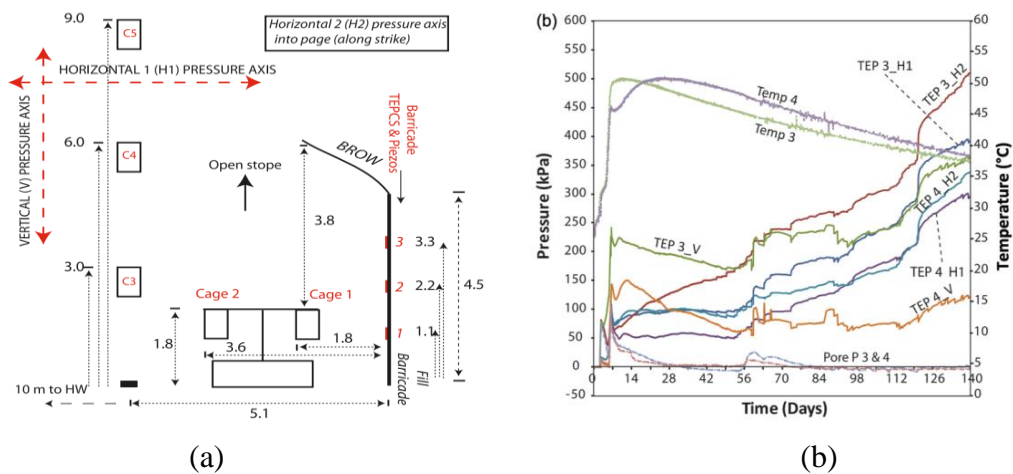


Figure 2-23: Measurements in the 715 stope: (a) measuring points and (b) long-term total earth pressures (TEP), pore pressures (Pore P) and temperature (Temp) for Cages 3 and 4 (taken from Thompson et al. 2012)

Wang et al. (2019) measured the vertical stress in a backfilled slope 70.91 m high with two stress boxes (shown in Figure 2-24a). The influence of the excavation of adjacent stopes was investigated and the measured stresses were plotted with time. As shown in Figures 2-24b and 2-24c, AB represents the backfill process of the monitoring stope; BC is the curing process of the cemented backfill; CD and DE are the excavation and backfilling of the secondary stope near the back wall of the primary stope, respectively; EF represents the condition when the cemented backfill was exposed in the front wall and pressed by the back wall and FG is the backfilling process of the stope excavated in the stage EF. It is found that the maximum stress occurs at point F.

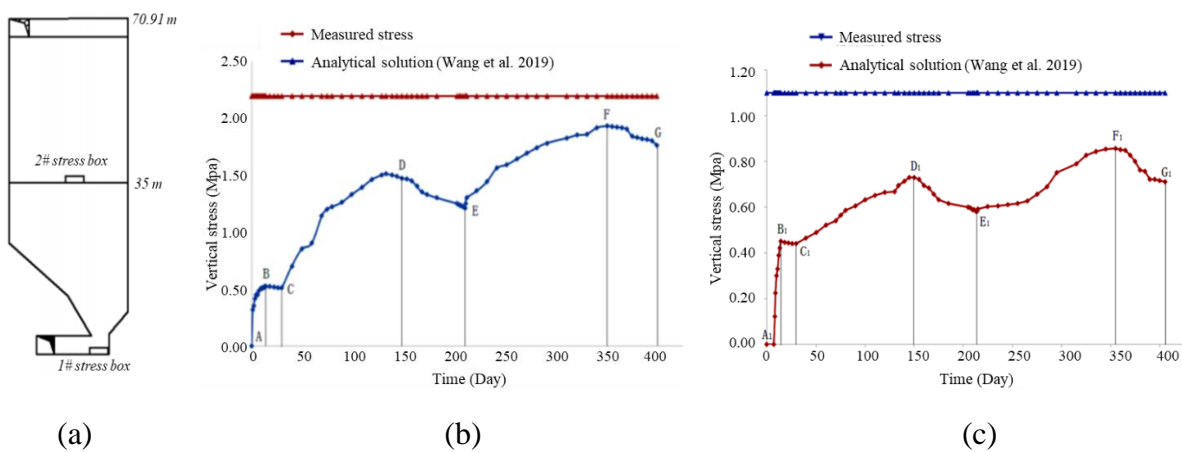


Figure 2-24: Field experiments: (a) The position of the stress boxes; (b) vertical stress of 1# stress box; (c) vertical stress of 2# stress box (adapted from Wang et al. 2019)

2.1.3.1.2 Laboratory models

Pirapakaran and Sivakugan (2007b) designed a laboratory apparatus to measure the vertical stress at the bottom of the square and circular columns filled with sand. By filling the column in layers, the vertical stress at the stope bottom with different filling heights was plotted and the arching effect was clearly observed. Besides, the measured stress was also successfully reproduced by numerical simulations conducted with FLAC and FLAC3D.

Ting et al. (2012) improved the apparatus of Pirapakaran and Sivakugan (2007b) to apply it to measure the vertical stress at the bottom of an inclined stope (shown in Figure 2-25a). Four strain gauges were placed on the outside surface of both sidewalls to analyze the shear stress and it was reported that shear stress at the footwall was higher than that at the hanging wall. Besides, it was

also indicated that a rougher wall surface led to lower vertical stress. As shown in Figure 2-25b, the vertical stress increased to its maximum at an inclination angle of 80° . Numerical simulations were also conducted with FLAC to model the experimental tests. It was seen that the numerical results agreed well with the measured stress in the column with rough and medium-roughness surfaces but underestimated the stress measured in the column with a smooth interface. However, it is unreasonable to place the strain gauges on the outside surface of the column. When the slope inclination angle changes, the gauges will no longer stay at the same height. Besides, there may be sand attached to the footwall especially for the case with a rough interface when filling the column, which may influence the measured stress.

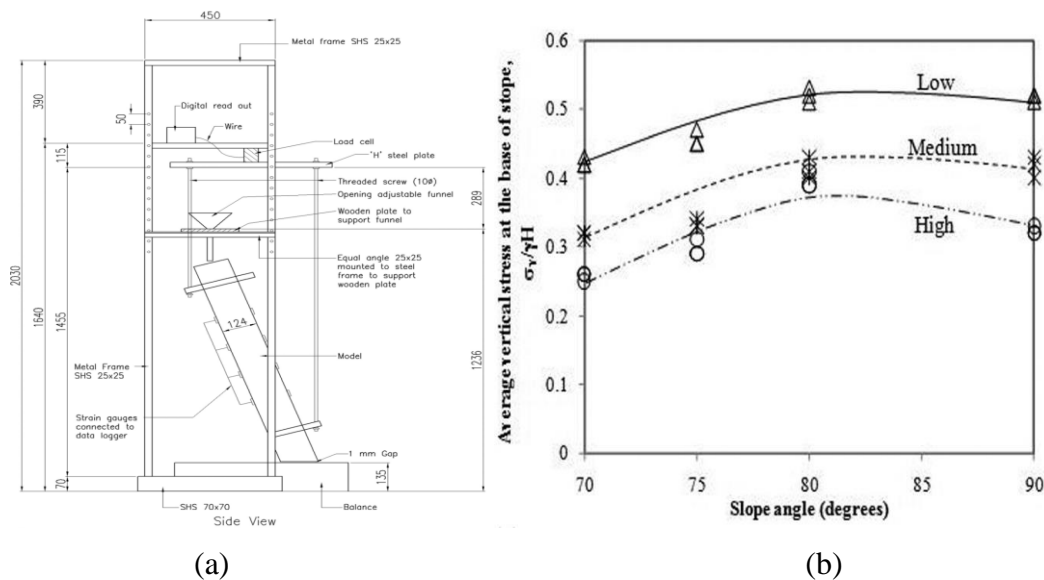


Figure 2-25: Laboratory tests measuring the vertical stress in inclined stopes: (a) a side view of the experimental apparatus and (b) the average vertical stress at the base with different inclination angles (taken from Ting et al. 2012)

Sivakugan and Widisinghe (2013) used the apparatus of Pirapakaran and Sivakugan (2007b), conducted additional experiments in circular and square stopes, and found the vertical stress increase linearly even at larger depth. These experimental results contradicted with those of Pirapakaran and Sivakugan (2007b). The possible reason may due to clearance between the stope and the balance. If the clearance is too small, the column is likely to contact with the bottom tray, and some loads carried by the wall will transform to the bottom.

2.1.3.2 Silos

2.1.3.2.1 *Experiments in square silos*

Janssen (1895) conducted experiments in four square silos with different side lengths and measured the vertical load on the bottom using corn, wheat, and rye as the filling material. The results showed the occurrence of arching effects in backfilled silos and the experimental results corresponded well with his proposed analytical solution. The experimental apparatus is simple, flexible, and effective, which has been extended for many experiments (Pirapakaran and Sivakugan 2007b; Ting et al. 2012; Han et al. 2018).

Jarrett et al. (1995) used pressure cells to measure the vertical and horizontal stresses in a square silo with a side length of 2 m and a height of 3 m. The large-scale laboratory tests showed that the horizontal stress at the corner of the wall was higher than that in the center of the wall and the difference enlarged with the increasing filling height, which could be explained by the variable deformation of the flexible walls. The vertical pressure showed a pronounced arching effect. The experimental results were compared with Janssen's analytical solution, and the pressure at the center of the wall was observed to be close to Janssen's theory using an active earth pressure coefficient. In their experiments, the pressure cells were placed 10 mm from the wall, but the way to fix the cells was not illustrated in detail. How to make sure that the pressure cells do not move or rotate throughout the experiments is an aspect to be considered.

2.1.3.2.2 *Experiments in circular silos*

Deutsch and Schmidt (1969) performed experiments to investigate the overpressures on the silo walls and found the lateral pressure on the walls during discharge could reach four times the static pressure within the pipe feed zone. The stress obtained from previous codes of practice were compared with the measured results, showing an underestimation of the pressure. Besides, the static pressure measured in the silo indicated Janssen's theory predicted well the stress when using an active pressure coefficient.

Blight (1986) carried out a series of experiments in full-scale silos to measure the horizontal stress during the continuously filling and emptying process (shown in Figure 2-26). The results indicated Janssen's theory fitted the measurements reasonably well during the filling and emptying process.

It is also seen that a lot of data falling outside the curve and the overburden stress using an at-rest earth pressure coefficient was suggested to provide an upper envelope for the horizontal stress in the filling process. In addition, the horizontal stress increased moderately at the start of the emptying process, but almost all the measurements fell inside the envelope defined by the overburden stress. In addition, horizontal stress was observed nonuniform in some cases and no significant switch pressure was found when the emptying process began.

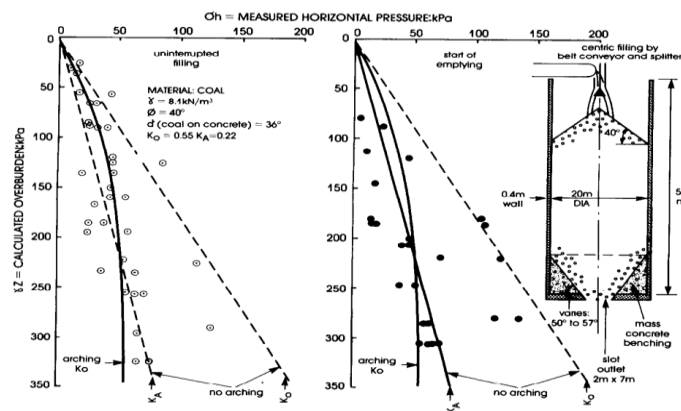


Figure 2-26: The horizontal pressure in a coal silo with 20 m in diameter and 54 m high (taken from Blight 1986)

Ramirez et al. (2010a, 2010b) performed large-scale laboratory experiments to measure the horizontal stress on the cylindrical silo walls during the filling and discharging process. The stress during the filling procedure was shown to be 20 to 30% higher than that based on the Janssen (1895) solution at the bottom part of the silo. It was due to the 5 mm recess from the inner surface of the silo wall where the pressure cells were mounted. During the discharging process, the horizontal stress was much higher than that during the filling stress.

Li et al. (2014) conducted laboratory tests to measure both the horizontal and vertical stress in the silo during backfill by wild pouring (shown in Figure 2-27a). The pressure sensors were calibrated before and after the installation. The variation of the fill density in different heights was investigated using experimental tests. An expression was proposed by the application of the curve-fitting technique on test results. Figure 2-27 shows that the vertical stress (measured by Sensor 1) was better described by the arching analytical solution with the Rankine's active earth pressure coefficient at large depth. The horizontal stress perpendicular to the pouring plane (measured by Sensor 3) was better described by the analytical solution using Jaky's at-rest earth pressure

coefficient while the one parallel to the pouring plane (measured by Sensor 2) was even higher than the overburden pressure. It was because of the lack of free face in the horizontal directions, limiting the full release of excess stress induced by the transient impact. However, the accuracy of the pressure measurements may not be very high due to the very large stiffness and thickness of the used cells. Besides, the measured vertical stress and horizontal stresses were not in the same heights, the calculation of the lateral earth pressure coefficient might not be accurate.

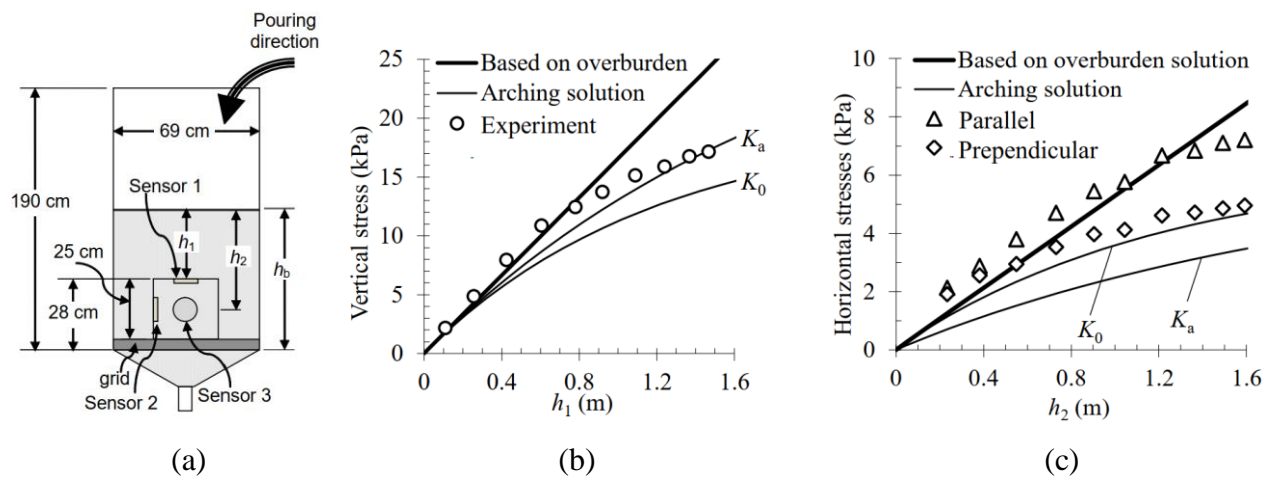


Figure 2-27: (a) Locations of pressure sensors in the backfilled silo; vertical (b) and horizontal (c) stresses measured and calculated with the analytical solutions (adapted from Li et al. 2014)

Han et al. (2018) designed a laboratory model to investigate the distribution of stress in the silo and verify Janssen's model (shown in Figures 2-28a and 2-28b). Earth pressure cells were used to measure the horizontal stress at the wall. Force sensors were applied to measure the friction force (force sensors 1) along the wall and the vertical load (force sensors 2) at the bottom. The measured vertical and horizontal stresses were observed to be slightly underestimated by those calculated by applying Janssen's arching theory. In Figure 2-28b, the ratio μ of the measured shear force to the horizontal force along the height was always smaller than $\tan \delta$, indicating a not fully mobilized shear at the fill-wall interface. The lateral pressure coefficient calculated by the laboratory data was also shown to be smaller than the Rankine's active earth pressure coefficient.

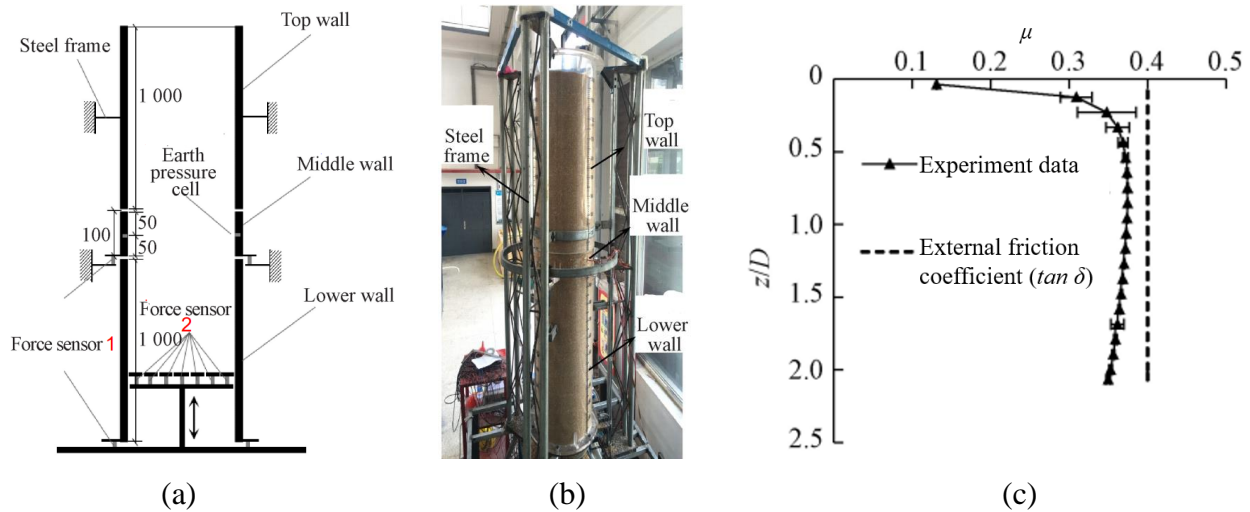


Figure 2-28: (a) a schematic diagram and (b) a photo of the laboratory model and (c) the variation of μ with the ratio z/D (z is the depth and D is the silo diameter) (adapted from Han et al. 2018)

2.1.3.3 Retaining walls

Frydman and Keissar (1987) conducted centrifuge tests to measure lateral earth pressure on retaining walls. In their model, the aluminum retaining wall could be rotated around its base by a disk to simulate an active state. The rockface modeled by wood was coated with a layer of sand on its surface to ensure the same friction angle with the fill material. For an at-rest state, the experimental results were in a fair agreement with the theoretical predictions. When the backfill was in the transition process from an at-rest to an active state, the modified coefficient tended to approach Rankine's active pressure coefficient of the sand.

Take and Valsangkar (2001) developed a centrifuge model to measure the lateral earth pressures on retaining walls. Soil and fluid were used for the calibration of pressure cells. The relationship between pressure cell output and the pressure was linear for fluid calibration but nonlinear for soil calibration. But it was not specified which one was used in the later calculation. Then the experiments were conducted using dense soil and loose soil with different wall roughness. Their experimental results demonstrated that Janssen's arching theory could be applied to describe the reduction of lateral earth pressure. In addition, the results showed that Janssen's theory using an average interface friction angle of the two side walls could better represent the stress distribution.

Yang and Tang (2017) measured the horizontal stress on the retaining walls at different heights using pressure cells (shown in Figure 2-29a). Three moving modes of the retaining wall were considered, namely translation mode (T), rotation around top mode (RT), and rotation around bottom mode (RB). The continuous and nonlinear failure surface was found related to the moving modes of retaining walls and backfill width. Figure 2-29b shows that the failure surfaces are all within the Coulomb failure surface with a sliding angle of $45^\circ + \varphi/2$. The measured horizontal stresses for all wall movement modes were smaller than those calculated by Coulomb's solution.

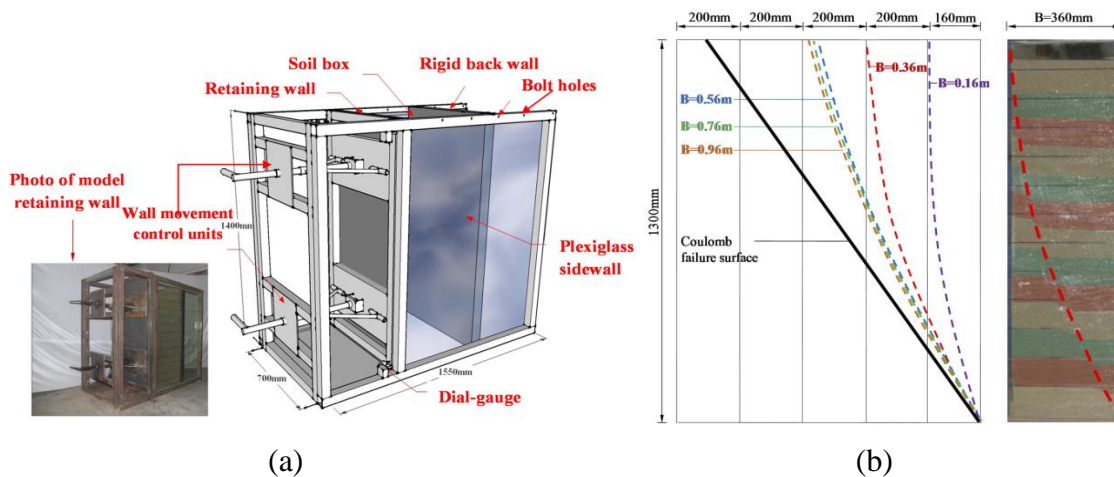


Figure 2-29: Experimental model and results: (a) a schematic model and (b) the failure surface of the backfill with translation mode (taken from Yang and Tang, 2017)

2.1.3.4 Trap doors

Terzaghi (1936) conducted a few trap-door experiments using dry sands and found that the lateral earth pressure coefficient was between K_0 and K_a . Besides, the pressure in saturated sand measured at the bottom of a permeable trap door corresponded well with the theoretical analysis. It was also stated that the change of the mass state due to vibrations may have an insignificant influence on the mobilization of the friction forces.

Ladanyi and Hoyaux (1969) measured the vertical stress acting on a vertically moving trap door to check the validity of the arching theory. Aluminum rods were used to simulate a granular material under a condition closer to 2D plane strain. An experimental apparatus was developed to measure the pressure on the trap door during upward and downward movement. The results indicated that the analytical solution of Janssen (1895) with the earth pressure coefficient $K = \cos^2\varphi/(1+\sin^2\varphi)$

predicted well the measured stress during a downward movement of the structure while the measured stress during an upward movement of the structure was in good agreement with that calculated by their proposed solution using the earth pressure coefficient $K = \cos^2 \phi$.

2.1.3.5 Trenches

Hong et al. (2016) developed an apparatus with an adjustable width to measure the vertical stress at the bottom of a trench. 12 groups of tests with 6 different widths and two densities were conducted. The results were compared with the Marston solution using different lateral earth pressure coefficients and interface friction angles. As shown in Figure 2-30a, a good agreement was observed when $\delta = 2/3\phi$ and $K = K_a$. The average product of K and $\tan \delta$ of the experimental results was 0.125 (shown in Figure 2-30b).

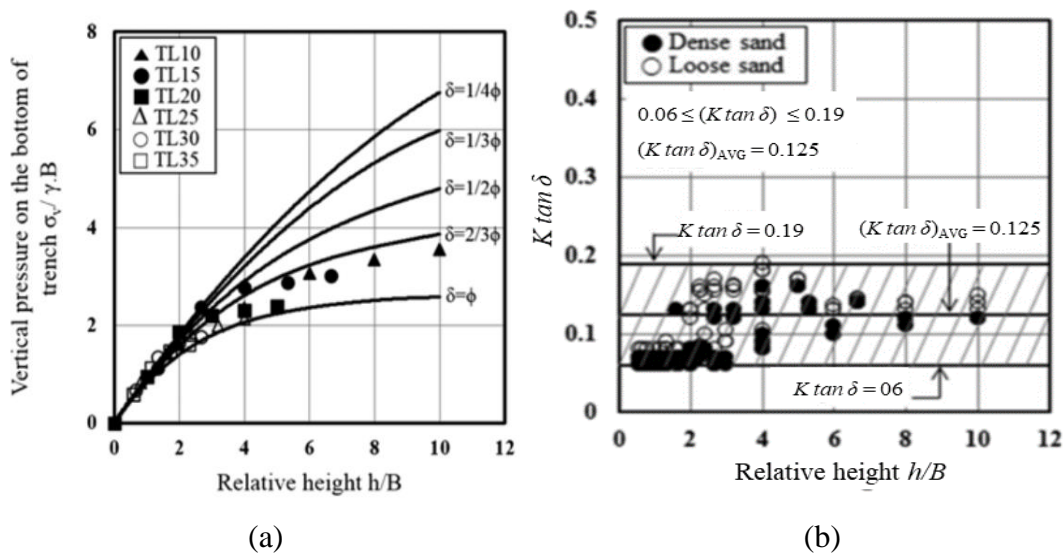


Figure 2-30: (a) Comparison between Marston solution and experimental results with loose sand and (b) variations of $K \tan \delta$ with the relative height (adapted from Hong et al. 2016)

2.1.3.6 Summary

Existing experiments to model backfilled slopes are quite limited, and more experiments are needed to validate analytical and numerical solutions, especially with the simultaneous measurements of the horizontal and vertical stresses, stress distribution along the depth as well as the stresses under saturated or unsaturated conditions.

Experimental results can help to better understand the stress state in backfilled stopes, but disadvantages are usually combined with advantages. Field measurements can reflect the complex geometry of backfilled stopes and real experimental conditions. However, it may be rather difficult to interpret the experimental results because even nearby activities can influence the measured stress. Besides, the high cost and long term of in-situ experimental may be another challenge. While in laboratory tests, many conditions can be controlled, including the material properties, model geometries, and testing methods. It is also easier to conduct a series of tests in a relatively short period. Whereas, laboratory models may be less representative of the real conditions. In both the laboratory and field experiments, the introduction of measuring systems may also affect the stress state. In addition, the disturbance of manual operation should be minimized.

2.2 Lateral earth pressure coefficient

The lateral earth pressure coefficient $K (= \sigma_h'/\sigma_v')$ is an important parameter in geotechnical and mining engineering. Throughout the years, many theories have been developed, among which Jaky's at-rest earth pressure coefficient, Rankine's active earth pressure coefficient, and passive earth pressure coefficient are usually used. The parameter is used in almost all the previous analytical solutions to calculate the vertical and horizontal stresses in backfilled stopes. However, which value should be used has been a debate for many years. It is important to have a good understanding and use of its value to obtain a good estimation of the stress state in the backfilled stopes.

2.2.1 Theory

2.2.1.1 Theoretical formulas of the earth pressure coefficient

In this section, only the equations for the lateral earth pressure coefficient will be presented. Detailed equations for the stress state using the coefficient can be found in Section 2.1.1.

2.2.1.1.1 At-rest earth pressure coefficient K_0

If a loose granular soil in a semi-infinite space is under normal consolidation without any horizontal strain, the soil is usually regarded as in an at-rest state and the at-rest earth pressure coefficient is commonly expressed by Jaky's semi-empirical equation as follows (Jaky 1948):

$$K_{0\varphi} = 1 - \sin\varphi' \quad (2-75)$$

In addition, for a homogeneous, isotropic, and linear elastic material, a theoretical formula using Hooke's law can also be used to determine the at-rest earth pressure coefficient:

$$K_{0\mu} = \frac{\mu}{1 - \mu} \quad (2-76)$$

2.2.1.1.2 Rankine's earth pressure coefficient

In geotechnical engineering, the value of the earth pressure coefficient K is usually related to the movement of the retaining wall. A wall of infinite stiffness and negligible thickness is placed in an initially at-rest soil in a semi-infinite space. Then the soil at one side of the wall is excavated without disturbing the soil at the other side. If the wall moves away enough from the remaining soil, the soil can yield and reaches an active state. The Rankine's active pressure coefficient K_a is calculated by the following equation (Rankine 1856):

$$K_a = \tan^2 \left(45^\circ - \frac{\varphi'}{2} \right) = \frac{1 - \sin \varphi'}{1 + \sin \varphi'} \quad (2-77)$$

If the wall moves sufficiently towards the soil, the soil can yield and reaches a passive state. The Rankine's passive pressure coefficient K_p is obtained by the following equation (Rankine 1856):

$$K_p = \tan^2 \left(45^\circ + \frac{\varphi'}{2} \right) = \frac{1 + \sin \varphi'}{1 - \sin \varphi'} \quad (2-78)$$

2.2.1.1.3 Krynine (1945) K_K

Due to stress rotation in the soil, the horizontal and vertical stresses are no longer the principal stresses. The principal stress ratio K_{ps} is different from the earth pressure coefficient. Krynine (1945) proposed an equation as follows for K at rough walls using the Mohr's circle:

$$K_K = \frac{1 - \sin^2 \varphi'}{1 + \sin^2 \varphi'} \quad (2-79)$$

2.2.1.1.4 Handy (1985) K_h

Handy (1985) proposed the following equation considering the stress rotation:

$$K_H = \frac{\cos^2 \theta + K_a \sin^2 \theta}{\sin^2 \theta + K_a \cos^2 \theta} \quad (2-80)$$

where θ is the angle between the minor principal stress and vertical direction.

For ideal smooth walls, the equation can be simplified to K_a with $\theta = 90^\circ$. For rough vertical walls, the equation can be simplified to K_K with $\theta = 45^\circ + \varphi/2$.

2.2.1.1.5 K obtained by curve fitting

Caceres (2005) obtained the following earth pressure coefficient K_C used in inclined stopes by curve fitting with numerical results conducted with FLAC (shown in Figure 2-31):

$$K_C = 1.4 \sin^2 \varphi - 2 \sin \varphi + 1 \quad (2-81)$$

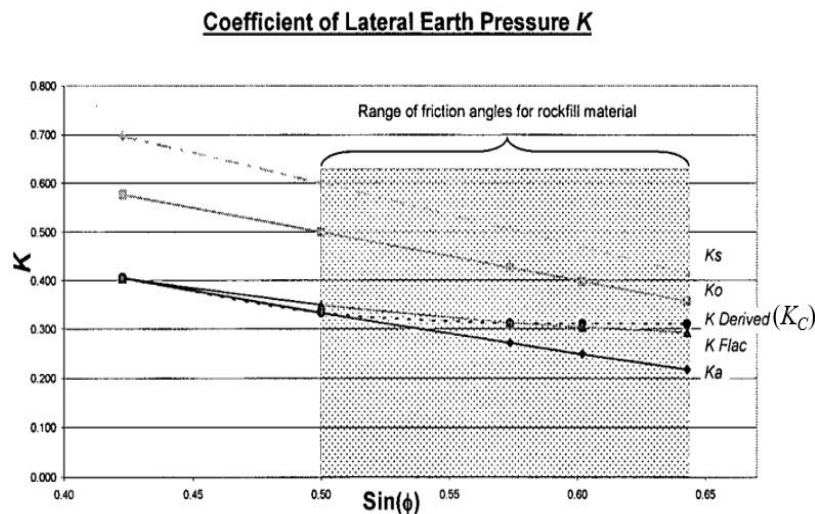


Figure 2-31: The earth pressure coefficient obtained from FLAC and curve-fitting derived for the rock friction angle range (taken from Caceres 2005)

2.2.1.1.6 Empirical coefficient

Jahanbakhshzadeh et al. (2017) also proposed a lateral earth pressure coefficient K_β by considering the nonuniform distribution of stress in inclined stopes:

$$K_\beta = K_a \times f_h \times f_w \quad (2-82)$$

$$f_h = (1 + \cos \beta) - \left(\frac{h}{H} \tan \varphi \cos^2 \beta \right) \quad (2-83)$$

$$f_w = 1 + 3 \left(1 - \frac{x_h}{B}\right)^4 \tan \varphi \cos(\beta - 10^\circ) \quad (2-84)$$

2.2.1.1.7 K obtained from theoretical analyses

Ting et al. (2012) applied the basic concept of soil mechanics to calculate the normal stress on a plane, and deduced the lateral earth pressure coefficient K_T in inclined stopes:

$$K_T = \frac{1 + K_0}{2} + \frac{1 - K_0}{2} \cos 2\beta + K \sin 2\beta \tan \delta \quad (2-85)$$

Sobhi et al. (2017) modified the formula of Ting et al. (2012) and proposed an equation for the earth pressure coefficient K_S along the central line of inclined stopes as follows:

$$K_S = \frac{1 + K_a}{2} + \frac{1 - K_a}{2} \cos 2\beta \quad (2-86)$$

Jaouhar et al. (2018) assumed a uniform minor principal stress σ_3 along the arc layer element and deduced a lateral earth pressure coefficient K_M in vertical stopes:

$$K_M = \frac{K_a - (1 - K_a) \left(\frac{x}{\xi_x B \kappa}\right)^2}{1 - (1 - K_a) \left(\frac{x}{\xi_x B \kappa}\right)^2} \quad (2-87)$$

2.2.1.1.8 K obtained from triaxial strength criteria

Sun et al. (2018) derived the earth pressure coefficient by considering the intermediate stress effect using four triaxial failure criteria. Using the Drucker-Prager (D-P) criterion led to the following expression for the earth pressure coefficient K_{DP} :

$$K_{DP} = \frac{3\sqrt{3} - (6 + \sqrt{3}) \sin \varphi}{3\sqrt{3} + (6 + \sqrt{3}) \sin \varphi} \quad (2-88)$$

Using the Matsuoka-Nakai (M-N) criterion, the earth pressure coefficient K_{MN} became:

$$K_{MN} = \frac{8}{3} \tan^2 \varphi + 1 - \frac{4}{3} \tan \varphi \sqrt{4 \tan^2 \varphi + 3} \quad (2-89)$$

Using the Lade-Duncan (L-D) criterion led to the following expression for the earth pressure coefficient K_{LD} :

$$K_{LD} = 1 + \frac{4 \tan \varphi}{27(1 - \sin \varphi)} \left[2 \tan \varphi (9 - 7 \sin \varphi) - \sqrt{(9 - 7 \sin \varphi)[27(1 - \sin \varphi) + 4 \tan^2 \varphi (9 - 7 \sin \varphi)]} \right] \quad (2-90)$$

Using the unified strength theory (UST), the earth pressure coefficient K_{UST} can be given as follows:

$$K_{UST} = \frac{(2 + b)(1 - \sin \varphi)}{2 + b + (2 + 3b) \sin \varphi} \quad (2-91)$$

The four analytical formulas were applied to calculate the wall pressures in silos, which were compared with previous measurements of wall stress in deep and squat silos. As shown in Figure 2-32, applying the UST method with $b = 0$ yielded the maximum pressure and overestimated the stress due to the total neglect of the intermediate stress effect. Applying the D-P method yielded the minimum pressure and underestimated the stress because of the overestimation of the intermediate stress effect. The best agreement was obtained between the measured pressures and those calculated by applying the L-D method.

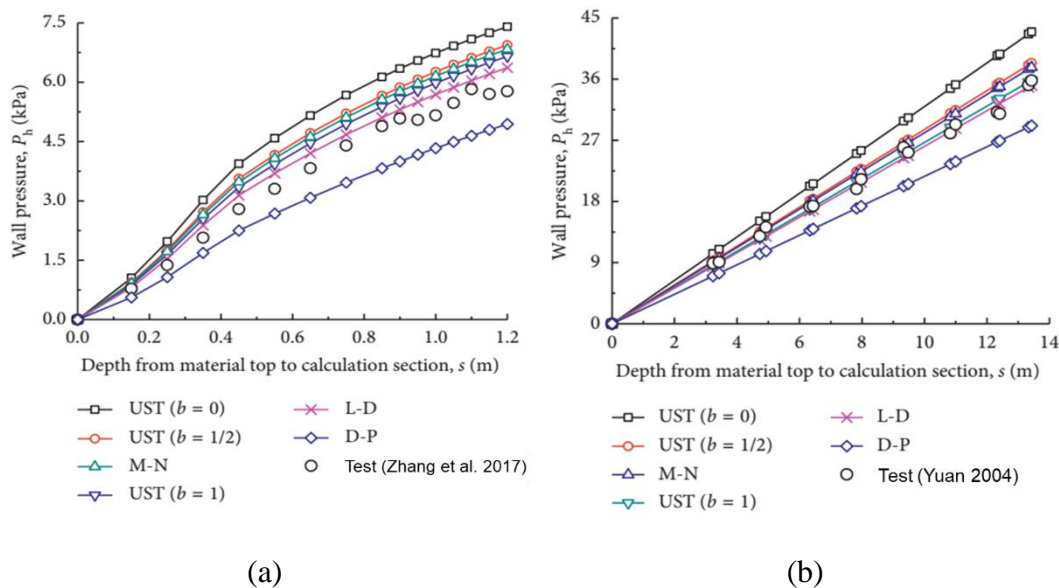


Figure 2-32: Comparisons between measured wall pressures and calculated pressures by applying analytical formulas for (a) deep silos and (b) squat silos (taken from Sun et al. 2018)

2.2.1.2 K used in analytical solutions

Table 2-4 shows a summary of the lateral earth pressure coefficient used in previous analytical solutions. It is seen that there is not a consensus about which value should be used to determine the stress state in backfilled stopes.

Table 2-4: K used in analytical solutions

Analytical solutions	K used	Notes
Janssen (1895)	μ/K_f	Obtained from experiments
Marston (1930)	K_a	--
Aubertin et al. (2003)	K_0, K_a, K_p	Used for comparisons
Li et al. (2005,2006)	K_0, K_a, K_p	Used for comparisons
Caceres (2005)	K_C	The fit curve from numerical results
Pirapakaran and Sivakugan (2007a)	K_0	$\delta=2/3\varphi$
Li and Aubertin (2008)	K_a	--
Li and Aubertin (2009c)	K_a	$\delta=\varphi$
Ting et al. (2011)	K_T	Obtained from theoretical analyses
Singh et al. (2011)	K_a	$\delta=2/3\varphi$
Sivakugan and Widisinghe (2013)	K_0	$\delta=\varphi$
Rajeev et al. (2016)	K_0, K_a	Dependent on the wall roughness
Hong et al. (2016)	K_0, K_a, K_K	$K=K_a, \delta=2/3\varphi; K=K_0, K_K, \delta=1/2\varphi$
Jahanbakhshzadeh et al. (2017)	K_β	The fit curve from numerical results
Jahanbakhshzadeh et al. (2018b)	K_β	The fit curve from numerical results
Jaouhar et al. (2018)	K_M	Obtained from theoretical analyses
Xu et al. (2018)	K_H	--
Sun et al. (2018)	$K_{DP}, K_{MN}, K_{LD}, K_{UST}$	Obtained from triaxial strength criteria

2.2.2 Numerical simulations

Li et al. (2003) conducted numerical simulations with FLAC to investigate the arching effect in backfilled stopes. They found that the lateral earth pressure coefficient across the width was closer to an active state.

Fahey et al. (2009) investigated the influence of dilation angle and hydraulic conductivity on the variation of the earth pressure coefficient. It was found that the earth pressure coefficient along the VCL in a fully drained stope was between the value of $K_{0\varphi}$ and K_{0v} when the dilation angle was 0. Besides, it tended to be closer to K_a with a negative dilation angle while closer to K_p with a positive dilation angle (shown in Figure 2-33a). As shown in Figure 2-33b, the lateral earth pressure

coefficients in partially drained stopes fluctuated along the height but were similar for different hydraulic conductivities.

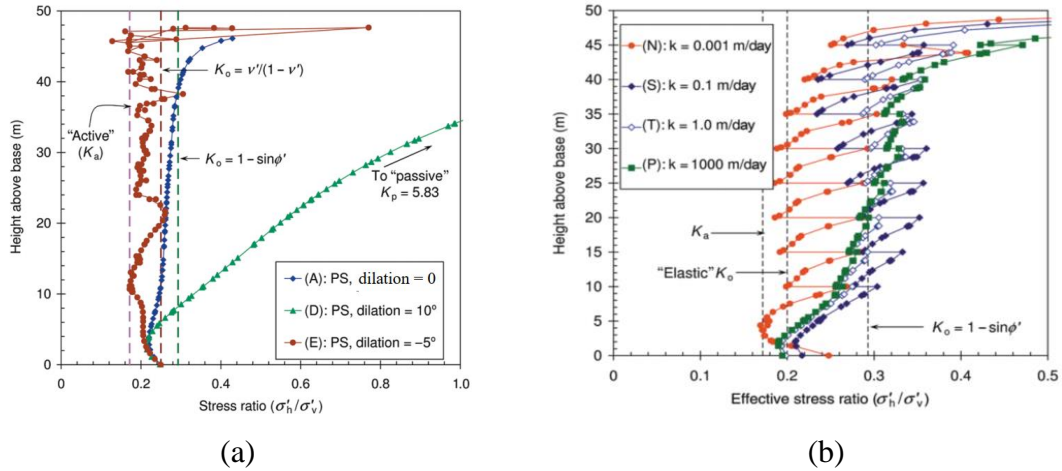


Figure 2-33: The earth pressure coefficient for (a) different dilation angles in dry stopes and (b) different hydraulic conductivities in partially drained stopes (taken from Fahey et al. 2009)

Sobhi et al. (2017) conducted a series of numerical simulations with SIGMA/W (GEO-SLOPE 2010) to investigate the lateral earth pressure coefficient along the central line (CL) of backfilled stopes. It was indicated that the lateral earth pressure coefficient in vertical stopes was close to K_a except near the top of the stope for different stope widths, Young’s modulus, and friction angles (shown in Figure 2-34a). However, in inclined stopes, K_a can be used only for stopes with a large inclination angle. Therefore, a new earth pressure coefficient K_S (Eq. 2-86) was proposed. In Figure 2-34b, K_S was shown to express well the earth pressure coefficient with various inclination angles.

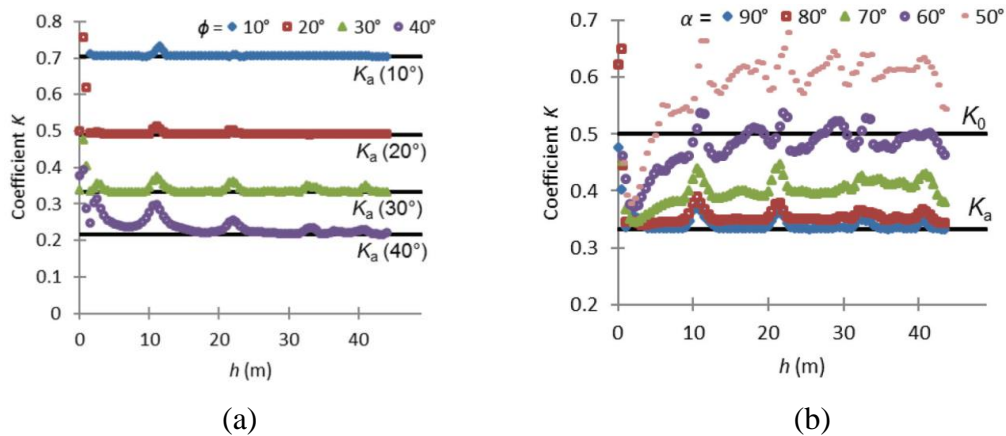


Figure 2-34: The lateral earth pressure coefficient along the CL of backfilled stopes with different (a) friction angles and (b) inclination angles (taken from Sobhi et al. 2017)

Yang et al. (2017b) performed numerical simulations mainly to evaluate the lateral earth pressure coefficient and principal stress ratio K_{ps} near the rock walls considering the dependence of φ and ν . The influence of the slope width, Young's modulus, internal friction angle, Poisson's ratio, and interface elements were assessed. The numerical results indicated that the principal stress ratio was close to K_a , while the lateral earth pressure coefficient was close to K_0 for dependent φ and ν and was uncertain for independent values of φ and ν .

Later, Yang et al. (2018) theoretically analyzed the earth pressure coefficient along the VCL of the cohesionless backfilled stopes according to the Mohr-Coulomb criterion (shown in Figure 2-35a). It was concluded that when $\mu \leq (1 - \sin \varphi)/2$, $K = K_a$, and when $\mu > (1 - \sin \varphi)/2$, $K = K_0$. Numerical simulations were conducted with FLAC to verify the theoretical analyses and a good agreement was obtained (shown in Figure 2-35b).

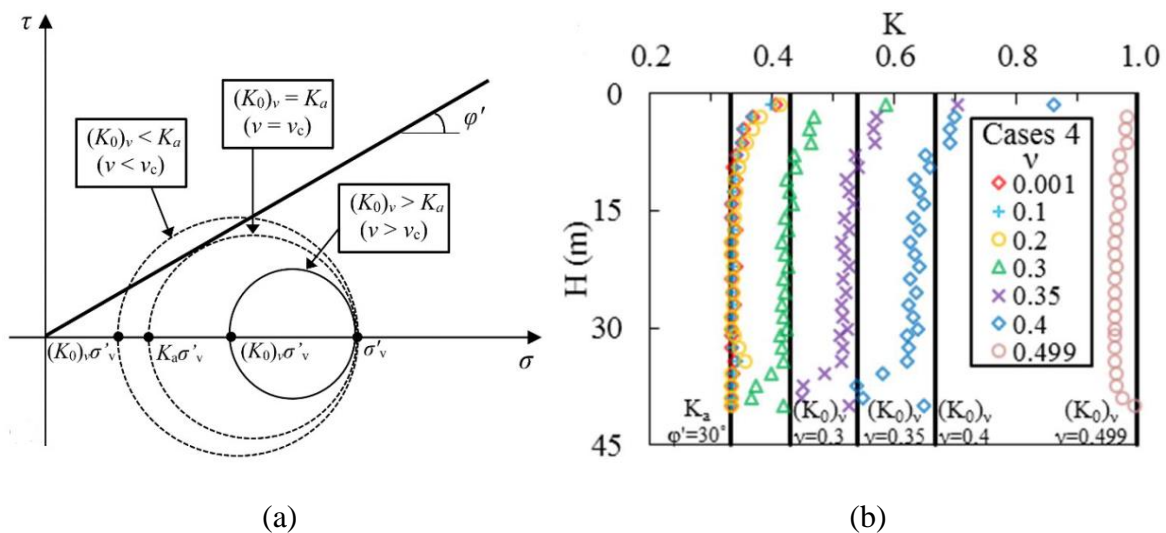


Figure 2-35: (a) The state of the backfill for different relationships between μ and φ and (b) the earth pressure coefficient along the VCL as a function of μ (taken from Yang et al. 2018)

2.2.3 Experiments

Previous experiments conducted to measure the stress in stopes or similar structures gave some evidence of the lateral earth pressure coefficient. The details of those experiments can be found in Section 2.1.3 and some conclusions about the earth pressure coefficient are shown as follows.

As shown in Figure 2-36a, Jarrett et al. (1995) found the pressure at the center of the wall was close to Janssen's theory using an active earth pressure. Li et al. (2014) concluded that the lateral earth coefficient was near an at-rest condition for the stress perpendicular to the pouring direction while the stress parallel to the pouring direction was between an at-rest and a passive state (shown in Figure 2-36b). In Figure 2-36c, Han et al. (2018) showed the lateral pressure coefficient in the silo was smaller than the active earth pressure coefficient.

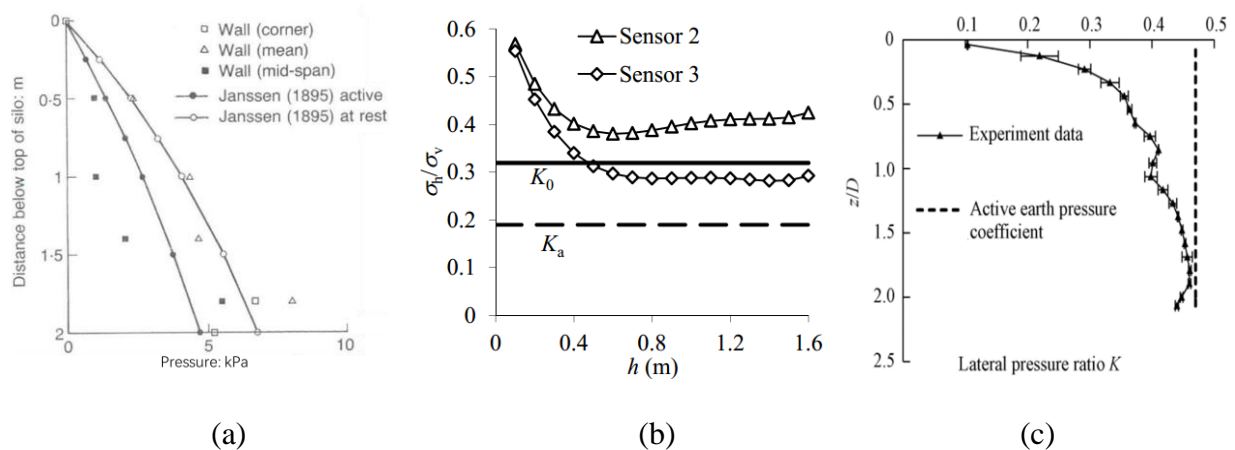


Figure 2-36: K measured in laboratory tests: (a) pressures near the central and corner of the wall (taken from Jarrett et al. 1995); (b) K at different fill heights h (taken from Li et al. 2014); (c) K at different depths z (D is the silo diameter, taken from Han et al. 2018).

Thompson et al. (2012) found in the field measurements that the earth pressure coefficient was variable with depth and time.

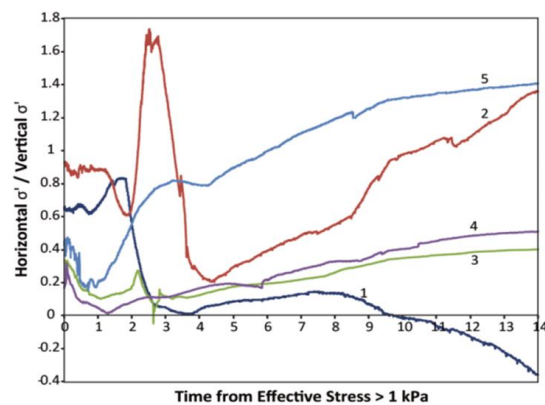


Figure 2-37: K calculated from field measurement at different positions in the 715 slope (adapted from Thompson et al. 2012)

2.3 The stability of side-exposed backfill

In open stoping mining, the ore body is usually mined out in the form of primary and secondary stopes. Primary stopes are first excavated and then backfilled with a cemented backfill. After a certain time of curing when the backfill gains enough strength and is able to support itself under gravity, the neighboring secondary stope is excavated. If the backfill in the primary stope is not well designed, it can fail during or after the excavation of the adjacent secondary stope, resulting in several problems, such as damage of equipment, ore dilution or loss, and even threatening the safety of the miners.

Numerous investigations have been conducted to determine the minimum required cohesion of side-exposed backfill. For example, many analytical solutions have been proposed as a preliminary tool, among which Mitchell et al. (1982) solution is the most used one in practice. Besides, experimental tests and numerical simulations have also been applied to assess the side-exposed stability of the mine backfill.

2.3.1 Analytical solutions

2.3.1.1 Traditional solution

Traditionally, the backfill is designed by considering the vertical stress based on the overburden solution (Askew et al. 1978; Mitchell et al. 1982). The unconfined uniaxial compressive strength (UCS) of backfill should be higher than the vertical overburden stress (γz), which leads to a nonuniform backfill along the depth. Another way is to use a uniform backfill with the $UCS \geq \gamma H/2$, which is determined by the limit equilibrium analyses of a 2D wedge model for cohesionless backfill. The solutions result in very conservative design because the shear strengths along the fill-rock interfaces are ignored.

2.3.1.2 Mitchell et al. (1982) solution

Mitchell et al. (1982) analyzed the stability of side-exposed backfill based on a wedge model shown in Figure 2-38. The factor of safety (FS) is calculated by considering the equilibrium of the wedge as follows:

$$FS = \frac{\tan \varphi}{\tan \alpha} + \frac{2cL}{H^*(\gamma L - 2c_b) \sin 2\alpha} \quad (2-92)$$

where $\alpha (= 45^\circ + \varphi/2)$ is the sliding angle between the assumed sliding plane and the horizontal; c_b is the cohesion along the interface between the backfill and the sidewalls and $H^* (= H - (B \tan \alpha)/2, m)$ is the equivalent height of the wedge block.

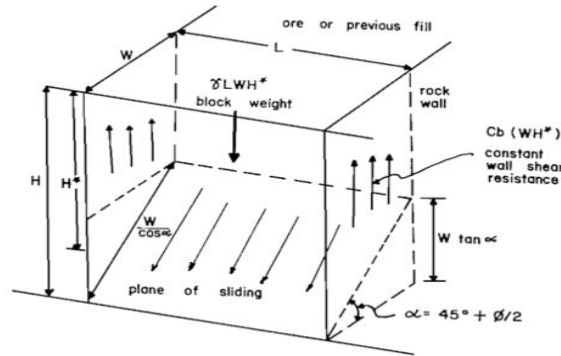


Figure 2-38: The wedge model of Mitchell et al. (1982) solution (taken from Mitchell et al. 1982)

By assuming $c_b = c$, $H \gg B$, and $FS = 1$, the minimum required cohesion of the backfill is calculated by:

$$c = \frac{\gamma H}{2 \left(\frac{H}{L} + \tan \alpha \right)} \quad (2-93)$$

By further assuming $\varphi = 0$ for the backfill, the minimum required unconfined uniaxial compressive strength (UCS) becomes:

$$UCS = 2c = \frac{\gamma}{\left(\frac{1}{L} + \frac{1}{H} \right)} = \frac{\gamma H}{\left(\frac{H}{L} + 1 \right)} \quad (2-94)$$

The Mitchell et al. (1982) solution contains several assumptions, as discussed by Li and Aubertin (2012). For example, the sliding surface is assumed as an inclined plane, which should be a curved surface according to their experimental results. The solution is not applicable to the backfill in a low-aspect-ratio stope because the sliding plane may intersect the top surface of the backfill. Moreover, the friction angle of the fill-wall interface, stope inclination, and surcharge on the top surface of the backfill are not considered in the Mitchell et al (1982) model.

2.3.1.3 Wedge model with different shapes

Dight and Coulthard (1980) proposed a 3D solution by considering a sliding wedge of different shape and confining pressure σ_c (kPa) applied at the sidewalls (shown in Figure 2-39). FS is expressed as follows:

$$FS = \frac{cA_B + W \cos \alpha \tan \varphi + \frac{2cA_S \cos \omega}{\cos \alpha} + 2\sigma_c A_S \tan \varphi \cos \zeta \left(\frac{\cos \omega \cos \zeta}{\cos \alpha} - \sin \zeta \sin \alpha \right)}{W \sin \alpha + \sigma_c A_S \sin 2\zeta \cos \alpha} \quad (2-95)$$

with

$$W = \gamma \left(\frac{1}{6} B \times (3HL + 3H_t L - 2Hl - 4H_t l) \right) \quad (2-96)$$

$$l = B \tan \zeta \quad (2-97)$$

$$A_B = \frac{(L - l)(H - H_t)}{\sin \alpha} \quad (2-98)$$

$$A_S = \frac{(H^2 - H_t^2)}{2 \tan \alpha} \quad (2-99)$$

$$\tan \omega = \tan \alpha \cos \zeta \quad (2-100)$$

where ζ ($^\circ$) is the angle between the wedge side plane and the backfill sidewall plane; ω ($^\circ$) is an angle made between the two lines of intersection formed by the wedge side plane, sliding plane and the horizontal base shown in Figure 2-39; $2l$ is the decrease of the wedge length due to the angle ζ ; A_B (m^2) and A_S (m^2) are the base area and the section area of the sidewalls of the wedge, respectively and H_t (m) is the depth of tension crack.

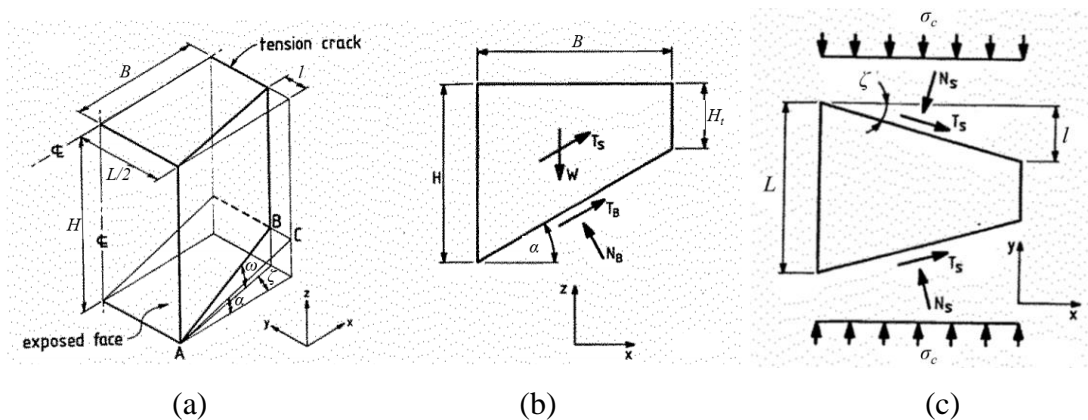


Figure 2-39: Forces and geometry for 3D wedge analysis: (a) a general view of half of the wedge, (b) side view and (c) plan view (taken from Dight and Coulthard 1980)

Their parametric studies indicated that the horizontal stress below a certain value exerted on the backfill could increase the stability. However, it could be detrimental to the stability of the backfill when its value was larger than a certain critical value.

2.3.1.4 Inclined stopes

Based on the Mitchell et al. (1982) solution for vertical stopes, Smith et al. (1983) proposed an analytical solution for the minimum required cohesion of the backfill at Black Mountain Mine for stopes with a wall inclination angle of 55° (shown in Figure 2-40):

$$c = \frac{\gamma H}{2 \left(X + 0.75 \frac{H}{L} \right)} \quad (2-101)$$

with

$$X = \frac{\sqrt{(H - H_t)^2 + (H/3)^2}}{0.27(H + H_t)} \quad (2-102)$$

where X is a geometric parameter. It is worth noting that X was taken as 2.21 based on curve-fitting with their experimental results.

Even though the analytical solution agrees well with the experimental results based on curve-fitting, no further results were illustrated to show if the analytical solution could be used to predict the stability of exposed backfill under different situations. In fact, the minimum required cohesion obtained by Eq. 2-102 is insensitive to the variation of the inclination angle β . Besides, the solution inherits all the drawbacks of the Mitchell et al. (1982) solution, including the neglect of the stope width and backfill friction angle.

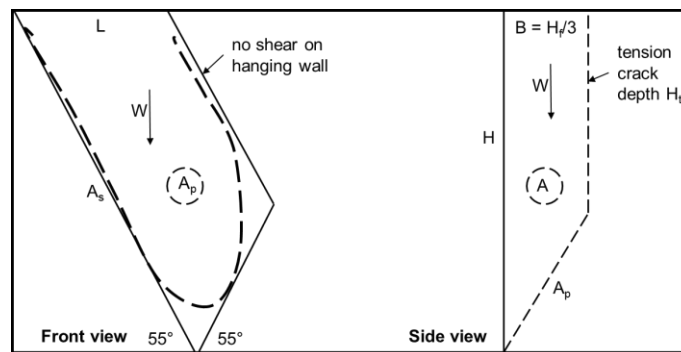


Figure 2-40: Geometry of the Smith et al. (1983) model for side-exposed backfill in an inclined stope (taken from Smith et al. 1983)

Mitchell (1989) modified the Mitchell et al. (1982) solution and proposed a solution to evaluate the stability of side-exposed backfill in inclined stopes by curve-fitting with experimental data. The minimum required cohesion is expressed as follows:

$$c = 0.2 \frac{\gamma H \sin \beta}{1 + H/L} \quad (2-103)$$

The proposed analytical formula was observed to predict the experimental data reasonably, which were however obtained by applying different wall closure stresses, neglected in Eq. 2-103. Further validation of the formula is still needed. Besides, the solution inherits the limitations of the Mitchell et al. (1982) model.

Dirige and De Souza (2008) developed analytical solutions to assess the stability of side-exposed backfill in inclined stopes. Figure 2-41 shows the wedge model for stability analyses. Two different wall roughness, namely smooth and rough rock wall surfaces, are considered, respectively.

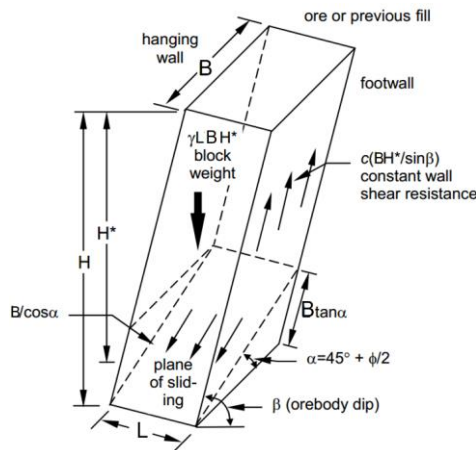


Figure 2-41: A schematic model for side-exposed backfill in inclined stopes (adapted from Dirige and De Souza 2008)

For rough rock walls with a cohesion c , the factor of safety is given as:

$$FS = \frac{\tan \varphi}{\tan \alpha} + \frac{\cos \beta \tan \varphi}{\sin \alpha} + \frac{c}{H^*(\gamma L(1 - \cos \beta \tan \varphi) - c / \sin \beta)} * \left(\frac{L}{\cos \alpha} + \frac{H^*}{\sin \beta} \right) \quad (2-104)$$

where $H^* (= H - (B \tan \alpha)/2, \text{ m})$ is the equivalent height of the sliding wedge. The required cohesion of the backfill is expressed as:

$$c = \frac{\gamma L(1 - \cos \beta \tan \varphi)}{\left(\frac{L}{\frac{H^* \sin \alpha \cos \alpha}{FS - \frac{\tan \varphi}{\tan \alpha}} + \frac{1}{\frac{\cos \beta \tan \varphi}{\sin \alpha}}} \right) + \frac{1}{\sin \beta}} \quad (2-105)$$

For smooth rock walls, the factor of safety is expressed as:

$$FS = \frac{\tan \varphi}{\tan \alpha} + \frac{\cos \beta \tan \varphi}{\sin \alpha} + \frac{c}{\gamma H^*(1 - \cos \beta \tan \varphi) \sin \alpha \cos \alpha} \quad (2-106)$$

The required cohesion of the backfill is expressed as:

$$c = \gamma H^*(1 - \cos \beta \tan \varphi) \sin \alpha \cos \alpha \left(FS - \frac{\tan \varphi}{\tan \alpha} + \frac{\cos \beta \tan \varphi}{\sin \alpha} \right) \quad (2-107)$$

In the Dirige and De Souza (2008) model, the shear stress along the hanging wall was neglected, independently on the wall inclination angles. Besides, the normal forces along the hanging wall and footwall in inclined stopes are not considered in the equilibrium analysis of the wedge model. Besides, the angle of the sliding plane was incorrectly regarded as the angle made between the two lines of intersection formed by the side (hanging or foot) wall, sliding plane, and the horizontal base.

2.3.1.5 Surcharge

Zou and Nadarajah (2006) extended Mitchell et al. (1982) solution by involving a load factor f_p defined as the ratio of surcharge to the weight of the wedge block. The critical height of the backfill is calculated as follows by setting $FS = 1$:

$$H = \frac{\frac{2c_b BL}{\sin 2\alpha (FS - \tan \varphi / \tan \alpha)} + \frac{B}{2} \tan \alpha [(1 + f_p)\gamma BL - 2c_b B]}{(1 + f_p)\gamma BL - 2c_b B} \quad (2-108)$$

According to the formula, the critical height of the backfill increases with an increase of the cohesion and the friction angle.

Li and Aubertin (2012) modified the Mitchell et al. (1982) solution by incorporating the surcharge on the stope surface of the backfill. The factor of safety and the required cohesion of the backfill are calculated as follows:

$$FS = \frac{\tan \varphi}{\tan \alpha} + \frac{2c}{p_0 + H^*(\gamma - (2r_b c)/L) \sin 2\alpha} \quad (2-109)$$

$$c = \frac{(p_0 + \gamma H^*)/2}{((FS - \tan \varphi / \tan \alpha) \sin 2\alpha)^{-1} + (r_b H^*)/L} \quad (2-110)$$

where p_0 (kPa) is the surcharge and r_b is the adherence ratio of the interface cohesion to the backfill cohesion. The modified solution was seen to represent well the experimental results of Mitchell et al. (1982). It is noted that the values of the internal friction angle and adherence ratio used in the analytical solution were obtained by curve-fitting with the model tests of Mitchell et al. (1982).

2.3.1.6 Backfill with a low aspect ratio

Li and Aubertin (2012) also proposed an analytical solution for the stability analyses of side-exposed backfill with a low aspect ratio (shown in Figure 2-42). The factor of safety and the required cohesion of the backfill are calculated as follows:

$$FS = \frac{\tan \varphi}{\tan \alpha} + \frac{2c}{p_0 + H(\gamma/2 - (r_b c)/L) \sin 2\alpha} \quad (2-111)$$

$$c = \frac{(p_0 + \gamma H)/2}{2((FS - \tan \varphi / \tan \alpha) \sin 2\alpha)^{-1} + (r_b H)/L} \quad (2-112)$$

Then the solution of Li and Aubertin (2012) was compared with the Mitchell et al. (1982) solution to assess the influence of the slope geometry, interface property, and surcharge, which suggested that the Mitchell et al. (1982) solution was conservative.

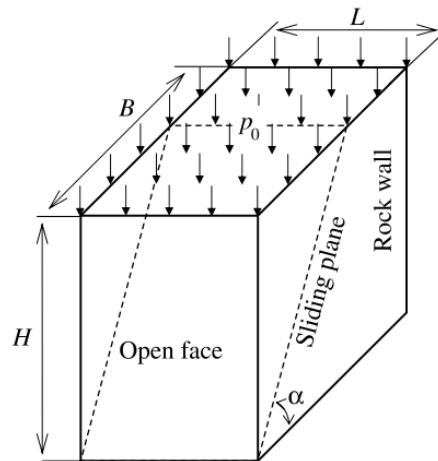


Figure 2-42: The backfill with a low aspect ratio (taken from Li and Aubertin 2012)

2.3.1.7 Considering the plug pour of backfill

Li (2014a) developed an analytical solution for estimating the required strength of side-exposed backfill by considering the reinforcing effect of the high cemented plug. Two critical positions of the sliding plane were considered. As shown in Figure 2-43a, when the sliding plane is within the plug, the factor of safety and the required cohesion of the side-exposed backfill are deduced as:

$$FS = \frac{\tan \varphi}{\tan \alpha} + \frac{2r_p}{\left(p_0 + \left(\gamma - \frac{2r_{if}c}{L}\right)H_f + \left(\gamma_p - \frac{2r_{ip}r_p c}{L}\right)\left(H_p - H_s - \frac{B \tan \alpha}{2}\right) \sin 2\alpha\right)} \quad (2-113)$$

$$c = \frac{p_0 + \gamma H_f + \gamma_p \left(H_p - H_s - \frac{B \tan \alpha}{2}\right)}{2 \left(\frac{r_p}{(FS - \tan \varphi / \tan \alpha) \sin 2\alpha} + \frac{r_{if} H_f}{L} + \frac{r_{ip} r_p}{L} \left(H_p - H_s - \frac{B \tan \alpha}{2}\right) \right)} \quad (2-114)$$

where r_p is the ratio of the plug pour cohesion c_p (kPa) to the final pour cohesion c (kPa); r_{ip} is the ratio of the interface cohesion between the plug pour and sidewall c_{ip} (kPa) to the plug pour cohesion c_p (kPa); r_{if} is the ratio of the interface cohesion between the final pour and sidewall c_{if} (kPa) to the final pour cohesion c (kPa); H_s (m) is the elevation of the intersection line between the sliding plane and the front wall.

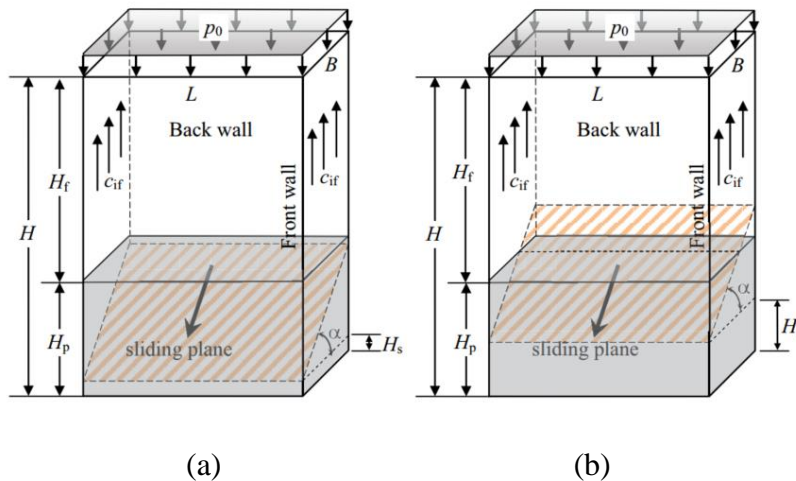


Figure 2-43: Backfilled containing a plug with the sliding plane (a) in the plug and (b) intersecting with the top surface of the plug (taken from Li 2014a)

For the case of the sliding plane intersecting the plug surface (shown in Figure 2-43b), the factor of safety and the required cohesion of the backfill are calculated by:

$$FS = \frac{\tan \varphi}{\tan \alpha} + \frac{c}{\sin^2 \alpha} \frac{\tan \alpha + \frac{(r_p - 1)(H_p - H_s)}{B}}{p_0 + \left(\gamma - \frac{2r_{if}c}{L}\right) \left(H_f - \frac{(B \tan \alpha - H_p + H_s)^2}{2B \tan \alpha}\right) + \left(\gamma_p - \frac{2r_{ip}r_p c}{L}\right) \frac{(H_p - H_s)^2}{2B \tan \alpha}} \quad (2-115)$$

$$c = \frac{p_0 + \gamma \left(H_f - \frac{(B \tan \alpha - H_p + H_s)^2}{2B \tan \alpha}\right) + \gamma_p \frac{(H_p - H_s)^2}{2B \tan \alpha}}{\frac{\tan \alpha + (r_p - 1)(H_p - H_s)/B}{(FS - \tan \varphi / \tan \alpha) \sin^2 \alpha} + \frac{2}{L} \left(r_{if} \left(H_f - \frac{(B \tan \alpha - H_p + H_s)^2}{2B \tan \alpha}\right) + r_{ip}r_p \frac{(H_p - H_s)^2}{2B \tan \alpha}\right)} \quad (2-116)$$

Compared to the Mitchell et al. (1982) solution and the modified solution of Li and Aubertin (2012), this solution predicted a smaller value of the minimum required cohesion if the cement ratio of the plug pour is higher than the final pour.

2.3.1.8 Shear strength calculated by arching solutions for the stress state

Li (2014b) proposed a generalized solution for the stability of side-exposed backfilled stopes considering the cohesion of fill-rock interfaces and different aspect ratios. The shear strength at the fill-rock interface was calculated by a 2D arching solution of Li et al. (2003). For high aspect ratio stopes, the factor of safety and required cohesion are shown below:

$$FS = \frac{\tan \varphi'}{\tan \alpha} + \frac{2}{\sin 2\alpha} \left(\frac{p'}{c} - r_a \frac{H'}{B} - \frac{2r_s H^*}{L} \right)^{-1} \quad (2-117)$$

$$c = p' \left[\frac{2}{(FS - \tan \varphi' / \tan \alpha) \sin 2\alpha} + \frac{H'}{B} + \frac{2r_s H^*}{L} \right]^{-1} \quad (2-118)$$

with

$$p' = \frac{L}{2K \tan \delta} \left[\gamma - \frac{1}{B \tan \alpha} \left(\frac{\gamma L}{2K \tan \delta} - p_0 \right) \times \left(e^{-\frac{2K \tan \delta}{L} H'} - e^{-\frac{2K \tan \delta}{L} H} \right) \right] \quad (2-119)$$

where H' ($= H - B \tan \delta$, m) the height of the wedge model at the back wall.

For low-aspect-ratio stopes, the factor of safety and required cohesion are described as:

$$FS = \frac{\tan \varphi'}{\tan \alpha} + \frac{2}{\sin 2\alpha} \left(\frac{p''}{c} - r_s \frac{H}{L} \right)^{-1} \quad (2-120)$$

$$c = p'' \left[\frac{2}{(FS - \tan \varphi' / \tan \alpha) \sin 2\alpha} + \frac{r_s H}{L} \right]^{-1} \quad (2-121)$$

with

$$p'' = \frac{L}{2K \tan \delta} \left[\gamma - \frac{1}{H} \left(\frac{\gamma L}{2K \tan \delta} - p_0 \right) \times \left(1 - e^{-\frac{2K \tan \delta}{L} H} \right) \right] \quad (2-122)$$

Compared to the Mitchell et al. (1982) solution and the Li and Aubertin (2012) solution, the application of this solution predicted a relatively smaller required cohesion and larger FS. Through parameters calibration, a good agreement was obtained between this solution and the experimental results of the Mitchell et al. (1982). However, the normal stress on the wall was obtained by applying a 2D arching solution while the stress state should be estimated by taking into account the 3D geometry and influence of sidewall exposure. Besides, cohesion was neglected in the arching solution.

Through numerical modeling with FLAC3D, Li and Aubertin (2014) found that the shear resistance acted vertically along the upper part of the sliding wedge while nearly parallel to the sliding direction in the lower part. So, the wedge block was divided into two parts (shown in Figure 2-44). The shear strength at the fill-wall interface was calculated by applying the 3D arching solution of Li et al. (2005). The factor of safety is expressed as:

$$FS = \frac{\tan \varphi}{\tan \alpha} + \frac{c \left(\frac{1}{\cos \alpha} + \frac{r_{bs} H_w}{L} \right) + \frac{\left(\frac{\gamma}{M} - p_1 \right) \left(\frac{1 - e^{-MH_w}}{MH_w} - 1 \right) + \frac{\gamma H_w}{2}}{1 + L/B}}{\left(p_1 + \frac{\gamma H_w}{2} \right) \sin \alpha} \quad (2-123)$$

with

$$H_w = B \tan \alpha \quad (2-124)$$

$$M = 2K(B^{-1} + L^{-1}) \tan \delta \quad (2-125)$$

$$p_1 = p_0 - \frac{\gamma(H - H_w) + (p_0 - \gamma/M)(1 - e^{-(H-H_w)M})}{1 + L/B} + (H - H_w) \left[\gamma - c \left(\frac{2r_{bs}}{L} + \frac{r_{bb}}{B} \right) \right] \quad (2-126)$$

where r_{bs} and r_{bb} are the ratios of the interface cohesion of the sidewalls and the back wall to the backfill cohesion, respectively; H_w (m) is the height of the lower wedge; K is the lateral earth pressure coefficient.

A good agreement was obtained between the experimental results of Mitchell et al. (1982) and the proposed solution using selected internal friction angle and adherence ratio obtained by the curve-fitting method.

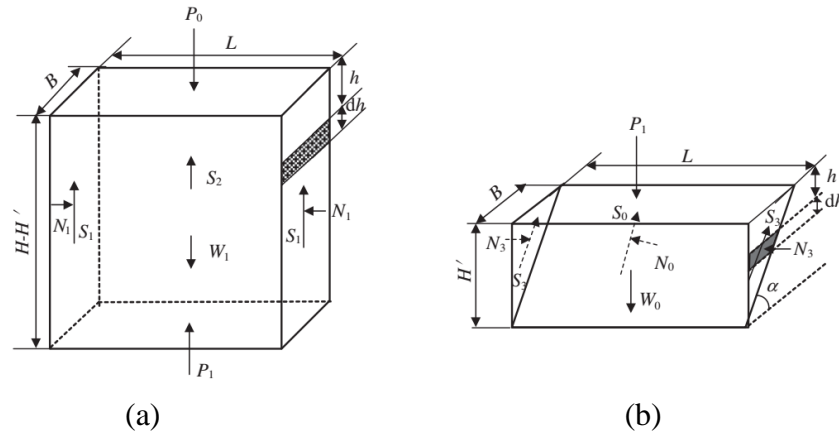


Figure 2-44: Forces on the two parts of the model: (a) the upper block and (b) the lower wedge
(taken from Li and Aubertin 2014)

2.3.1.9 Tension cracks

Li and Aubertin (2012) also considered the tension cracks in the side-exposed backfill, and the depth of the tension cracks H_t (m) can be estimated by

$$H_t = \frac{2c}{\gamma \tan(45^\circ - \varphi/2)} \quad (2-127)$$

The equivalent width of the sliding wedge B_t (m) can be obtained by

$$B_t = (H - H_t)/\tan \alpha \quad (2-128)$$

Then the situation can be regarded as a high-aspect-ratio slope using the equivalent width B_t to substitute the width B in the modified solution of Li and Aubertin (2012).

Yang et al. (2017a) performed numerical simulations with FLAC3D to analyze the stability of side-exposed backfill. Their numerical results showed that the tension crack and wedge sliding may occur at the same time. They further developed an analytical solution by considering the tension crack (shown in Figure 2-45) as follows:

$$FS = \frac{\tan \varphi'}{\tan \alpha} + \frac{2}{\sin 2\alpha} \left(\frac{p}{c} - \frac{H_t}{B_t} - \frac{r_s(2H - B_t \tan \alpha)}{L} \right)^{-1} \quad (2-129)$$

$$c = p \left[\frac{2}{(FS - \tan \varphi' / \tan \alpha) \sin 2\alpha} + \frac{H_t}{B_t} + \frac{r_s(2H - B_t \tan \alpha)}{L} \right]^{-1} \quad (2-130)$$

with

$$p = \frac{L}{2K \tan \delta} \left[\gamma - \frac{1}{B_t \tan \alpha} \left(\frac{\gamma L}{2K \tan \delta} - p_0 \right) \times \left(e^{-\frac{2K \tan \delta}{L} H_t} - e^{-\frac{2K \tan \delta}{L} H} \right) \right] \quad (2-131)$$

Then numerical simulations with a zero and a nonzero (UCS/10) tension cut-off were conducted. A better agreement was obtained between their proposed solution and the numerical results.

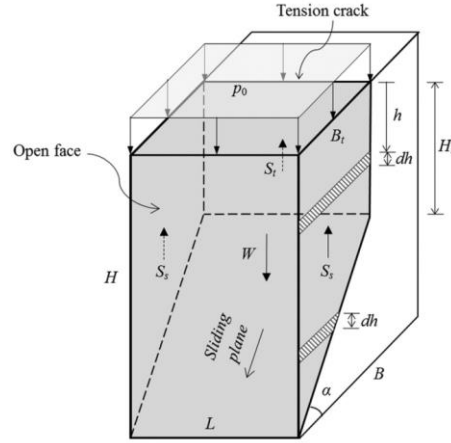


Figure 2-45: Side-exposed backfill with tension crack (taken from Yang et al. 2017a)

Zhao et al. (2019) proposed an analytical solution to evaluate the FS of side-exposed backfill with a tension crack by applying the differential slice method. Their analytical solution was not in closed form, but the FS can be obtained by calculations in iteration. Eight centrifuge tests for the side-exposed stability were conducted and all the backfill models were brought to failure. An average FS of 0.97 was obtained by applying their analytical solution. The prediction error on the FS by using their analytical solution was 0.29, which is smaller than the error of 0.67 calculated by the Mitchell et al. (1982) solution. It suggested the validity of their analytical solution.

2.3.1.10 The pressure at the back wall

Liu et al. (2018) proposed an analytical solution for the stability analysis of the backfill with the front wall exposed and the back wall pressured by uncemented backfill. FS is estimated by the following equation:

$$FS = \frac{cL(B/\cos \alpha) + [Y - 2S_s \sin(\alpha_s - \alpha)] \tan \varphi}{Z - 2S_s \cos(\alpha_s - \alpha)} \quad (2-132)$$

with

$$Y = (\gamma H^* + p_0)LB \cos \alpha - \frac{1}{2} \gamma_u L (H - B \tan \alpha)^2 \sin \alpha \quad (2-133)$$

$$Z = (\gamma H^* + p_0)LB \sin \alpha + \frac{1}{2} \gamma_u L (H - B \tan \alpha)^2 \cos \alpha \quad (2-134)$$

$$S_s = BH^* \left(r_s c + \frac{L}{2} \gamma \right) + \left(\frac{\gamma L}{2K \tan \delta} - p_0 \right) \left[\frac{L^2}{4K \tan \alpha \tan \delta} \left(e^{-\frac{2K \tan \delta}{L} H_b} - e^{-\frac{2K \tan \delta}{L} H} \right) - \frac{LB}{2} \right] \quad (2-135)$$

where α_s ($^\circ$) is the angle between the direction of the shear force at the fill-side wall interface and the horizontal. α and α_s were assumed as some certain values and four formulas were developed and compared with numerical results obtained with FLAC3D. It is indicated that the analytical solution predicted better the numerical results when $\alpha = 45^\circ + \varphi/2$ and $\alpha_s = 45^\circ - \varphi/2$.

2.3.1.11 Confining pressure induced by the surrounding rock

Wang et al. (2019) developed an analytical solution for the cemented backfill stability with the front wall exposed, the back wall pressed by tailings fills, the side walls confined by the surrounding rock, and a surcharge due to the broken rock mass (shown in Figure 2-46). Based on the limit equilibrium theory, the required cohesion is calculated as follows:

$$c = \frac{2(\gamma H^* + p_0)BL \sin \alpha (\sin \alpha - \cos \alpha \tan \varphi) + 2F_b \cos \alpha (\cos \alpha + \sin \alpha \tan \varphi) \tan \alpha - 4N_s \sin \alpha \tan \varphi}{4r_b H^* B \sin \alpha + 2LB \tan \alpha} \quad (2-136)$$

with

$$N_s = \frac{1}{2} BH (\gamma_R H + 2 \gamma_{BR} b_1) \tan^2 \left(\frac{\pi}{4} - \frac{\varphi_R}{2} \right) \quad (2-137)$$

$$b_1 = \frac{L + 2H \cot(45^\circ + \varphi_R/2)}{2f} \quad (2-138)$$

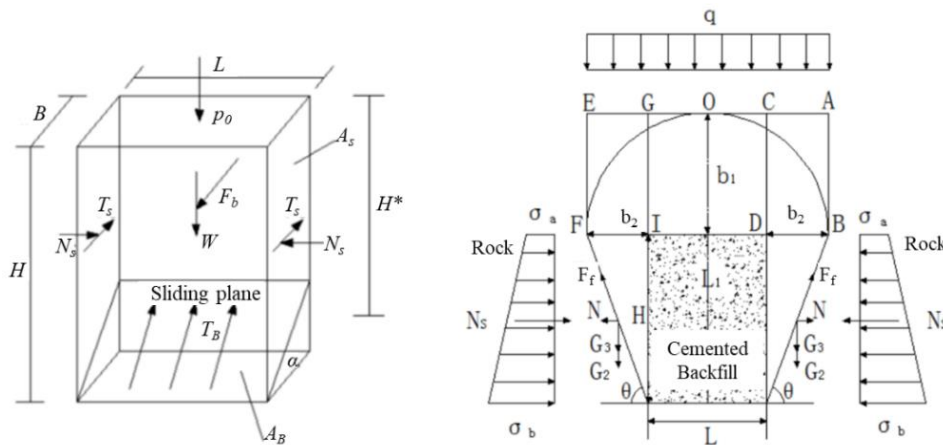


Figure 2-46: Mechanical model of a cemented backfill (taken from Wang et al. 2019)

where F_b (kPa) is the pressure on the back wall calculated by considering the densifying effect due to gravity; N_s (kPa) is the normal stress applied on the backfill induced by the surrounding rock; γ_R (kN/m³) and φ_R (°) are the unit weight and friction angle of the surrounding rock; γ_{BR} (kN/m³) is the unit weight of the broken rock at the top; b_1 (m) is the height of the broken rock; f is the Peripheral hardness coefficient of the rock.

When φ varied from 5° to 45°, the values of the two terms $[2 \sin \alpha (\sin \alpha - \cos \alpha \tan \varphi)]$ and $[2 \cos \alpha (\cos \alpha + \sin \alpha \tan \varphi)]$ in Eq. 2-136 are both appropriately equals to 1. Then, the required strength can be estimated as

$$UCS = c \frac{2 \cos \varphi}{1 - \sin \varphi} = \frac{(\gamma H^* + p_0)BL + F_b \tan \alpha - 4N_s \sin \alpha \tan \varphi}{\gamma H^* BL \times (2r_b H^* \sin \alpha + L \tan \alpha)} \times \frac{2 \cos \varphi}{1 - \sin \varphi} \quad (2-139)$$

The UCS calculated by Eq. 2-139 was then applied as the design strength of the backfill in the Dahongshan Mine. The stress variation during the backfilling was measured and shown in Figure 2-24. The measured stresses were always smaller than the UCS of the backfill, suggesting the validity of the proposed analytical solution.

2.3.2 Numerical simulations

2.3.2.1 Early research for qualitative analyses of side-exposed stability

Barrett et al. (1978) assessed the side-exposed stability of the backfill with a 2D finite-element code TNJTEP and 3D finite-element code NONSAP, respectively. The influence of the position where the exposure starts on the stability of the backfill was investigated. It was revealed that fewer failure zones occurred when the exposure position was closer to the backfill top. As the backfill width increased, the failure areas and the displacement of the exposure face would increase. In addition, the displacements of backfill after exposure obtained by 3D numerical simulations were found to be less than those obtained by 2D numerical simulations.

Cundall et al. (1978) modeled the stability of the backfill in transverse pillar extraction using a 3D finite-difference program. Three types of filling materials were used to investigate their failure mechanism. The mining sequence was modeled by first removing one-tenth of the pillar instantaneously followed by the removal of one quarter, one half, and finally all of the pillar. It was found that the stability of cemented hydraulic backfill was mainly governed by gravity while the

influence of rock deformation on the backfill stability upon exposure was insignificant. The numerical results also showed that the stability of cemented rock backfill was affected by the deformation of surrounding rock.

Dight and Coulthard (1980) employed the 2D program TNJTEPISA based on the Drucker-Prager criterion and investigated the influence of the backfill geometry and properties on its stability upon side exposure. The effects of the exposure height and depth and the backfill width on the failure areas were studied (shown in Figure 2-47). The results corresponded well to those of Barrett et al. (1978). Besides, a wedge shape with a tension crack was found to represent well the failure zone during the sequential exposure process.

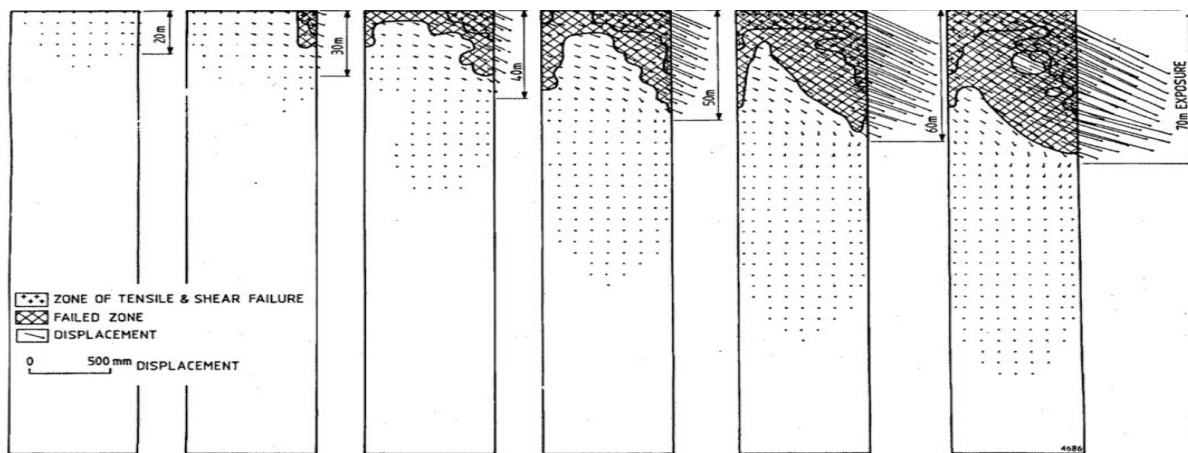


Figure 2-47: Failure zones with an exposure height of 20, 30, 40, 50, 60 and 70 m (taken from Dight and Coulthard 1980)

Pierce (2001) applied FLAC3D (Version 2.00) to roughly evaluate the required cohesion of the backfill with a side or base exposure, respectively. For side-exposed conditions, it was demonstrated that the required cohesion increased with a growing exposure width. Besides, the shear failure dominated in the side-exposed backfill, and a smaller friction angle resulted in a larger required cohesion. The overlaying backfill was found to have a small effect on the stability of the backfill exposed below due to the occurrence of arching effects in the overlaying backfill.

2.3.2.2 Inclined stopes

Dirige and De Souza (2008) applied FLAC3D to model the inclined backfill with side exposure to verify their analytical solutions. The backfill was assigned a specific cohesion and the convergence

of the displacement was used as a criterion to determine the backfill state. However, only a few stable conditions were considered. More numerical simulations are still needed to obtain the minimum required cohesion of side-exposed backfill to verify their analytical solution.

2.3.2.3 Blast vibrations

Emad et al. (2012) conducted numerical simulations with FLAC3D to investigate the influence of blast vibrations on the side-exposed stability of cemented rockfill. As shown in Figure 2-48, tensile stress occurred at the top of the backfill under dynamic analyses, indicating the failure of the backfill. The blast vibration was proved to decrease the stability and increase ore dilution. Besides, the higher the peak compressive stress of the blasting load, the larger influence can be observed.

Emad et al. (2014) then evaluated the stability of a side-exposed cemented rockfill at northern Manitoba with FLAC3D. Their numerical results showed that the backfill remained stable under static conditions. After considering the effect of blast vibration, tensile stress developed in the backfill and the backfill became unstable.

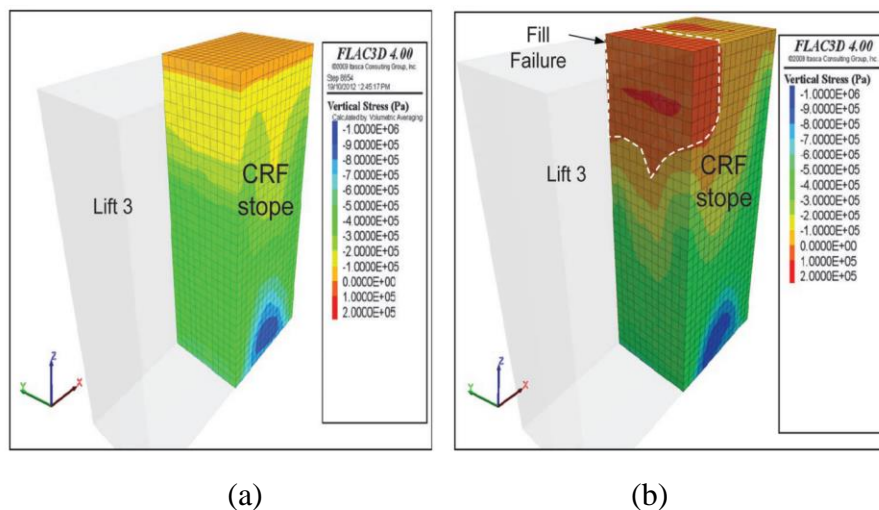


Figure 2-48: Vertical stresses in backfill after the excavation of the secondary stope: (a) static analysis; (b) dynamic analysis (taken from Emad et al. 2014)

2.3.2.4 Critical cohesion

Falahnaz (2014) carried out numerical simulations with FLAC3D to estimate the minimum required cohesion of side-exposed backfill using the trial and error method. The displacement and the strength-stress ratio were used to analyze the stability of the side-exposed backfill. It was found

that the critical cohesion would increase as the backfill length or height increased but seemed to be insensitive to the backfill width. Besides, exposing the backfilling in more steps tended to reduce the displacement and increase the factor of safety.

2.3.2.5 Reproducing experimental tests

Liu et al. (2016b) conducted a series of numerical modelings with FLAC3D to reproduce the experimental results of the physical model tests of Mitchell et al. (1982). The gradual exposure of the backfill by removing the timber at the exposed face one by one until the failure of the backfill was reproduced by the sequential numerical simulations. The yield state and strength-stress ratio of the backfill were used to determine the state of the backfill in the numerical simulations. The numerical results (shown in Figure 2-49) indicated that the model tests of Mitchell et al. (1982) were performed under undrained conditions. This explained why a good agreement was observed between the experimental results and the Mitchell et al. (1982) solution with a backfill friction angle $\phi = 0^\circ$.

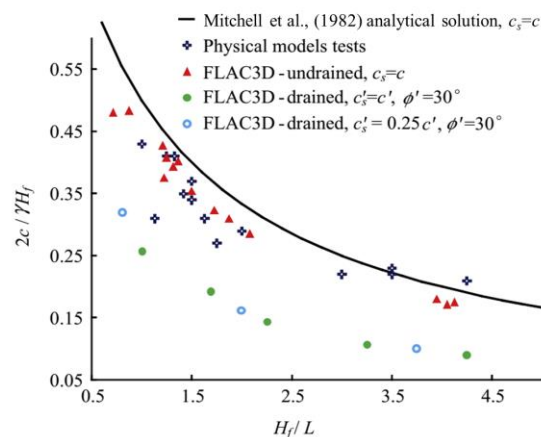


Figure 2-49: Comparisons of the numerical results with the analytical solution and experimental data of Mitchell et al. (1982) (taken from Liu et al. 2016b)

2.3.2.6 Tension crack

Yang et al. (2017a) conducted a series of numerical simulations with FLAC3D to verify their analytical solution proposed by considering the tension crack. The critical cohesion was obtained by the trial and error method. The state of the backfill was evaluated by observing the displacement

along the VCL of the exposed face and the yielding state of the backfill. The tension crack was also observed in their numerical models.

2.3.2.7 The pressure at the back wall

Liu et al. (2018) obtained the minimum required cohesion of the backfill with the front wall exposed and the back wall pressured from numerical models conducted with FLAC3D. The displacement and the strength-stress ratio were used to distinguish if the backfill is stable or unstable.

2.3.3 Experimental tests

2.3.3.1 Vertical backfill

Mitchell et al. (1982) performed 26 small-scaled laboratory model tests (shown in Figure 2-50a) to measure the critical exposed height of the backfill with different stope geometries and backfill properties. Those models had widths of 0.2 m and 0.4 m, lengths of 0.4 m, 0.6 m, and 0.8 m and heights varying from 0.6 m to 1.8 m. The backfill in the boxes was kept saturated and cured for 2.5 to 5 hours before its exposure by removing the 0.1 m-high timber at the front face one by one quickly. The maximum exposed height of the backfill was recorded and plotted in Figure 2-50b. It was found that the experimental results corresponded well with their proposed analytical solutions.

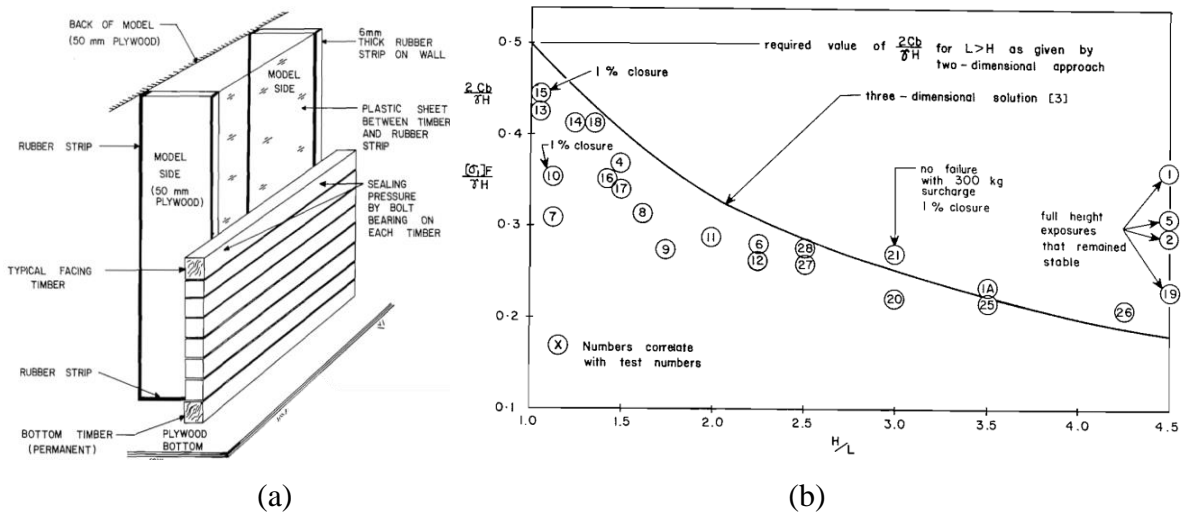


Figure 2-50: Experimental tests for the side-exposed stability of backfill: (a) model construction and (b) comparisons with the analytical solution (taken from Mitchell et al. 1982)

Mitchell (1986) conducted eight centrifuge tests with cemented sand to measure the critical failure height of the prototype backfill. The tested samples were cast with three different cement ratios and cured for 28 days. The experimental results indicated that the critical height calculated by the standard upper-bound equation for vertical slope stability ($H = 2 \text{ UCS}/\gamma$) was conservative. Besides, Mitchell et al. (1982) solution underestimated the critical height. It was also observed that tension crack (shown in Figure 2-51) would occur, accompanied by the failure. The falling mass could reach 30 to 50% of the total mass of the backfill, causing unacceptable ore dilution. A similar tension crack was also observed in the centrifuge tests conducted by Zhao et al. (2019).

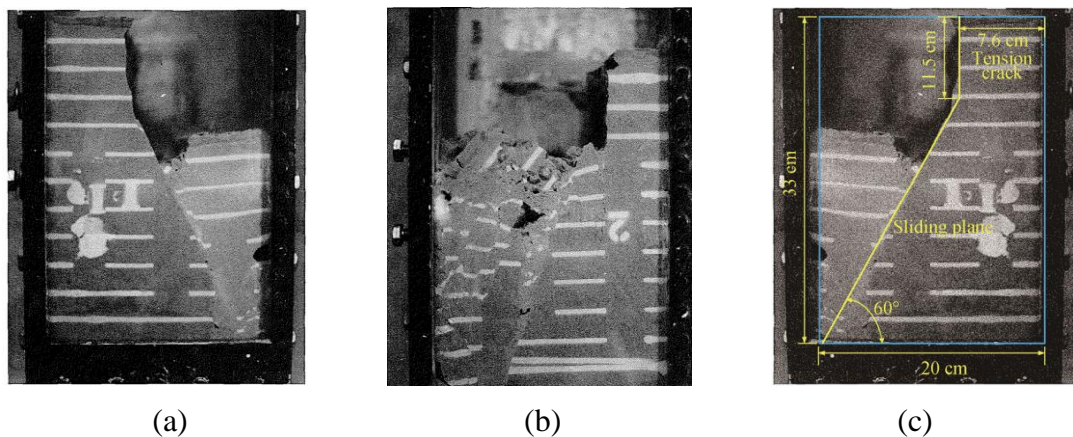


Figure 2-51: Tension crack during the failure of the model: (a) test 1a and (b) test 2a (taken from Mitchell 1986) and (c) test No. 1a (taken from Zhao et al. 2019)

Antonov (2005) performed two laboratory experiments to investigate the stability of side-exposed backfill using the retaining wall model shown in Figure 2-52a. In the model, the retaining wall with a high cement ratio should be able to support itself and the backfill with a low cement ratio after the excavation of the secondary stope. As shown in Figure 2-52b, a wooden box with a geometry of 1.24 m high, 1.0 m long, and 0.6 m wide was assembled and the front wall could be lifted to simulate the exposing process. The thickness of the retaining wall decreased from 0.1 m at the base to 0.05 m at the top. The retaining wall was first constructed with a cement ratio of 2% and cured for 7 days before filled with uncemented sand. For the first model, both the outer extremities of the retaining wall were fixed horizontally with a 1 cm wide and 1 cm thick wooden stick. After the removal of the front wall, the retaining wall remained stable for several days, even with some obvious tension cracks. In the second model, the outer extremities of the retaining wall were not fixed. The retaining wall finally became unstable and collapsed at an exposure height of 0.99 m.

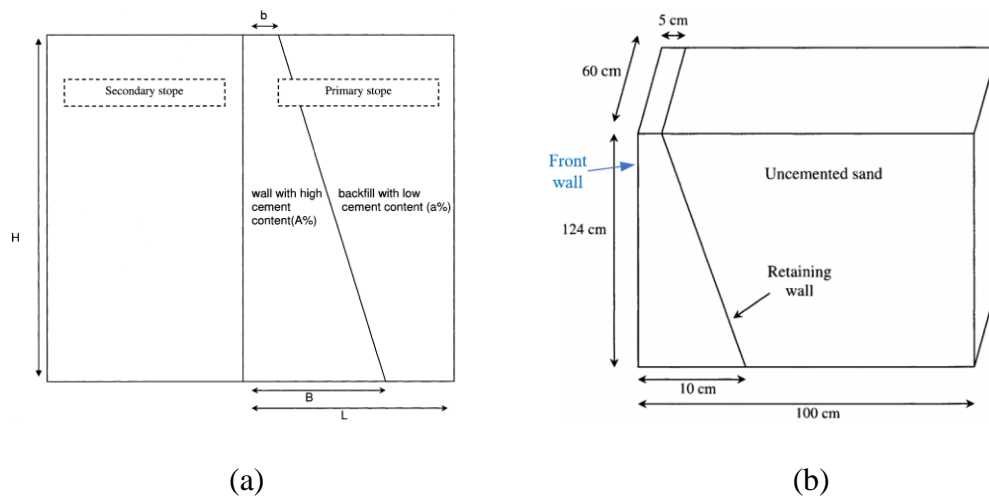


Figure 2-52: A schematic view of (a) the retaining wall model and (b) laboratory model (taken from Antonov 2005)

Yang et al. (2015) conducted laboratory tests with a scale ratio of 1:170 to investigate the backfill stability of a stope in Sijiaying Iron Mine (50 m in length, 25 m in width, and 100 m in height). As shown in Figure 2-53a, pressure cells are placed in the pillars and at the roof of the backfill. Displacement meters are fixed at the roof of the backfill and the ground surface. A cement-tailing ratio of 1:8 was used in the backfill. Figure 2-53b shows the side-exposed backfill after the excavation of the left secondary stope. It is indicated that although a few pieces of backfill fell down near the top, the backfill remained stable, which suggested the designed cement-tailing ratio was effective.

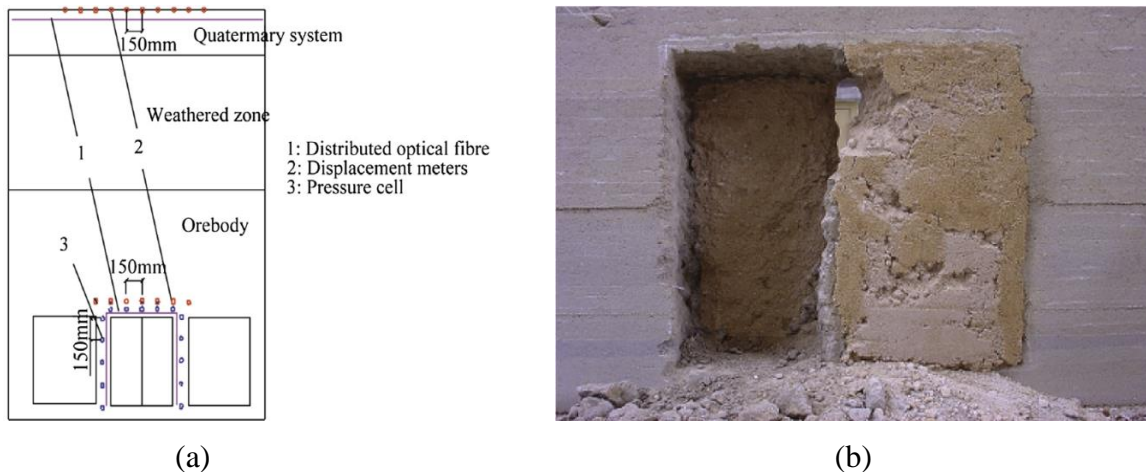


Figure 2-53: (a) The positions of the measuring systems and (b) the side-exposed backfill (taken from Yang et al. 2015)

2.3.3.2 inclined backfill

Smith et al. (1983) conducted nine model tests with a height varying from 1.8 m to 4.2 m to investigate the side-exposed stability of the backfill in inclined stopes at Black Mountain Mine (shown in Figure 2-54a). The testing procedure was similar to that of Mitchell et al. (1982). Tests on the samples taken from the model indicated that the uniaxial compressive strength was equal to twice the cohesion. The UCS obtained from their experimental results was used to calibrate their analytical solution (Eq. 2-101). As shown in Figure 2-54b, $X = 2.21$ was obtained through curve-fitting and used in the equation.

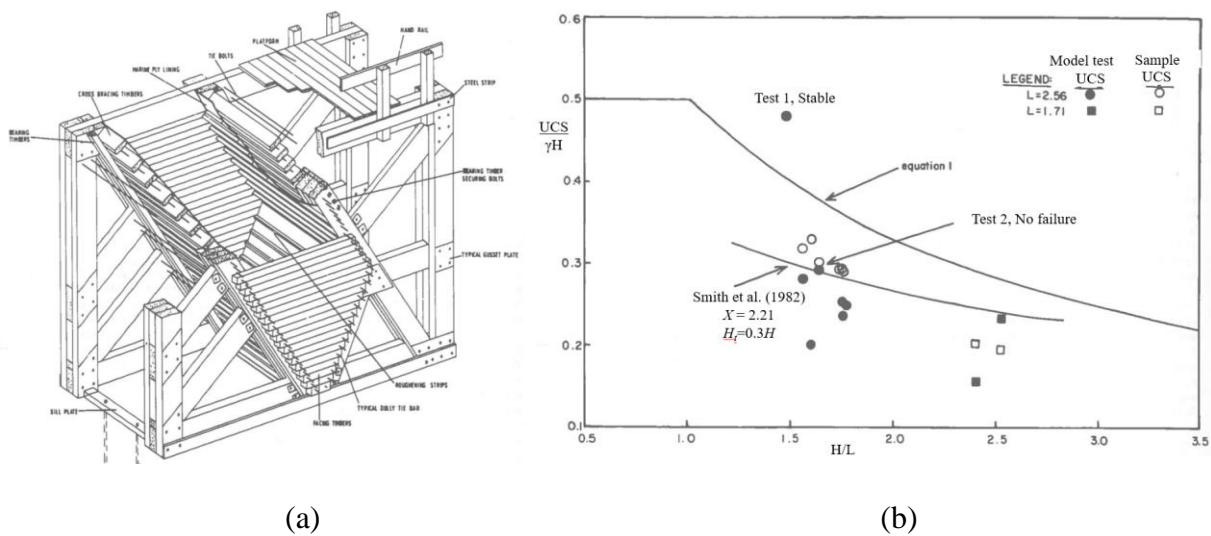


Figure 2-54: Experimental tests for the side-exposed stability of inclined backfill: (a) model construction and (b) comparisons with the analytical solution (taken from Smith et al. 1983)

Mitchell (1989) conducted several centrifuge experiments to investigate the influence of stope wall inclination and wall closure stress on the stability of side-exposed backfill. The cemented backfill with a cement content of 2.5% was cured for 28 days before exposure. As shown in Figure 2-55a, a curved failure surface, intersecting the hanging wall and footwall, was observed. The Mitchell et al. (1982) solution was found to largely overestimate the required strength of experimental models. Therefore, Eq. 2-103 was proposed by calibrating with the experimental results. As shown in Figure 2-55b, the solution predicted well the experimental results.

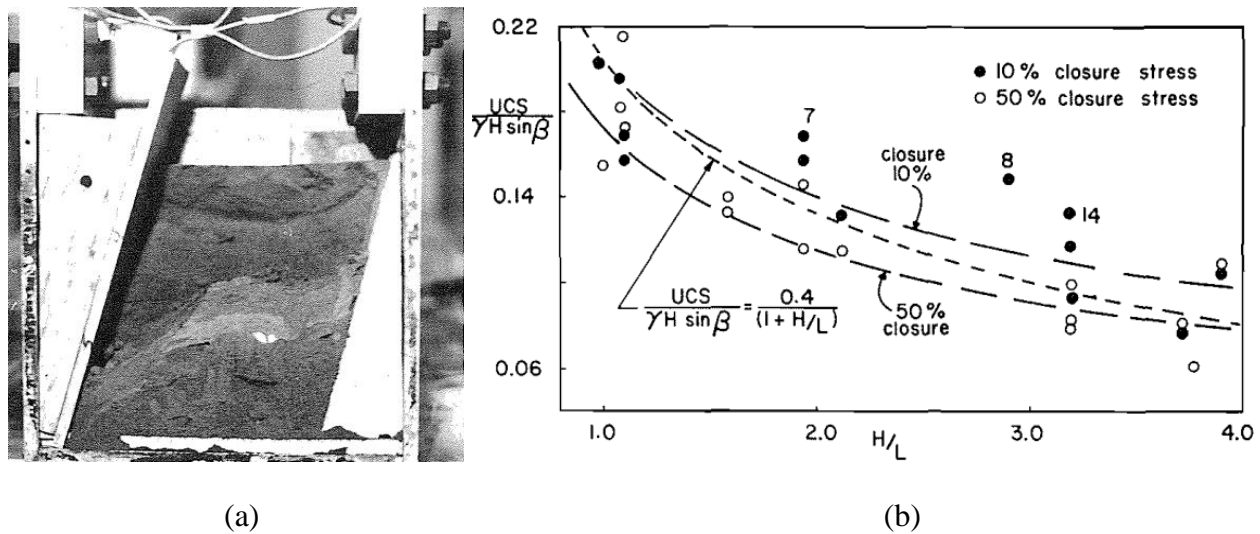


Figure 2-55: (a) Model 3 (with 10% UCS wall closure stress and a wall inclination angle of 75°) after failure and (b) comparisons of the analytical solution and experimental data (taken from Mitchell 1989)

Dirige and De Souza (2008) conducted four centrifuge tests to evaluate the stability of the side-exposed backfill with a slope wall inclination angle of 75° . All the exposed backfill remained stable at the designed gravity levels. As shown in Figure 2-56, a few tension cracks have started to develop near the top of Model 4. Besides, a potential sliding surface making an angle of about $60^\circ \sim 65^\circ$ to the horizontal was observed.

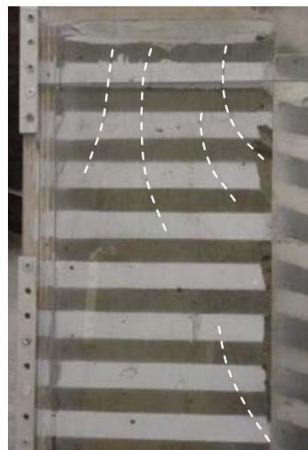


Figure 2-56: Tension cracks and failure surface development in Model 4 (taken from Dirige and De Souza 2008)

2.4 Final remarks

The literature review indicates that many analytical, numerical, and experimental investigations have been conducted in the past years on the fill-wall interactions in terms of stress state and stability of side-exposed backfill. Based on this literature review, the following remarks can be given:

- (1) For the stress state in backfilled stopes, a more generalized analytical solution is desired to estimate the stresses in various conditions. It is also interesting to carefully investigate the stresses near the bottom of backfilled stopes by taking into account the kink effect because it is closely related to the design of barricades, side-exposed backfill, and based-exposed sill mat. It is also interesting to correctly take into account the influence of cohesion, wall inclination angle, and the stress state after side exposure of the backfill. In terms of experimental works, a detailed measurement of the stress distribution along the whole depth is of vital importance.
- (2) For the lateral earth pressure coefficient, more efforts are still needed to fully understand its distribution in backfilled stopes.
- (3) For the side-exposed backfill design, more work is needed to investigate the stability of side-exposed backfill in real conditions even though the Mitchell et al. (1982) solution has been widely used in the practice. It is worth noting the existing analytical solutions for the stability of side-exposed backfill in inclined stopes contain some limitations and more efforts are required. The influence of confining pressures and blasting vibrations should be taken into account. Laboratory experiments and field measurements are needed for the verification of the proposed analytical solutions and numerical simulations.

CHAPTER 3 ARTICLE 1: NUMERICAL AND ANALYTICAL INVESTIGATIONS OF STRESS DISTRIBUTION IN BACKFILLED STOPES CONSIDERING THE KINK EFFECT NEAR THE BOTTOM

Shupeng Chai, Jian Zheng, Li Li

This article was submitted to *International Journal of Geomechanics* in January 2020.

Abstract: Mining backfill is increasingly used in underground mine stopes around the world. A good understanding of the stress distribution in backfilled stopes is a critical concern for the design of barricades or sill mats and side-exposed backfills. This can be realized by using arching analytical solutions or by numerical modelings. The former will give exactly the same distribution between the stress and depth and that between the stress at the bottom and thickness of backfill while the latter does not always show the same trend. More specifically, a sudden increase of vertical stress near the bottom of the stope can be observed on the distribution curves of stress and depth. This is called the kink effect. It can significantly affect the stress estimation for the design of barricades because their construction is made in access drift at the base of stopes. However, the mechanism of the kink effect has never been fully investigated. It has never been considered in analytical solutions developed for evaluating the stresses. In this paper, the mechanism of the kink effect will first be analyzed. A conceptual analytical solution is then proposed to evaluate the stress distribution in backfilled stopes by considering the kink effect near the bottom. The proposed solution is further validated by additional numerical modelings performed with FLAC.

Keywords: Backfilled stope; Numerical modeling; Stress at the bottom; Stress along the depth; Kink effect; Analytical solutions

3.1 Introduction

Using backfill in underground mine stopes has become a common practice around the world. Stope backfilling can bring several advantages, including improved ground stability, increased ore recovery, and reduced volume of mine wastes to be disposed of on surface (Aubertin et al. 2003; Potvin et al. 2005; Darling 2011; Li 2014a, 2014b).

The successful application of backfill requires a good understanding of the stress distribution in backfilled stopes. This can be important for the design of barricades (Li and Aubertin 2009a, 2009b, 2011; Yang et al. 2017), sill mats (Mitchell 1991) or side-exposed backfill (Li and Aubertin 2012; Li 2014a, 2014b; Yang et al. 2017a).

Over the years, a number of analytical solutions based on the arching theory (Marston 1930; Janssen 1895) have been proposed for evaluating the stresses in backfilled openings. The horizontal (σ_h ; kPa) and vertical (σ_v ; kPa) normal stresses in an opening backfilled with cohesionless backfill can be estimated as follows (Li et al. 2003):

$$\sigma_v = \frac{\gamma B}{2K \tan \delta} \left(1 - e^{-2K \frac{z}{B} \tan \delta} \right) \quad (3-1)$$

$$\sigma_h = \frac{\gamma B}{2 \tan \delta} \left(1 - e^{-2K \frac{z}{B} \tan \delta} \right) \quad (3-2)$$

where γ (kN/m³) is the unit weight of the backfill; B (m) is the width of the opening; δ (°) is the friction angle along the fill-wall interfaces, which is taken as the internal friction angle of the backfill φ (°) for rock walls with rough surfaces; K ($= \sigma_h/\sigma_v$, the pore water pressure is not considered in this study) is the earth pressure coefficient. In Marston (1930), z (m) is the thickness of backfill while σ_h and σ_v are the horizontal and vertical stresses at the base of the backfilled opening, respectively. In backfilled stopes, σ_h and σ_v are usually taken as the horizontal and vertical stresses at a depth z (m) from the top surface of the backfill for a given thickness of backfill. Even though the physical meanings of σ_h , σ_v , and z (m) are different in the two cases, the stress-thickness curves and stress-depth curves based on Eqs. 3-1 and 3-2 will superpose with each other. This tends to indicate that the distinction between the two cases is not necessary. However, these two types of stress profiles can be very different in numerical modelings. For instance, the numerical modelings conducted by Sivakugan et al. (2014) showed that the vertical stress at bottom increases

monotonously and tends to become stable as the thickness increases while the vertical stress also monotonously increases with the depth and tends to become stable with depth, but suddenly increase with depth near the bottom. This last trend has also been observed in numerical modelings conducted by Li et al. (2003), Fahey et al. (2009), and Xu et al. (2018). The sudden increase of the stress near the bottom of the backfilled opening was called kink effects by Sivakugan et al. (2014).

It should be noted that the kink effect near the bottom can significantly influence the pressures on barricades. This is because the horizontal pressure on barricades is determined by the horizontal stress applied by backfill near the bottom of the stope with the same height range as the access drift (barricade). The kink effect has been partly explained by the limited deformation of the backfill near the stiff base of openings by Sivakugan et al. (2014) and Liu et al. (2017). This, however, cannot explain the absence of kink effects shown in other numerical modelings (Li et al. 2003; Pirapakaran and Sivakugan 2007a; Sobhi et al. 2016). The mechanism of the kink effect is not yet fully understood. Moreover, an analytical solution is necessary to take into account the kink effect for better estimating the stress-depth relationship in backfilled stopes.

In this paper, the mechanism of the kink effect near the bottom is first investigated. An analytical solution is then proposed to evaluate the stresses in backfilled stopes, after taking into account the mechanism of the kink effect. The proposed analytical solution is further validated by additional numerical modelings performed with FLAC.

3.2 Mechanism of kink effects

The kink effect was observed through numerical modeling performed by Sivakugan et al. (2014), who explained it as a result of not fully mobilized fill-wall interface friction near the bottom due to the stiff base restriction on the downward movement of backfill. More loads thus transfer to the bottom, resulting in higher vertical stress near the bottom compared to the vertical stress based on full arching theory. However, this cannot explain the absence of kink effects shown in other numerical modelings (Li et al. 2003; Pirapakaran and Sivakugan 2007a; Fahey et al. 2009; Sobhi et al. 2016). Here, the occurrence of the kink effect is related to the stress and yield states of backfill.

Figure 3-1 shows the yield envelop following the Mohr-Coulomb criterion for cohesionless backfill and the possible stress states of backfill along the vertical central line (VCL) of a vertical opening,

where the vertical σ_v and horizontal σ_h stresses correspond to the major σ_1 and minor σ_3 principal stresses, respectively. On the figure, K_a is the Rankine's active earth pressure coefficient expressed as follows:

$$K_a = \tan^2 \left(45^\circ - \frac{\varphi}{2} \right) = \frac{1 - \sin \varphi}{1 + \sin \varphi} \quad (3-3)$$

and $K_{0\mu}$ is the at-rest earth pressure coefficient due to the effect of Poisson's ratio, written as follows:

$$K_{0\mu} = \frac{\mu}{1 - \mu} \quad (3-4)$$

where μ is the Poisson's ratio.

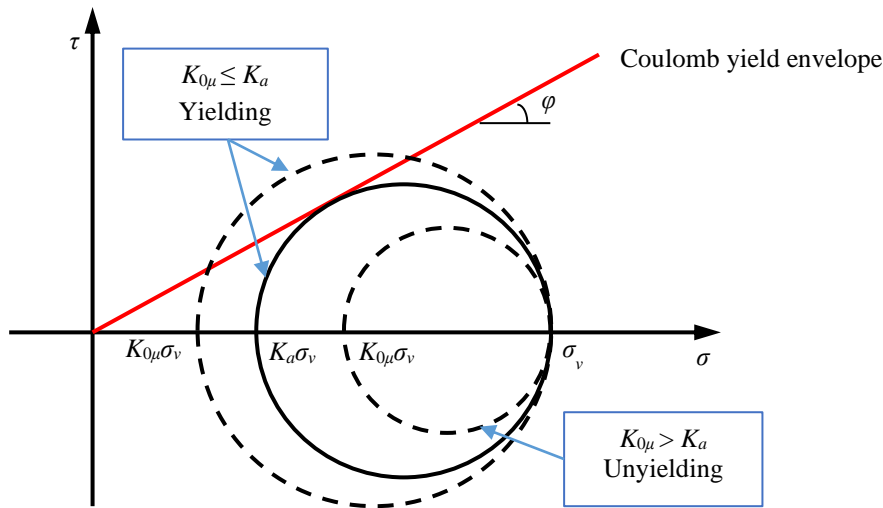


Figure 3-1: Possible stress states in the backfilled stope (adapted from Yang et al. 2018)

For a given friction angle φ , when the value of Poisson's ratio μ is larger than a critical value μ_c defined by the following equation (Yang et al. 2018):

$$\mu_c = \frac{1 - \sin \varphi}{2} \quad (3-5)$$

one will have $K_{0\mu} > K_a$. The Mohr circle of stress state is below the yield envelope and the backfill is in an at-rest (elastic) state. No large deformation occurs during the beginning of backfill placement. The frictional shear strength of the backfill and the fill-wall interfaces is little mobilized. The arching effect should not be significant and the stress variation with depth should be close to

that based on overburden solution at a given small thickness of backfill. When more backfill is placed, large deformation of upper layers can occur due to the gravity and softness of the backfill; something like a large number of small deformations can result in large deformation. The large deformation and movement of the backfill will lead to a full mobilization of the frictional shear strength of the backfill or fill-wall interfaces, resulting in a full development of arching effects and a reduction of the stresses along the upper part of the backfill. Near the bottom of the stope, however, the stiff base limits the downward movement of the backfill. The frictional shear strength of the backfill or fill-wall interfaces, resulting in little arching effect along this part of the backfill near the bottom of the opening. A kink effect can be observed in the stress profile along the height of a backfilled stope.

When Poisson's ratio μ is smaller than the critical value of μ_c defined by Eq. 3-5, one will have $K_{0\mu} < K_a$. The Mohr circle of stress state tends to exceed the yield envelope, which is impossible. The backfill yields and large (plastic) deformation occurs from the beginning to the end of placement of any thickness. The friction shear strength of the backfill or fill-wall interfaces is fully mobilized along the whole height of the backfill. The arching effect should be fully developed from the bottom to the top of the backfill. The absence of kink effects is expected.

Table 3-1 shows a summarization of previous numerical results of stresses in backfilled openings. The backfill is considered as an elastoplastic material obeying the Mohr-Coulomb criterion in all the numerical models shown in the table. It is seen again that the kink effect is observed when μ is larger than the critical value μ_c , but absent when μ is smaller than the critical value μ_c .

3.3 Analytical solution

The analysis in the previous section indicates that the kink effect is absent on stress distribution along the height of backfilled opening when $\mu < \mu_c$, but observed when $\mu > \mu_c$. For the former case, Eqs. 3-1 and 3-2 can still be used to evaluate the stresses in backfilled openings without any modification. The Rankine's active earth pressure K_a should be used in the solution because the backfill is in a yielded and active state. For the latter case, slight modification needs to be considered.

Table 3-1: A summary of previous numerical results regarding the occurrence of kink effects

μ	φ (°)	μ_c	$\mu > \mu_c?$	Kink?	Literature	Software		
0.2	10	0.413	No	No	Yang (2016)	FLAC		
0.2	20	0.329			Li et al. (2003)			
0.2	30	0.250			Pirapakaran and Sivakugan (2007a)			
0.2	30	0.250			Li and Aubertin (2008)			
0.2	35	0.213			Xu et al. (2018)		ABAQUS	
0.2	30	0.250			Sobhi et al. (2017)		SIGMA/W	
0.2	30	0.250			Yang (2016)	FLAC		
0.2	35	0.213			Liu et al. (2017)	FLAC3D		
0.3	14	0.379			Yang (2016)	FLAC		
0.3	21	0.321						
0.333	0	0.500						
0.333	10	0.413						
0.2	40	0.179			Yes	Yes	Pirapakaran and Sivakugan (2007a)	FLAC
0.2	45	0.146					Yang (2016)	
0.2	40	0.179	Fahey et al. (2009)	PLAXIS 2D				
0.2	45	0.146	Pirapakaran and Sivakugan (2007b)	FLAC/FLAC3D				
0.25	35	0.213	Sivakugan (2014)					
0.25	36	0.206	Liu et al. (2017)	FLAC3D				
0.3	28	0.265	Falaknaz et al. (2015)	FLAC				
0.3	35	0.213	Yang (2016)					
0.333	20	0.329						
0.333	30	0.250						
0.333	45	0.146						
0.4	45	0.146						
0.49	45	0.146						
0.495	45	0.146						
0.499	45	0.146						
					Fahey et al. (2009)	PLAXIS 2D		

Figure 3-2 shows a conceptual model of backfilled opening with the possible stress distribution along the whole height from the base to the top of the backfill for a given thickness of backfill in the opening. On the figure, B (m) is the width of the opening, H (m) is the final thickness or height of the backfill at the end of filling operation, z (m) is the depth of calculation point below the top surface of the backfill, h_{kv} and h_{kh} are the critical heights from the bottom of the vertical and horizontal stresses, respectively.

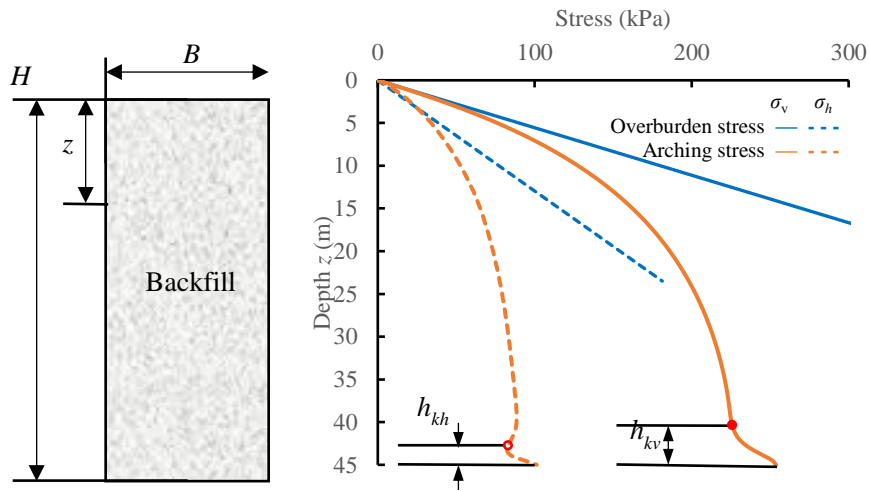


Figure 3-2: A backfilled stope and possible stress distribution with kink effects

As stated in Section 3.2, full arching effects develop in the upper part of the backfill even though the backfill is in an unyielding and at-rest state. The vertical stress above the critical heights ($z \leq H - h_{kv}$) can then be estimated with Eqs. 3-1 by using $K = K_{0\mu}$ as follows:

$$\sigma_v = \frac{\gamma B}{2K_{0\mu} \tan \delta} \left(1 - e^{-2K_{0\mu} \frac{z}{B} \tan \delta} \right) \quad \text{for } z \leq H - h_{kv} \quad (3-6)$$

The vertical stress at the critical height ($z = H - h_{kv}$) can then become as follows:

$$\sigma_{vkv} = \frac{\gamma B}{2K_{0\mu} \tan \delta} \left(1 - e^{-2K_{0\mu} \frac{H-h_{kv}}{B} \tan \delta} \right) \quad (3-7)$$

It can be considered as surcharge pressure on top of the kink section. Near the bottom below the critical height ($z > H - h_{kv}$), the vertical stress can then be obtained by using the overburden solution (without arching effect) as follows:

$$\sigma_v = \sigma_{vkv} + \gamma[z - (H - h_{kv})] \quad \text{for } z > H - h_{kv} \quad (3-8)$$

Similarly, the horizontal stress above the critical height ($z \leq H - h_{kh}$) can be estimated with Eq. 3-2 by using $K = K_{0\mu}$ as follows:

$$\sigma_h = \frac{\gamma B}{2 \tan \delta} \left(1 - e^{-2K_{0\mu} \frac{z}{B} \tan \delta} \right) \quad \text{for } z \leq H - h_{kh} \quad (3-9)$$

The horizontal stress at the critical height ($z = H - h_{kh}$) is given as:

$$\sigma_{hkh} = \frac{\gamma B}{2 \tan \delta} \left(1 - e^{-2K_{0\mu} \frac{H-h_{kh}}{B} \tan \delta} \right) \quad (3-10)$$

The horizontal stress below the critical height ($z > H - h_{kh}$) can then be obtained by:

$$\sigma_h = \sigma_{hkh} + K_{0\mu} \gamma [z - (H - h_{kh})] \quad \text{for } z > H - h_{kh} \quad (3-11)$$

Eqs. 3-6 to 3-11 constitute the proposed solution for estimating the vertical and horizontal stresses along the depth of backfilled stope upon the presence of kink effects. The solution contains two parameters (h_{kv} and h_{kh}), which need to be determined by numerical modelings.

3.4 Numerical simulations and comparisons

In order to test the validity of the proposed solution (Eqs. 3-6 to 3-11), numerical modelings were conducted with FLAC. A few numerical models will first be used to obtain the values of parameters h_{kv} and h_{kh} through calibration. The predictability of the proposed and calibrated solution (i.e. Eqs. 3-6 to 3-11 with the calibrated parameters h_{kv} and h_{kh}) will then be tested against additional numerical simulations. The proposed mechanism of kink effects will also further be verified.

3.4.1 Numerical models

Figure 3-3a schematically shows a typical vertical backfilled stope, having a width of 6 m and filled to a final height of 45 m with a space of 0.5 m left between the top surface of the backfill and stope roof. The rock mass is considered as isotropic, homogenous, and linearly elastic. Its properties are: $\gamma_R = 27 \text{ kN/m}^3$ (unit weight), $E_R = 30 \text{ GPa}$ (Young's modulus), and $\mu_R = 0.3$ (Poisson's ratio). The cohesionless backfill is elastoplastic and obeys the Mohr-Coulomb criterion. It is characterized by $\gamma = 18 \text{ kN/m}^3$ (unit weight), $E = 300 \text{ MPa}$ (Young's modulus), $\mu = 0.3$ (Poisson's ratio), $\varphi = 30^\circ$ (internal friction angle), and $\psi = 0^\circ$ (dilation angle).

Figure 3-3b shows a numerical model of the vertical backfilled stope built with FLAC. Interface elements are used along the fill-wall contact. The cohesionless interfaces have a friction angle $\delta = \varphi$. The normal (k_n) and shear (k_s) stiffness of the interfaces are calculated by a formula recommended in the FLAC manual (Itasca, 2011). The two vertical outer boundaries of the numerical model are fixed in the horizontal direction but can freely move in the vertical direction. The upper outer boundary of the numerical model is free in all directions while the lower outer boundary is fixed in all directions.

The mesh of the backfill is determined as $0.25 \text{ m} \times 0.25 \text{ m}$ while a radial mesh is used for the rock mass. The domain from the stope walls to the rock walls (external boundaries) is chosen as 150 m along the four directions. The domain and mesh size were determined after a series of sensitivity analyses (shown in Appendix B1). The numerical simulations were conducted by excavating the stope instantaneously and filled the backfill in 45 layers (1 m/layer). The displacements induced by the excavation are reset to zero before the simulation of backfilling.

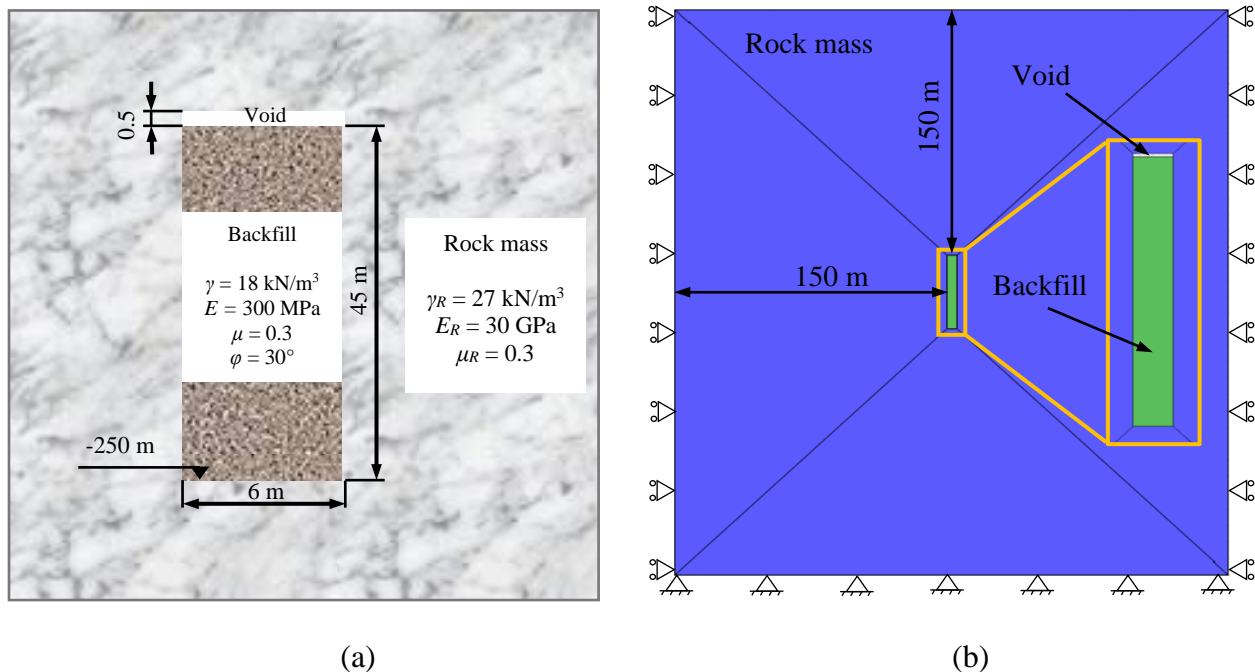


Figure 3-3: (a) A physical model and (b) a numerical model built with FLAC of a vertical backfilled stope

Table 3-2 shows the program of numerical modelings by varying the Poisson's ratio μ and internal friction angle φ to obtain two different relationships between μ and μ_c .

Table 3-2: Program of additional numerical simulations

Case	Figure No.	φ (°)	μ	B (m)	H (m)	E (kPa)	δ (°)	μ_c	$\mu > \mu_c?$	Kink expected?
0	3-4, 3-6a	30	0.3	6	45	300	30	0.25	Yes	Yes
1	3-5, 3-6b	15	0.3	6	45	300	30	0.371	No	No
		20						0.329		
		35						0.213	Yes	Yes
2	3-7, 3-8	30	0.2	6	45	300	30	0.25	No	No
			0.35						Yes	Yes
3	3-9a	30	0.3	12	45	300	30	0.25	Yes	Yes
4	3-9b	30	0.3	6	35	300	30	0.25	Yes	Yes
5	3-9c	30	0.3	6	45	30	30	0.25	Yes	Yes
6	3-9d	30	0.3	6	45	300	20	0.25	Yes	Yes

3.4.2 Validation of the proposed mechanism

Figure 3-4 shows the variation of the vertical (Figure 3-4a) and horizontal (Figure 3-4b) stresses along the VCL of the backfilled slope for a given Poisson's ratio $\mu = 0.3$ as the internal friction angle φ varies from 15° to 35° (Table 2, Cases 0 and 1). As expected, kink effects clearly occur when the internal friction angle is 30° and 35° , respectively while it is absent when $\varphi = 15^\circ$ or unobvious when $\varphi = 20^\circ$.

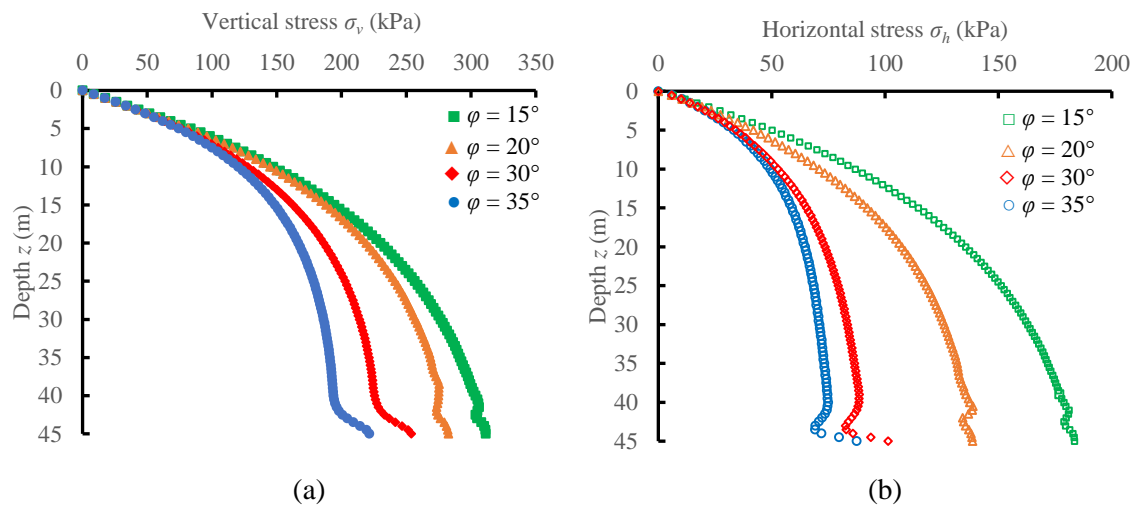


Figure 3-4: Variation of the vertical (a) and horizontal (b) stresses along the VCL of the backfilled slope for a given Poisson's ratio with different internal friction angles (details given in Table 2, Cases 0 and 1)

Figure 3-5 shows the variation of the vertical (Figure 3-5a) and horizontal (Figure 3-5b) stresses along the VCL of the backfilled slope for a given friction angle $\varphi = 30^\circ$ as the Poisson's ratio μ varies from 0.2 to 0.35 (Table 2, Cases 0 and 2). As expected again, kink obviously occurs when Poisson's ratio equals 0.3 or 0.35 while it is not significant when Poisson's ratio is taken as 0.2.

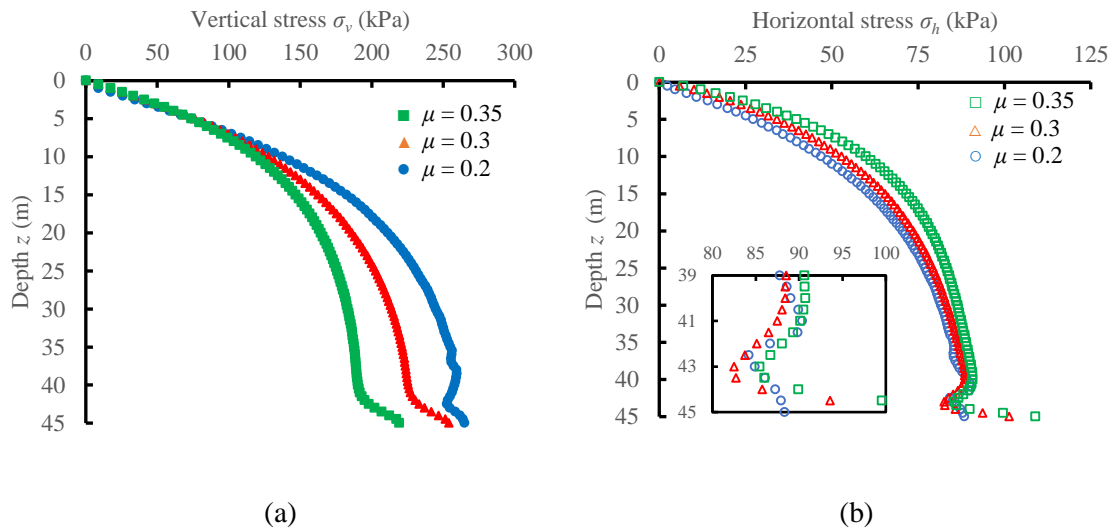


Figure 3-5: Variation of the vertical (a) and horizontal (b) stresses along the VCL of the backfilled slope for a given internal friction angle with different Poisson's ratios (details given in Table 2, Cases 0 and 2)

3.4.3 Calibration of the proposed analytical solution

The numerical results of Cases 0, 1c and 2b (Figures 3-4 and 3-5) are used to calibrate the two critical heights h_{kv} and h_{kh} of the proposed solution (Eqs. 3-6 to 3-11). Analyses on the results shown in Figures 3-4 and 3-5 tend to indicate that the two critical heights are proportional to the final height of the backfill at the end of filling operation. They are thus proposed to be as follows:

$$h_{kv} = aH \quad (3-12)$$

$$h_{kh} = bH \quad (3-13)$$

where $a = 1/10$ and $b = 1/20$.

Figure 3-6 shows the vertical and horizontal stresses of Cases 0 (Figure 3-6a), 1c (Figure 3-6b) and 2b (Figure 3-6c) with kink effects, obtained by numerical modeling and calculated by applying the proposed solution (Eqs. 3-6 to 3-13 with $a = 1/10$ and $b = 1/20$). It can be seen that the horizontal

stress calculated by the proposed analytical solution agrees well with the numerical results obtained with FLAC for all three cases. For the vertical stress, the proposed solution slightly overestimates the numerical results in the kink range, but slightly underestimates the numerical results above the kink range. Despite the slight difference, the proposed analytical solution can well capture the variation of vertical and horizontal stresses due to kink effects.

Eqs. 3-6 to 3-13 with $a = 1/10$ and $b = 1/20$ constitute the proposed and calibrated analytical solution for estimating the vertical and horizontal stresses in backfilled stopes with kink effects.

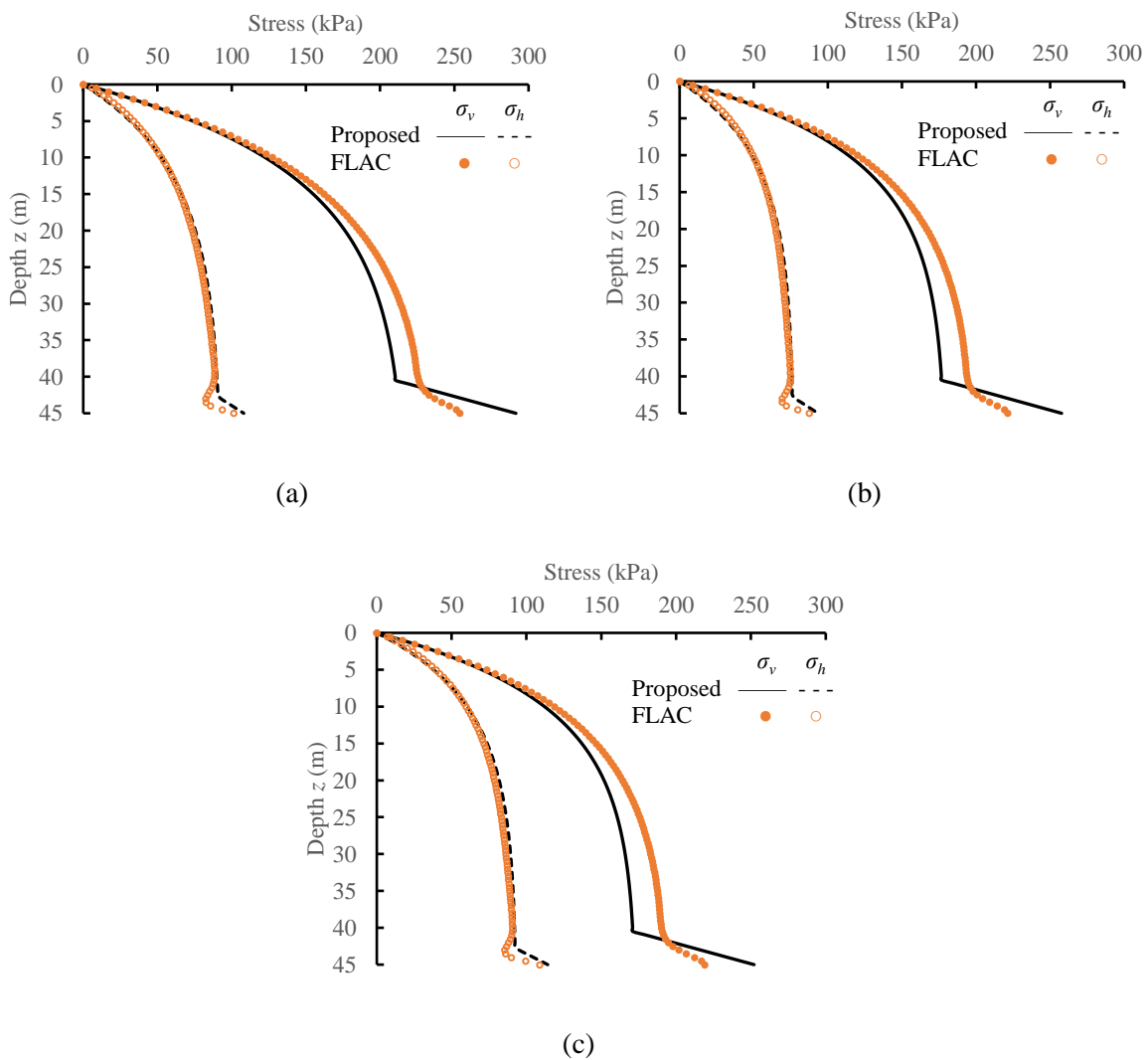


Figure 3-6: Vertical and horizontal stresses obtained by numerical modeling and predicted by applying the proposed solution (Eqs. 3-6 to 3-13 with $a = 1/10$ and $b = 1/20$) for (a) Case 0, (b) Case 1c and (c) Case 2b

3.4.4 Tests of the ability of prediction of the proposed and calibrated analytical solution

Figure 3-7 shows the distribution of vertical and horizontal stresses along the whole depth of the backfilled stope at the end of deposition for Cases 3 to 6 with different widths, heights, Young's modulus of the backfill, or internal friction angles of the fill-wall interface, calculated by the proposed and calibrated analytical solutions (Eqs. 3-6 to 3-13 with $a = 1/10$ and $b = 1/20$) and obtained by numerical simulations performed with FLAC. One sees that the vertical and horizontal stresses predicted by the proposed solution agree well with those obtained by numerical modelings with FLAC.

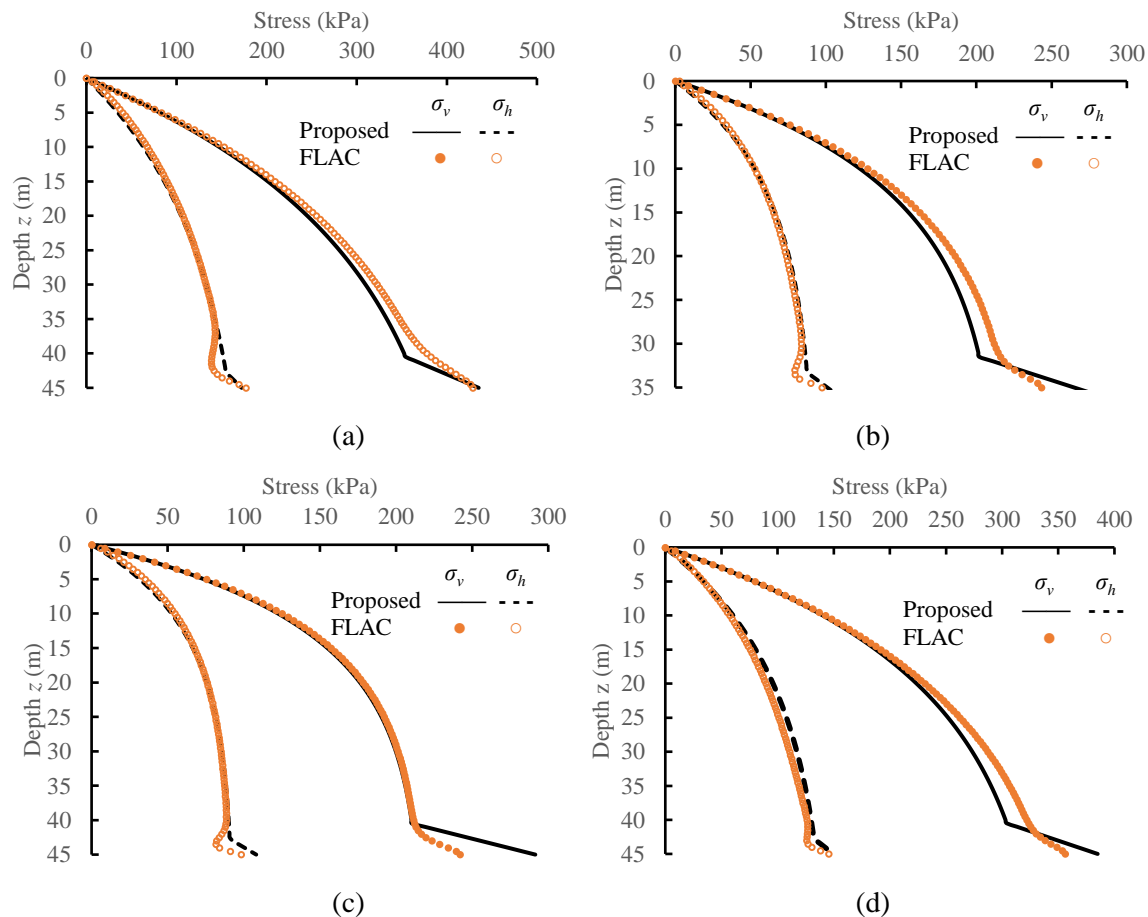


Figure 3-7: Vertical and horizontal stresses obtained by numerical modeling and predicted by the proposed solution (Eqs. 3-6 to 3-13 with $a = 1/10$ and $b = 1/20$) with different parameters for (a) Case 3 with $B = 12$ m, (b) Case 4 with $H = 35$ m, (c) Case 5 with $E = 30$ MPa and (d) Case 6 with $\delta = 20^\circ$

Figure 3-8 shows the vertical and horizontal stresses obtained by numerical modeling and those predicted with the proposed and calibrated solution (Eqs. 3-6 to 3-13 with $a = 1/10$ and $b = 1/20$). It can be seen that the agreements between the numerical and analytical results are quite good. The proposed and calibrated solution (Eqs. 3-6 to 3-13 with $a = 1/10$ and $b = 1/20$) can be used to predict the stresses in backfilled stopes with kink effects.

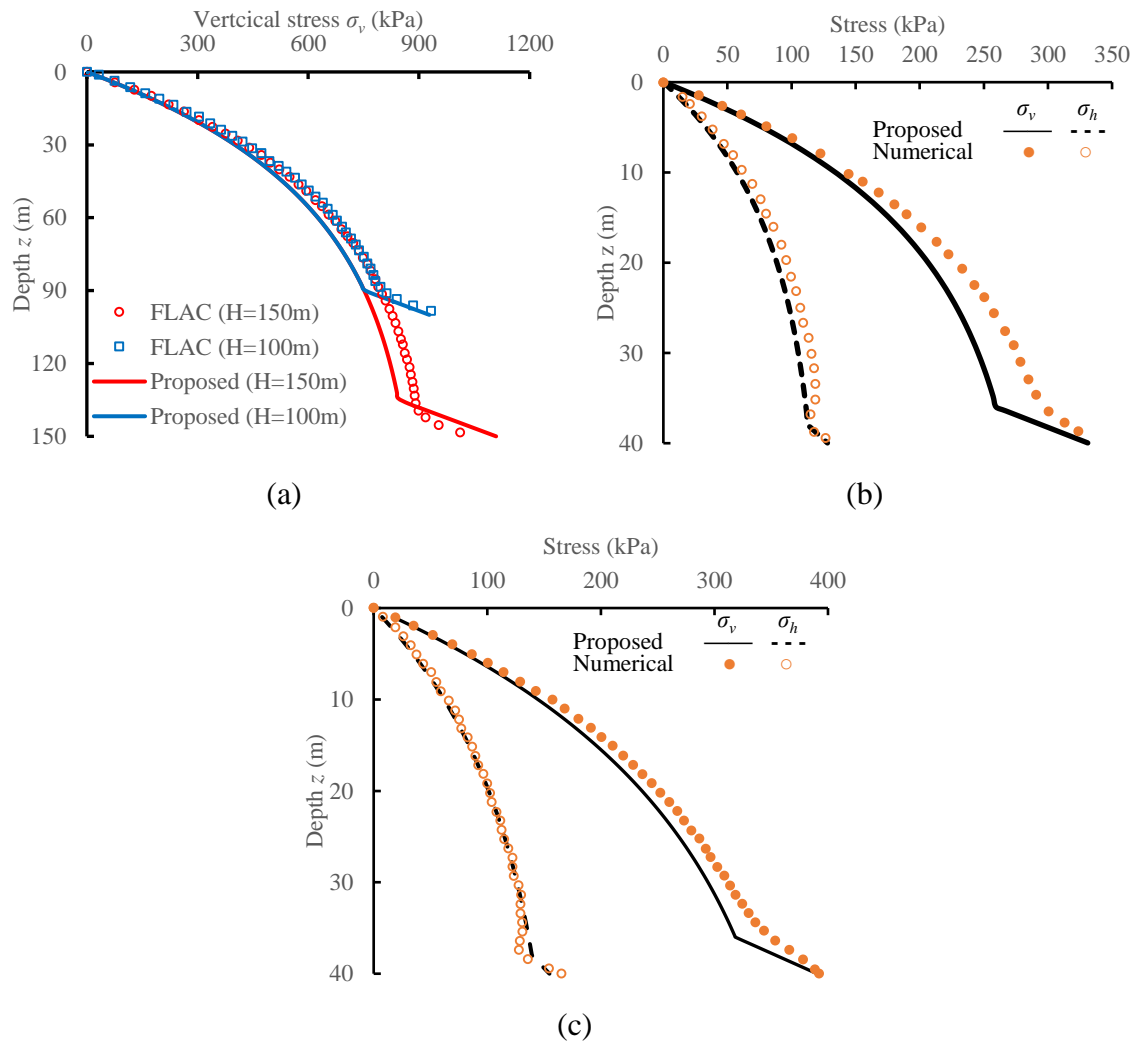


Figure 3-8: Vertical and horizontal stresses obtained by numerical modeling and predicted with the proposed solution (Eqs. 3-6 to 3-13 with $a = 1/10$ and $b = 1/20$). Comparisons with numerical results taken from (a) Sivakugan et al. (2014) with $\gamma = 17.65 \text{ kN/m}^3$, $E = 50 \text{ MPa}$, $\mu = 0.25$, $\varphi = 36^\circ$, $\delta = 36^\circ$, $H = 100$ or 150 m , $B = 25 \text{ m}$; (b) Yang (2016) with $\gamma = 18 \text{ kN/m}^3$, $E = 300 \text{ MPa}$, $\mu = 0.3$, $\varphi = 30^\circ$, $\delta = 30^\circ$, $H = 40 \text{ m}$, $B = 8 \text{ m}$; (c) Liu et al. (2017) with $\gamma = 18 \text{ kN/m}^3$, $E = 300 \text{ MPa}$, $\mu = 0.3$, $\varphi = 35^\circ$, $\delta = 28^\circ$, $H = 40 \text{ m}$, $B = 10 \text{ m}$

3.5 Discussion

This paper first theoretically investigated the mechanism of the kink effect in vertical backfilled stopes. A new conceptual analytical solution was then proposed to estimate the stresses in backfilled stopes by considering the kink effect. The proposed mechanism and conceptual analytical solution were then validated by numerical modeling results. However, it should be noted that the analytical and numerical analyses contain some limitations.

For instance, the proposed solution is considered for dry backfill without considering the pore water pressure. It can be directly used for the stability analyses of side-exposed backfill, as the backfill can be considered in the dry condition upon exposure. However, the pore water pressure needs to be considered for the design of barricades. In this case, the proposed solution cannot be directly used, and more work is required to improve this aspect.

Another limitation is related to the calibration of the two critical heights h_{kv} and h_{kh} (kink range) for the vertical and horizontal stresses, respectively. The calibration of these two critical heights was based on the numerical results available in the literature and obtained in this study. The two critical heights are found to be proportional to the final backfill heights H , which can be taken as $a = 1/10$ and $b = 1/20$ of the final height. Although good agreements were obtained between the proposed solution and numerical results, more work is required to determine the kink range with more physical meanings.

It should be noted that both the theoretical investigation of the kink effect and the proposed analytical solutions need to be verified by experimental data. This validation would require the measurement of the backfill properties (e.g., Poisson's ratio and internal friction angle), and vertical and horizontal stresses along the whole depth of the backfill, especially near the bottom. However, the measurement of Poisson's ratio is never an easy task (Suwal and Kuwano 2013). Moreover, most of the previous laboratory tests were performed by only measuring the vertical or/and horizontal stresses at the bottom of the stope with different thicknesses of backfill (Pirapakaran and Sivakugan 2007b; Ting et al. 2007; Han et al. 2018). To the authors' knowledge, there are no laboratory tests existed to measure the stresses along the whole depth at the end of backfilling. A few field measurements were conducted to measure the stress distribution along the depth during and after the filling operation (Belem et al. 2004; Thompson et al. 2012; Wang et al.

2019). However, only a few measuring (at most three) points were monitored along the depth of the slope, which cannot capture the stress variation along the depth of the slope (especially near the bottom). The laboratory tests need to be considered in the future.

Finally, this study only investigated the kink effect in a vertical slope backfilled with a cohesionless backfill. Additional work is required and ongoing to consider three-dimensional geometry, inclined slope, cohesion induced by cement hydration, confining effects caused by the lateral displacements of surrounding rock mass.

3.6 Conclusions

In this paper, the mechanism of the kink effect was first theoretically investigated. A new analytical solution was then proposed to estimate the vertical and horizontal stresses in vertical backfilled slopes by incorporating the kink effect near the bottom. The proposed mechanism for the occurrence of kink effects and the proposed analytical solution were then validated by the numerical modeling results obtained with FLAC. The results show that the occurrence of kink effect is closely related to the state of the backfill, which is determined by the relationship between the Poisson's ratio μ and internal friction angle φ of the backfill. The kink can occur when $\mu > (1 - \sin \varphi)/2$ while not occur when $\mu \leq (1 - \sin \varphi)/2$. The vertical and horizontal stresses calculated by the proposed conceptual analytical solution agree well with the numerical results. The proposed solution can well represent the kink effect near the bottom of the slope when kink occurs. The presented results in this study constitute a simple tool to evaluate the probability of the occurrence of kink effect and then estimate the stresses in backfilled slopes when kink occurs.

Acknowledgements

The authors acknowledge the financial support from the Natural Sciences and Engineering Research Council of Canada (NSERC 402318), Fonds de recherche du Québec—Nature et Technologies (2015-MI-191676), Mitacs Elevate Postdoctoral Fellowship (IT12572), and industrial partners of the Research Institute on Mines and the Environment (RIME UQAT-Polytechnique; <http://rime-irme.ca/>).

3.7 References

- Aubertin, M., Li, L., Arnoldi, S., Belem, T., Bussi re, B., Benzaazoua, M., and Simon, R. (2003). "Interaction between backfill and rock mass in narrow stopes." *Proc., Soil and Rock America 2003*, Verlag Gl ckauf Essen (VGE), Essen, Germany, Vol. 1, pp. 1157-1164.
- Belem, T., Harvey, A., Simon, R., and Aubertin, M. (2004). "Measurement and prediction of internal stresses in an underground opening during its filling with cemented fill." *Proc., fifth Int. Symp. on Ground Support in Mining and Underground Construction: Ground Support 2004, Perth*, Western Australia, Taylor and Francis Group, London., pp. 28-30.
- Darling, P. (2005). "*SME mining engineering handbook, 3rd Ed.*". Society for Mining, Metallurgy, and Exploration, Denver.
- Fahey, M., Helinski, M., and Fourie, A. (2009). "Some aspects of the mechanics of arching in backfilled stopes." *Can. Geotech. J.*, 46(11), 1322-1336. <https://doi.org/10.1139/T09-063>.
- Falaknaz, N., Aubertin, M., and Li, L. (2015). "Numerical investigation of the geomechanical response of adjacent backfilled stopes." *Can. Geotech. J.*, 52(10), 1507-1525. <https://doi.org/10.1139/cgj-2014-0056>.
- Han, Y., Li, D., Chen, J., Jing, H., and Duan, J. (2018). "Experimental study on boundary pressure and wall friction under static grain storage in silo." *Trans. Chin. Soc. Agric. Eng.*, 34(13), 296-302. <https://doi.org/10.11975/j.issn.1002-6819.2018.13.036>.
- Itasca. (2011). "FLAC-Fast Lagrangian Analysis of Continua; User's Guide". Itasca Consulting Group, Inc., Minneapolis, MN, USA.
- Janssen, H. (1895). "Versuche uber getreidedruck in silozellen." *Verein Deutscher Ingenieure*, 39(35), 1045-1049.
- Li, L. (2014a). "Analytical solution for determining the required strength of a side-exposed mine backfill containing a plug." *Can. Geotech. J.*, 51(5), 508-519. <https://doi.org/10.1139/cgj-2013-0227>.
- Li, L. (2014b). "Generalized solution for mining backfill design." *Int. J. Geomech.*, 14(3). [https://doi.org/10.1061/\(ASCE\)GM.1943-5622.0000329](https://doi.org/10.1061/(ASCE)GM.1943-5622.0000329).

- Li, L., and Aubertin, M. (2008). "An improved analytical solution to estimate the stress state in subvertical backfilled stopes." *Can. Geotech. J.*, 45(10), 1487-1496. <https://doi.org/10.1139/t08-060>.
- Li, L., and Aubertin, M. (2009a). "Horizontal pressure on barricades for backfilled stopes. Part I: Fully drained conditions." *Can. Geotech. J.*, 46(1), 37-46. <https://doi.org/10.1139/T08-104>.
- Li, L., and Aubertin, M. (2009b). "Horizontal pressure on barricades for backfilled stopes. Part II: Submerged conditions." *Can. Geotech. J.*, 46(1), 47-56. <https://doi.org/10.1139/T08-105>.
- Li, L., and Aubertin, M. (2011). "Limit equilibrium analysis for the design of backfilled stope barricades made of waste rock." *Can. Geotech. J.*, 48(11), 1713-1728. <https://doi.org/10.1139/t11-063>.
- Li, L., and Aubertin, M. (2012). "A modified solution to assess the required strength of exposed backfill in mine stopes." *Can. Geotech. J.*, 49(8), 994-1002. <https://doi.org/10.1139/t2012-056>.
- Li, L., Aubertin, M., Simon, R., Bussiere, B., and Belem, T. (2003). "Modeling arching effects in narrow backfilled stopes with FLAC." *Proc., Flac and Numerical Modeling in Geomechanics - 2003*, R. Brummer, P. Andrieux, C. Detournay, and R. Hart, eds., Balkema, Rotterdam, The Netherlands, 211-219.
- Liu, G., Li, L., Yang, X., and Guo, L. (2017). "Numerical analysis of stress distribution in backfilled stopes considering interfaces between the backfill and rock walls." *Int. J. Geomech.*, 17(2). [https://doi.org/10.1061/\(ASCE\)GM.1943-5622.0000702](https://doi.org/10.1061/(ASCE)GM.1943-5622.0000702).
- Marston, A. (1930). "The theory of external loads on closed conduits in the light of the latest experiments." *Bulletin No. 96*, Iowa, Engineering Experiment Station, Ames, Iowa.
- Mitchell, R. J. (1991). "Sill mat evaluation using centrifuge models." *Mining Science and Technology*, 13(3), 301-313. [https://doi.org/10.1016/0167-9031\(91\)90542-K](https://doi.org/10.1016/0167-9031(91)90542-K).
- Pirapakaran, K., and Sivakugan, N. (2007a). "Arching within hydraulic fill stopes." *Geotech. Geol. Eng.*, 25(1), 25-35. <https://doi.org/10.1007/s10706-006-0003-6>.
- Pirapakaran, K., and Sivakugan, N. (2007b). "A laboratory model to study arching within a hydraulic fill stope." *Geotech. Test. J.*, 30(6), 496-503. <https://doi.org/10.1520/GTJ100653>.

- Potvin, Y., Thomas, E., and Fourie, A. (2005). “*Handbook on mine fill*”. Australian Centre for Geomechanics, University of Western Australia, Nedlands, Australia.
- Sivakugan, N., Widisinghe, S., and Wang, V. Z. (2014). “Vertical stress determination within backfilled mine stopes.” *Int. J. Geomech.*, 14(5), 06014011. [https://doi.org/10.1061/\(ASCE\)GM.1943-5622.0000367](https://doi.org/10.1061/(ASCE)GM.1943-5622.0000367).
- Sobhi, M. A., Li, L., and Aubertin, M. (2017). “Numerical investigation of earth pressure coefficient along central line of backfilled stopes.” *Can. Geotech. J.*, 54(1), 138-145. <https://doi.org/10.1139/cgj-2016-0165>.
- Suwal, L., and Kuwano, R. (2013). “Statically and Dynamically Measured Poisson's Ratio of Granular Soils on Triaxial Laboratory Specimens.” *Geotech. Test. J.*, 36(4), 493-505. <https://doi.org/10.1520/GTJ20120108>.
- Thompson, B. D., Bawden, W. F., and Grabinsky, M. W. (2012). “In situ measurements of cemented paste backfill at the Cayeli Mine.” *Can. Geotech. J.*, 49(7), 755-772. <https://doi.org/10.1139/t2012-040>.
- Ting, C. H., Sivakugan, N., and Shukla, S. K. (2012). “Laboratory simulation of the stresses within inclined stopes.” *Geotech. Test. J.*, 35(2), 280-294. <https://doi.org/10.1520/GTJ103693>.
- Wang, J., Qiao, D., Han, R., Li, G., and Xie, J. (2019). “Strength model of cemented backfill body in subsequent filling at the stage of open stope and its application.” *Rock and Soil Mechanics*, 40(3), 1-8.
- Xu, C., Chen, Q., Luo, W., and Liang, L. (2018). “Analytical solution for estimating the stress state in backfill considering patterns of stress distribution.” *Int. J. Geomech.*, 19(1), 04018189. [https://doi.org/10.1061/\(ASCE\)GM.1943-5622.0001332](https://doi.org/10.1061/(ASCE)GM.1943-5622.0001332).
- Yang, P. (2016). “Investigation of the geomechanical behavior of mine backfill and its interaction with rock walls and barricades.” Ph.D. Thesis, Polytechnique Montreal, Montreal, QC, Canada.
- Yang, P., Li, L., and Aubertin, M. (2017). “A new solution to assess the required strength of mine backfill with a vertical exposure.” *Int. J. Geomech.*, 17(10). [https://doi.org/10.1061/\(ASCE\)GM.1943-5622.0000975](https://doi.org/10.1061/(ASCE)GM.1943-5622.0000975).

Yang, P., Li, L., and Aubertin, M. (2018). "Theoretical and numerical analyses of earth pressure coefficient along the centerline of vertical openings with granular fills." *Appl. Sci.*, 8(10). <https://doi.org/10.3390/app8101721>.

Yang, P., Li, L., Aubertin, M., Brochu-Baekelmans, M., and Ouellet, S. (2017). "Stability analyses of waste rock barricades designed to retain paste backfill." *Int. J. Geomech.*, 17(3), 04016079. [https://doi.org/10.1061/\(ASCE\)GM.1943-5622.0000740](https://doi.org/10.1061/(ASCE)GM.1943-5622.0000740).

CHAPTER 4 ARTICLE 2: A NEW SOLUTION TO EVALUATE THE STABILITY OF SIDE-EXPOSED BACKFILL IN INCLINED STOPES

Shupeng Chai, Ruofan Wang, Li Li

This article was submitted to *International Journal of Geomechanics* in March 2020.

Abstract: Backfilling is a common practice in underground mines. It helps to maintain ground stability, increase ore recovery, reduce ore dilution, and minimize the environmental impact associated with surface disposal of mine wastes. Ensuring the stability of the side-exposed cemented backfill is a critical issue. Several publications have been devoted to analyzing the stability of side-exposed backfill in vertical stopes even though underground stopes are always more or less inclined. Only a few studies have been reported to analyze the stability of side-exposed backfill in inclined stopes. The resistances along the fill-hanging wall interface were ignored. In this study, a new analytical solution is proposed to assess the stability and required cohesion of side-exposed backfill in inclined stopes. The proposed analytical solution has been validated by numerical modeling conducted with FLAC3D and experimental results available in the literature. The results show that a critical stope wall inclination angle exists, at which the minimum required cohesion of side-exposed backfill in inclined stopes reaches a peak value, from which the minimum required cohesion decreases whatever the stope wall inclination angle increases or decreases. The good agreements between the minimum required cohesion obtained by the numerical modeling with FLAC3D and predicted by applying the proposed solution indicate that the proposed solution can be used to assess the stability or required cohesion of side-exposed backfill in inclined stopes.

Keywords: Inclined stopes; Side-exposed backfill; Stability; Required cohesion; Analytical solution; Numerical simulations.

4.1 Introduction

The application of backfill continuously increases in underground mines because it involves several advantages such as enhancing ground stability, improving recovery of ore, reduced subsidence due to underground mining activities, improved ventilation efficiency (Potvin et al. 2005; Darling 2011; Li 2014a, 2014b; Yang et al. 2017a). Underground stope backfilling has also the advantage to minimize surface deposal of mine waste (Aubertin et al. 2003; Bussière 2007; Yang et al 2015; Liu et al. 2018).

Among the different underground mining methods, open stoping is largely applied when ore and surrounding rock are of good quality (Hartman 1992; Darling 2011). To avoid loss of ore pillars, a common practice in the open stoping mining method is to divide the stopes into primary and secondary stopes as schematically shown in Figure 4-1. The primary stopes must be filled with cemented backfill, which should remain self-standing during the secondary stope excavation. It is a critical task to determine the minimum required strength of the cemented backfill in the primary stopes in order to ensure a safe and economic design of the backfill (Cundall et al. 1978; Dight and Coulthard 1980; Mitchell et al. 1982; Li 2014a; Yang et al. 2017a).

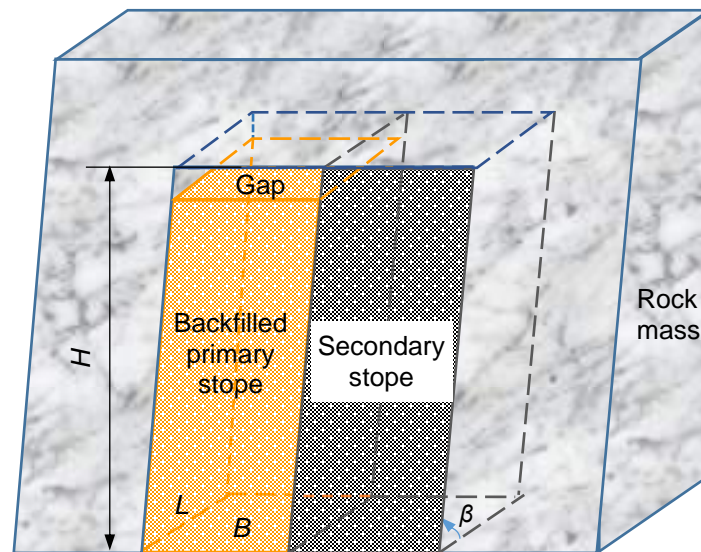


Figure 4-1: Open stoping with a primary and a secondary stope: β ($^{\circ}$) is the wall inclination angle; B (m), L (m) and H (m) are the width, length, and height of the backfill in the primary stope, respectively

Over the years, a number of solutions have been developed, mostly based on a wedge model proposed by Mitchell et al. (1982) to evaluate the stability of side exposed backfill in a vertical stope (Zou and Nadarajah 2006; Li and Aubertin 2012, 2014; Li 2014a, 2014b, Yang et al. 2017a; Liu et al. 2018; Zhao et al. 2019).

However, it is noted that most of the previous studies focus on vertical backfilled stopes. In practice, ore veins are usually more or less inclined. A solution that takes into account wall inclination angle β ($^{\circ}$) (see Figure 4-1) is necessary to estimate the stability of cemented backfill in inclined stopes upon the exposure of the secondary stope.

Smith et al. (1983) proposed a solution to evaluate the required strength of backfill in inclined stopes. The solution was developed for the specific condition with a stope wall inclination angle of 55° . The minimum (i.e. factor of safety FS = 1) required cohesion c (kPa) is expressed as follows:

$$c = \frac{\gamma H}{2(X + 0.75H/L)} \quad (4-1)$$

where γ (kN/m^3) denotes the unit weight of the backfill; L (m) and H (m) are the length and height of the backfilled stope, respectively; X is a geometric constant which was recommended to be equal to 2.21 based on a calibration with experimental results (Smith et al. 1983). The application of Eq. 4-1 is limited due to the omission of the stope wall inclination angle. In addition, the solution inherits all drawbacks of the Mitchell et al. (1982) model, including the neglect of stope width B (m) and backfill friction angle φ ($^{\circ}$).

Mitchell (1989) also modified the Mitchell et al. (1982) solution and proposed a new equation to calculate the required cohesion of side-exposed backfill in inclined stopes by calibrating with experimental results. The required cohesion is expressed as follows:

$$c = 0.2 \frac{\gamma H \sin \beta}{1 + H/L} \quad (4-2)$$

It is worth noting that the experimental results suggested that wall closure stresses would influence the backfill stability, but it was not incorporated in Eq. 4-2. As the curve-fitting technique was used to obtain the equation, further validation is still needed. Besides, there are also similar limitations in the solution as the Mitchell et al. (1982) solution.

Dirige and De Souza (2008) proposed a generalized solution by considering the slope wall inclination angle. Figure 4-2 shows a cemented backfill confined in an inclined stope with a face exposed along the front wall. In the figure, W (kN) denotes the weight of the wedge part; F_f (kN) and F_h (kN) are normal forces on the footwall and hanging wall, respectively; S_f (kN) and S_h (kN) are shear forces along the fill-foot wall and fill-hanging wall interfaces, respectively. Along the back wall, the backfill tends to be separate from the wall and no forces or resistances are considered. The sliding plane of backfill was assumed to extend from the toe of the open face to the back wall and make an angle of $\alpha = 45^\circ + \phi/2$ with the horizontal. θ ($^\circ$) is an angle made between the two lines of intersection formed by the side (hanging or foot) wall, sliding plane, and the horizontal base. Its value is related to α and β as follows:

$$\tan \theta = \frac{\tan \alpha}{\sin \beta} \quad (4-3)$$

In Dirige and De Souza (2008), θ was taken as equal to $45^\circ + \phi/2$ ($= \alpha$). Eq. 4-3 shows that this can be valid only for vertical stopes ($\beta = 90^\circ$).

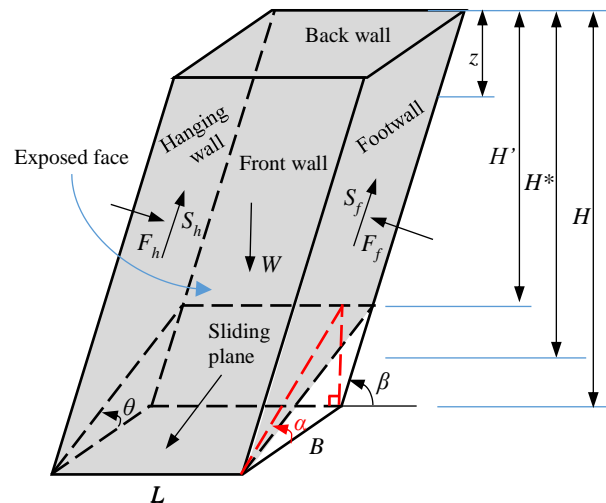


Figure 4-2: Wedge model of side-exposed backfill in an inclined stope (adapted from Dirige and De Souza 2008)

By assuming that the backfill does not have contact with the hanging wall (thus $F_h = S_h = 0$), Dirige and De Souza (2008) proposed the following equation to evaluate the stability of the cemented backfill in terms of factor of safety (FS):

$$FS = \frac{\tan \varphi}{\tan \theta} + \frac{\cos \beta \tan \varphi}{\sin \theta} + \frac{cB}{\left(H - \frac{B \tan \varphi}{2}\right) \left(\gamma BL(1 - \cos \beta \tan \varphi) - \frac{cB}{\sin \beta}\right) \sin \alpha} * \left(\frac{L}{\cos \theta} + \frac{H - (B \tan \varphi)/2}{\sin \beta}\right) \quad (4-4)$$

while the required cohesion of the cemented backfill was expressed as by Dirige and De Souza (2008):

$$c = \frac{\gamma L(1 - \cos \beta \tan \varphi)}{\left(\frac{L/(\cos^2 \theta (H - (B \tan \varphi)/2)) + 1/(\cos \theta \sin \beta)}{FS \tan \theta - \tan \varphi - \cos \beta \tan \varphi / \cos \theta}\right) + \frac{1}{\sin \beta}} \quad (4-5)$$

It should be noted that neglecting the resistances on the hanging wall can be an unrealistic assumption when the slope wall inclination angle is larger than the certain critical value (further addressed in Appendix I). In addition, the solution of Dirige and De Souza (2008) cannot be reduced to the Mitchell et al. (1982) solution for vertical backfilled slopes ($\beta = 90^\circ$) even though the former is a generalized solution of the latter.

In this paper, a new analytical solution will first be proposed to estimate the stability and required strength of side-exposed backfill in inclined slopes. The proposed solution and some previous solutions will be further compared with numerical results conducted with FLAC3D in various conditions. Experimental results available in the literature will also be used for validation. The capability and limitations of the proposed solutions will be illustrated and discussed.

4.2 Proposed solutions

Considering the limit equilibrium of the forces along the sliding direction of the wedge model for a high-aspect-ratio slope ($H > B \tan \alpha$) shown in Figure 4-2 leads to an equation as follows:

$$W_n \cos \alpha \tan \varphi + cLB/\cos \alpha = W_n \sin \alpha \quad (4-6)$$

where W_n (kN) is the net weight of the sliding wedge. It can be further expressed as follows:

$$W_n = \gamma BLH^* - (S_f + S_h) \sin \beta + (F_h - F_f) \cos \beta \quad (4-7)$$

where H^* (m) is an equivalent height of the sliding wedge, calculated by the following equation:

$$H^* = H - \frac{B}{2} \tan \theta \sin \beta = H - \frac{B}{2} \tan \alpha \quad (4-8)$$

The normal stresses on the footwall σ_f (kPa) and hanging wall σ_{hw} (kPa) can be estimated as follows by considering the two-dimensional arching solution of the stresses in backfilled stopes (detailed formulation shown in Appendix I):

$$\sigma_f = \gamma L m \left(1 - e^{-\frac{z}{RL}}\right) \quad (4-9)$$

$$\sigma_{hw} = \gamma L n \left(1 - e^{-\frac{z}{RL}}\right) \quad (4-10)$$

with

$$m = \frac{1}{2} \sin 2\beta \frac{\tan \beta + r_\beta \tan \delta_h}{\tan \delta_f + r_\beta \tan \delta_h} \quad (4-11)$$

$$n = \frac{1}{2} \sin 2\beta \frac{\tan \beta - \tan \delta_f}{\tan \delta_f + r_\beta \tan \delta_h} \quad (4-12)$$

where δ_f ($^\circ$) and δ_h ($^\circ$) are the interface friction angles along the fill-foot wall and fill-hanging wall, respectively; r_β is a coefficient applied to adjust the shear stress along the fill-hanging wall interface, defined as follows (detailed given in Appendix I):

$$r_\beta = \left\langle \frac{2\beta - 90^\circ - \phi}{90^\circ - \phi} \right\rangle \quad (4-13)$$

where $\langle X \rangle = (X + |X|)/2$ is the Macaulay brackets.

$$R = \frac{2 \sin^2 \beta (1 + r_\beta \tan \delta_h \tan \delta_f) + \cos 2\beta \tan \beta (r_\beta \tan \delta_h - \tan \delta_f)}{2(\tan \delta_f + r_\beta \tan \delta_h)} \quad \text{for } 0 < \beta < 90^\circ \quad (4-14)$$

For vertical stopes ($\beta \rightarrow 90^\circ$, $r_\beta \rightarrow 1$ and $\delta_h \rightarrow \delta_f$), one has

$$\lim_{\beta \rightarrow 90^\circ, \delta_h \rightarrow \delta_f} \tan \beta (r_\beta \tan \delta_h - \tan \delta_f) = -\frac{360^\circ}{(90^\circ - \phi)\pi} \tan \delta_f \quad (4-15)$$

and the coefficient R is expressed as follows:

$$R = \frac{1 + \tan^2 \delta_f}{2 \tan \delta_f} + \frac{90^\circ}{(90^\circ - \phi)\pi} \quad \text{for } \beta = 90^\circ \quad (4-16)$$

The shear stresses at the footwall τ_f (kPa) and hanging wall τ_h (kPa) are calculated by following the Coulomb criterion as follows:

$$\tau_f = c_f + \sigma_f \tan \delta_f \quad (4-17)$$

$$\tau_h = r_\beta (c_h + \sigma_{hw} \tan \delta_h) \quad (4-18)$$

where c_f (kPa) and c_h (kPa) are the adherence of the fill-footwall and fill-hanging wall interfaces, respectively:

$$c_f = r_f c \quad (4-19)$$

$$c_h = r_h c \quad (4-20)$$

where $r_f (= c_f / c; 0 \leq r_f \leq 1)$ and $r_h (= c_h / c; 0 \leq r_h \leq 1)$ are adherence ratios of the footwall and hanging wall, respectively.

Integrating Eq. 4-9 along the height of the wedge (see Figure 4-2) leads to the following expression for the normal force on the footwall F_f :

$$F_f = \int_0^{H'} \sigma_f \frac{dz}{\sin \beta} B + \int_{H'}^H \sigma_f \frac{dz}{\sin \beta} \frac{H-z}{\sin \beta \tan \theta} = amBL \quad (4-21)$$

with

$$a = \gamma \left[\frac{H^*}{\sin \beta} - \frac{RL}{\sin \beta} - \frac{R^2 L^2}{B \sin^2 \beta \tan \theta} \left(e^{-\frac{H}{RL}} - e^{-\frac{H'}{RL}} \right) \right] \quad (4-22)$$

where H' (m) is the height of the sliding wedge at the back wall, expressed as follows:

$$H' = H - B \tan \theta \sin \beta = H - B \tan \alpha \quad (4-23)$$

The shear force along the footwall S_f can then be written as:

$$S_f = c_f B H^* / \sin \beta + F_f \tan \delta_f = c_f B H^* / \sin \beta + amBL \tan \delta_f \quad (4-24)$$

Similarly, the normal (F_h) and shear (S_h) forces on the hanging wall are deduced as follows:

$$F_h = \int_0^{H'} \sigma_{hw} \frac{dz}{\sin \beta} B + \int_{H'}^H \sigma_{hw} \frac{dz}{\sin \beta} \frac{H-z}{\sin \beta \tan \theta} = anBL \quad (4-25)$$

$$S_h = r_\beta (c_h B H^* / \sin \beta + F_h \tan \delta_h) = r_\beta (c_h B H^* / \sin \beta + anBL \tan \delta_h) \quad (4-26)$$

The net weight of the sliding wedge W_n can then be expressed as follows:

$$W_n = \gamma B L H^* - (S_f + S_h) \sin \beta + (F_h - F_f) \cos \beta = BL \left(p - \frac{r_f + r_\beta r_h}{L} c H^* \right) \quad (4-27)$$

with

$$p = \gamma \left[RL + \frac{R^2 L^2}{B \tan \alpha} \left(e^{-\frac{H}{RL}} - e^{-\frac{H'}{RL}} \right) \right] \quad (4-28)$$

For a given cemented backfill and cohesion c , the stability of the exposed backfill is evaluated as follows in terms of FS:

$$FS = \frac{W_n \cos \alpha \tan \varphi + cLB / \cos \alpha}{W_n \sin \alpha} = \frac{\tan \varphi}{\tan \alpha} + \frac{2}{\sin 2\alpha \left(\frac{p}{c} - \frac{r_f + r_\beta r_h}{L} H^* \right)} \quad (4-29)$$

Imposing $FS = 1$ on Eq. 4-29 leads to the following expression for the minimum required cohesion c of the side-exposed backfill in an inclined slope:

$$c = \frac{p}{\frac{2}{(FS - \tan \varphi / \tan \alpha) \sin 2\alpha} + \frac{r_f + r_\beta r_h}{L} H^*} \quad (4-30)$$

Eqs. 4-29 and 4-30 are the proposed solution for estimating the FS or required cohesion of side-exposed backfill in inclined stopes.

4.3 Numerical modeling

4.3.1 Numerical models

The proposed analytical solution (Eqs. 4-29 and 4-30) is developed with several simplifying assumptions. It should be validated by other means such as experimental models and numerical models. The former can further be divided into field tests and laboratory tests. The conditions of field tests are more representative than those of laboratory tests, but the tests are too expensive and time-consuming. The safety and access to the open stopes and exposed backfill may be a serious concern. Many parameters (geometries, rockmass and fill properties, blasting) may remain unknown or/and contain a high level of uncertainty. The reliability of the result interpretation can be a critical issue. Laboratory tests do not have the mentioned limitations but significantly suffer from scale problems (Mitchell et al. 1982; Mitchell 1986). Numerical models have been shown to be a cost-effective and efficient way to validate or calibrate analytical solutions. In this study, FLAC3D of Itasca (2013) is used to assess the stability of side-exposed backfill in an inclined stope. It has been applied to study the backfill behavior in the underground stopes in several publications (Li et al. 2003; Sivakugan et al. 2014; Yang et al. 2017a; Liu et al. 2018). Its validation has also been shown by Liu et al. (2016), who reproduced with success the physical model tests of Mitchell et al. (1982) through numerical modeling with FLAC3D. In addition, Liu et al. (2016) have shown

that the exposed backfills of Mitchell et al. (1982) are short-term stability problems and the shear strengths were obtained under conditions close to undrained conditions.

Figure 4-3a shows the geometry of a side-exposed backfill in an inclined stope. This is taken as the reference case. The backfill is an elastoplastic material obeying the Mohr-Coulomb criterion. It is characterized by a dry unit weight $\gamma = 18 \text{ kN/m}^3$, a Young's modulus $E = 300 \text{ MPa}$, a Poisson's ratio $\mu = 0.2$, an internal friction angle $\varphi = 30^\circ$, a cohesion c (kPa), and a dilation angle $\psi = 0^\circ$. The tensile strength T_0 (kPa) of the backfill is considered as one-tenth of its unconfined uniaxial compressive strength (UCS), based on previous studies (Mitchell and Wong 1982; Yang et al. 2017a). The rock mass is a linearly elastic material with a unit weight $\gamma_R = 27 \text{ kN/m}^3$, a Young's modulus $E_R = 30 \text{ GPa}$ and a Poisson's ratio $\mu_R = 0.3$.

Figure 4-3b presents a numerical model of the side-exposed backfill and surrounding rockmass, built with FLAC3D. Mitchell et al. (1982) have shown that the wall closures do not have an influence on the stability or required cohesion of exposed backfill. In this study, wall closure is neglected, and a small domain is sufficient to represent the rockmass in the numerical model. The backfill is modeled by quadrilateral elements with elements of 0.5 m (same size in length, height and width) after mesh sensitivity analyses while the rockmass is modeled by a radially graded mesh (shown in Appendix C2).

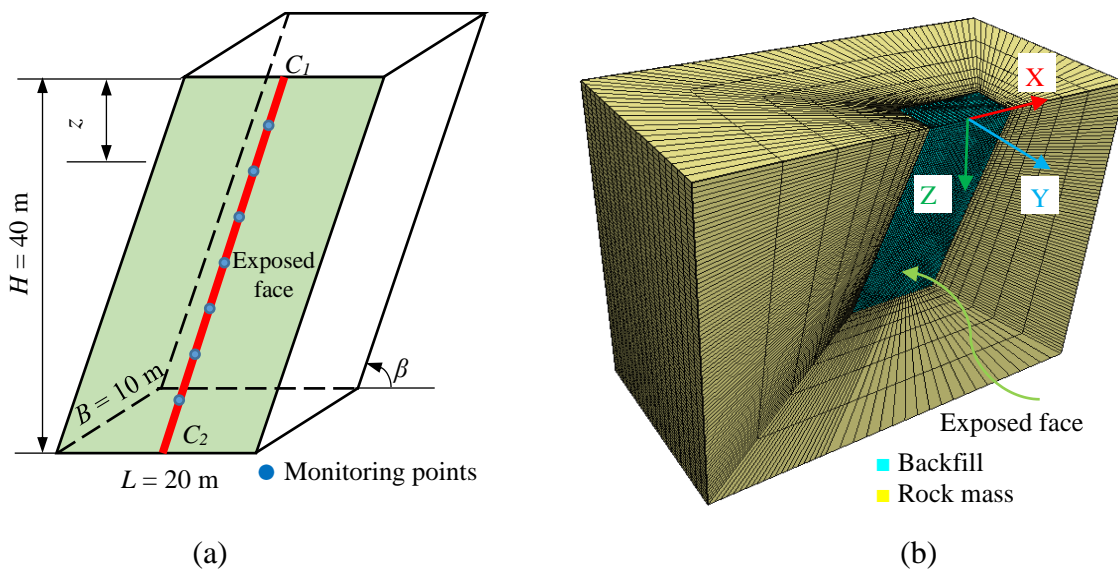


Figure 4-3: The geometry of (a) a physical model and (b) the FLAC3D numerical model of a side-exposed backfill in an inclined stope

The top boundary of the model is free to move in all directions while displacements along the bottom boundary are prohibited in the vertical and two horizontal directions. Displacements along the four lateral boundaries are prohibited in the X and Y horizontal directions but allowed in the vertical direction. The rock walls are considered as rough. Interface elements are introduced in the numerical models between the backfill and rock walls by considering their shear strengths (cohesion and friction angle) equal to that of the backfill (Liu et al. 2017). The normal and shear stiffness of the fill-rock interfaces are determined as ten times the equivalent stiffness of the stiffest neighboring zone, as recommended in the FLAC3D manual (Itasca 2013). The response of the backfill has been simulated by the four following steps:

- (1) Simulation of the initial equilibrium state;
- (2) Excavation of the primary stope;
- (3) Placement of backfill in the primary stope in layers. Each layer has a thickness of 5 m based on sensitivity analyses (shown in Appendix C2). The displacements are reset to zero before any backfilling;
- (4) Exposure of the backfill by freeing the boundary restrictions at the open face of the backfill.

The calculations were performed by applying the large strain mode (Itasca 2013). The largely deformed geometry of unstable exposed backfill can then be visualized. But the calculations stop when bad geometry associated with excessively large displacements occurs.

The program of numerical simulations is presented in Table 4-1.

Table 4-1: Program of numerical simulations (with $\gamma_R = 27 \text{ kN/m}^3$, $E_R = 30 \text{ GPa}$, and $\mu_R = 0.3$ for the rock mass and $\gamma = 18 \text{ kN/m}^3$, $E = 300 \text{ MPa}$ and $\mu = 0.2$ for the cemented backfill)

Case	Figure	β ($^\circ$)	H (m)	L (m)	B (m)	φ ($^\circ$)
0	4-3 ~ 4-6	70	40	20	10	30
1	4-7a, 4-12	Variable	40	20	10	30
2	4-7b	Variable	45	15	6	35
3	4-8a	70	Variable	20	10	30
4	4-8b	70	40	Variable	10	30
5	4-8c	70	40	20	Variable	30
6	4-9	70	40	20	10	Variable

4.3.2 Criterion of instability

The minimum required strength of the inclined side-exposed backfill is progressively approached and obtained by gradually reducing the cohesion c until the occurrence of instability. The instability of the exposed backfill can be evaluated by the examining the yield state of the material (Barrett et al. 1978; Cundall et al. 1978; Coulthard 1980; Pierce 2001), the convergence of the numerical calculations (Dirige and De Souza 2008; Dirige et al. 2009), the displacement of some key locations (Yang et al. 2017a; Liu et al. 2018), the strength-stress ratio (Liu et al. 2016, 2018), and the development of tension stress (Emad et al. 2014). Combined indicators have also been applied in some publications, as shown in Table 4-2.

Yield state is largely used as an indicator to evaluate the failure of materials. For exposed backfill, however, the use of this indicator can lead to subjective assessment because the structure of the exposed backfill can remain stable if minor yield appears in limited areas. This is commonly observed during the slope stability analysis with an overall FS > 1 while the local FS can be smaller than the unity near the base of the slope. In this study, the convergence of numerical calculations, displacement, and strength-stress ratio are considered to reduce the subjectivity in the instability assessment of the exposed backfill. The total displacement and vertical stress along the central line C_1C_2 of the open face shown in Figure 4-3a are monitored.

Table 4-2: Combined indicators to evaluate the instability of exposed backfill

References	Indicators for assessing the instability		
	Displacement	Yield state	Strength-stress ratio
Falaknaz (2014)	√		√
Liu et al. (2016)		√	√
Yang et al. (2017a)	√	√	
Liu et al. (2018)	√		√
Pagé et al. (2019)	√	√	

Figure 4-4 shows the total displacements monitored along the central line C_1C_2 of the open face in Case 0 when the cohesion of the backfill is taken as $c = 70$ kPa (Figure 4-4a) and $c = 69$ kPa (Figure 4-4b), respectively. When $c = 70$ kPa, the displacements tend to become constant with an increasing

number of iteration steps, indicating the achievement of numerical calculation convergence. When the cohesion c reduces to 69 kPa, the displacements increase ceaselessly at an accelerated pace with an increasing number of iteration steps, indicating a divergence of numerical calculations. The side-exposed backfill is then considered as stable at a cohesion of 70 kPa and unstable when the cohesion reduces to 69 kPa.

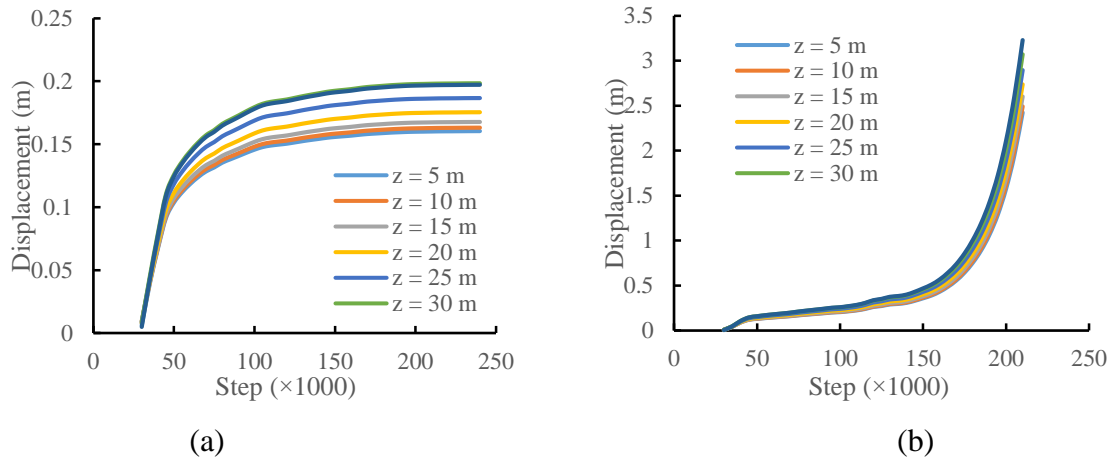


Figure 4-4: The variation of the total displacement of the open face as the iteration steps increase for Case 0 (Table 4-1) with (a) $c = 70$ kPa and (b) $c = 69$ kPa

Figure 4-5 shows the variation of the total displacements at $z = 10$ m (10 m from the top surface of the backfill) on the central line C_1C_2 of the open face in Case 0 when the backfill cohesion decrease from 96 kPa to 69 kPa. A jump of the total displacement from 0.16 m to 2.44 m is observed when the cohesion decreases from 70 kPa to 69 kPa. The minimum required cohesion of the backfill for Case 0 is then determined as 70 kPa.

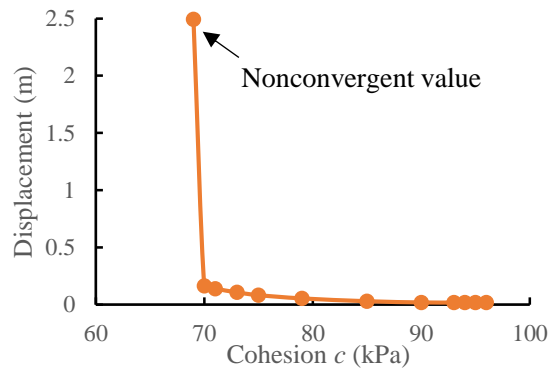


Figure 4-5: Variation of the total displacement at $z = 10$ m on the central line C_1C_2 of the open face as a function of backfill cohesion for Case 0 (Table 4-1)

Figure 4-6 shows the strength-stress ratios of the side-exposed backfill for Case 0 with c equal to 70 kPa (Figure 4-6a) and 69 kPa (Figure 4-6b), respectively. It is seen that the strength-stress ratio is higher than the unity everywhere through the exposed backfill when the backfill cohesion is taken as $c = 70$ kPa. The backfill is considered as stable. When the cohesion c is reduced to 69 kPa, a sliding plane appears with the coalescence of strength-stress ratio smaller than the unity. In addition, failure zones near the top part of the backfill are also observed, which are due to tension, as reported by Yang et al. (2017). This indicates the occurrence of the instability of the side-exposed backfill. The minimum required cohesion of the side-exposed backfill is determined again as 70 kPa.

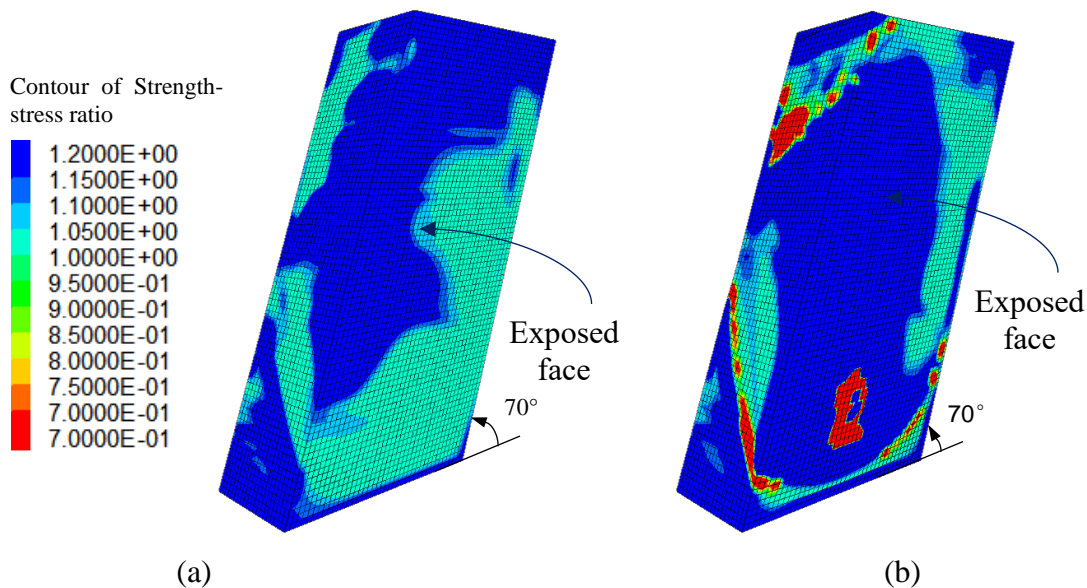


Figure 4-6: Strength-stress ratio iso-contours of the side-exposed backfill for Case 0 (Table 4-1) with (a) $c = 70$ kPa and (b) $c = 69$ kPa

The above analysis indicates that the convergence of numerical calculation, the total displacement, and the strength-stress ratio can be used to evaluate the occurrence of instability and assess the minimum required cohesion of side-exposed backfill.

4.3.3 Comparison between numerical modeling and analytical solution

The same procedure of numerical simulations and assessment applied to the reference case has been taken to the remaining cases shown in Table 4-1 in order to obtain the minimum required cohesions by numerical modeling for different cases.

Figure 4-7 illustrates the variation of the minimum required backfill cohesion c as a function of the slope wall inclination angle β (Figure 4-7a, Case 1, Table 4-1; Figure 4-7b, Case 2, Table 4-1), obtained by the numerical modeling and predicted by applying the proposed analytical solution (Eq. 4-30). The results calculated with the analytical solutions of Smith et al. (1983; Eq. 4-1), Mitchell (1989; Eq. 4-2), and Dirige and De Souza (2008; Eq. 4-5) are also presented in the figure. The numerical results shown in Figure 4-7a indicate that the minimum required cohesion moderately increases as β increases from 50° to 70° and then decreases as β further increases from 70° to 90° . This indicates that the most unstable case takes place at a slope wall inclination angle of 70° . These results can be explained by the absence of effective contacts between the hanging wall and backfill when the slope wall inclination angle β is smaller than a critical angle ($\approx 45^\circ + \varphi/2$). When the slope wall inclination angle is higher than this critical angle, the backfill starts to have effective contact with the hanging wall and the tightness of fill-hanging wall contact increases as β increases. The exposed backfill becomes more stable and the minimum required cohesion is reduced.

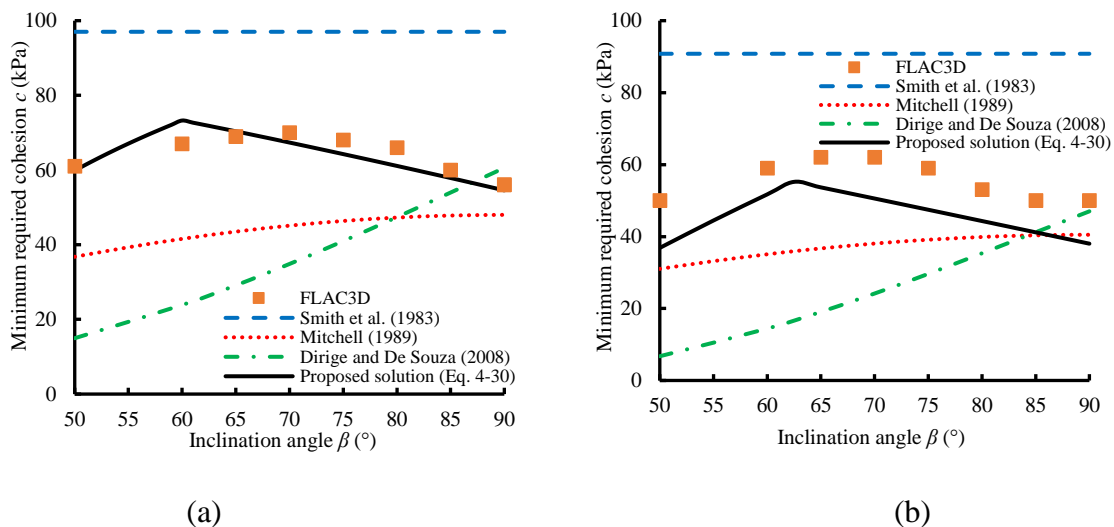


Figure 4-7: Variation of the minimum required cohesion c as a function of slope wall inclination angles β , obtained by numerical modeling and predicted by applying the proposed solution; predictive results obtained by applying existing analytical solutions are also plotted on the figure for (a) Case 1 in Table 4-1 and (b) Case 2 in Table 4-1

Very similar numerical results are obtained for Case 2 (Table 4-1) with different geometries ($H = 45$ m, $L = 15$ m, $B = 6$ m) and backfill friction angle ($\varphi = 35^\circ$), as shown in Figure 4-7b. The peak

value of the minimum required cohesion is obtained at a wall inclination angle of around 65° in this case, probably due to the difference in the backfill friction angle that Case 1.

In both Cases 4-1 and 4-2, Figure 4-7 shows that an application of the Smith et al. (1983) solution largely overestimates the minimum required cohesion while the application of the Mitchell (1989) solution and the Dirige and De Souza (2008) solution results in a considerable underestimation of the minimum required cohesion. A relatively good agreement is obtained between the minimum required cohesions obtained by the numerical modeling and those predicted with the proposed solution (Eq. 4-30). The proposed solution (Eq. 4-30) is partly validated by the numerical modeling. However, it is worth mentioning that the application of the proposed solution tends to underestimate the minimum required cohesion for Case 2, Table 4-1, as indicated by Figure 4-7b. This can thus result in a nonconservative design of backfill. Care is necessary in applying the proposed solution for backfill design in this case.

Figure 4-8 shows the variation of the minimum required cohesions of side-exposed backfill as a function of backfill height H (Figure 4-8a; Case 3, Table 4-1), slope length L (Figure 4-8b; Case 4, Table 4-1) and slope width B (Figure 4-8c; Case 5, Table 4-1), obtained by numerical modeling with FLAC3D and predicted by applying the proposed solution (Eq. 4-30) and the existing solutions (Eqs. 4-1, 4-2 and 4-5).

The numerical results show that the minimum required cohesion increases when the backfill height H or length L increases but decreases as the backfill width B increases. In all cases, the application of the Smith et al. (1983) solution overestimates the minimum required cohesion while the application of the Mitchell (1989) solution and the Dirige and De Souza (2008) solution largely underestimates the minimum required cohesion, compared to the numerical results. The good agreement between the minimum required cohesion obtained by the numerical modeling with FLAC3D and those predicted by applying the proposed solution (Eq. 4-30) indicates again the validity of the proposed solution.

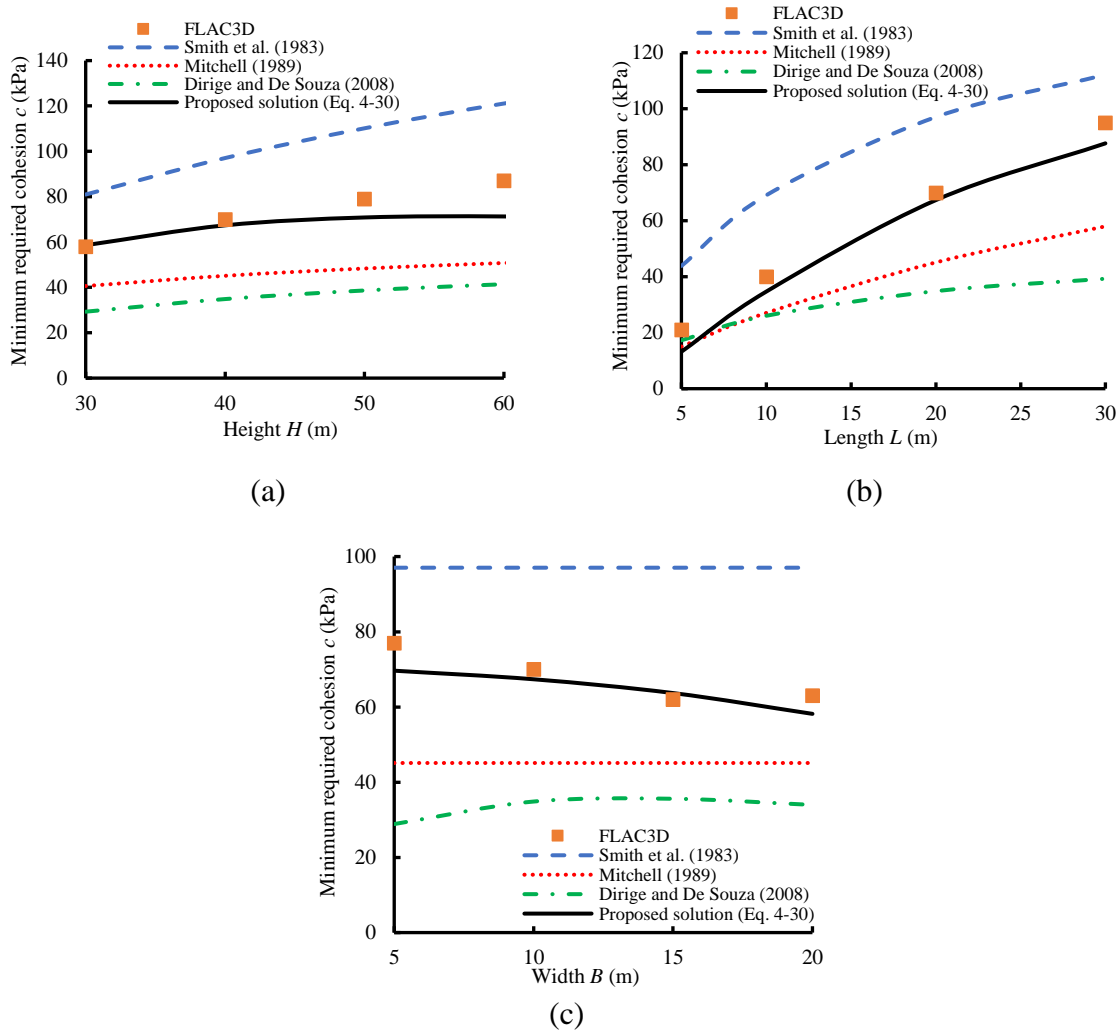


Figure 4-8: Variation of the minimum required cohesion c as a function of (a) backfill height H (Case 3, Table 4-1), (b) stope length L (Case 4, Table 4-1) and (c) stope width B (Case 5, Table 4-1), obtained by numerical modeling and predicted by the proposed and existing solutions

Figure 4-9 shows the variation of the minimum required backfill cohesion as a function of fill friction angle ϕ (Case 6, Table 4-1), obtained by numerical modeling with FLAC3D and predicted by applying the existing solutions (Eqs. 4-1, 4-2 and 4-5) and the proposed solution (Eq. 4-30). The numerical results show that the minimum required cohesion significantly decreases as the fill friction angle ϕ increases from 20° to 40° .

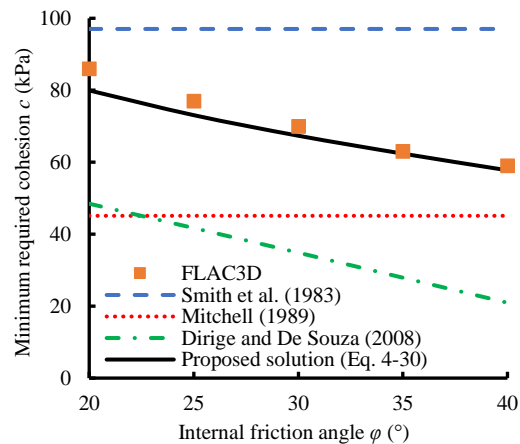


Figure 4-9: Variation of the minimum required cohesion c as a function of the backfill internal friction angles ϕ (Case 6 in Table 4-1), obtained by numerical modeling and predicted by the proposed and existing solutions.

Again, the minimum required cohesions are largely overestimated by applying the Smith et al. (1983) solution and considered underestimated by applying the Mitchell (1989) solution and the Dirige and de Souza (2008) solution, compared to the numerical results. A good agreement between the minimum required cohesion obtained by the numerical modeling and those predicted by the proposed solution (Eq. 4-30) illustrates again the validity of the proposed solution.

4.4 Comparison with experimental results

A few experimental tests have been conducted to evaluate the stability of side-exposed backfill in inclined stopes (Smith et al. 1983; Mitchell 1989; Dirige and De Souza 2008). However, some of them cannot be applied to verify the proposed analytical solution (Eq. 4-30) due to the different conditions or lack of adequate experimental data. Smith et al. (1983) considered a special geometry like an inclined funnel and the stope geometry parameters were incomplete. Dirige and De Souza (2008) only conducted four tests and all the backfill remained stable upon exposure. Mitchell (1989) successfully obtained the minimum required strength of the backfill upon exposure with different wall inclination angles. Therefore, the experimental data of Mitchell (1989) are used here to illustrate the improvement of the proposed analytical solution for the required cohesion of side-exposed backfill in inclined stopes. Table 4-3 shows the experimental results for unstable backfill

in high-aspect-ratio stopes ($H > B \tan \alpha$). It is noted that two wall closure stresses were applied at the hanging wall in the model tests, respectively.

Figure 4-10 compares the measured cohesion and the required cohesion calculated with the Mitchell (1989) solution (Eq. 4-2) and the proposed solution (Eq. 4-30) for the tests with 10% UCS wall closure stress (Figure 4-10a) and 50% UCS wall closure stress (Figure 4-10b), and for all the tests (Figure 4-10c). When applying the Mitchell (1989) solution for the tests with 10% UCS wall closure stress, the error on the prediction of the minimum required cohesion is

$$\text{Error} = \sqrt{\sum_{i=1}^{N_{10}} (c_{\text{calculated}} - c_{\text{measured}})_i^2} = 14.787$$

where N_{10} is the number of tests with 10% UCS wall closure stress.

Table 4-3: Model tests of backfill stability (data taken or calculated from Mitchell 1989)

Test No.	Wall closure stress (% UCS)	Prototype H (m)	Prototype B (m)	Prototype L (m)	β (°)	UCS (kPa)	c (kPa)
1	10	32.2	12.5	15.0	60	70	35
3	10	28.8	9.5	26.2	75	103	51.5
4	10	25.3	8.6	12.9	75	73	36.5
5	10	39.4	13.4	10.0	75	76	38
6	10	20.8	6.9	20.6	90	80	40
7	10	22.4	7.6	11.4	90	72	36
8	10	26.8	6.8	9.1	90	76	38
15	50	23.8	7.8	21.2	60	66	33
16	50	20.5	6.7	18.3	60	73	36.5
19	50	23.3	7.7	21.2	75	78	39
20	50	25.3	8.6	12.9	75	71	35.5
21	50	36.1	12.3	9.2	75	68	34
22	50	24.6	8.1	24.4	90	72	36
23	50	35	11.9	17.9	90	77	38.5

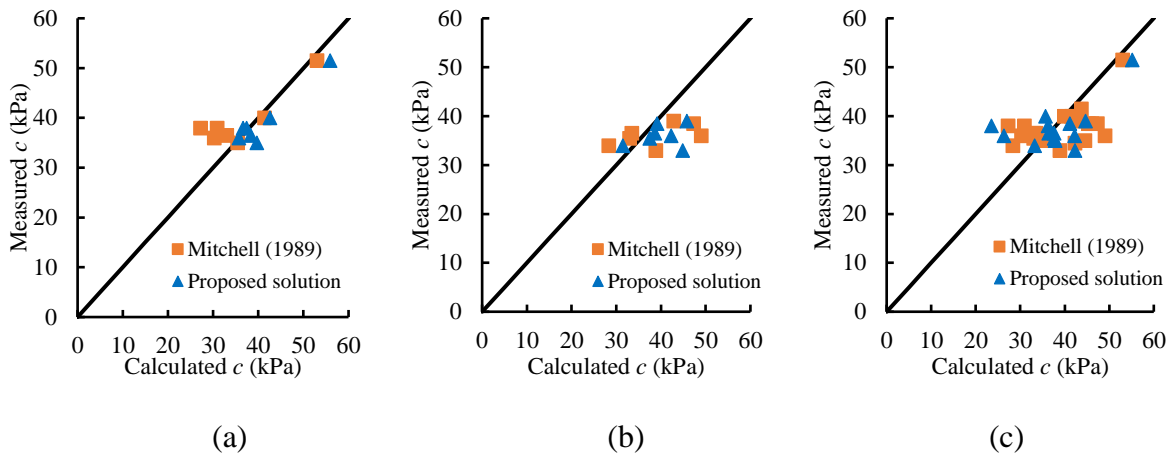


Figure 4-10: Comparison of the required cohesion obtained from experimental results of Mitchell (1989) and predicted by the proposed analytical solution (Eq. 4-30) and the Mitchell (1989) solution (Eq. 4-2) for tests with (a) 10% UCS wall closure stress and (b) 50% UCS wall closure stress, and (c) for all the tests

When the proposed solution (Eq. 4-30) is used, the curve fitting technique leads to $\delta_h = \delta_f \approx 42.77^\circ$, $\varphi = 43^\circ$, $r_h = 0.4$ and $r_f = 0.7$, with a prediction error

$$\text{Error} = \sqrt{\sum_{i=1}^{N_{10}} (c_{\text{calculated}} - c_{\text{measured}})_i^2} = 7.375$$

The smaller error of the proposed solution suggests that the proposed analytical solution by applying the curve-fitting technique is more representative of the experimental results for the tests with 10% UCS wall closure stress.

Similarly, for analyzing only the tests with 50% UCS wall closure stress and all the tests, the parameters used in the proposed analytical solution and the prediction errors of analytical solutions are summarized in Table 4-4, respectively. Again, a smaller error can be obtained with the proposed solution, indicating an improvement of the solution has been achieved.

Nonetheless, it is worth noting that the internal friction angle of the backfill and interface are taken as around 43° in the proposed analytical solution by the curve-fitting technique. This is different from the zero friction angle used in the Mitchell (1989) solution but closer to the physical conditions of the experiments. The backfill was placed in the centrifuge after 28 days' curing,

which is different from the undrained conditions upon exposure considered in the model tests of Mitchell et al. (1982). Thus, the internal friction angle should never be zero.

It is observed that the smallest prediction error is obtained by only considering the tests with 10% UCS wall closure stress. This is mainly dependent on the parameters used in the analytical solutions. The difference in the parameters used in the three conditions shown in Table 4-4 may indicate the influence of wall closure stress on backfill stability. More work is still needed to analyze the experimental results of Mitchell (1989) as well as the influence of wall closure on the stability of side-exposed backfill in inclined stopes.

Table 4-4: Parameters used in the proposed solution and prediction errors of analytical solutions

Wall closure stress	δ_h (°)	δ_f (°)	ϕ (°)	r_h	r_f	Error	
						Proposed solution	Mitchell (1989)
10% UCS	42.77	42.77	43	0.4	0.7	7.375	14.787
50% UCS	41	41	41	0.5	1	15.552	18.355
10% + 50% UCS	43	43	43	0.1	0.9	22.729	23.570

4.5 Discussion

In this study, a new analytical solution has been proposed to assess the stability or required cohesion of side-exposed backfill in inclined stopes. The proposed solution was validated by a number of numerical simulations performed with FLAC3D and experimental results available in the literature. It can thus be considered as a useful tool to evaluate the stability or minimum required cohesion of side-exposed backfill in inclined stopes. However, the proposed analytical solutions have been developed by considering several simplifying assumptions, including:

- (1) The proposed model considers high-aspect-ratio stopes ($H > B \tan \alpha$). The sliding plane can thus extend from the base of the exposed backfill face to the back wall. More work is necessary for low-aspect-ratio stopes ($H < B \tan \alpha$) by taking into account possible tension cracks near the upper part of the cemented backfill (Dight and Coulthard 1980; Li 2014b; Yang et al. 2017a).

- (2) The proposed solution was developed by considering a plane sliding plane. The numerical modeling showed that the sliding plane is more or less curved. In addition, the numerical modeling showed that the sliding plane does not pass at the bottom of the backfill but starts somewhere above the bottom of the exposed backfill face. These aspects need to be considered in the future.
- (3) Previous numerical simulations (Li and Aubertin 2009; Liu et al. 2017) have shown that the vertical and horizontal stresses in backfilled stopes decrease as the interface cohesion increases. However, they never decrease to zero or become negative, independently on the values of the interface cohesion. Rather, they tend to become constant and remain positive when the interface cohesion exceeds a certain value. When one applied some existing analytical solutions developed for estimating the stresses in backfilled stopes, negative stresses can appear once the cohesion is higher than a certain value (Li et al. 2005; Ting et al. 2011; Xu et al. 2018). This is a well-known limitation of the limit equilibrium analysis, by which the interface strength is always considered as fully mobilized, resulting in an overestimation of the arching effect with high shear strength materials. To overcome this problem, Liu et al. (2019) considered that the calculated stresses become constant once the cohesion reaches a threshold of 50 kPa. The solution was proposed for a specific stope geometry; its validity for general cases has not yet been shown. In this study, the stress estimation along the hanging wall and footwall was performed by considering cohesionless fill-rock interfaces. More work is necessary to develop an analytical solution that can be used to estimate the stress state in stopes backfilled with cemented backfill.
- (4) A two-dimensional (strain plane) arching solution was used to estimate the normal stresses along the hanging wall and footwall after the exposure of the backfill. However, stress redistribution can take place in the backfill upon side exposure of the backfill (Falaknaz 2014; Liu et al. 2019). More efforts are needed to obtain a more realistic solution that can be used to evaluate the stress state in the side-exposed backfill in inclined stopes.
- (5) In this study, the side-exposed backfill is considered as a homogeneous and isotropic material obeying the elastoplastic Mohr-Coulomb criterion. However, backfill placed in underground stopes may become non-homogeneous and anisotropic due to segregation (Liu et al. 2017; Dalcé et al. 2019) and two stages backfilling (Li 2014a; Thompson et al. 2012). More works

are required to take into account the more realistic spatial distribution of material and more representative constitutive models in the future.

- (6) The proposed solution was developed by considering stiff rock walls. The influence of rock wall closure associated with the excavation of an adjacent secondary slope is neglected. However, the closure of rock walls can become non-negligible in deep mines, especially when the rockmass exhibits creep feature (Wang et al. 2019; Qi and Fourie 2019). Mitchell et al. (1982) have shown that the wall closure has little impact on the stability and required cohesion of side-exposed backfill. Their tests were realized by using soft backfill under short-term stability conditions (Liu et al. 2016). More work is necessary to analyze the influence of the rock wall closure on the required cohesion and stability of dry and hard backfill upon exposure.
- (7) Even though the proposed analytical solution has been partially verified by the experimental results of Mitchell (1989), some parameters are obtained by curve-fitting and the experimental conditions are not exactly consistent with the conditions of the proposed analytical solution. More experimental work is still necessary for further validation of the proposed solution.

4.6 Conclusions

A new analytical solution is proposed to assess the stability and required cohesion of side-exposed backfill in inclined stopes. Numerical simulations are conducted with FLAC3D to verify the minimum required cohesion predicted by applying the proposed analytical solution. The results illustrate that the peak value of the minimum required cohesion occurs at a stope wall inclination angle of $\beta \approx 45^\circ + \phi/2$ as β varies from 50° to 90° . The minimum required cohesion will then decrease from the peak value whatever the stope wall inclination angle further increases or decreases from the critical stope wall inclination angle. The good agreements between the minimum required cohesion obtained by the numerical modeling with FLAC3D and those predicted by applying the proposed analytical solution indicate that the proposed solution can be considered as a useful tool to assess the stability or required cohesion of side-exposed backfill in inclined stopes.

4.7 Appendix I: Formulation for deducing the normal stresses at the hanging wall and footwall in an inclined backfilled stope

In vertical stopes, the normal stresses on the sidewalls can be obtained by directly applying the divers arching solutions (Aubertin et al. 2003; Li et al. 2003, 2005). The shear forces along the walls can then be estimated without difficulty (Li 2014b; Yang et al. 2017a; Liu et al. 2018). For inclined stopes, a few analytical solutions have been proposed for estimating the stresses in inclined backfilled stopes (Ting et al. 2011; Jahanbakhshzadeh et al. 2017, 2018b; Yan et al. 2019). These solutions, however, focus on the vertical and horizontal stresses, which cannot directly be used to obtain the normal and shear forces along the hanging wall and footwall. In addition, the determination of the earth pressure coefficient K contained in these arching solutions still remains an unsolved issue (Sobhi et al. 2017; Yang et al. 2017b, 2018). In this study, a two-dimensional (strain plane) solution is proposed to estimate the normal stresses along the hanging wall and footwall in an inclined backfilled stope; the earth pressure coefficient K is not involved.

Figure 4-11 schematically shows an inclined narrow backfilled stope with a wall inclination angle β ($0 < \beta \leq 90^\circ$). A horizontal isolated layer element with the acting forces is presented on the right side. The acting forces include: the weight of the layer element W_L (kN); the vertical forces V (kN) on the upper face and $V + dV$ (kN) on the lower face, respectively; normal forces on the footwall F_{fL} (kN) and hanging wall F_{hL} (kN), respectively; shear forces on the footwall S_{fL} (kN) and hanging wall S_{hL} (kN), respectively.

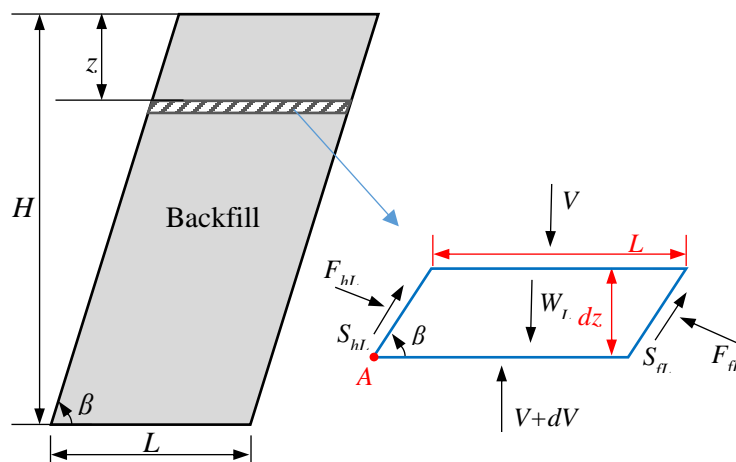


Figure 4-11: An inclined narrow backfilled stope with an isolated differential layer element

The weight of the isolated layer element W_L is given as:

$$W_L = \gamma L dz \quad (4-31)$$

Considering a uniform distribution of vertical stress σ_{v0} (kPa) along the upper surface of the layer element leads to the vertical force V expressed as follows:

$$V = \sigma_{v0} L \quad (4-32)$$

Similarly, F_{fL} and F_{hL} can be given as:

$$F_{fL} = \sigma_{f0} \frac{dz}{\sin \beta} \quad (4-33)$$

$$F_{hL} = \sigma_{h0} \frac{dz}{\sin \beta} \quad (4-34)$$

where σ_{f0} (kPa) and σ_{h0} (kPa) are the normal stresses at the footwall and hanging wall, respectively.

The shear strengths along the footwall τ_{f0} (kPa) and hanging wall τ_{h0} (kPa) are estimated as

$$\tau_{f0} = c_f + \sigma_{f0} \tan \delta_f \quad (4-35)$$

$$\tau_{h0} = c_h + \sigma_{h0} \tan \delta_h \quad (4-36)$$

The shear forces S_{fL} (kN) on the footwall and S_{hL} (kN) on the hanging wall can then be expressed as:

$$S_{fL} = \tau_{f0} \frac{dz}{\sin \beta} = (\sigma_{f0} \tan \delta_f) \frac{dz}{\sin \beta} \quad (4-37)$$

$$S_{hL} = \tau_{h0} \frac{dz}{\sin \beta} = (\sigma_{h0} \tan \delta_h) \frac{dz}{\sin \beta} \quad (4-38)$$

It is noted that the adherences along the fill-footwall interface c_f (kPa) and fill-hanging wall interface c_h (kPa) are considered as zero to avoid unrealistic stress estimation.

Considering the static equilibrium of the layer element in the vertical and horizontal directions leads to:

$$dV + (S_{fL} + S_{hL}) \sin \beta + (F_{fL} - F_{hL}) \cos \beta - W = 0 \quad (4-39)$$

$$(S_{fL} + S_{hL}) \cos \beta + (F_{hL} - F_{fL}) \sin \beta = 0 \quad (4-40)$$

The consideration of moment equilibrium of the layer element around the rotation axis A leads to the following equation:

$$\begin{aligned} \frac{L}{2}(V + dV) - V\left(\frac{L}{2} + \frac{dz}{\tan \beta}\right) + S_{fL}L \sin \beta + F_{fL}\left(\frac{dz}{2 \sin \beta} + L \cos \beta\right) \\ - F_{hL}\frac{dz}{2 \sin \beta} - \frac{W_L}{2}\left(\frac{dz}{\tan \beta} + L\right) = 0 \end{aligned} \quad (4-41)$$

Submitting Eqs. 4-31~4-38 into Eqs. 4-39 and 4-40 leads to the normal stresses on the walls expressed as follows:

$$\sigma_{f0} = L\left(\gamma - \frac{d\sigma_{v0}}{dz}\right)m_0 \quad (4-42)$$

$$\sigma_{h0} = L\left(\gamma - \frac{d\sigma_{v0}}{dz}\right)n_0 \quad (4-43)$$

with

$$m_0 = \sin \beta \cos \beta \frac{\tan \beta + \tan \delta_h}{\tan \delta_f + \tan \delta_h} \quad (4-44)$$

$$n_0 = \sin \beta \cos \beta \frac{\tan \beta - \tan \delta_f}{\tan \delta_f + \tan \delta_h} \quad (4-45)$$

Introducing Eqs. 4-42 and 4-43 into Eq. 4-41 results in the following equation:

$$\frac{d\sigma_{v0}}{dz} + \frac{\sigma_{v0}}{R_0L} + \frac{d\sigma_{v0}}{2R_0L} - \gamma = 0 \quad (4-46)$$

with

$$R_0 = \frac{2 \sin^2 \beta (1 + \tan \delta_h \tan \delta_f) + \cos 2\beta \tan \beta (\tan \delta_h - \tan \delta_f)}{2(\tan \delta_f + \tan \delta_h)} \quad (4-47)$$

By neglecting the small term $d\sigma_{v0}/(2R_0L)$, Eq. 4-46 can then be simplified as:

$$\frac{d\sigma_{v0}}{dz} + \frac{\sigma_{v0}}{R_0L} - \gamma = 0 \quad (4-48)$$

Solving Eq. 4-48 and considering $\sigma_{v0} = 0$ at $z = 0$ lead to the following expression for the vertical stress:

$$\sigma_{v0} = \gamma LR_0 \left(1 - e^{-\frac{z}{R_0L}}\right) \quad (4-49)$$

Introducing Eq. 4-49 into Eqs. 4-42 and 4-43, the normal stress on sidewalls at a depth of z can be expressed as follows:

$$\sigma_{f0} = \gamma L m_0 \left(1 - e^{-\frac{z}{R_0L}}\right) \quad (4-50)$$

$$\sigma_{h0} = \gamma L n_0 \left(1 - e^{-\frac{z}{R_0 L}} \right) \quad (4-51)$$

It is worth noting that the full contact has been considered between the backfill and rock walls in the above derivation. This has been shown true for vertical and sub-vertical stopes by numerical modeling (Li and Aubertin 2009; Jahanbakhshzadeh et al. 2017, 2018b). For inclined stopes with small inclination angles, the contact between the backfill and the hanging wall can become ineffective, as shown in Figure 4-12.

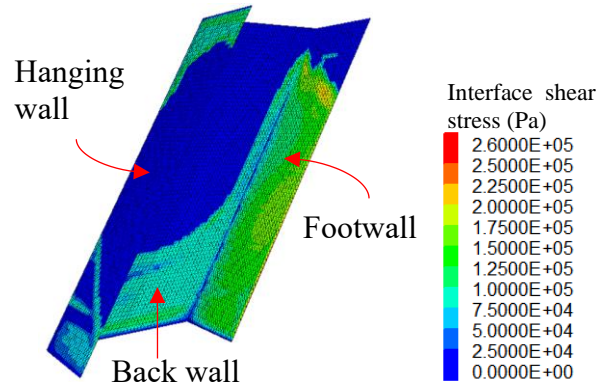


Figure 4-12: Shear stress iso-contours along fill-rock wall interfaces upon exposure of the backfill in a stope with wall inclination angle $\beta = 60^\circ$ (Case 1 in Table 4-1)

In this study, it is considered that the contact between the backfill and the hanging wall will become ineffective when the stope wall inclination angle $\beta \leq 45^\circ + \phi/2$. The following equation is proposed to describe the state of contact between the backfill and hanging wall:

$$r_\beta = \frac{\langle \beta - (45^\circ + \frac{\phi}{2}) \rangle}{90^\circ - (45^\circ + \frac{\phi}{2})} = \frac{\langle 2\beta - 90^\circ - \phi \rangle}{90^\circ - \phi} = \langle \frac{2\beta - 90^\circ - \phi}{90^\circ - \phi} \rangle \quad (4-52)$$

where r_β is a coefficient applied to adjust the shear stress along the fill-hanging wall interface, $\langle X \rangle = (X + |X|)/2$ is the Macaulay brackets.

τ_{h0} in Eq. 4-38 can then be modified as $\tau_h (= r_\beta \tau_{h0})$ and S_{hL} is shown as follows:

$$S_{hL} = \tau_h \frac{dz}{\sin \beta} = r_\beta \tau_{h0} \frac{dz}{\sin \beta} = (r_\beta \sigma_{h0} \tan \delta_h) \frac{dz}{\sin \beta} \quad (4-53)$$

Repeating the derivation process from Eq. 4-31 to Eq. 4-51 with the modified τ_h given in Eq. 4-53, the normal stresses at the hanging wall σ_{hw} and footwall σ_f are deduced and given as Eqs. 4-9 and 4-10.

Acknowledgments

The authors acknowledge the financial support from the Natural Sciences and Engineering Research Council of Canada (NSERC 402318), Fonds de recherche du Québec—Nature et Technologies (2015-MI-191676), China Scholarship Council (201706420059) and industrial partners of the Research Institute on Mines and the Environment (RIME UQAT-Polytechnique; <http://rime-irme.ca/>).

4.8 References

- Aubertin, M., Li, L., Arnoldi, S., Belem, T., Bussi re, B., Benzaazoua, M., and Simon, R. (2003). “Interaction between backfill and rock mass in narrow stopes.” *Proc., Soil and rock America 2003*, Verlag Gl uckauf Essen (VGE), Essen, Germany, Vol. 1, pp. 1157-1164.
- Barrett, J., Coulthard, M., and Dight, P. (1978). “Determination of fill stability.” *Proc., 12th Canadian Rock Mechanics Symp. on Mining with Backfill*, Canadian Institute of Mining and Metallurgy, Montreal, Canada, Vol. 19, pp. 85-91.
- B eket Dalc e, J., Li, L., and Yang, P. (2019). “Experimental study of uniaxial compressive strength (UCS) distribution of hydraulic backfill associated with segregation.” *Minerals.*, 9(3), 147. <https://doi.org/10.3390/min9030147>.
- Bussi re, B. (2007). “Colloquium 2004: Hydrogeotechnical properties of hard rock tailings from metal mines and emerging geoenvironmental disposal approaches.” *Can. Geotech. J.*, 44(9), 1019-1052. <https://doi.org/10.1139/T07-040>.
- Coulthard, M. (1980). “Numerical analysis of fill pillar stability: Three dimensional linearly elastic finite element calculations.” Division of Applied Geomechanics, Commonwealth Scientific and Industrial Research Organization, Mt. Waverley, VC, Australia.

- Cundall, P., Shillabeer, J., and Herget, G. (1978). "Modelling to predict rock fill stability in transverse pillar extraction." *Proc., 12th Canadian Rock Mechanics Symp. on Mining with Backfill*, Canadian Institute of Mining and Metallurgy, Montreal, Canada, pp. 92-99.
- Darling, P. (2011). *SME mining engineering handbook*. (3rd ed.). Society for Mining, Metallurgy, and Exploration, Littleton, Colorado.
- Dight, P., and Coulthard, M. (1980). "Numerical analysis of fill pillar stability: Two dimensional analysis of exposures." Division of Applied Geomechanics, Commonwealth Scientific and Industrial Research Organization, Mt. Waverley, VC, Australia.
- Dirige, A., McNearney, R., and Thompson, D. (2009). "The effect of stope inclination and wall rock roughness on back-fill free face stability." *Proc., Rock Engineering in Difficult Conditions, 3rd Canada-US Rock Mechanics Symp.*, Toronto, Canada, pp. 9-15.
- Dirige, A. P. E., and De Souza, E. (2008). "Engineering design of backfill systems in adjacent pillar mining." *Proc., 42nd U.S. Rock Mechanics Symp. (USRMS)*, San Francisco, California, pp. 1584-1593.
- Emad, M. Z., Mitri, H., and Kelly, C. (2014). "Effect of blast-induced vibrations on fill failure in vertical block mining with delayed backfill." *Can. Geotech. J.*, 51(9), 975-983. <https://doi.org/10.1139/cgj-2013-0305>.
- Falaknaz, N. (2014). "Analysis of geomechanical behavior of two adjacent backfilled stopes based on two and three dimensional numerical simulations." Ph.D. Thesis, Polytechnique Montreal, Montreal, QC, Canada.
- Hartman, H. L. (1992). *SME mining engineering handbook*. (2nd ed.). Society for Mining, Metallurgy, and Exploration Denver, Littleton, Colorado.
- Itasca. (2013). *FLAC3D—Fast Lagrangian analysis of continua in 3 dimensions; user's guide, version 5.01*, Itasca Consulting Group, Minneapolis, MN.
- Jahanbakhshzadeh, A., Aubertin, M., and Li, L. (2017). "A new analytical solution for the stress state in inclined backfilled mine stopes." *Geotech. Geol. Eng.*, 35(3), 1151-1167. <https://doi.org/10.1007/s10706-017-0371-0>.

- Jahanbakhshzadeh, A., Aubertin, M., and Li, L. (2018). "Three-dimensional stress state in inclined backfilled stopes obtained from numerical simulations and new closed-form solution." *Can. Geotech. J.*, 55(6), 810-828. <https://doi.org/10.1139/cgj-2016-0385>.
- Li, L. (2014a). "Analytical solution for determining the required strength of a side-exposed mine backfill containing a plug." *Can. Geotech. J.*, 51(5), 508-519. <https://doi.org/10.1139/cgj-2013-0227>.
- Li, L. (2014b). "Generalized solution for mining backfill design." *Int. J. Geomech.*, 14(3), 04014006. [https://doi.org/10.1061/\(ASCE\)GM.1943-5622.0000329](https://doi.org/10.1061/(ASCE)GM.1943-5622.0000329).
- Li, L., and Aubertin, M. (2009). "Numerical investigation of the stress state in inclined backfilled stopes." *Int. J. Geomech.*, 9(2), 52-62. [https://doi.org/10.1061/\(ASCE\)1532-3641\(2009\)9:2\(52\)](https://doi.org/10.1061/(ASCE)1532-3641(2009)9:2(52)).
- Li, L., and Aubertin, M. (2012). "A modified solution to assess the required strength of exposed backfill in mine stopes." *Can. Geotech. J.*, 49(8), 994-1002. <https://doi.org/10.1139/t2012-056>.
- Li, L., and Aubertin, M. (2014). "An improved method to assess the required strength of cemented backfill in underground stopes with an open face." *Int. J. Min. Sci. Technol.*, 24(4), 549-558. <https://doi.org/10.1016/j.ijmst.2014.05.020>.
- Li, L., Aubertin, M., and Belem, T. (2005). "Formulation of a three dimensional analytical solution to evaluate stresses in backfilled vertical narrow openings." *Can. Geotech. J.*, 42(6), 1705-1717. <https://doi.org/10.1139/t05-084>.
- Li, L., Aubertin, M., Simon, R., Bussiere, B., and Belem, T. (2003). "Modeling arching effects in narrow backfilled stopes with FLAC." *Proc., Flac and Numerical Modeling in Geomechanics - 2003*, pp. 211-219.
- Liu, G., Li, L., Yang, X., and Guo, L. (2016). "Stability analyses of vertically exposed cemented backfill: A revisit to Mitchell's physical model tests." *Int. J. Min. Sci. Technol.*, 26(6), 1135-1144. <https://doi.org/10.1016/j.ijmst.2016.09.024>.
- Liu, G., Li, L., Yang, X., and Guo, L. (2017). "Numerical analysis of stress distribution in backfilled stopes considering interfaces between the backfill and rock walls." *Int. J. Geomech.*, 17(2), 06016014. [https://doi.org/10.1061/\(ASCE\)GM.1943-5622.0000702](https://doi.org/10.1061/(ASCE)GM.1943-5622.0000702).

- Liu, G., Li, L., Yang, X., and Guo, L. (2018). "Required strength estimation of a cemented backfill with the front wall exposed and back wall pressured." *Int. J. Min. Mineral Eng.*, 9(1), 1-20. <https://doi.org/10.1504/IJMME.2018.091214>.
- Liu, G., Li, L., Yao, M., Landry, D., Malek, F., Yang, X., and Guo, L. (2017). "An investigation of the uniaxial compressive strength of a cemented hydraulic backfill made of alluvial sand." *Minerals*, 7(1), 4. <https://doi.org/10.3390/min7010004>.
- Liu, G., Yang, X., and Guo, L. (2019). "Models of three-dimensional arching stress and strength requirement for the backfill in open stoping with subsequent backfill mining." [in Chinese.] *J. China Coal Soc.*, 44(5), 1391-1403. <https://doi.org/10.13225/j.cnki.jccs.2019.6025>.
- Mitchell, R. J. (1986). "Centrifuge model tests on backfill stability." *Can. Geotech. J.*, 23(3), 341-345. <https://doi.org/10.1139/t86-048>.
- Mitchell, R. J. (1989). "Model studies on the stability of confined fills." *Can. Geotech. J.*, 26(2), 210-216. <https://doi.org/10.1139/t89-030>.
- Mitchell, R. J., Olsen, R. S., and Smith, J. D. (1982). "Model studies on cemented tailings used in mine backfill." *Can. Geotech. J.*, 19(1), 14-28. <https://doi.org/10.1139/t82-002>.
- Mitchell, R. J., and Wong, B. C. (1982). "Behaviour of cemented tailings sands." *Can. Geotech. J.*, 19(3), 289-295. <https://doi.org/10.1139/t82-035>.
- Pagé, P., Li, L., Yang, P., and Simon, R. (2019). "Numerical investigation of the stability of a base-exposed sill mat made of cemented backfill." *Int. J. Rock Mech. Min. Sci.*, 114, 195-207. <https://doi.org/10.1016/j.ijrmms.2018.10.008>.
- Pierce, M. (2001). "Stability analysis of paste back fill exposes at Brunswick mine." *Proc., 2nd international FLAC Symp.*, Lyon, France, pp. 147-156.
- Potvin, Y., Thomas, E., and Fourie, A. (2005). *Handbook on mine fill*. Australian Centre for Geomechanics, University of Western Australia, Nedlands, Australia.
- Qi, C., and Fourie, A. (2019). "Numerical investigation of the stress distribution in backfilled stopes considering creep behaviour of rock mass." *Rock Mech. Rock Eng.*, 52(9), 3353-3371. <https://doi.org/10.1007/s00603-019-01781-0>.

- Sivakugan, N., Widisinghe, S., and Wang, V. Z. (2014). "Vertical stress determination within backfilled mine stopes." *Int. J. Geomech.*, 14(5), 06014011. [https://doi.org/10.1061/\(ASCE\)GM.1943-5622.0000367](https://doi.org/10.1061/(ASCE)GM.1943-5622.0000367).
- Smith, J., Dejongh, C., and Mitchell, R. (1983). "Large scale model tests to determine backfill strength requirements for pillar recovery at the Black Mountain Mine." *Proc., International Symp. on Mining with Backfill*, Lulea, pp. 7-9.
- Sobhi, M. A., Li, L., and Aubertin, M. (2017). "Numerical investigation of earth pressure coefficient along central line of backfilled stopes." *Can. Geotech. J.*, 54(1), 138-145. <https://doi.org/10.1139/cgj-2016-0165>.
- Thompson, B. D., Bawden, W. F., and Grabinsky, M. W. (2012). "In situ measurements of cemented paste backfill at the Cayeli Mine." *Can. Geotech. J.*, 49(7), 755-772. <https://doi.org/10.1139/t2012-040>.
- Ting, C. H., Shukla, S. K., and Sivakugan, N. (2011). "Arching in soils applied to inclined mine stopes." *Int. J. Geomech.*, 11(1), 29-35. [https://doi.org/10.1061/\(ASCE\)GM.1943-5622.0000067](https://doi.org/10.1061/(ASCE)GM.1943-5622.0000067).
- Wang, J., Qiao, D., Han, R., Li, G., and Xie, J. (2019). "Strength model of cemented backfill in subsequent filling at the stage of open stope and its application." [in Chinese.] *Rock Soil Mech.*, 40(3), 1105-1112. <https://doi.org/10.16285/j.rsm.2017.1771>.
- Xu, C., Chen, Q., Luo, W., and Liang, L. (2018). "Analytical solution for estimating the stress state in backfill considering patterns of stress distribution." *Int. J. Geomech.*, 19(1), 04018189. [https://doi.org/10.1061/\(ASCE\)GM.1943-5622.0001332](https://doi.org/10.1061/(ASCE)GM.1943-5622.0001332).
- Yan, B., Zhu, W., Hou, C., and Guan, K. (2019). "A three-dimensional analytical solution to the arching effect in inclined backfilled stopes." *Geomech. Geoengin.*, 14(2), 136-147. <https://doi.org/10.1080/17486025.2019.1574031>.
- Yang, P., Li, L., and Aubertin, M. (2017a). "A new solution to assess the required strength of mine backfill with a vertical exposure." *Int. J. Geomech.*, 17(10), 04017084. [https://doi.org/10.1061/\(ASCE\)GM.1943-5622.0000975](https://doi.org/10.1061/(ASCE)GM.1943-5622.0000975).

- Yang, P., Li, L., and Aubertin, M. (2017b). "Stress ratios in entire mine stopes with cohesionless backfill: A numerical study." *Minerals.*, 7(10), 201. <https://doi.org/10.3390/min7100201>.
- Yang, P., Li, L., and Aubertin, M. (2018). "Theoretical and numerical analyses of earth pressure coefficient along the centerline of vertical openings with granular fills." *Appl. Sci.*, 8(10), 1721. <https://doi.org/10.3390/app8101721>.
- Yang, Z., Zhai, S., Gao, Q., and Li, M. (2015). "Stability analysis of large-scale stope using stage subsequent filling mining method in Sijiaying iron mine." *J. Rock Mech. Geotech. Eng.*, 7(1), 87-94. <https://doi.org/10.1016/j.jrmge.2014.11.003>.
- Zhao, X., Fourie, A., and Qi, C. (2019). "An analytical solution for evaluating the safety of an exposed face in a paste backfill stope incorporating the arching phenomenon." *Int. J. Min. Met. Mater.*, 26(10), 1206-1216. <https://doi.org/10.1007/s12613-019-1885-7>.
- Zou, D. H., and Nadarajah, N. (2006). "Optimizing backfill design for ground support and cost saving." *Proc., 41st U.S. Rock Mechanics Symp., ARMA's Golden Rocks 2006: 50 Years of Rock Mechanics*, Golden, CO, United states.

CHAPTER 5 DISCUSSION

In this thesis, an analytical solution has been proposed for estimating the stress distribution in backfilled stopes by considering the kink effect. Another analytical solution is given for evaluating the stability and required strength of side-exposed backfill in inclined stopes. The first one is validated by numerical results obtained with FLAC while the second one by numerical results obtained with FLAC3D. The good agreements between the proposed analytical solutions and the numerical results tend to indicate that the first analytical solution can provide a useful estimation on the stress distribution in vertically backfilled stopes while the second one on the stability or required cohesion of side-exposed backfill in inclined stopes. However, it should be noted that the two proposed analytical solutions are developed based on some assumptions, thus contain some limitations.

In Chapter 3, the theoretical analysis has shown that the occurrence of kink effects is closely related to the yielding state of backfill. When $\mu \leq (1 - \sin \varphi)/2$, the backfill is a yielding state and arching effects are fully mobilized throughout the backfill. The kink effect will be absent. When $\mu > (1 - \sin \varphi)/2$, the backfill will not yield. Arching will be absent near the bottom due to the fixed boundary conditions, and the stresses near the bottom are close to those based on the overburden solution. In the upper part, arching takes place due to the large deformation associated with the deformable backfill even the backfill remains unyielded. In this condition, kink effects occur in the stress-depth profile. This theory has been verified by numerical results obtained by FLAC. An analytical solution has also been proposed, based on this mechanism of kink effect, for estimating the stress distribution along the depth for a given thickness of backfill. The proposed solution has been verified by numerical results obtained with FLAC. However, the application of the proposed solution needs the knowledge of an earth pressure coefficient. Based on the mechanism analysis of kink effects, Rankine's active earth pressure coefficient K_a should be used when kink is absent. This corresponds to the numerical results shown by several researchers (Li and Aubertin 2008, 2009c; Singh et al. 2011; Sobhi et al. 2018; Yang et al. 2018a, 2018b). It is further confirmed here by the numerical results, as shown in Appendix B3.3. If $\mu > (1 - \sin \varphi)/2$ and the kink effect occurs, previous numerical studies showed that the at-rest earth pressure coefficient due to Poisson's effect $K_{0\mu}$ should be used (Yang 2016; Yang et al. 2018a, 2018b). Again, this is further confirmed here by the numerical results shown in Chapter 3. All these results indicate that Poisson's ratio is a key

parameter to evaluate if kink effects occur and whether $K_{0\mu}$ or K_a should be taken. Nonetheless, it is well known that measuring Poisson's ratio of soils and backfill is a big issue and very challenging (Suwal and Kuwano 2013). In addition, the kink effect has only been shown through numerical modeling (Sivakugan et al. 2014; Yang 2016). No experimental data are available to further verify these theoretical and numerical results because most of the previous relevant laboratory tests were performed by only measuring the vertical stresses at the bottom of the slope with different fill heights (Pirapakaran and Sivakugan 2007b; Ting et al. 2012; Han et al. 2018). The resulting curves are stress-thickness profiles, instead of stress-depth profiles. One can also find a few field tests with the measurements of the stresses at different positions as a function of filling time (and subsequently backfill thickness; Belem et al. 2004; Thompson et al. 2012; Wang et al. 2019). The very few measurement points do not allow showing the stress distribution along the depth at a given time of filling or thickness of backfill. More experimental work is thus necessary to measure the horizontal and vertical stresses at different positions for a given backfill.

When the kink effect occurs, one can observe a slight decrease before the sudden increase in the horizontal stress-depth profile. Liu et al. (2017) explained this phenomenon was induced by a beam-like behavior of the backfill. More effort is needed to fully understand the mechanism.

It is also noted that the proposed solution is mainly applied to estimate the vertical and horizontal stress along the central line of dry and cohesionless backfill. The solution can be useful to estimate the required strength of backfill exposed on one side (Li 2014b; Yang et al. 2017a) or at the base (Mitchell 1991) when the wall closure is negligible. It can also be applied to estimate the total stresses of hydraulic backfill for barricade design if the presence of pore water pressure is taken into account (Li and Aubertin 2009a, 2009b). All these indicate that further improvement is still needed for its wider application in engineering. Other influencing factors, such as the slope wall inclination, wall closure, backfill cohesion, and three-dimensional geometry should be considered in future work.

In Chapter 4, an improved analytical solution is proposed to assess the side-exposed stability and required strength of backfill in inclined slopes. The proposed solution was verified by numerical simulations conducted with FLAC3D. Even though the proposed analytical solution agrees quite well with numerical results, there are still some notable simplifications and assumptions in both

the analytical solution and numerical models due to the complex interactions between the backfill and surrounding rock mass.

To analyze the stability and evaluate the required strength of side-exposed backfill in inclined stopes, the normal stresses at the hanging wall and footwall are needed. Several analytical solutions exist to evaluate the horizontal and vertical stresses in inclined backfilled stopes (Ting et al. 2011; Jahanbakhshzadeh et al. 2017, 2018b; Yan et al. 2019). These solutions cannot be directly used to calculate the normal and shear forces at the hanging wall and footwall because all of them were developed mainly for the vertical and horizontal stresses. Near the hanging wall and footwall, the vertical and horizontal stresses are not normal stresses. The normal stresses along the hanging wall and footwall cannot be calculated using the existing solutions. Besides, those previous arching solutions need the knowledge of the earth pressure coefficient K . Yang et al. (2017b) have found that its value near the walls can neither be represented by the at-rest earth pressure coefficient K_0 nor by the active earth pressure coefficient K_a . Therefore, the normal stresses along the hanging wall and footwall are obtained by analyzing the equilibriums of forces and moments of a layer element. The resulting solution does not need the knowledge of earth pressure coefficient. However, the proposed solution for the normal stress estimation contains a reducing coefficient used to consider the contact intensity between the hanging wall and backfill with the variation of the wall inclination angle. More work still needs to be done to further understand this aspect. Besides, more work is necessary to obtain a solution for estimating the normal stresses on the hanging wall and footwall before and after side exposure of the backfill.

Another limitation for the stress estimation is closely associated with the zero cohesion considered in the model. Some analytical solutions considering non-zero cohesion have indeed been proposed by different researchers (Li et al. 2005; Ting et al. 2011; Xu et al. 2018). However, the application of these solutions may result in negative values of horizontal and vertical stresses as long as the cohesion exceeds a certain value. This is mainly due to the limit equilibrium analysis, which considers the backfill in a full mobilized condition. The frictional and cohesive shear strengths are considered to be fully mobilized along the fill-rock wall interfaces, which results in a large overestimation of the arching effect and negative stresses in the backfilled stopes when the cohesion of the backfill becomes high enough. In fact, numerical simulations (Liu et al. 2016a, Liu et al. 2017) have shown that the stresses first decrease as the interface cohesion increases and

finally becomes stable once the cohesion exceeds a threshold value. Recently, Liu et al. (2019) proposed an empirical model in which the stresses remain constant once the interface cohesion exceeds 50 kPa. The solution was developed for a specific stope geometry and it cannot be used as a general solution. Therefore, more efforts are needed to investigate the stress distribution in cohesive backfill.

Besides, the confining effects induced by wall closure was neither considered in the proposed analytical solutions nor in the numerical simulations. The validity of the proposed solution can be limited to shallow mines with good rock conditions. In deep mines, the confining effects can become non-negligible especially when creep occurs in the rock mass (Wang et al. 2019; Qi and Fourie 2019). In general, a limited confining effect can contribute to stabilizing the side-exposed backfill, but too large confining stress is likely to cause failure to the backfill by crushing. Further works are still required to study the effect of confining effects on the stability of side-exposed backfill in inclined stopes.

The proposed solution is developed for the side-exposed stability analyses of backfill with a high aspect ratio ($H > B \tan \alpha$). When the backfilled stope is low and large with a low-aspect-ratio, tension cracks may occur in the upper part of the backfill upon exposure (Dight and Coulthard 1980; Li 2014b; Yang et al. 2017a). Additional efforts are still needed to analyze the mechanism of tension cracks and incorporate it into the stability analysis of side-exposed backfill in inclined stopes.

The proposed model considers a sliding plane passing through the bottom of the exposed face of the backfill. The numerical simulations showed that the sliding plane starts somewhere above the bottom of the exposed face. In addition, the sliding face is somehow curved, intersecting the hanging wall and footwall at different heights. These aspects need to be taken into account in future work.

Finally, more experimental work for evaluating the stability of side-exposed backfill in inclined stopes is necessary to verify the analytical solution and numerical simulations.

CHAPTER 6 CONCLUSIONS AND RECOMMENDATIONS

6.1 Conclusions

The design of backfilled stopes needs the knowledge of stresses and the required strength of backfill. In this thesis, the stress distribution along the depth of vertical backfilled stopes has been investigated after taking into account the kink effect near the bottom. The stability of side-exposed backfill in inclined stopes has also be analyzed.

The design of barricade and side-exposed backfill requires a good understanding of the stress state in backfilled stopes. In Chapter 3, the stress distribution in backfilled stopes considering the kink effect is analytically and numerically investigated. The mechanism of the kink effect is first theoretically analyzed. An analytical solution is then proposed for the vertical and horizontal stresses along the depth of vertical backfilled stopes by considering the kink effect. Numerical simulations are then conducted with FLAC to verify the theory of kink effect and the proposed analytical solutions developed for estimating the stresses as a function of depth. The main conclusions are shown as follows:

- The occurrence of kink effects is mainly related to the yield state of the backfill, which depends on the relationship between μ and φ (or $K_{0\mu}$ and K_a). It was found that kink occurs when $\mu > (1 - \sin \varphi)/2$. When $\mu \leq (1 - \sin \varphi)/2$, no kink occurs;
- The good agreements of the stress distribution obtained by the numerical results with that predicted by the proposed analytical solution suggested that the proposed analytical solution can be used to estimate the stresses along the depth of the backfill in a vertical stope;
- Additional results in Appendix B3 also indicate that the stress-depth profile is the same as the stress-thickness profile when the kink effect does not occur. In contrast, the two stress profiles differ a lot when the kink effect occurs in the stress-depth profile.

Another critical issue is to evaluate the stability or determine the required strength of the backfill in a primary stope in order for the backfill to remain stable upon the exposure of the backfill on one side due to the excavation of a secondary stope. In Chapter 4, an improved analytical solution is first proposed to evaluate the stability and required strength of side-exposed backfill in inclined stopes by incorporating the normal and shear forces at the hanging wall and footwall. Then,

numerical simulations are conducted with FLAC3D to verify the proposed analytical solution. The main conclusions are presented below:

- The good agreements between the minimum required cohesion obtained by the numerical modeling with FLAC3D and predicted by applying the proposed solution indicate that the proposed solution can be used to assess the stability or required cohesion of side-exposed backfill in inclined stopes;
- The instability criterion combining the convergence of numerical calculation, displacement and strength-stress ratio can be applied to determine the state of backfill structure in numerical modelings;
- The results illustrate that the peak value of the minimum required cohesion occurs at a critical wall inclination angle of $\beta \approx 45^\circ + \varphi/2$ as β varies from 50° to 90° . The minimum required cohesion will then decrease from the peak value whatever the stope wall inclination angle further increases or decreases from the critical wall inclination angle. This has been attributed to the fact that the contact between the backfill and the hanging wall will become ineffective when the wall inclination angle is less than the critical value;
- The minimum required cohesion of side-exposed backfill in inclined stopes is found to increase with the increase in the backfill length and height while decrease with the increase in the backfill width. In addition, increasing the internal friction angle of the backfill can lead to a reduced minimum required cohesion.

6.2 Recommendations

More efforts are required to better understand the stress distribution in backfilled stopes and the stability of side-exposed backfill in inclined stopes. These can include:

- The proposed solution for evaluating the stress state in backfilled stopes with the consideration of kink effects was developed for dry backfill. More work is required to take into account the pore water pressure in the proposed solution, which can be of interest to the barricade design;
- The kink effect is only evaluated in vertical backfilled stopes, and additional work is still needed to assess it in inclined stopes;

- The proposed mechanism for the kink effect and the proposed analytical solution incorporating the kink effect have not been validated by experimental data. It is very useful to measure the Poisson's ratio and internal friction angle of the backfill as well as the horizontal and vertical total stresses along the depth of the backfilled stopes (especially near the bottom) to validate the proposed mechanism and analytical solutions;
- The stress state in the backfill after side exposure needs to be investigated;
- It is more reasonable to consider a curved sliding surface in the analytical model to evaluate the stability of the side-exposed backfill;
- It is suggested to take into account the influence of the dynamic responses induced by the blasting on the stability analysis of the side-exposed backfill;
- More work is suggested to evaluate the stability of inclined backfill with a low aspect ratio, in which the tension crack is more likely to occur during the failure;
- The backfill can remain unsaturated even after a long curing and consolidation period. It is preferable to consider the unsaturated conditions in the stability analysis of backfill upon side exposure;
- It is recommended to conduct centrifuge tests to represent the realistic backfill geometry and properties to investigate the stability of side-exposed backfill;
- Numerical simulations of the side-exposed backfill conducted with FLAC3D in the thesis only consider homogeneous and isotropic materials obeying the Mohr-coulomb model. The wall closure induced by the excavation of the orebody in the secondary stope is also not considered. More work is required to consider more representative mining sequences, stope geometries, and backfill properties and more elaborated constitutive models.

REFERENCES

- Antonov, D. (2005). *Optimization of the use of cement in backfilling operations*. Ph.D. Thesis, Polytechnique Montreal, Montreal, QC, Canada.
- Askew, J., McCarthy, P., and Fitzgerald, D. (1978). *Backfill research for pillar extraction at ZC/NBHC*. In: Proceedings of the 12th Canadian Rock Mechanics Symposium on Mining with Backfill, Canadian Institute of Mining and Metallurgy, Montreal, Canada, Vol. 12, 100-110.
- Aubertin, M., Li, L., Arnoldi, S., Belem, T., Bussière, B., Benzaazoua, M., and Simon, R. (2003). *Interaction between backfill and rock mass in narrow stopes*. In: Proceedings of the Soil and rock America 2003, Verlag Glückauf Essen (VGE), Essen, Germany, Vol. 1, 1157-1164.
- Barrett, J., Coulthard, M., and Dight, P. (1978). *Determination of fill stability*. In: Proceedings of the 12th Canadian Rock Mechanics Symposium on Mining with Backfill, Canadian Institute of Mining and Metallurgy, Montreal, Canada, Vol. 19, 85-91.
- Béket Dalcé, J., Li, L., and Yang, P. (2019). Experimental study of uniaxial compressive strength (UCS) distribution of hydraulic backfill associated with segregation. *Minerals*, 9(3), 147. doi:10.3390/min9030147.
- Belem, T., Harvey, A., Simon, R., and Aubertin, M. (2004). *Measurement and prediction of internal stresses in an underground opening during its filling with cemented fill*. In: Proceedings of the fifth international symposium on ground support in mining and underground construction, 28-30.
- Blight, G. (1986). Pressures exerted by materials stored in silos: part I, coarse materials. *Géotechnique*, 36(1), 33-46. doi:10.1680/geot.1986.36.1.33.
- Bussière, B. (2007). Colloquium 2004: Hydrogeotechnical properties of hard rock tailings from metal mines and emerging geoenvironmental disposal approaches. *Canadian Geotechnical Journal*, 44(9), 1019-1052. doi:10.1139/T07-040.
- Caceres, C. (2005). *Effect of delayed backfill on open stope mining methods*. Master Thesis, University of British Columbia, Vancouver, Canada.

- Coulthard, M. (1980). *Numerical analysis of fill pillar stability: Three dimensional linearly elastic finite element calculations*. Division of Applied Geomechanics, Commonwealth Scientific and Industrial Research Organization, Mt. Waverley, VC, Australia.
- Cundall, P., Shillabeer, J., and Herget, G. (1978). *Modelling to predict rock fill stability in transverse pillar extraction*. In: Proceedings of the 12th Canadian Rock Mechanics Symposium on Mining with Backfill, Canadian Institute of Mining and Metallurgy, Montreal, Canada, 92-99.
- Darling, P. (2011). *SME mining engineering handbook*, 3rd ed. Society for Mining, Metallurgy, and Exploration. Littleton, Colorado.
- Deutsch, G. P., and Schmidt, L. (1969). Pressures on silo walls. *Journal of Engineering for Industry*, 91(2), 450-457.
- Dight, P., and Coulthard, M. (1980). *Numerical analysis of fill pillar stability: Two dimensional analysis of exposures*. Division of Applied Geomechanics, Commonwealth Scientific and Industrial Research Organization, Mt. Waverley, VC, Australia.
- Dirige, A., McNearny, R., and Thompson, D. (2009). *The effect of stope inclination and wall rock roughness on back-fill free face stability*. In: Proceedings of the Rock Engineering in Difficult Conditions: 3rd Canada–US Rock Mechanics Symposium, Toronto, Canada, 9-15.
- Dirige, A. P. E., and De Souza, E. (2008). *Engineering design of backfill systems in adjacent pillar mining*. In: Proceedings of the 42nd U.S. Rock Mechanics Symposium (USRMS), San Francisco, California, 1584-1593.
- Emad, M. Z., Mitri, H., and Kelly, C. (2014). Effect of blast-induced vibrations on fill failure in vertical block mining with delayed backfill. *Canadian Geotechnical Journal*, 51(9), 975-983. doi:10.1139/cgj-2013-0305.
- Emad, M. Z., Mitri, H. S., and Henning, J. G. (2012). Effect of blast vibrations on the stability of cemented rockfill. *International Journal of Mining, Reclamation and Environment*, 26(3), 233-243. doi:10.1080/17480930.2012.707527.
- Fahey, M., Helinski, M., and Fourie, A. (2009). Some aspects of the mechanics of arching in backfilled stopes. *Canadian Geotechnical Journal*, 46(11), 1322-1336. doi:10.1139/T09-063.

- Falaknaz, N. (2014). *Analysis of geomechanical behavior of two adjacent backfilled stopes based on two and three dimensional numerical simulations*. Ph.D. Thesis, Polytechnique Montreal, Montreal, QC, Canada.
- Falaknaz, N., Aubertin, M., and Li, L. (2015a). Numerical Analyses of the Stress State in Two Neighboring Stopes Excavated and Backfilled in Sequence. *International Journal of Geomechanics*, 15(6), 04015005. doi:10.1061/(ASCE)GM.1943-5622.0000466.
- Falaknaz, N., Aubertin, M., and Li, L. (2015b). Numerical investigation of the geomechanical response of adjacent backfilled stopes. *Canadian Geotechnical Journal*, 52(10), 1507-1525. doi:10.1139/cgj-2014-0056.
- Falaknaz, N., Aubertin, M., and Li, L. (2015c). Evaluation of the stress state in two adjacent backfilled stopes within an elasto-plastic rock mass. *Geotechnical Geological Engineering* 1-24. doi:10.1007/s10706-015-9868-6.
- Frydman, S., and Keissar, I. (1987). Earth pressure on retaining walls near rock faces. *Journal of Geotechnical Engineering*, 113(6), 586-599.
- Han, Y., Li, D., Chen, J., Jing, H., and Duan, J. (2018). Experimental study on boundary pressure and wall friction under static grain storage in silo. [in Chinese]. *Transactions of the Chinese Society of Agricultural Engineering*, 34(13), 296-302. doi:10.11975/j.issn.1002-6819.2018.13.036.
- Handy, R. L. (1985). The arch in soil arching. *Journal of Geotechnical Engineering*, 111(3), 302-318. doi:10.1061/(ASCE)0733-9410(1985)111:3(302).
- Harrop-Williams, K. (1989). Arch in soil arching. *Journal of geotechnical Engineering*, 115(3), 415-419.
- Hartman, H. L. (1992). *SME mining engineering handbook*, 2nd ed. Society for Mining, Metallurgy, and Exploration Denver. Littleton, Colorado.
- Harvey, A. (2004). *Étude comparative des contraintes triaxiales dans le remblai en pâte selon la portée des chantiers*. Master Thesis, Polytechnique Montreal, Montreal, QC, Canada.
- Hasan, A., Karrech, A., and Chareyre, B. (2017). Evaluating Force Distributions within Virtual Uncemented Mine Backfill Using Discrete Element Method. *International Journal of Geomechanics*, 17(7), 06016042. doi:10.1061/(ASCE)GM.1943-5622.0000850.

- Helinski, M. (2007). *Mechanics of mine backfill*. Ph.D. Thesis, University of Western Australia, Perth, Australia.
- Hong, W. P., Bov, M. L., and Kim, H.-M. (2016). Prediction of vertical pressure in a trench as influenced by soil arching. *KSCE Journal of Civil Engineering*, 20(7), 2711-2718. doi:10.1007/s12205-016-0120-6.
- Itasca. (2011). *FLAC-Fast Lagrangian Analysis of Continua; User's Guide*. Itasca Consulting Group, Inc. Minneapolis, MN, USA.
- Itasca. (2013). *FLAC3D-Fast Lagrangian analysis of continua in 3 dimensions; user's guide, version 5.01*. Itasca Consulting Group, Minneapolis, MN.
- Jahanbakhshzadeh, A., Aubertin, M., and Li, L. (2017). A new analytical solution for the stress state in inclined backfilled mine stopes. *Geotechnical and Geological Engineering*, 35(3), 1151-1167. doi:10.1007/s10706-017-0171-6.
- Jahanbakhshzadeh, A., Aubertin, M., and Li, L. (2018a). Analysis of the stress distribution in inclined backfilled stopes using closed-form solutions and numerical simulations. *Geotechnical and Geological Engineering*, 36(2), 1011-1036. doi:10.1007/s10706-017-0371-0.
- Jahanbakhshzadeh, A., Aubertin, M., and Li, L. (2018b). Three-dimensional stress state in inclined backfilled stopes obtained from numerical simulations and new closed-form solution. *Canadian Geotechnical Journal*, 55(6), 810-828. doi:10.1139/cgj-2016-0385.
- Jaeger, J. C., and Cook, N. G. (1976). *Fundamentals of rock mechanics*, 3rd ed. John Wiley & Sons.
- Jaky, J. (1948). *Pressure in silos*. In: Proceedings of the 2nd International Conference on Soil Mechanics and Foundation Engineering, Rotterdam, The Netherlands, 103-107.
- Janssen, H. (1895). Versuche uber getreidedruck in silozellen. *Verein Deutscher Ingenieure*, 39(35), 1045-1049.
- Jaouhar, E.-M., Li, L., and Aubertin, M. (2018). An analytical solution for estimating the stresses in vertical backfilled stopes based on a circular arc distribution. *Geomechanics and Engineering*, 15(3), 889-898. doi:10.12989/gae.2018.15.3.889.
- Jarrett, N. D., Brown, C. J., and Moore, D. B. (1995). Pressure measurements in a rectangular silo. *Geotechnique*, 45(1), 95-104. doi:10.1680/geot.1995.45.1.95.

- Knutsson, S. (1981). *Stresses in the hydraulic backfill from analytical calculations and in-situ measurements*. In: Proceedings of the Application of Rock Mechanics to Cut and Fill Mining, Lulea, Swed, 261-268.
- Krynine, D. (1945). Discussion of stability and stiffness of cellular cofferdams by Karl Terzaghi. *Transactions, ASCE, 110*, 1175-1178.
- Ladanyi, B., and Hoyaux, B. (1969). A study of the trap-door problem in a granular mass. *Canadian Geotechnical Journal, 6*(1), 1-14. doi:10.1139/t69-001.
- Li, L. (2014a). Analytical solution for determining the required strength of a side-exposed mine backfill containing a plug. *Canadian Geotechnical Journal, 51*(5), 508-519. doi:10.1139/cgj-2013-0227.
- Li, L. (2014b). Generalized solution for mining backfill design. *International Journal of Geomechanics, 14*(3), 04014006. doi:10.1061/(ASCE)GM.1943-5622.0000329.
- Li, L., Aubertin, J. D., and Dubé, J.-S. (2014). Stress distribution in a cohesionless backfill poured in a silo. *The Open Civil Engineering Journal, 8*(1). doi:10.2174/1874149501408010001.
- Li, L., and Aubertin, M. (2008). An improved analytical solution to estimate the stress state in subvertical backfilled stopes. *Canadian Geotechnical Journal, 45*(10), 1487-1496. doi:10.1139/t08-060.
- Li, L., and Aubertin, M. (2009a). Horizontal pressure on barricades for backfilled stopes. Part I: Fully drained conditions. *Canadian Geotechnical Journal, 46*(1), 37-46. doi:10.1139/T08-104.
- Li, L., and Aubertin, M. (2009b). Horizontal pressure on barricades for backfilled stopes. Part II: Submerged conditions. *Canadian Geotechnical Journal, 46*(1), 47-56. doi:10.1139/T08-105.
- Li, L., and Aubertin, M. (2009c). Influence of water pressure on the stress state in stopes with cohesionless backfill. *Geotechnical and Geological Engineering, 27*(1), 1. doi:10.1007/s10706-008-9207-2.
- Li, L., and Aubertin, M. (2009d). A three-dimensional analysis of the total and effective stresses in submerged backfilled stopes. *Geotechnical and Geological Engineering, 27*(4), 559-569. doi:10.1007/s10706-009-9257-0.

- Li, L., and Aubertin, M. (2009e). Numerical investigation of the stress state in inclined backfilled stopes. *International Journal of Geomechanics*, 9(2), 52-62. doi:10.1061/(ASCE)1532-3641(2009)9:2(52).
- Li, L., and Aubertin, M. (2011). Limit equilibrium analysis for the design of backfilled stope barricades made of waste rock. *Canadian Geotechnical Journal*, 48(11), 1713-1728. doi:10.1139/t11-063.
- Li, L., and Aubertin, M. (2012). A modified solution to assess the required strength of exposed backfill in mine stopes. *Canadian Geotechnical Journal*, 49(8), 994-1002. doi:10.1139/t2012-056.
- Li, L., and Aubertin, M. (2014). An improved method to assess the required strength of cemented backfill in underground stopes with an open face. *International Journal of Mining Science and Technology*, 24(4), 549-558. doi:10.1016/j.ijmst.2014.05.020.
- Li, L., Aubertin, M., and Belem, T. (2005). Formulation of a three dimensional analytical solution to evaluate stresses in backfilled vertical narrow openings. *Canadian Geotechnical Journal*, 42(6), 1705-1717. doi:10.1139/t05-084.
- Li, L., Aubertin, M., and Belem, T. (2006). Erratum: Formulation of a three dimensional analytical solution to evaluate stresses in backfilled vertical narrow openings (vol 42, pg 1705, 2005). *Canadian Geotechnical Journal*, 43(3), 338-339. doi:10.1139/t06-017.
- Li, L., Aubertin, M., Simon, R., Bussiere, B., and Belem, T. (2003). *Modeling arching effects in narrow backfilled stopes with FLAC*. In: Proceedings of the Flac and Numerical Modeling in Geomechanics - 2003, 211-219.
- Liu, G., Li, L., Yang, X., and Guo, L. (2016a). A numerical analysis of the stress distribution in backfilled stopes considering nonplanar interfaces between the backfill and rock walls. *International Journal of Geotechnical Engineering*, 10(3), 271-282. doi:10.1080/19386362.2015.1132123.
- Liu, G., Li, L., Yang, X., and Guo, L. (2016b). Stability analyses of vertically exposed cemented backfill: A revisit to Mitchell's physical model tests. *International Journal of Mining Science and Technology*, 26(6), 1135-1144. doi:10.1016/j.ijmst.2016.09.024.

- Liu, G., Li, L., Yang, X., and Guo, L. (2017). Numerical analysis of stress distribution in backfilled stopes considering interfaces between the backfill and rock walls. *International Journal of Geomechanics*, 17(2), 06016014. doi:10.1061/(ASCE)GM.1943-5622.0000702.
- Liu, G., Li, L., Yang, X., and Guo, L. (2018). Required strength estimation of a cemented backfill with the front wall exposed and back wall pressured. *International Journal of Mining and Mineral Engineering*, 9(1), 1-20. doi:10.1504/IJMME.2018.091214.
- Liu, G., Li, L., Yao, M., Landry, D., Malek, F., Yang, X., and Guo, L. (2017). An investigation of the uniaxial compressive strength of a cemented hydraulic backfill made of alluvial sand. *Minerals*, 7(1), 4. doi:10.3390/min7010004.
- Liu, G., Yang, X., and Guo, L. (2019). Models of three-dimensional arching stress and strength requirement for the backfill in open stoping with subsequent backfill mining. [in Chinese]. *Journal of the China Coal Society*, 44(5), 1391-1403. doi:10.13225/j.cnki.jccs.2019.6025.
- Low, B., Tang, S., and Choa, V. (1994). Arching in piled embankments. *Journal of Geotechnical Engineering*, 120(11), 1917-1938.
- Marston, A. (1930). The theory of external loads on closed conduits in the light of the latest experiments. *Bulletin No. 96, Iowa, Engineering Experiment Station, Ames, Iowa*.
- Mitchell, R. J. (1986). Centrifuge model tests on backfill stability. *Canadian Geotechnical Journal*, 23(3), 341-345. doi:10.1139/t86-048.
- Mitchell, R. J. (1989). Model studies on the stability of confined fills. *Canadian Geotechnical Journal*, 26(2), 210-216. doi:10.1139/t89-030.
- Mitchell, R. J. (1991). Sill mat evaluation using centrifuge models. *Mining Science and Technology*, 13(3), 301-313. doi:10.1016/0167-9031(91)90542-K.
- Mitchell, R. J., Olsen, R. S., and Smith, J. D. (1982). Model studies on cemented tailings used in mine backfill. *Canadian Geotechnical Journal*, 19(1), 14-28. doi:10.1139/t82-002.
- Mitchell, R. J., and Wong, B. C. (1982). Behaviour of cemented tailings sands. *Canadian Geotechnical Journal*, 19(3), 289-295. doi:10.1139/t82-035.
- Newman, C., and Agioutantis, Z. (2018). *Stress Redistribution Around Single and Multiple Stope-and-Fill Operations*. In: Proceedings of the 52nd US Rock Mechanics/Geomechanics Symposium.

- Newman, C., Agioutantis, Z., and Esterhuizen, G. S. (2018). *Development of a numerical model for the approximation of stress distribution for a single vertical backfilled stope* In: Proceedings of the 37th International Conference on Ground Control in Mining, Morgantown, WV.
- Pagé, P., Li, L., Yang, P., and Simon, R. (2019). Numerical investigation of the stability of a base-exposed sill mat made of cemented backfill. *International Journal of Rock Mechanics and Mining Sciences*, 114, 195-207. doi:10.1016/j.ijrmms.2018.10.008.
- Pierce, M. (2001). *Stability analysis of paste back fill exposes at Brunswick mine*. In: Proceedings of the 2nd international FLAC Symposium, Lyon, France, 147-156.
- Pirapakaran, K., and Sivakugan, N. (2007a). Arching within hydraulic fill stopes. *Geotechnical and Geological Engineering*, 25(1), 25-35. doi:10.1007/s10706-006-0003-6.
- Pirapakaran, K., and Sivakugan, N. (2007b). A laboratory model to study arching within a hydraulic fill stope. *Geotechnical Testing Journal*, 30(6), 496-503. doi:10.1520/GTJ100653.
- Potvin, Y., Thomas, E., and Fourie, A. (2005). *Handbook on mine fill*. Australian Centre for Geomechanics. University of Western Australia, Nedlands, Australia.
- Qi, C., and Fourie, A. (2019). Numerical investigation of the stress distribution in backfilled stopes considering creep behaviour of rock mass. *Rock Mechanics and Rock Engineering*, 52(9), 3353-3371. doi:10.1007/s00603-019-01781-0.
- Rajeev, P., Sumanasekera, P. R., and Sivakugan, N. (2016). Average vertical stresses in underground mine stopes filled with granular backfills. *Geotechnical and Geological Engineering*, 34(6), 2053-2061. doi:10.1007/s10706-016-0082-y.
- Ramírez, A., Nielsen, J., and Ayuga, F. (2010a). On the use of plate-type normal pressure cells in silos: Part 1: Calibration and evaluation. *Computers and Electronics in Agriculture*, 71(1), 71-76. doi:10.1016/j.compag.2009.12.004.
- Ramírez, A., Nielsen, J., and Ayuga, F. (2010b). On the use of plate-type normal pressure cells in silos: Part 2: Validation for pressure measurements. *Computers and Electronics in Agriculture*, 71(1), 64-70. doi:10.1016/j.compag.2009.12.005.
- Rankine, W. M. (1856). On the stability of loose earth. *Philosophical Transactions of the Royal Society of London*, 147 185-187.

- Salencon, J. (1969). Contraction quasi-statique d'une cavite a symetrie spherique ou cylindrique dans un milieu elastoplastique. *Annales Des Ponts Et Chaussées*, 4 231-236.
- Singh, S., Shukla, S. K., and Sivakugan, N. (2011). Arching in inclined and vertical mine stopes. *Geotechnical Geological Engineering*, 29(5), 685-693. doi:10.1007/s10706-011-9410-4.
- Singh, S., Sivakugan, N., and Shukla, S. (2009). Can soil arching be insensitive to ϕ ? *International Journal of Geomechanics*, 10(3), 124-128. doi:10.1061/(ASCE)GM.1943-5622.0000047.
- Sivakugan, N., and Widisinghe, S. (2013). Stresses within granular materials contained between vertical walls. *Indian Geotechnical Journal*, 43(1), 30-38. doi:10.1007/s40098-012-0029-z.
- Sivakugan, N., Widisinghe, S., and Wang, V. Z. (2014). Vertical stress determination within backfilled mine stopes. *International Journal of Geomechanics*, 14(5), 06014011. doi:10.1061/(ASCE)GM.1943-5622.0000367.
- Smith, J., Dejongh, C., and Mitchell, R. (1983). *Large scale model tests to determine backfill strength requirements for pillar recovery at the Black Mountain Mine*. In: Proceedings of the International Symposium on Mining with Backfill, Lulea, 7-9.
- Sobhi, M. A., Li, L., and Aubertin, M. (2017). Numerical investigation of earth pressure coefficient along central line of backfilled stopes. *Canadian Geotechnical Journal*, 54(1), 138-145. doi:10.1139/cgj-2016-0165.
- Sperl, M. (2005). Experiments on corn pressure in silo cells – translation and comment of Janssen's paper from 1895. *Granular Matter*, 8(2), 59-65. doi:10.1007/s10035-005-0224-z.
- Sun, S., Zhao, J., and Zhang, C. (2018). Calculation of silo wall pressure considering the intermediate stress effect. *Advances in Civil Engineering*, 2018. doi:10.1155/2018/3673515.
- Suwal, L., and Kuwano, R. (2013). Statically and dynamically measured Poisson's ratio of granular soils on triaxial laboratory specimens. *Geotechnical Testing Journal*, 36(4), 493-505. doi:10.1520/GTJ20120108.
- Take, W. A., and Valsangkar, A. J. (2001). Earth pressures on unyielding retaining walls of narrow backfill width. *Canadian Geotechnical Journal*, 38(6), 1220-1230. doi:10.1139/cgj-38-6-1220.
- Terzaghi, K. (1936). *Stress distribution in dry and in saturated sand above a yielding trap-door*. In: Proceedings of the 1st International Conference on Soil Mechanics and Foundation Engineering, Cambridge, Mass, Vol. 1, 307-311.

- Terzaghi, K. (1943). *Theoretical soil mechanics*. John Wiley & Sons. New York: Chapman and Hall.
- Thompson, B. D., Bawden, W. F., and Grabinsky, M. W. (2012). In situ measurements of cemented paste backfill at the Cayeli Mine. *Canadian Geotechnical Journal*, 49(7), 755-772. doi:10.1139/t2012-040.
- Ting, C. H., Shukla, S. K., and Sivakugan, N. (2011). Arching in soils applied to inclined mine stopes. *International Journal of Geomechanics*, 11(1), 29-35. doi:10.1061/(ASCE)GM.1943-5622.0000067.
- Ting, C. H., Sivakugan, N., Read, W., and Shukla, S. K. (2012). Analytical Method to Determine Vertical Stresses within a Granular Material Contained in Right Vertical Prisms. *International Journal of Geomechanics*, 12(1), 74-79. doi:10.1061/(ASCE)GM.1943-5622.0000110.
- Ting, C. H., Sivakugan, N., and Shukla, S. K. (2012). Laboratory simulation of the stresses within inclined stopes. *Geotechnical Testing Journal*, 35(2), 280-294. doi:10.1520/GTJ103693.
- Wang, J., Qiao, D., Han, R., Li, G., and Xie, J. (2019). Strength model of cemented backfill in subsequent filling at the stage of open stope and its application. [in Chinese]. *Rock and Soil Mechanics*, 40(3), 1105-1112. doi:10.16285/j.rsm.2017.1771.
- Xu, C., Chen, Q., Luo, W., and Liang, L. (2018). Analytical solution for estimating the stress state in backfill considering patterns of stress distribution. *International Journal of Geomechanics*, 19(1), 04018189. doi:10.1061/(ASCE)GM.1943-5622.0001332.
- Yan, B., Zhu, W., Hou, C., and Guan, K. (2019). A three-dimensional analytical solution to the arching effect in inclined backfilled stopes. *Geomechanics and Geoengineering*, 14(2), 136-147. doi:10.1080/17486025.2019.1574031.
- Yang, M., and Tang, X. (2017). Rigid retaining walls with narrow cohesionless backfills under various wall movement modes. *International Journal of Geomechanics*, 17(11), 04017098. doi:10.1061/(ASCE)GM.1943-5622.0001007.
- Yang, P. (2016). *Investigation of the geomechanical behavior of mine backfill and its interaction with rock walls and barricades*. Ph.D. Thesis, Polytechnique Montreal, Montreal, QC, Canada.

- Yang, P., Li, L., and Aubertin, M. (2017a). A new solution to assess the required strength of mine backfill with a vertical exposure. *International Journal of Geomechanics*, 17(10), 04017084. doi:10.1061/(ASCE)GM.1943-5622.0000975.
- Yang, P., Li, L., and Aubertin, M. (2017b). Stress ratios in entire mine stopes with cohesionless backfill: A numerical study. *Minerals*, 7(10), 201. doi:10.3390/min7100201.
- Yang, P., Li, L., and Aubertin, M. (2018). Theoretical and numerical analyses of earth pressure coefficient along the centerline of vertical openings with granular fills. *Applied Sciences*, 8(10), 1721. doi:10.3390/app8101721.
- Yang, P., Li, L., Aubertin, M., Brochu-Baekelmans, M., and Ouellet, S. (2017). Stability analyses of waste rock barricades designed to retain paste backfill. *International Journal of Geomechanics*, 17(3), 04016079. doi:10.1061/(ASCE)GM.1943-5622.0000740.
- Yang, Z., Zhai, S., Gao, Q., and Li, M. (2015). Stability analysis of large-scale stope using stage subsequent filling mining method in Sijiyang iron mine. *Journal of Rock Mechanics and Geotechnical Engineering*, 7(1), 87-94. doi:10.1016/j.jrmge.2014.11.003.
- Zhao, X., Fourie, A., and Qi, C. (2019). An analytical solution for evaluating the safety of an exposed face in a paste backfill stope incorporating the arching phenomenon. *International Journal of Minerals, Metallurgy, and Materials*, 26(10), 1206-1216. doi:10.1007/s12613-019-1885-7.
- Zheng, J., Li, L., and Li, Y. (2019). Total and effective stresses in backfilled stopes during the fill placement on a pervious base for barricade design. *Minerals*, 9(1), 38. doi:10.3390/min9010038.
- Zou, D. H., and Nadarajah, N. (2006). *Optimizing backfill design for ground support and cost saving*. In: Proceedings of the 41st U.S. Rock Mechanics Symposium, ARMA's Golden Rocks 2006: 50 Years of Rock Mechanics, Golden, CO, United states.

APPENDIX A VALIDATION OF USED NUMERICAL CODES

In this appendix, the validation of FLAC and FLAC3D against the analytical solution for cylindrical hole problems will be presented.

A1 Problem statement

The stresses and displacements around a cylindrical hole in a linear elastic or Mohr-Coulomb elastoplastic medium are evaluated by using analytical solutions and numerical modeling with FLAC (Itasca 2011) and FLAC3D (Itasca, 2013).

Figure A-1 shows a cylindrical hole in an infinite space. a (m) is the radius of the cylindrical hole; p_1 (MPa) and p_2 (MPa) are the vertical and horizontal field stress, respectively; σ_r (MPa) and σ_θ (MPa) are the radial and tangential induced stress at point (r, θ) , respectively; u (m) and v (m) are the radial and tangential displacement at point (r, θ) , respectively.

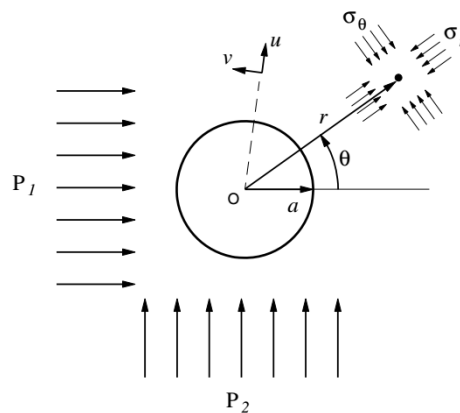


Figure A-1: A schematic view of the cylindrical hole problem

A2 Analytical solutions

A2.1 Classic Kirsch solution for the cylindrical hole in an elastic medium

The stresses and displacement around a cylindrical hole in an infinite, isotropic, and elastic medium under a plane strain condition can be predicted by the classic Kirsch solution (Jaeger 2009). After the excavation of a cylindrical hole with a radius of a (m) (shown in Figure A-1), the radial and tangential stress at the point (r, θ) can be obtained by:

$$\sigma_r = \frac{p_1 + p_2}{2} \left(1 - \frac{a^2}{r^2}\right) + \frac{p_1 - p_2}{2} \left(1 - \frac{4a^2}{r^2} + \frac{3a^4}{r^4}\right) \cos 2\theta \quad (\text{A-1})$$

$$\sigma_\theta = \frac{p_1 + p_2}{2} \left(1 + \frac{a^2}{r^2}\right) - \frac{p_1 - p_2}{2} \left(1 + \frac{3a^4}{r^4}\right) \cos 2\theta \quad (\text{A-2})$$

The radial displacement u is

$$u = \frac{p_1 + p_2}{4G} \frac{a^2}{r} + \frac{p_1 - p_2}{4G} \frac{a^2}{r} \left(4(1 - \mu) - \frac{a^2}{r^2}\right) \cos 2\theta \quad (\text{A-3})$$

where G (kPa) and μ are the shear modulus and the Poisson's ratio, respectively.

A2.2 Salencon solution for the cylindrical hole in an elastoplastic medium

Salencon (1969) solution can be used to calculate the stresses and displacements around a cylindrical hole in an infinite, isotropic, and elastoplastic medium obeying the Mohr-Coulomb yielding criterion. After the excavation of a cylindrical hole with a radius of a (m) (shown in Figure A-1), the critical radius R_0 separating the plastic zone and the elastic zone is expressed as

$$R_0 = a \left(\frac{2}{K_p + 1} \frac{P_0 + q/(K_p - 1)}{P_i + q/(K_p - 1)} \right)^{1/(K_p - 1)} \quad (\text{A-4})$$

The radial stress at the elastic/plastic interface σ_{re} is calculated as

$$\sigma_{re} = -\frac{1}{K_p + 1} (2P_0 - q) \quad (\text{A-5})$$

where $P_0 (=P_1 = P_2)$ and P_i are the initial field stress and internal pressure; $K_p = (1 + \sin \varphi)/(1 - \sin \varphi)$; φ is the internal friction angle and $q = 2c \tan (45^\circ + \varphi/2)$.

The radial and tangential stress and the radial displacement at a distance r (m) from the hole center in the elastic zone can be obtained by

$$\sigma_r = -P_0 + (P_0 - \sigma_{re}) * \left(\frac{R_0}{r}\right)^2 \quad (\text{A-6})$$

$$\sigma_\theta = -P_0 - (P_0 - \sigma_{re}) * \left(\frac{R_0}{r}\right)^2 \quad (\text{A-7})$$

$$u_r = -\left(P_0 - \frac{2P_0 - q}{K_p + 1}\right) \left(\frac{R_0}{2G}\right) \left(\frac{R_0}{r}\right) \quad (\text{A-8})$$

In the plastic zone, the stresses and displacement are

$$\sigma_r = \frac{q}{K_p - 1} - \left(P_i + \frac{q}{K_p - 1} \right) * \left(\frac{r}{a} \right)^{K_p - 1} \quad (\text{A-9})$$

$$\sigma_\theta = \frac{q}{K_p - 1} - K_p \left(P_i + \frac{q}{K_p - 1} \right) * \left(\frac{r}{a} \right)^{K_p - 1} \quad (\text{A-10})$$

$$u = -\frac{r}{2G} (2\mu - 1) \left(P_o + \frac{q}{K_p - 1} \right) + \left(\frac{(1 - \mu)(K_p^2 - 1)}{K_p + K_{ps}} \right) \left(P_i + \frac{q}{K_p - 1} \right) \left(\frac{R_o}{a} \right)^{K_p - 1} \left(\frac{R_o}{r} \right)^{K_{ps} + 1} \\ + \left((1 - \mu) \frac{K_p K_{ps} + 1}{K_p + K_{ps}} - \mu \right) \left(P_i + \frac{q}{K_p - 1} \right) \left(\frac{r}{a} \right)^{K_p - 1} \quad (\text{A-11})$$

where G and μ are the shear modulus and the Poisson's ratio, respectively; ψ is the dilation angle and $K_{ps} = (1 + \sin \psi) / (1 - \sin \psi)$.

A3 Validation of FLAC

A3.1 Numerical model

The boundary conditions and numerical model with mesh in FLAC are shown in Figure A-2. The coordinate of the hole center is (0, 0) and the distance from the hole center to the outer boundary (or domain size) is R (m).

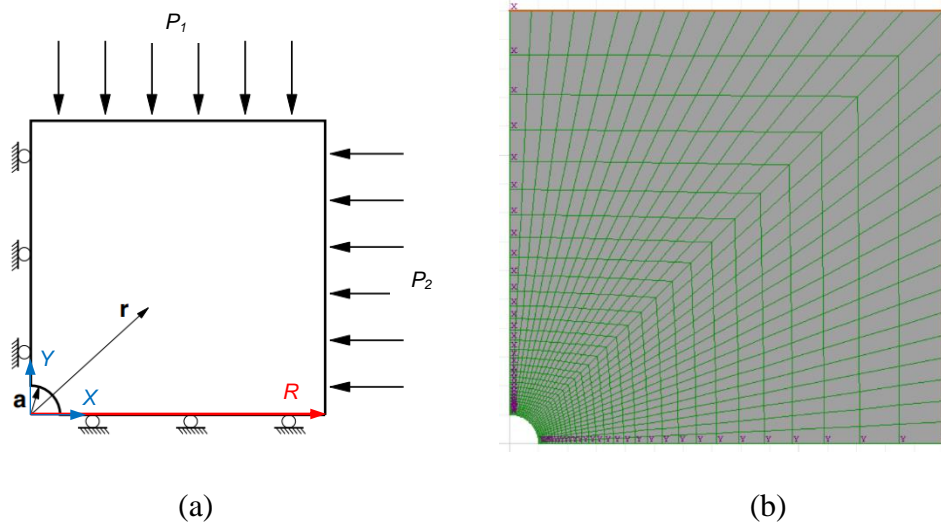


Figure A-2: (a) Boundary conditions (adapted from Itasca 2011) and (b) numerical model of the cylindrical hole problem in FLAC

A3.2 Validation of the elastic model

The properties used in the elastic model are shown in Table A-1.

Table A-1: The properties of the elastic model

density ρ (kg/m ³)	shear modulus G (MPa)	bulk modulus K (MPa)	Field stress $p_1 = p_2$ (MPa)	Radius of the hole a (m)
2500	2800	3900	30	1

A3.2.1 Sensitivity analyses

For the sensitivity analyses, the domain and the mesh are considered and two points, (1, 0) and (2, 0), are selected as a reference.

(1) Domain

In the following analysis, the distance from the hole center to the boundary (or domain size) R (m) is analyzed to see its influence on stresses and displacement. From Figure A-3, the stresses and the displacement become constant at $R = 15$ m, which is selected for the numerical model.

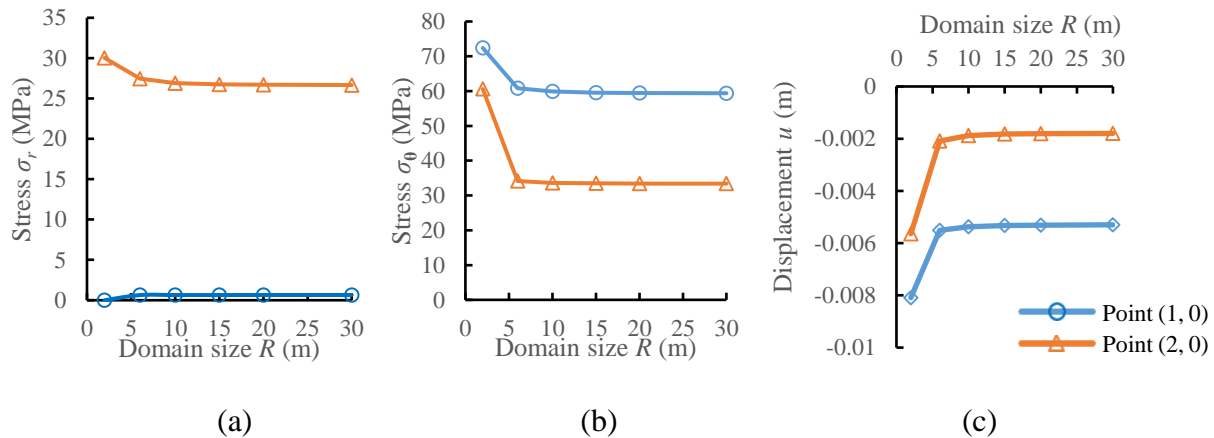


Figure A-3: Sensitivity analysis of the domain in an elastic model: (a) the variation of radial stress, (b) tangential stress and (c) radial displacement with domain size R

(2) Mesh

Different element sizes of the hole boundary are used to observe the variation of the stresses and displacement at the two monitoring points (shown in Figure A-4). The stresses and the displacement become constant when the mesh size is 0.05 m.

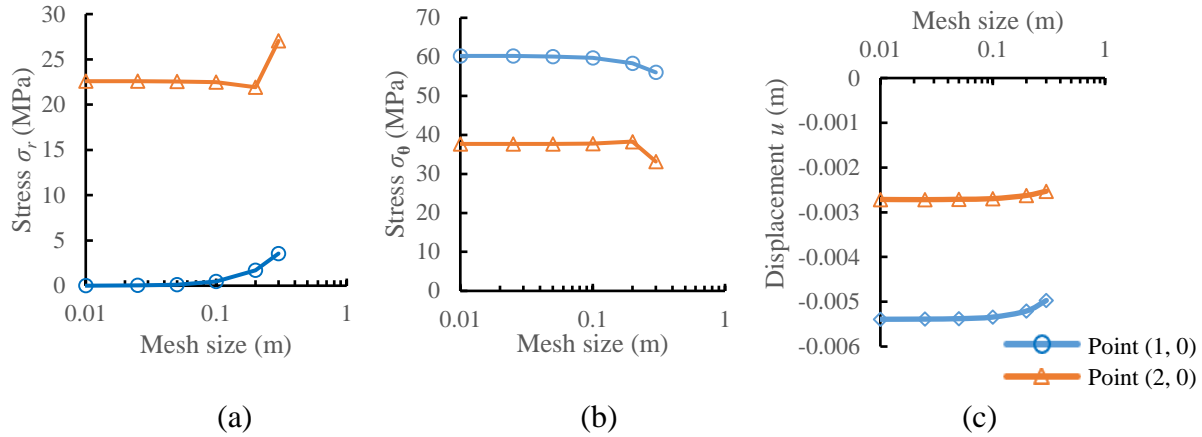


Figure A-4. Sensitivity analysis of the mesh size in an elastic model: (a) the variation of radial stress, (b) tangential stress and (c) radial displacement with the mesh size

A3.2.2 Comparisons between analytical results and numerical results

As shown in Figure A-5, the stresses and displacement obtained from the numerical simulations agree well with the analytical solutions (Eqs. A-1 to A-3).

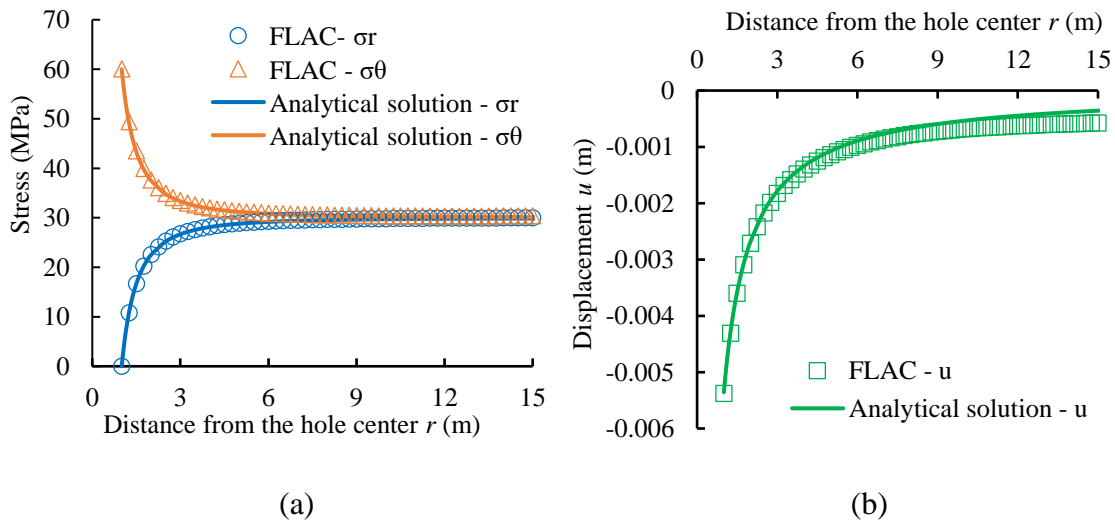


Figure A-5. Comparisons between analytical results and numerical results in an elastic model: (a) the variation of radial and tangential stresses and (b) the variation of radial displacement

A3.3 Validation of the Mohr-Coulomb model

The material properties in an elastoplastic medium are shown in Table A-2. Two dilation angles are considered, with one equal to 0 to study the nonassociated flow rule of the Mohr-Coulomb criteria and the other equal to the friction angle to study the associated flow rule.

Table A-2: The properties of the Mohr-Coulomb model

density ρ (kg/m ³)	shear modulus G (MPa)	bulk modulus K (MPa)	cohesion c (MPa)	friction angle φ (°)	dilation angle ψ (°)	Field stress p_0 $= (p_1 = p_2)$ (MPa)	Radius of the hole a (m)
2500	2800	3900	3.45	30	0	30	1
2500	2800	3900	3.45	30	30	30	1

A3.3.1 Sensitivity analyses

Considering the Mohr-Coulomb Model, the sensitivity analyses of the domain and the mesh are conducted and the two points, (1, 0) and (2, 0), are selected as a reference.

(1) Domain

The distance from the hole center to the boundary (or domain size) R is analyzed to see its influence on stress and displacement. From Figures A-6 and A-7, when the dilation angle is equal to 0° or 30°, the stresses and the displacement become constant at $R = 15$ m.

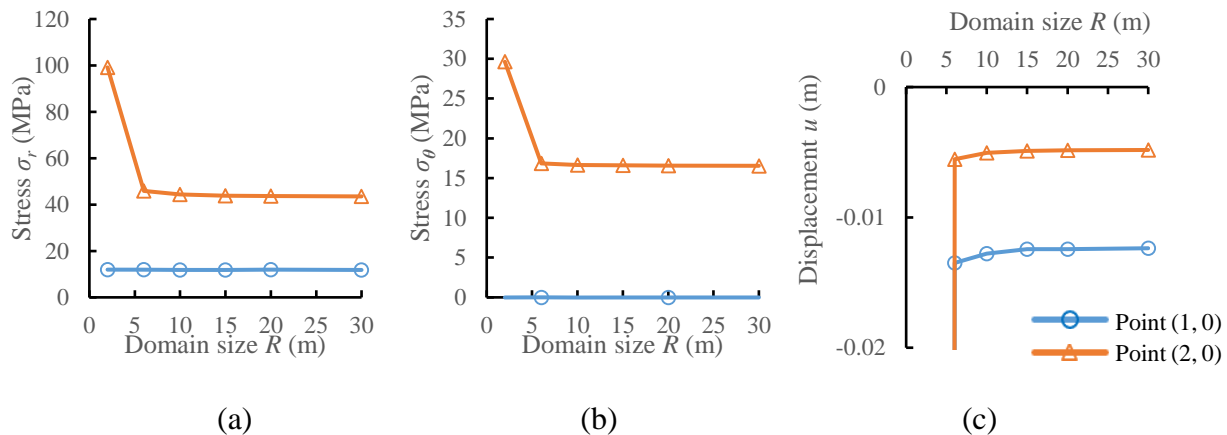


Figure A-6: Sensitivity analysis of the domain in Mohr-Coulomb model with $\psi = 0^\circ$: (a) the variation of radial stress, (b) tangential stress and (a) radial displacement with Radius

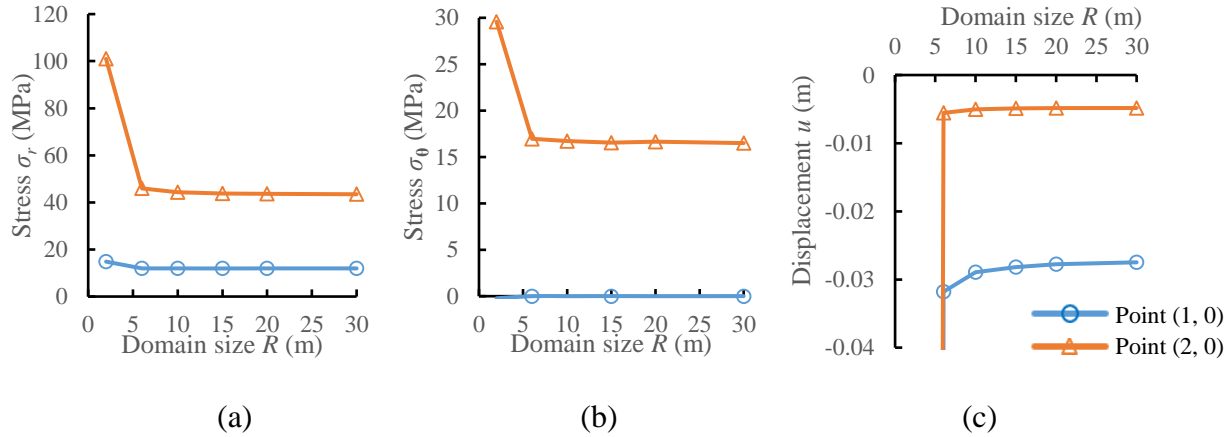


Figure A-7: Sensitivity analysis of the domain in Mohr-Coulomb model with $\psi = 30^\circ$: (a) the variation of radial stress, (b) tangential stress and (a) radial displacement with Radius

(2) Mesh

The element size of the hole boundary is used to represent the conditions of the mesh size. From Figures A-8 and A-9, the stresses and the displacement become constant in the Mohr-Coulomb model when the mesh size is 0.05 m.

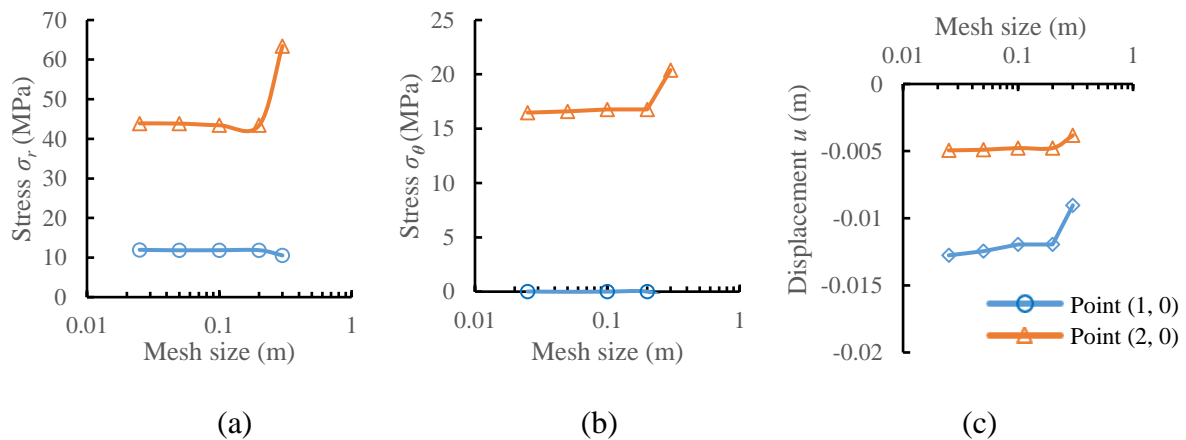


Figure A-8. Sensitivity analysis of the mesh size in the Mohr-Coulomb model with $\psi = 0^\circ$: (a) the variation of radial stress, (b) tangential stress and (a) radial displacement with mesh size

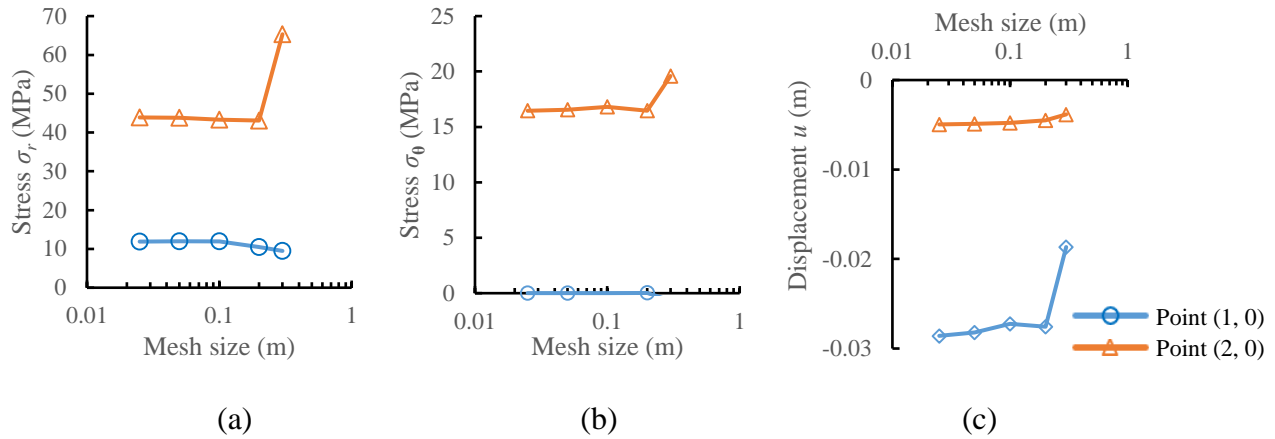


Figure A-9. Sensitivity analysis of the mesh size in the Mohr-Coulomb model with $\psi = 30^\circ$: (a) the variation of radial stress, (b) tangential stress and (a) radial displacement with mesh size

A3.3.2 Comparisons between analytical results and numerical results

For the numerical models, when $\psi = 0^\circ$, the distance from the hole center to the boundary is 15 m and the element size of the hole boundary is 0.05 m. As shown in Figure A-10, the numerical results correspond well with the analytical solutions (Eqs. A-4 to A-11).

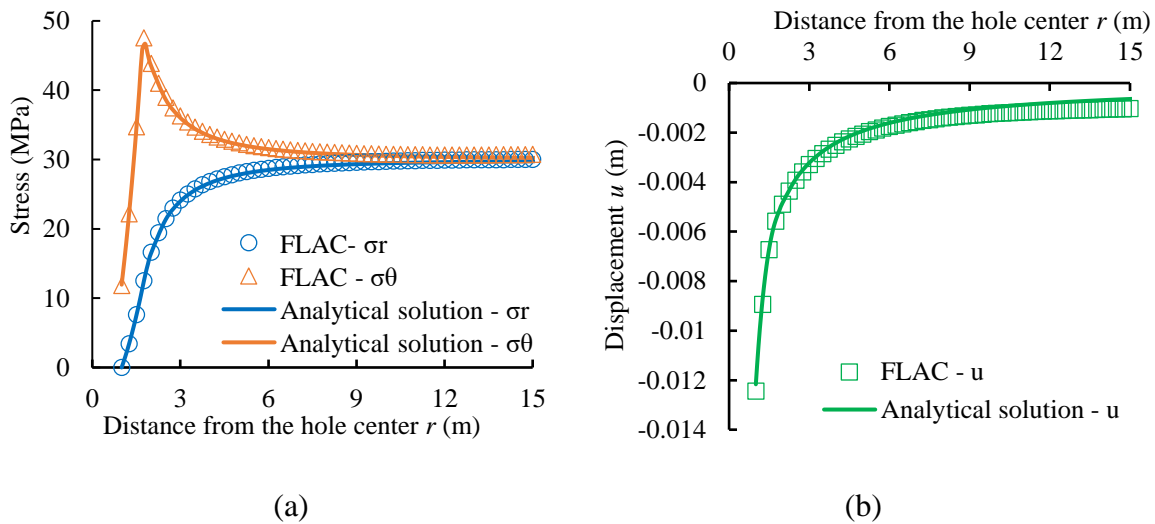


Figure A-10: Comparisons between analytical results and numerical results in the Mohr-Coulomb model with $\psi = 0^\circ$: (a) the variation of radial and tangential stresses and (b) radial displacement when $\psi = 30^\circ$, the distance from the hole center to the boundary is 15 m and the element size of the hole boundary is 0.05 m. The variations of the stresses and displacement with the distance from

the hole center are shown in Figure A-11, from which we can observe that the numerical results agree well with the (Eqs. A-4 to A-11).

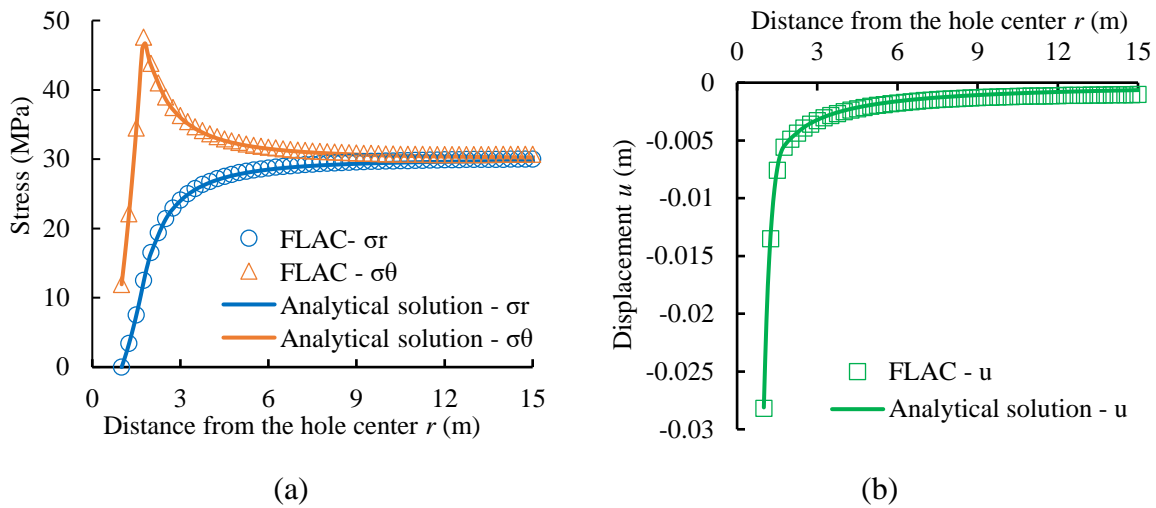


Figure A-11: Comparisons between analytical results and numerical results in the Mohr-Coulomb model with $\psi = 30^\circ$: (a) the variation of radial and tangential stresses and (b) radial displacement

A4 Validation of FLAC3D

A4.1 Numerical model

The boundary conditions and numerical model with mesh in FLAC3D are shown in Figure A-12. The coordinate of the hole center is $(0, 0, 0)$ and the distance from the hole center to the outer boundary (or domain size) is R (m).

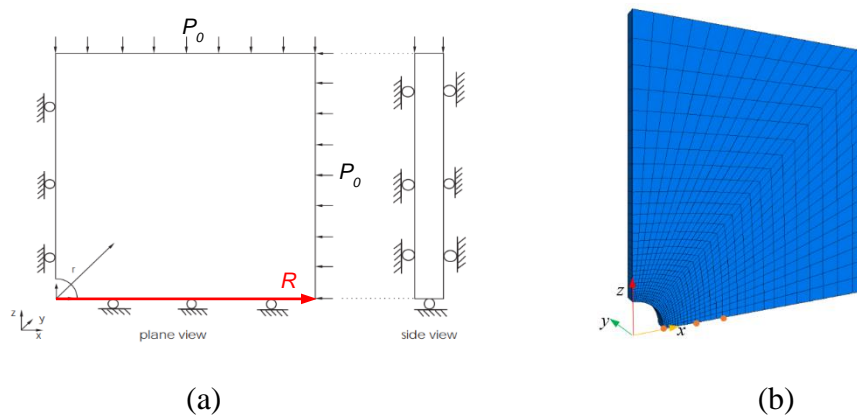


Figure A-12: (a) Boundary conditions (adapted from Itasca 2013) and (b) numerical model of the cylindrical hole problem in FLAC3D

A4.2 Validation of the elastic model

The material properties are shown in Table A-1.

A4.2.1 Sensitivity analyses

The stresses and displacements at the point (1, 0, 0), (2, 0, 0) and (3, 0, 0) are monitored (shown in Figure C-1b) for the sensitivity analyses of the domain and mesh size.

(1) Domain

By changing the distance R from the hole center to the boundary, the stresses and displacement at the three monitoring points are plotted in Figure A-13. From Figure A-13, the stresses and the displacement become constant at $R = 10$ m.

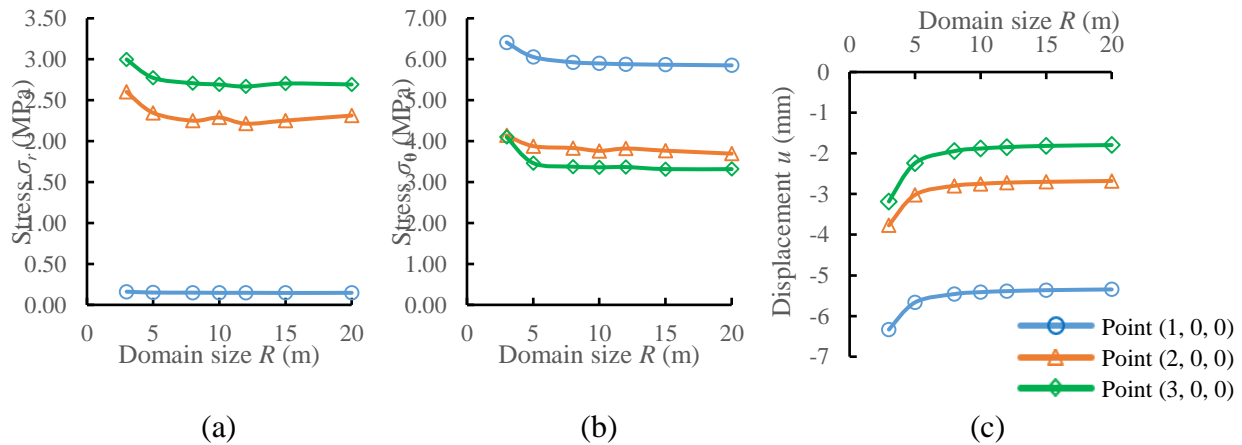


Figure A-13: Sensitivity analysis of the domain in an elastic model: (a) the variation of radial stress, (b) tangential stress and (a) radial displacement with domain size R

(2) Mesh

Different element sizes of the hole boundary are used to observe the variation of the stresses and displacement at the three monitoring points (shown in Figure A-14). It is seen that the stresses and the displacement become constant when element size = 0.025 m.

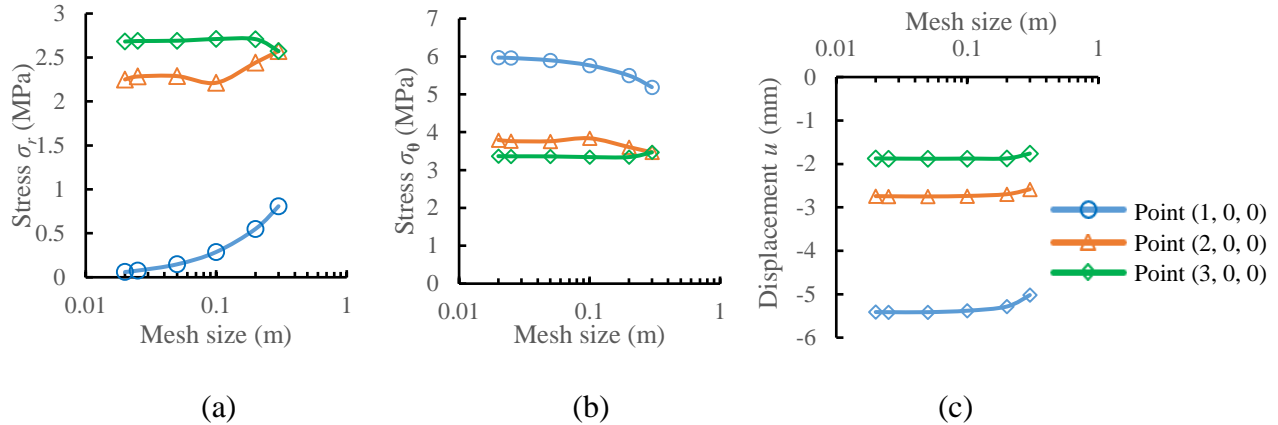


Figure A-14: Sensitivity analysis of the mesh size in an elastic model: (a) the variation of radial stress, (b) tangential stress and (a) radial displacement with mesh size

A4.2.2 Comparisons between analytical results and numerical results

As shown in Figure A-15, the stresses and displacement obtained from FLAC3D agree well with the analytical solutions (Eqs. A-1 to A-3).

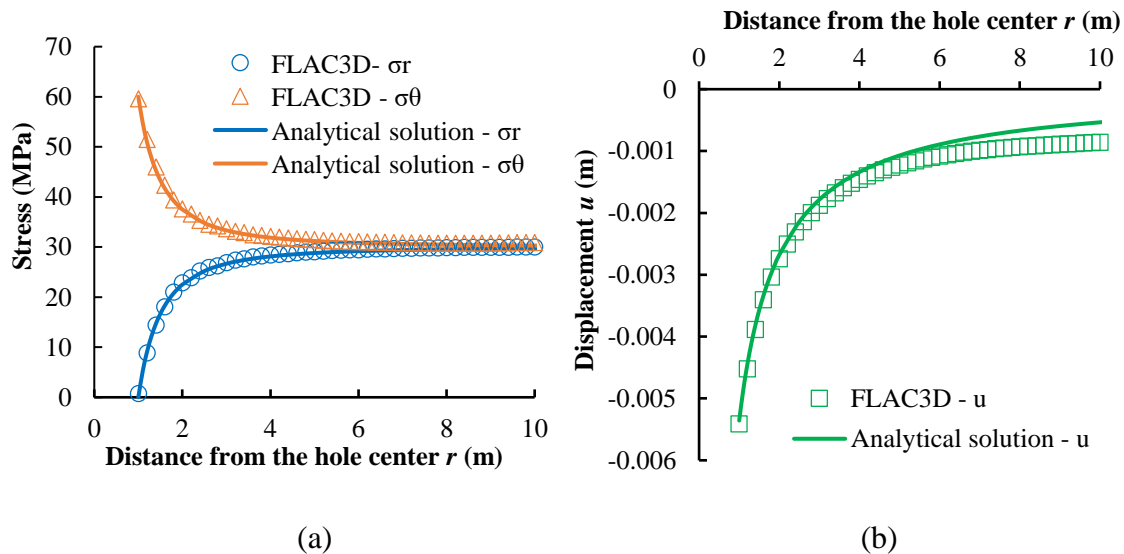


Figure A-15: Comparisons between analytical results and FLAC3D results in an elastic model: (a) the variation of radial and tangential stresses; and (b) the variation of radial displacement

A4.3 Validation of the Mohr-Coulomb model

The material properties in an elastoplastic medium are shown in Table A-2.

A4.3.1 Sensitivity analyses

For the sensitivity analyses of the Mohr-Coulomb Model, the stresses and displacements at the point (1, 0, 0), (2, 0, 0) and (3, 0, 0) are monitored (shown in Figure A-12b).

(1) Domain

By changing the distance R from the hole center to the boundary, the stresses and displacement at the three monitoring points are plotted. From Figure A-16 and Figure A-17, when the dilation angle is equal to 0° or 30° , the stresses and the displacement become constant at $R = 10$ m.

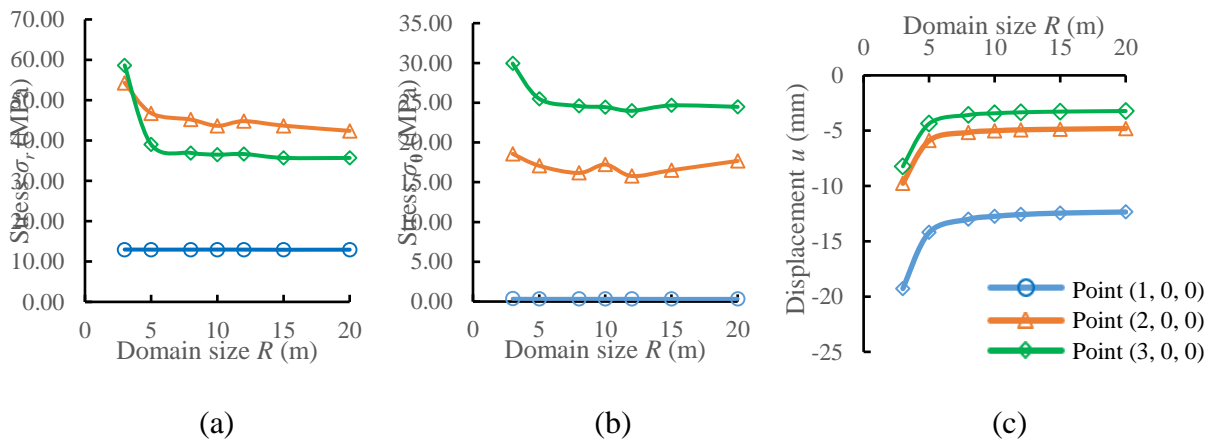


Figure A-16: Sensitivity analysis of the domain in Mohr-Coulomb model with $\psi = 0^\circ$: (a) the variation of radial stress, (b) tangential stress and (a) radial displacement with domain size R

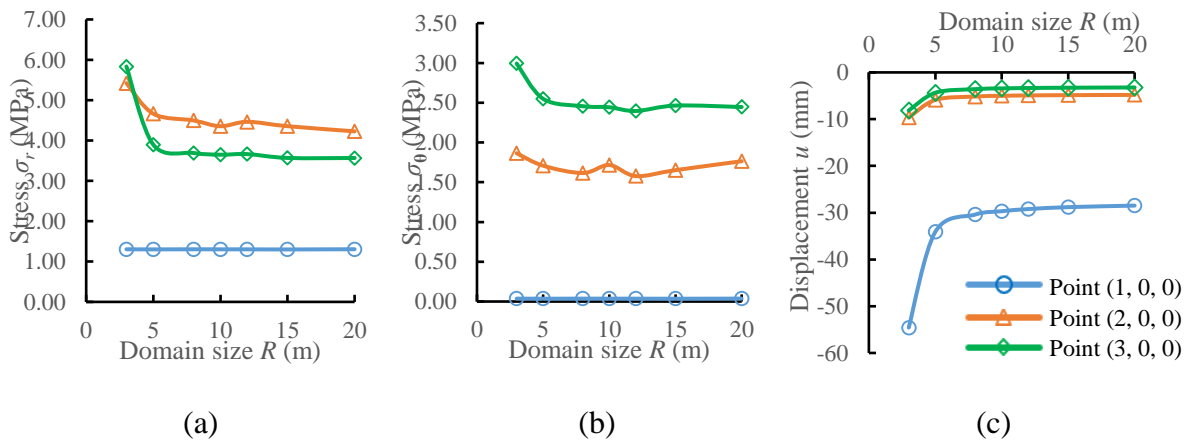


Figure A-17: Sensitivity analysis of the domain in Mohr-Coulomb model with $\psi = 30^\circ$: (a) the variation of radial stress, (b) tangential stress and (a) radial displacement with domain size R

(2) Mesh

The variation of the stresses and displacement at the three monitoring points is plotted in Figures A-18 and A-19 with different element sizes of the hole boundary. It is seen that the values become stable when element size = 0.025 m for both the two dilation angles.

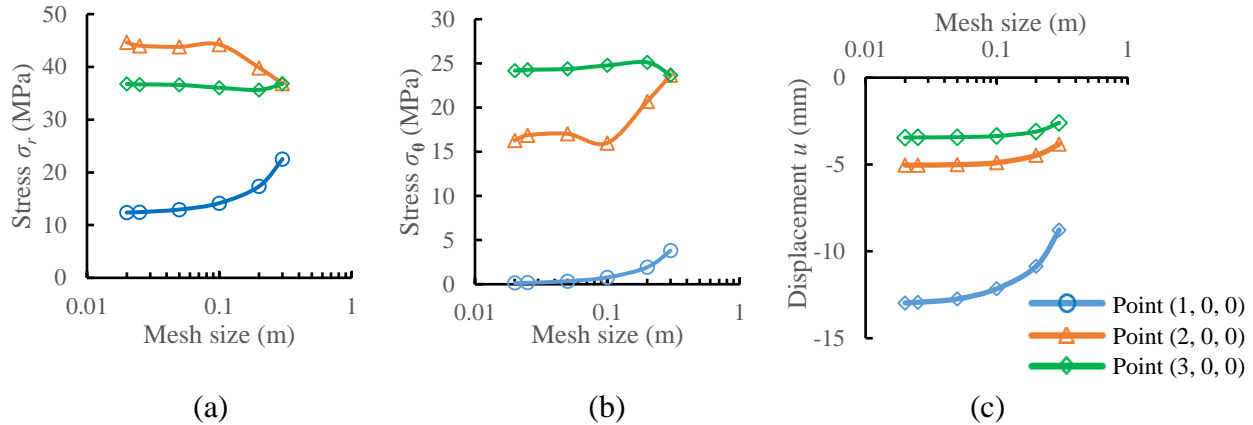


Figure A-18: Sensitivity analysis of the mesh size in Mohr-Coulomb model with $\psi = 0^\circ$: (a) the variation of radial stress, (b) tangential stress and (a) radial displacement with mesh size

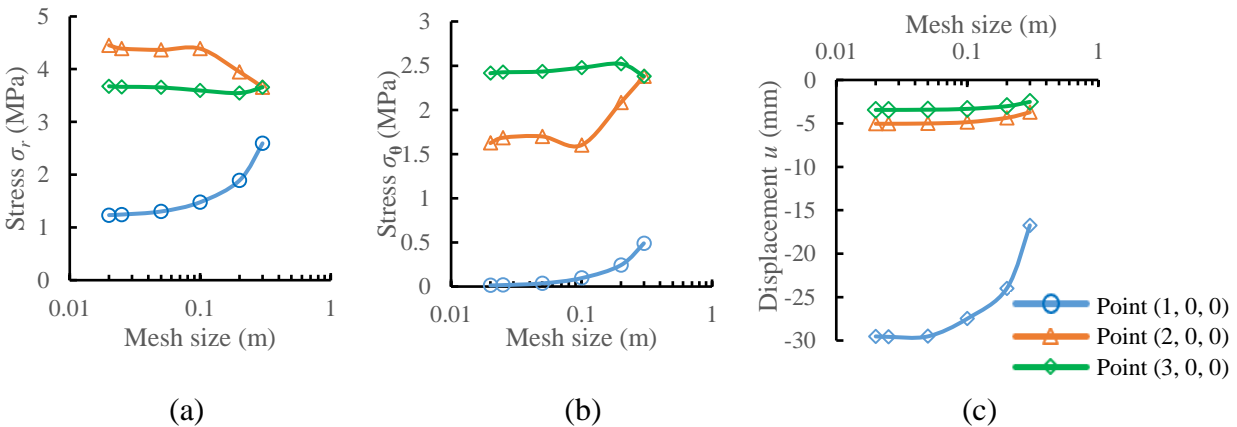


Figure A-19: Sensitivity analysis of the mesh size in Mohr-Coulomb model with $\psi = 30^\circ$: (a) the variation of radial stress, (b) tangential stress and (a) radial displacement with mesh size

A4.3.2 Comparisons between analytical results and numerical results

When $\psi = 0^\circ$ or 30° , the distance from the hole center to the boundary is selected as 10 m and the element size of the hole boundary is 0.025 m in the numerical model. As shown in Figures A-20 and A-21, the FLAC3D results agree well with the analytical solutions (Eqs. A-4 to A-11).

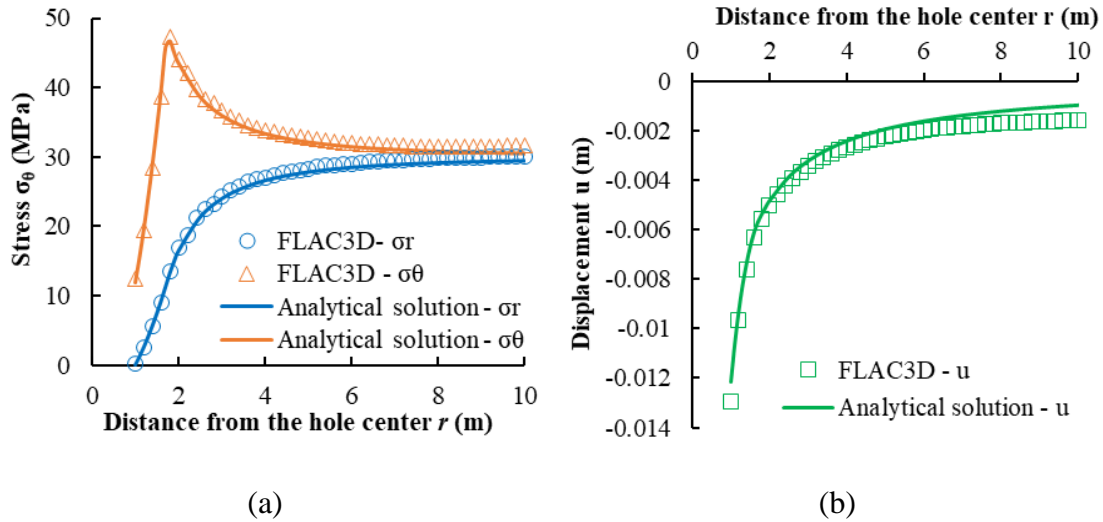


Figure A-20: Comparisons between analytical results and numerical results in the Mohr-Coulomb model with $\psi = 0^\circ$: (a) the variation of radial and tangential stresses and (b) radial displacement

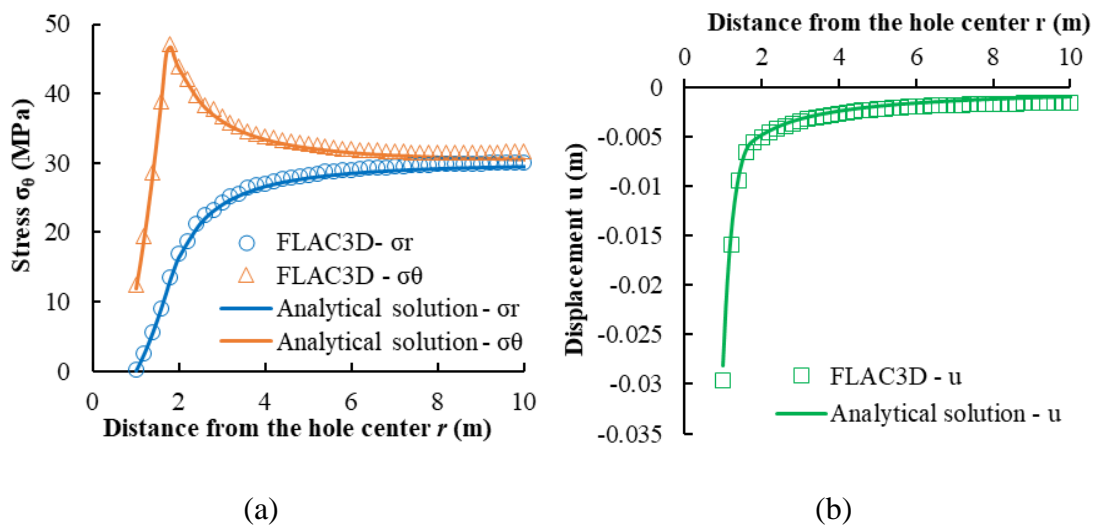


Figure A-21: Comparisons between analytical results and numerical results in the Mohr-Coulomb model with $\psi = 30^\circ$: (a) the variation of radial and tangential stresses and (b) radial displacement

APPENDIX B ADDITIONAL RESULTS RELATED TO CHAPTER 3

In this appendix, the sensitivity analyses of the mesh and domain size for the numerical model used in Chapter 3 are conducted. Then, the FLAC code for Case 0 in Chapter 3 is also shown for reference. Finally, some additional results regarding the stress at the bottom of the backfill with different filling heights are presented.

B1 Sensitivity analyses of the numerical model

Figure B-1 shows a schematic view of the backfill with the four monitoring points at the central line. The depth of the four points from the top of the backfill is -20 m, -30 m, -40 m, and -44.8 m, respectively. In particular, the point at $z = -44.8$ m is used to represent the bottom of the backfill. The model geometry and backfill properties are the same as the reference case (Case 0) in Chapter 3.

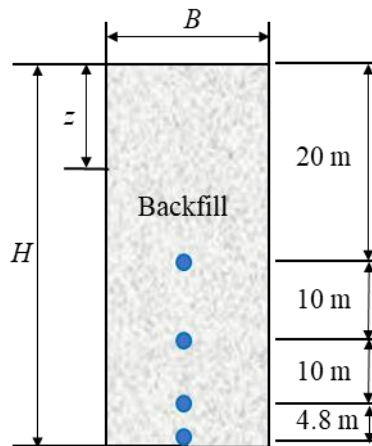


Figure B-1: Positions of the monitoring points for the sensitivity analyses of the backfill model

As shown in Figure B-2, the optimum mesh size obtained by reducing it from 3 m to 0.2 m. It is found that both the vertical and horizontal stress converge when the mesh size is 0.25 m. Figure B-3 illustrates the variations of the vertical and horizontal stress when the domain size (the distance from the backfill boundary to the rock mass boundary) increases from 50 m to 300 m. It is seen that the optimum domain size is 150 m.

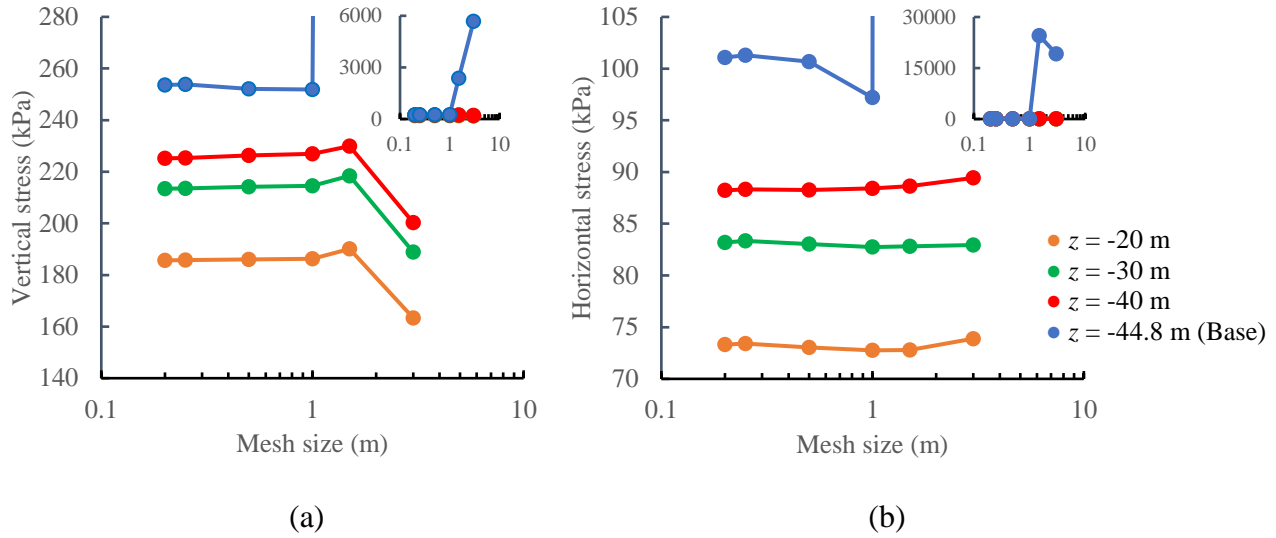


Figure B-2: Variation of the (a) vertical and (b) horizontal stresses at the four monitoring points with different element sizes

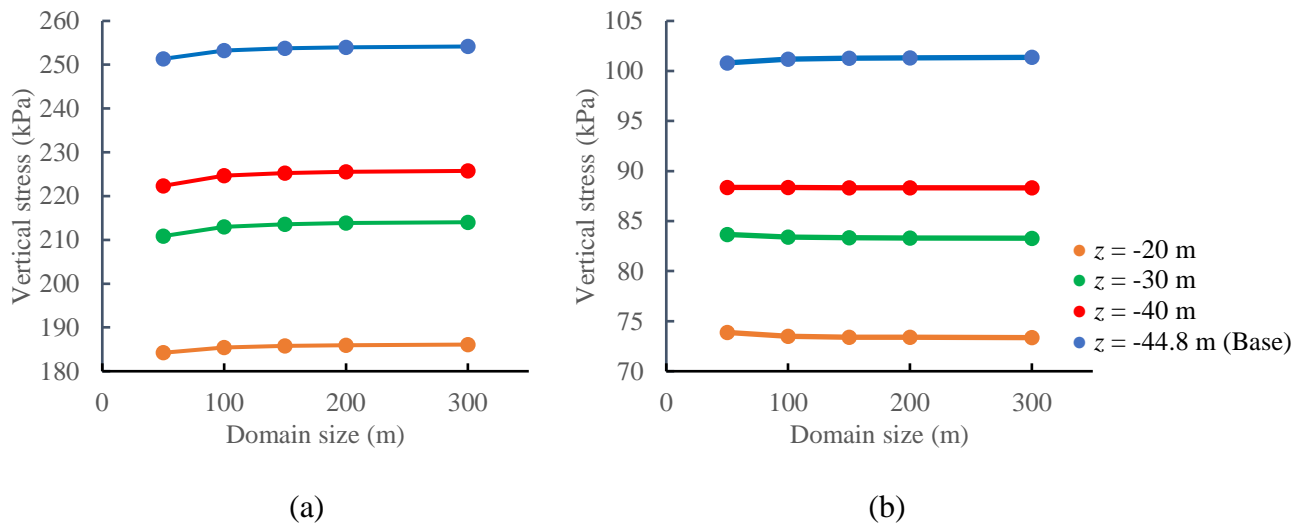


Figure B-3: Variation of the (a) vertical and (b) horizontal stresses at the four monitoring points with different domain sizes

B2 FLAC code of the reference case

```

; FLAC (Version 7.0) code of the reference case 0
; File: Record_R0.dat
; Units: SI: meter-kilogram-second
; Title: Reference case_0
; Branch 1: initial_R0.sav
    
```

; Source: Radial grid

config

grid 106,262

gen -153.0,-400.0 -153.0,-54.5 -3.0,-204.5 -3.0,-250.0 ratio 0.89686096,1.0 i=1,41 j=1,183

gen -153.0,-400.0 -3.0,-250.0 3.0,-250.0 153.0,-400.0 ratio 1.0,0.89686096 i=42,66 j=1,41

gen 3.0,-250.0 3.0,-204.5 153.0,-54.5 153.0,-400.0 ratio 1.115,1.0 i=67,107 j=1,183

gen -3.0,-250.0 -3.0,-204.5 3.0,-204.5 3.0,-250.0 i=42,66 j=41,223

gen -3.0,-204.5 -153.0,-54.5 153.0,-54.5 3.0,-204.5 ratio 1.0,1.115 i=42,66 j=223,263

model elastic i=1,40 j=1,182

model elastic i=42,65 j=1,40

model elastic i=67,106 j=1,182

model elastic i=42,65 j=41,222

model elastic i=42,65 j=223,262

; Attach grids

attach aside from 42,223 to 42,263 bside from 41,183 to 1,183

attach aside from 42,41 to 42,1 bside from 41,1 to 1,1

attach aside from 67,1 to 107,1 bside from 66,41 to 66,1

attach aside from 66,223 to 66,263 bside from 67,183 to 107,183

Def Rockproperty

Erm=3e10 *; Young's modulus of the rock mass (Pa)*

vrn=0.3 *; Poisson's ratio of the rock mass*

Drm=2700 *; Density of the rock mass (kg/m3)*

Krm=Erm/(3*(1-2*vrn)) *; Bulk modulus of the rock mass (Pa)*

Grm=Erm/(2*(1+vrn)) *; Shear modulus of the rock mass (Pa)*

knr=10*(Krm+4*Grm/3)/0.25 *; Normal stiffness of the interface element*

ksr=10*(Krm+4*Grm/3)/0.25 *; Shear stiffness of the interface element*

end

Rockproperty

; Interfaces

interface 1 aside from 41,1 to 41,183 bside from 42,41 to 42,223

interface 1 kn=knr ks=ksr

interface 2 aside from 67,1 to 67,183 bside from 66,41 to 66,223

interface 2 kn=knr ks=ksr

mark i=41,67 j=41

mark i=41,67 j=223

group 'Rock' notnull

model elastic notnull group 'Rock'

prop density=Drn bulk=Krm shear=Grm notnull group 'Rock'

fix x y i 42 66 j 1

```

fix x y i 1 j 1
fix x y i 107 j 1
fix x i 1 j 1 183
fix x i 107 j 1 183
initial sxx -13243500
initial syy -6621750.0
initial szz -13243500
set gravity=9.81
history 999 unbalanced
history sxx i 54 j 42
history syy i 54 j 42
solve
save initial_R0.sav

; Branch 2: excavation_R0.sav
model null i 42 65 j 41 222
solve
save excavation_R0.sav

; Branch 3: fill R0.sav
; Backfill_R0_Shupeng Chai
initial xdisp 0 ydisp 0
initial xvel 0 yvel 0
def fillproperty
Ef=3e8 ; Young's modulus of the fill materials (Pa)
vf=0.3 ; Poisson's ratio of the fill materials
Df=1800 ; Density of the fill materials (kg/m3)
Kf=Ef/(3*(1-2*vf)) ; Bulk modulus of the fill materials (Pa)
Gf=Ef/(2*(1+vf)) ; Shear modulus of the fill materials (Pa)
ff=30 ; Friction angle of the fill materials (°)
; interface
knf=10*(Kf+4*Gf/3)/0.25 ; Normal stiffness of the interface element
ksf=10*(Kf+4*Gf/3)/0.25 ; Shear stiffness of the interface element
fi=30 ; Friction angle of the interface (°)
end
fillproperty
def fill
loop k(2,44)
k1 = k*4+41

```

```

k2 = k1+3
k3 = k*4+1
k4 = k*4+41
k5 = k3+4
k6 = k4+4
k7 = k*2+3
k8 = k7+1
command
model mohr i 42 65 j k1 k2
prop density=Df bulk=Kf shear=Gf cohesion=0.0 friction=ff i 42 65 j k1 k2
interface k7 aside from 41, k3 to 41, k5 bside from 42, k4 to 42, k6
interface k7 kn=knf ks=ksf cohesion=0.0 dilation=0.0 friction=fi
interface k8 aside from 67, k3 to 67, k5 bside from 66, k4 to 66, k6
interface k8 kn=knf ks=ksf cohesion=0.0 dilation=0.0 friction=fi
solve
print syy line (0, -249.81) (0, -249.79) 3
print sxx line (0, -249.81) (0, -249.79) 3
end_command
end_loop
end
model mohr i 42 65 j 41 44
prop density=Df bulk=Kf shear=Gf cohesion=0.0 friction=ff i 42 65 j 41 44
interface 3 aside from 41, 1 to 41, 5 bside from 42, 41 to 42, 45
interface 3 kn=knf ks=ksf cohesion=0.0 dilation=0.0 friction=fi
interface 4 aside from 67, 1 to 67, 5 bside from 66, 41 to 66, 45
interface 4 kn=knf ks=ksf cohesion=0.0 dilation=0.0 friction=fi
solve
step 10000
print syy line (0, -249.81) (0, -249.79) 3
print sxx line (0, -249.81) (0, -249.79) 3
model mohr i 42 65 j 45 48
prop density=Df bulk=Kf shear=Gf cohesion=0.0 friction=ff i 42 65 j 45 48
interface 5 aside from 41, 5 to 41, 9 bside from 42, 45 to 42, 49
interface 5 kn=knf ks=ksf cohesion=0.0 dilation=0.0 friction=fi
interface 6 aside from 67, 5 to 67, 9 bside from 66, 45 to 66, 49
interface 6 kn=knf ks=ksf cohesion=0.0 dilation=0.0 friction=fi
solve
step 10000
print syy line (0, -249.81) (0, -249.79) 3

```

```

print sxx line (0, -249.81) (0, -249.79) 3
fill
print syy line (0, -205) (0, -250) 91
print sxx line (0, -205) (0, -250) 91
save fill_R0.sav

```

B3 Additional results for the stress distribution in backfilled stopes

The stress distribution along the depth of backfill (SD; stress-depth profile) has been well described in Chapter 3. In addition, the stress at the bottom of the backfill with different filling heights (SB; stress-thickness profile) is also monitored for the cases considered in Table 3-2. In this section, additional results for the stress distribution in backfilled stopes are presented.

B3.1 Comparisons of the SD and SB in FLAC

Figures B-4 to B-10 present the two kinds of stress under different backfill parameters. In the figures, HSD and VSD mean horizontal and vertical stresses along the depth, respectively while HSB and VSB mean horizontal and vertical stresses at the bottom, respectively. SB is obtained by monitoring the stress at the bottom of a 45 m-high stope by adding backfill in 45 layers (1 m/layer). It can be seen that the occurrence of kink is mainly dependent on the internal friction angle and Poisson's ratio of the backfill. If kink occurs, the SD is always below the SB, except near the top of the backfill, where the stresses are close to those based on the overburden solution. If no kink occurs, the two types of stress profiles are almost the same.

(1) Reference case (Case 0)

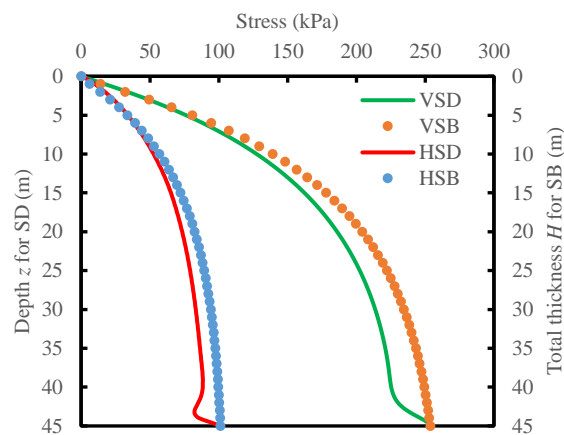


Figure B-4: The variations of (a) VSD, VSB and (b) HSD, HSB for the reference case

(2) Influence of backfill internal friction angle (Case 1)

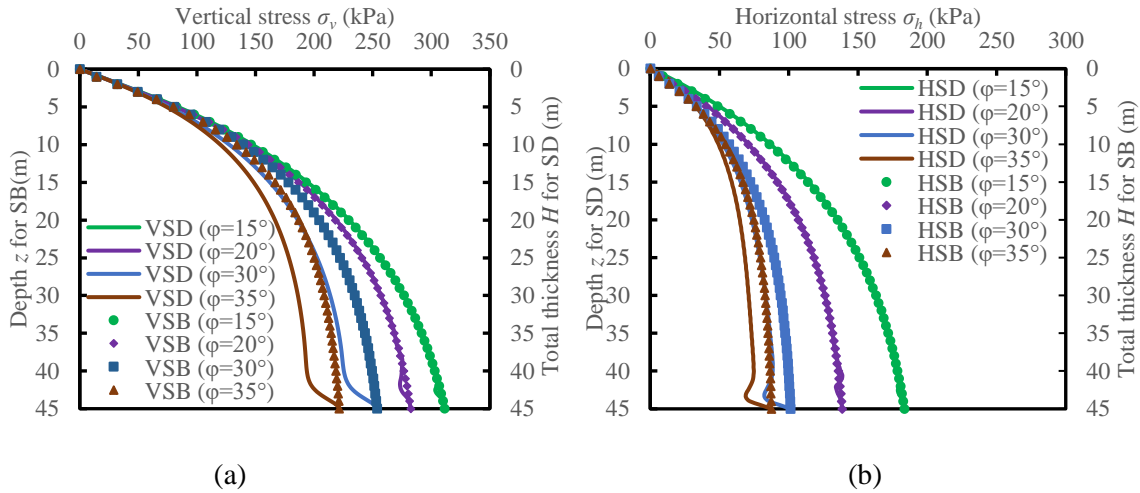


Figure B-5: The variations of (a) VSD, VSB and (b) HSD, HSB with different internal friction angles of the backfill

(3) Influence of the Poisson's ratio of backfill (Case 2)

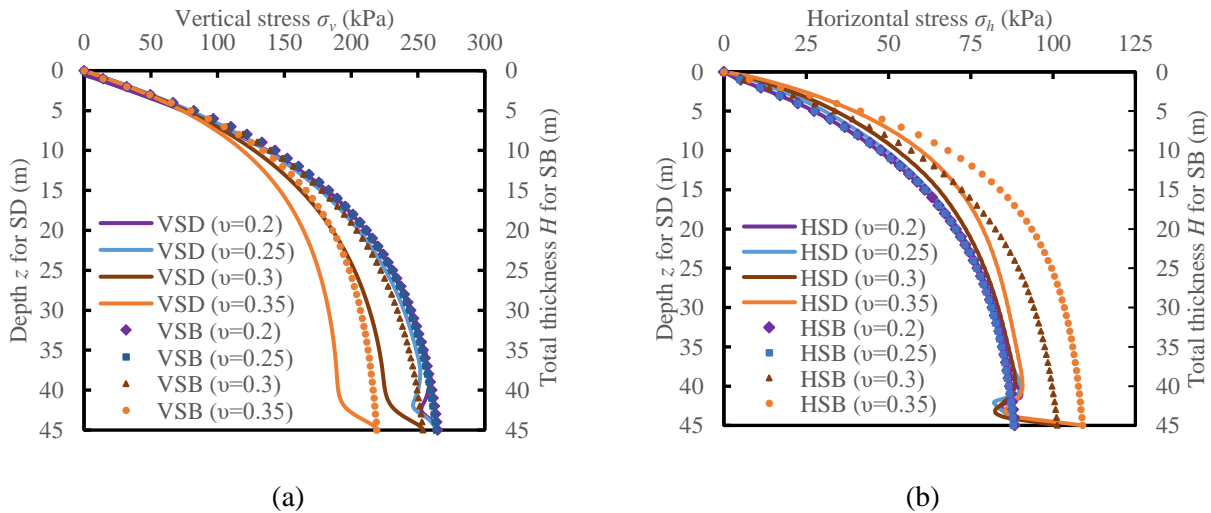


Figure B-6: The variations of (a) VSD, VSB and (b) HSD, HSB with different Poisson's ratios of the backfill

(4) Influence of backfill width (Case 3)

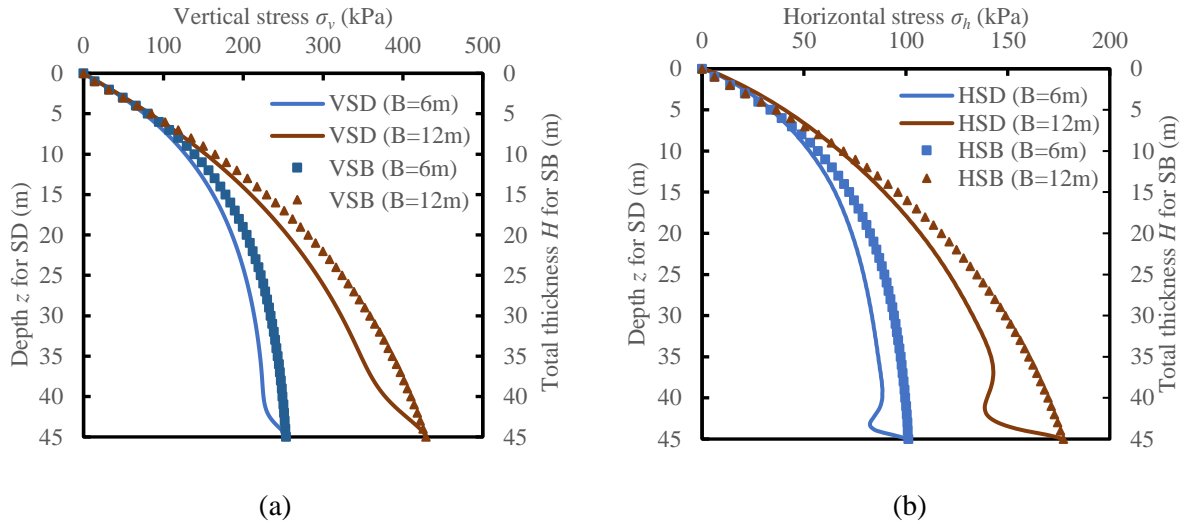


Figure B-7: The variations of (a) VSD, VSB and (b) HSD, HSB with different backfill widths

(5) Influence of backfill height (Case 4)

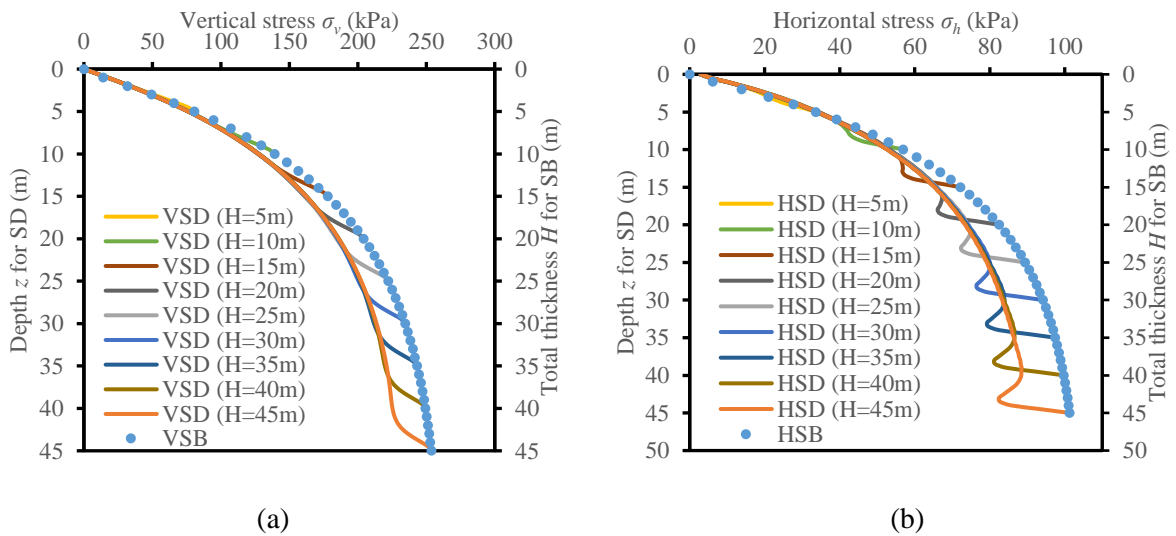


Figure B-8: The variations of (a) VSD, VSB and (b) HSD, HSB with different backfill heights

(6) Influence of Young's modulus of backfill (Case 5)

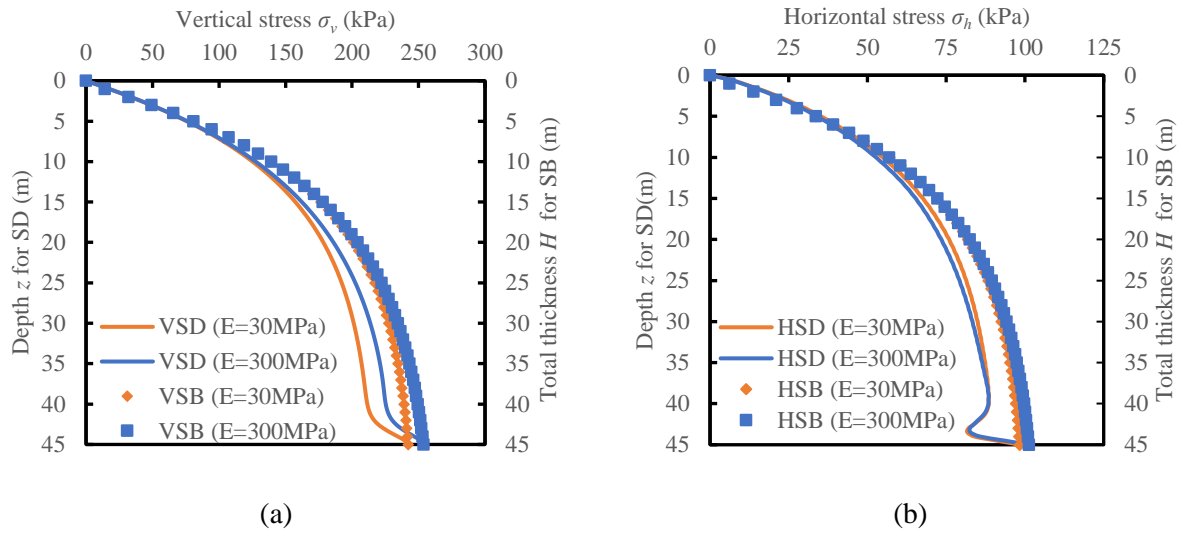


Figure B-9: The variations of (a) VSD, VSB and (b) HSD, HSB with different Young's modulus of the backfill

(7) Influence of fill-rock interface friction angle (Case 6)

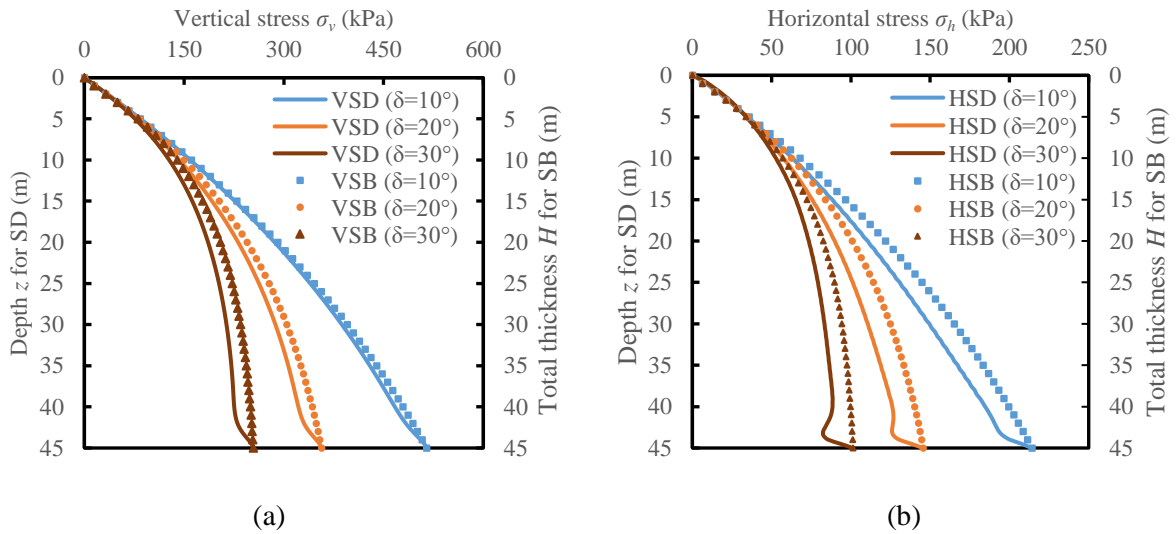


Figure B-10: The variations of (a) VSD, VSB and (b) HSD, HSB with different internal friction angles of the fill-rock interface

B3.2 Analytical solution for SB

It is found that when the kink does not occur, the SB is the same as the SD, agreeing well with the Marston solution using an active earth pressure coefficient K_a (shown in Figure B-11).

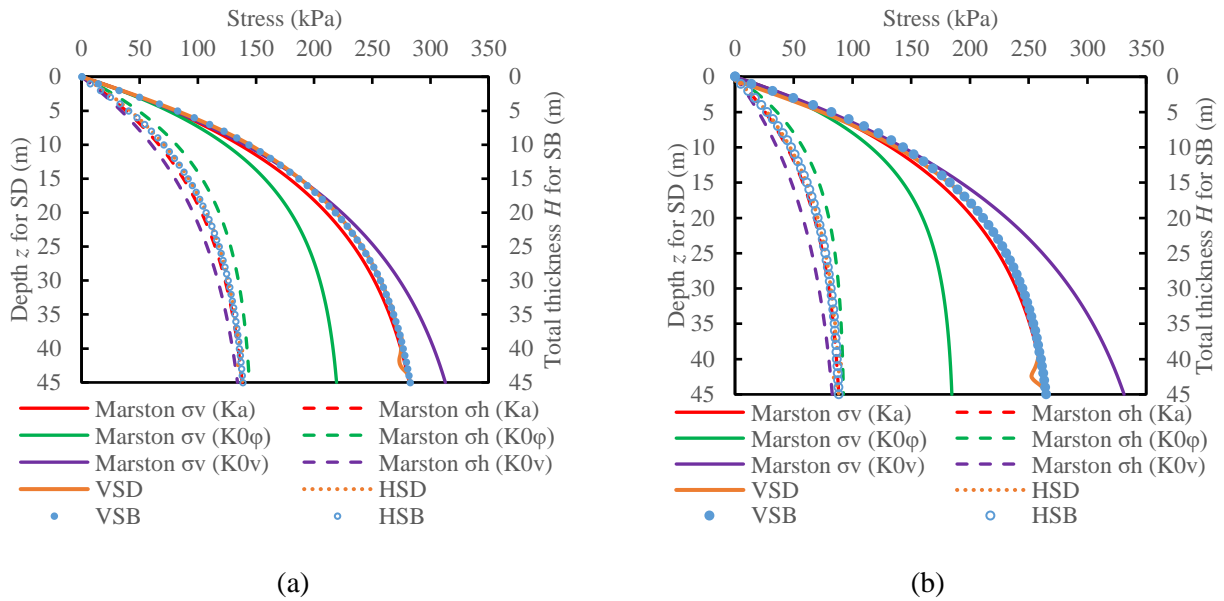
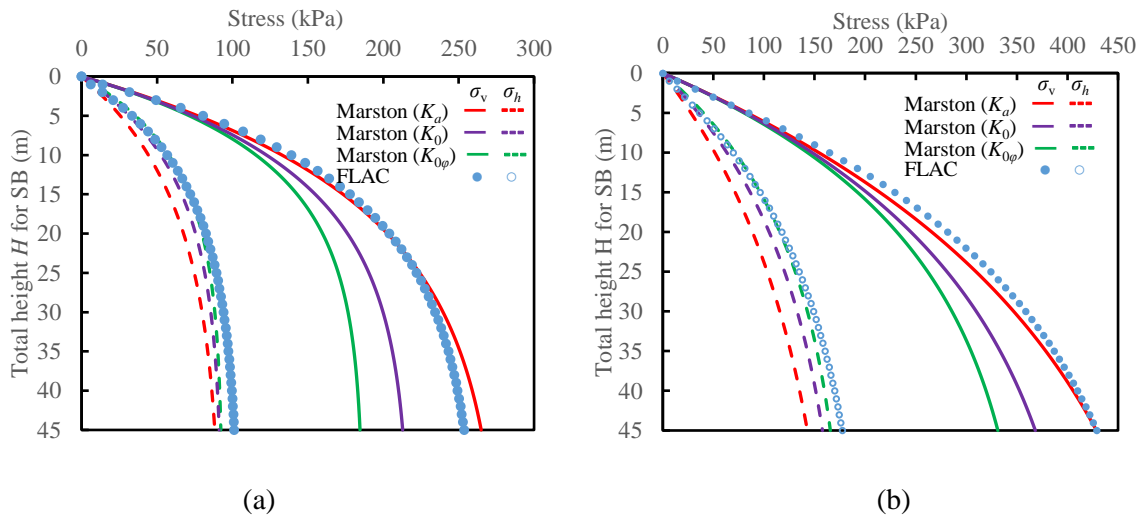


Figure B-11: Comparisons between analytical solutions and numerical simulations when no kink occurs: (a) Case 1 when $\phi = 20^\circ$ and (b) Case 2 when $\mu = 0.2$

If the kink occurs, the VSB is closer to the Marston solution using K_a while the HSB is in accordance with the Marston solution using $K_0\phi$ (shown in Figure B-12).



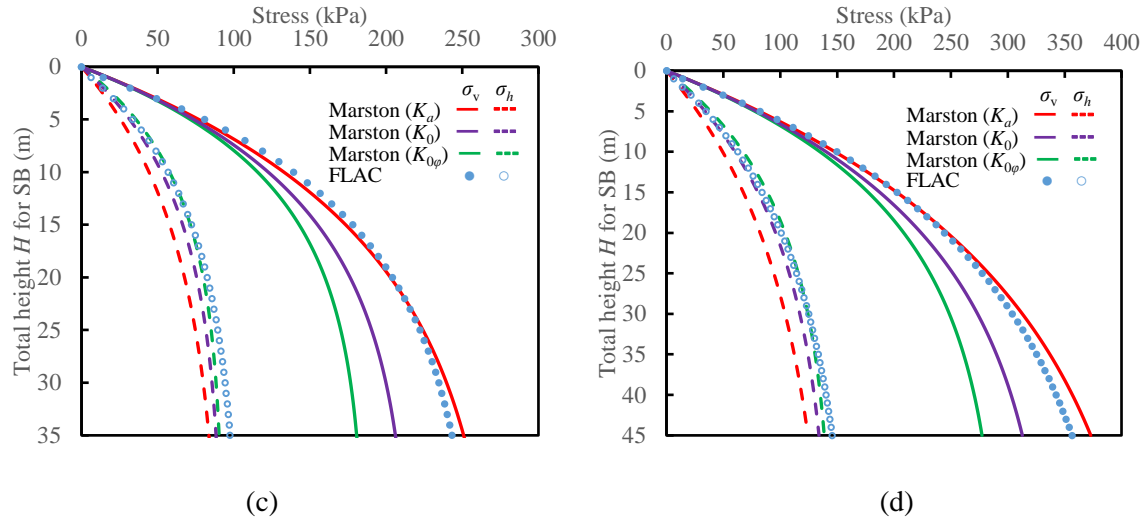


Figure B-12: Comparisons between the proposed analytical solutions and numerical simulations for different backfill properties when the kink occurs: (a) Case 0; (b) Case 3 when $B = 12$ m (c) Case 4 when $H = 35$ m and (d) Case 6 when $\delta=20^\circ$

B3.3 Summary of analytical solutions for the two stress profiles in the backfill

Table B-1 summarizes the analytical solution that can be applied to preliminarily predict the stress distribution in the cohesionless and dry backfill.

Table B-1: Summary of the analytical solution for the stress in the backfill

Whether the kink occurs	Stress along the depth (SD)		Stress at the bottom (SB)	
	Vertical	Horizontal	Vertical	Horizontal
When kink occurs	Proposed solution		Marston solution (K_a)	Marston solution ($K_{0\phi}$)
When no kink occurs	Marston solution (K_a)		Marston solution (K_a)	

APPENDIX C ADDITIONAL RESULTS RELATED TO CHAPTER 4

In this appendix, the results for the sensitivity analyses of the numerical model used in Chapter 4 are presented. Then, the FLAC3D code for Case 0 in Chapter 4 is given in Section C2 for reference. Finally, all the data used in the comparisons of analytical and numerical results are shown in Section C3.

C1 Sensitivity analyses of numerical model

Figure C-1 shows the geometry of the reference case (Case 0) and the position of the monitoring lines used to determine the optimum domain and mesh size of the numerical models. C_1C_2 is the central line of the exposed face and H_1H_2 is a horizontal line from the back wall to the exposed face at a height of 5 m above the bottom of the backfill. Other parameters related to the backfill properties and slope geometry can be found in Chapter 4.

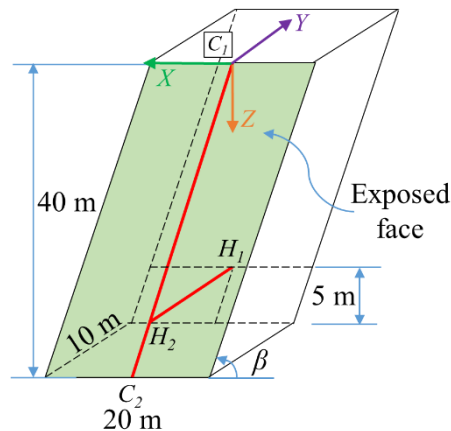


Figure C-1: A schematic view of the side-exposed backfill in inclined stopes with two monitoring lines C_1C_2 and H_1H_2

(1) Domain size

Although the influence of domain is neglectable in the numerical models, its influence is still checked here. The distance from the backfill boundary to the model boundary D is selected based on the factor F_d , which is defined as the ratio of D to the backfill height H . Figure C-2 shows the total displacement and the stress in the z and x directions along the two monitoring lines C_1C_2 and H_1H_2 . It is demonstrated that the numerical results are almost insensitive to the variation of the domain size. So, considering the computing capacity, the F_d is selected as 1 in all the numerical simulations conducted in Chapter 4.

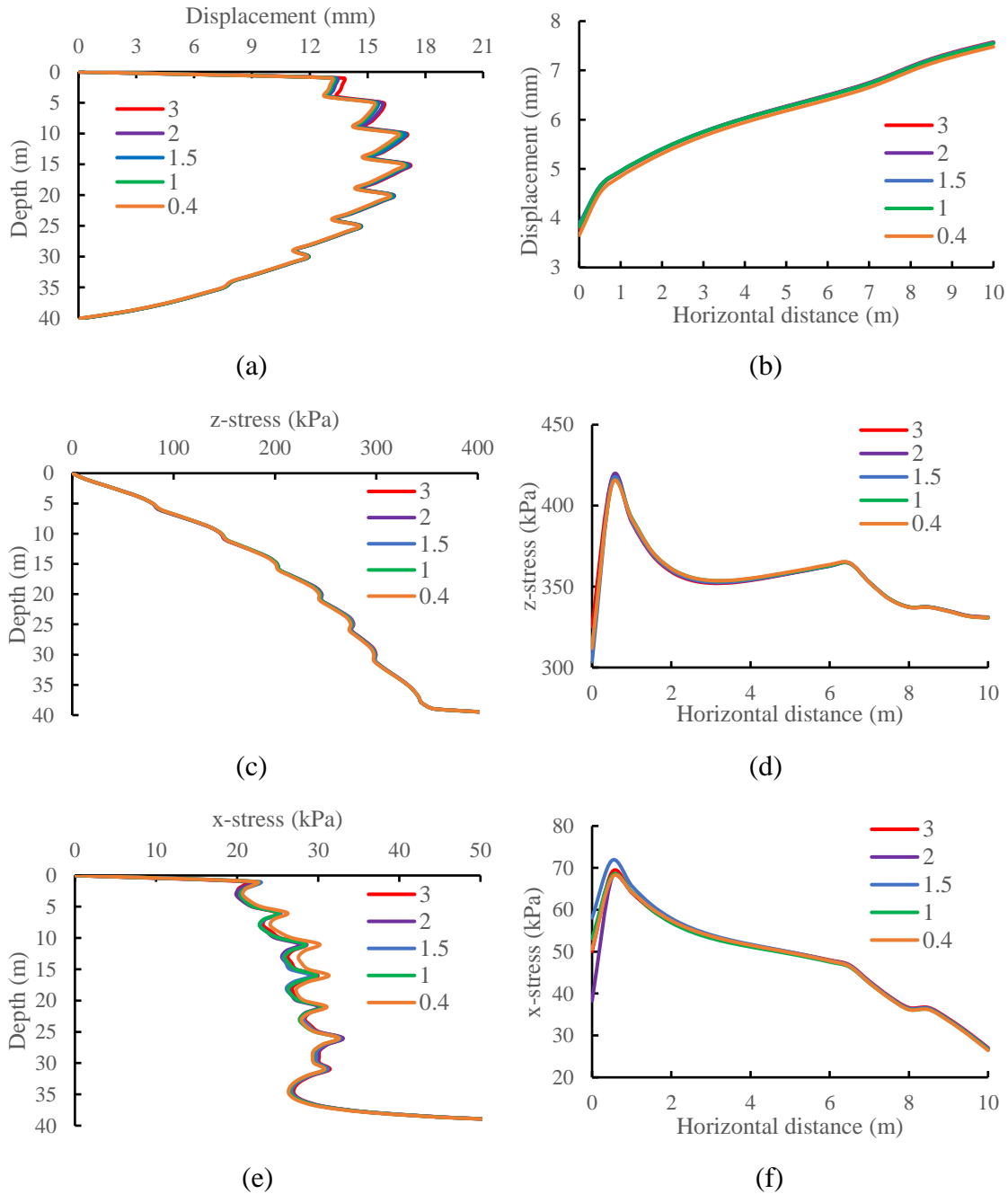


Figure C-2: Results for the sensitivity analyses of the domain size: the total displacement along the line (a) C_1C_2 and (b) H_1H_2 , the stress in the z -direction along the line (c) C_1C_2 and (d) H_1H_2 and the stress in the x -direction along the line (e) C_1C_2 and (f) H_1H_2

(2) Mesh size

The influence of mesh size of the backfill is also investigated. Figure C-3 shows the total displacement and the stresses in the z and x directions along the two monitoring lines C_1C_2 and

H_1H_2 . It is illustrated that the displacement and stresses become stable when the element size is smaller than 0.5 m. Thus, an element size of 0.5 m is used in all the numerical simulations performed in Chapter 4.

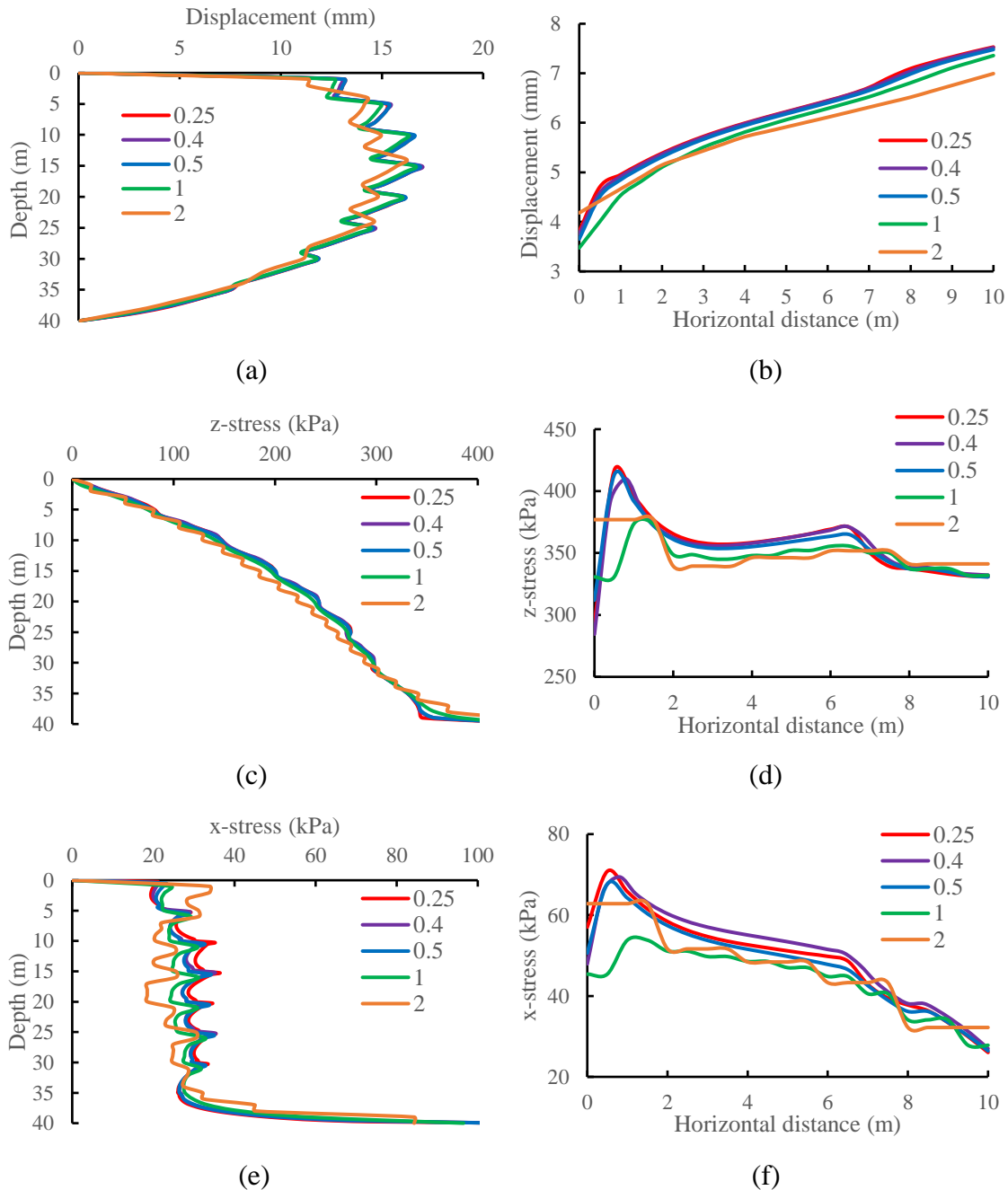


Figure C-3: Results for the sensitivity analyses of the mesh size: the total displacement along the line (a) C_1C_2 and (b) H_1H_2 , the stress in the z -direction along the line (c) C_1C_2 and (d) H_1H_2 and the stress in the x -direction along the line (e) C_1C_2 and (f) H_1H_2

(3) Thickness of the filling layer

Figure C-4 shows the total displacement and the stresses in the z and x directions along the two monitoring lines C_1C_2 and H_1H_2 with the variation of layer thickness from 5 m/layer to 40 m/layer.

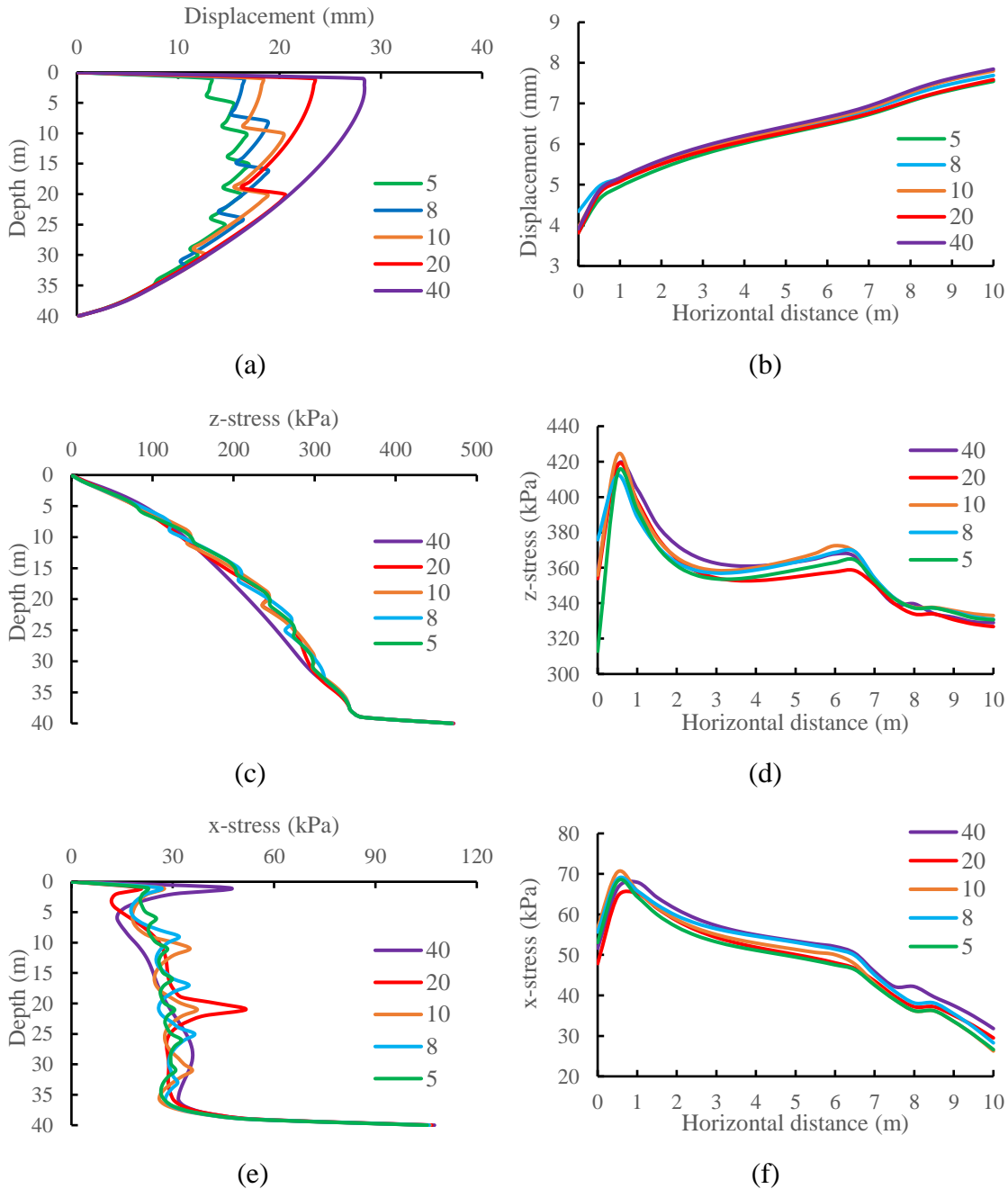


Figure C-4: Results for the sensitivity analyses of the filling layer thickness: the total displacement along the line (a) C_1C_2 and (b) H_1H_2 , the stress in the z -direction along the line (c) C_1C_2 and (d) H_1H_2 and the stress in the x -direction along the line (e) C_1C_2 and (f) H_1H_2

It is illustrated that the stresses become stable when the layer thickness is large than 8 m/layer. The displacement along the line H_1H_2 seems insensitive to the variation of the layer thickness while the displacement along the line C_1C_2 can be regarded as unchanged when the layer thickness is large than 8 m/layer but with some fluctuation of the values. Finally, the optimum layer thickness is selected as 5 m/layer.

C2 FLAC3D code of the reference case

; FLAC3D (Version 5.01) code of the reference case 0

;Parameters.f3dat

new

Define parameters

;Geometry

;Stope Geometry

Hs=40.0 *;Stope height (m)*

Ls=20.0 *;Stope length (m)*

Bs=10.0 *;Stope width (m)*

Hv=0.5 *;Height of the void (m)*

Ls2=Ls/2.0 *;Half of the stope length (m)*

Dsb=-Hs *;Depth of the stope bottom (m)*

Dst=0 *;Depth of the stope top (m)*

;Domain

Fd=1 *;Factor of the domain*

MS=Max(Hs,Ls,Bs) *;Maximum value of the stope height, length and width (m)*

Md=Fd*MS *;Size of the domain (m)*

;Model Geometry

Beta=70.0 *;Inclination angle (°)*

Hm=Hs+Md *;Model height(m)*

TB=tan(Beta*Pi/180.0)

Lml=Ls2+Md+Hs/2.0/TB *;Left model length (m)*

Lmr=Ls2+Md-Hs/2.0/TB *;Right model length (m)*

Bm=Bs+Md *;Model Width (m)*

;Coordinate

;right model

xrt=Lmr *;x-coordinate of the top face of right model (3,5,6,7)(m)*

xr0=0 *;x-coordinate of P(0,2,9) of right model (m)*

xr10=Ls2 *;x-coordinate of P(10,12) of right model (m)*

xr8=-Hs/TB *;x-coordinate of P(8,11) of right model (m)*

```

xr11=xr8           ;x-coordinate of P(8,11) of right model (m)
xr13=xr8+Ls2      ;x-coordinate of P(13,14) of right model (m)
xr14=xr13         ;x-coordinate of P(13,14) of right model (m)
xr1=-Hm/TB       ;x-coordinate of P(1,4) of right model (m)
xr4=xr1           ;x-coordinate of P(1,4) of right model (m)
;yrf=0           ;y-coordinate of the front face of right model (0,1,3,6,8,10,13)(m)
;yrb=Bmr         ;y-coordinate of the back face of right model (2,4,5,7)(m)
;yrs=Bs          ;y-coordinate of the slope width of right model (9,11,12,14)(m)
zrt=Dst          ;z-coordinate of the bottom face of right model (0,2,3,5,9,10,12)(m)
zrb=zrt-Hm       ;z-coordinate of the top face of right model (1,4,6,7)(m)
zrs=Dsb          ;z-coordinate of the slope height of right model (8,11,13,14)(m)
;left model
xll=-Lml         ;x-coordinate of the left face of left model (1,4,6,7)(m)
;xl0=0           ;x-coordinate of P(0,2,9) of left model (m)
xl8=-Ls2         ;x-coordinate of P(8,11) of left model (m)
xl11=-Ls2        ;x-coordinate of P(8,11) of left model (m)
xl10=-Hs/TB     ;x-coordinate of P(10,12) of left model (m)
xl12=xl10       ;x-coordinate of P(10,12) of left model (m)
xl13=xl10-Ls2   ;x-coordinate of P(13,14) of left model (m)
xl14=xl13       ;x-coordinate of P(13,14) of left model (m)
xl3=-Hm/TB      ;x-coordinate of P(3,5) of left model (m)
xl5=xl3         ;x-coordinate of P(3,5) of left model (m)
;ylf=0           ;y-coordinate of the front face of left model (0,1,3,6,8,10,13)(m)
;ylb=Bm         ;y-coordinate of the back face of left model (2,4,5,7)(m)
;yls=Bs         ;y-coordinate of the slope width of left model (9,11,12,14)(m)
zlt=Dst         ;z-coordinate of the top face of left model (0,1,2,4,8,9,11)(m)
zlb=zlt-Hm      ;z-coordinate of the bottom face of left model (3,5,6,7)(m)
zls=zlt-Hs      ;z-coordinate of the slope height of left model(10,12,13,14)(m)
;other
zmb=zlb         ;z-coordinate of the model bottom (m)
xml=-Lml        ;x-coordinate of the model left (m)
xmr=Lmr         ;x-coordinate of the model right (m)
ymb=Bm          ;y-coordinate of the model back (m)
ymf=0           ;y-coordinate of the model front (m)
t=0.001
;Mesh
esize=0.5       ;Element size (m)
Nh=int(Hs/esize) ;Element number along the bottom half slope height
Nls=int(Ls2/esize) ;Element number along the slope length

```

```

Nbs=int(Bs/esize)      ;Element number along the stope width
Nd=8                  ;Element number of the domain
Rd=1.5                ;Element ratio of the domain
;Material Properties
;Rock mass
Er= 3e10              ;Young's modulus of the rock mass (Pa)
vr= 0.3                ;Poisson's ratio of the rock mass (Pa)
Dr=2700.0             ;Density of the rock mass (kg/m3)
Kr=Er/(3*(1-2*vr))    ;Bulk modulus of the rock mass (Pa)
Gr=Er/(2*(1+vr))     ;Shear modulus of the rock mass (Pa)
Gamma=Dr*9.81         ;Unit weight of the rock mass (N/m3)
end
@parameters

;Initial.f3dat
;Generate grids
gen zone radbrick size @Nh @Nbs @Nls @Nd ratio 1 1 1 @Rd P0 0 0 @zrt P1 @xr1 0 @zrb &
P2 0 @Bm @zrt P3 @Lmr 0 @zrt P4 @xr4 @Bm @zrb P5 @Lmr @Bm @zrt &
P6 @Lmr 0 @zrb P7 @Lmr @Bm @zrb P8 @xr8 0 @zrs P9 0 @Bs @zrt P10 @Ls2 0 @zrt &
P11 @xr11 @Bs @zrs P12 @Ls2 @Bs @zrt P13 @xr13 0 @zrs P14 @xr14 @Bs @zrs &
fill group right
gen zone radbrick size @Nls @Nbs @Nh @Nd ratio 1 1 1 @Rd P0 0 0 @zlt P1 @xll 0 @zlt &
P2 0 @Bm @zlt P3 @xl3 0 @zlb P4 @xll @Bm @zlt P5 @xl5 @Bm @zlb P6 @xll 0 @zlb &
P7 @xll @Bm @zlb P8 @xl8 0 @zlt P9 0 @Bs @zlt P10 @xl10 0 @zls P11 @xl11 @Bs @zlt &
P12 @xl12 @Bs @zls P13 @xl13 0 @zls P14 @xl14 @Bs @zls fill group left
group rockmass range group Default
group backfill range group right any group left any
;Properties of the rockmass
model mech elastic
prop density=@Dr bulk=@Kr shear=@Gr
;Boundary conditions & initial conditions
fix x y z range z=@zmb
fix x y range x=@xml
fix x y range x=@xmr
fix x y range y=@ymf
fix x y range y=@ymb
set gravity 0, 0, -9.81
;History
hist unbal

```

```
set large
solve
```

; Excavation.f3dat

; Excavation

```
model null range group backfill
set large
solve
```

; Fillproperty.f3dat

Define fillproperty

; Fill materials

Ef= 3e8

; Young's modulus of the fill materials (Pa)

vf= 0.2

; Poisson's ratio of the fill materials (Pa)

Df=1800.0

; Density of the fill materials (kg/m3)

Kf=Ef/(3*(1-2*vf))

; Bulk modulus of the fill materials (Pa)

Gf=Ef/(2*(1+vf))

; Shear modulus of the fill materials (Pa)

ff=30.0

; Friction angle of the fill materials (°)

UCSf=2*cf*tan((45+ff/2.0)*Pi/180)

; UCS of the fill materials (Pa)

tf=UCSf*0.1

; Tension of the fill materials (Pa)

; interface

knf=10*(Kf+4*Gf/3)/esize

; normal stiffness of the interface element

ksf=10*(Kf+4*Gf/3)/esize

; shear stiffness of the interface element

fi=ff

; Friction angle of the interface (°)

ci=cf

; Cohesion of the interface (Pa)

fih=ff

; Friction angle of the hanging wall interface (°)

cih=cf

; Cohesion of the hanging wall interface (Pa)

end

@fillproperty

; Fill.f3dat

; Set displacement to zero

```
ini xdisp 0 ydisp 0 zdisp 0
```

```
ini xvel 0 yvel 0 zvel 0
```

; Interface

```
group face Inthw internal range group rockmass group backfill &
```

```
plane orig (@xl8,0,0) dip @Beta dd -90 distance 0.01
```

```
gen separate face orig (@xl8,0,0) range group Inthw
```

```
interface 1 face range group Inthw
```

```
interface 1 prop kn @knf ks @ksf fric @fih c @cih
```

```
group face Intfw internal range group rockmass group backfill &
```

```
plane orig (@Ls2,0,0) dip @Beta dd -90 distance 0.01
```

```

gen separate face orig (@xmr,0,0) range group Intfw
interface 2 face range group Intfw
interface 2 prop kn @knf ks @ksf fric @fi c @ci
group face Intbw internal range group rockmass group backfill &
plane orig (0,@Bs,0) dip 90 dd 0 distance 0.01
gen separate face orig (0,@Bs,0) range group Intbw
interface 3 face range group Intbw
interface 3 prop kn @knf ks @ksf fric @fi c @ci

```

;Backfill

Define backfill

;Fill procedure

TL=5 ;Thichness of each layer (m)

NL=int(Hs/TL) ;Number of filling layers

local k

loop k(1,NL)

k1=Dsb+TL*k+t

k2=Dsb+TL*(k-1)-t

numfill='fill_'+string(k)

command

group @numfill range group backfill plane orig (0,0,@k1) normal (0,0,1) below &

plane orig (0,0,@k2) normal (0,0,1) above

model mech mohr range group @numfill

prop density=@Df bulk=@Kf shear=@Gf friction=@ff cohesion=@cf &

tension=@tf range group @numfill

set large

solve

step 1000

end_command

end_loop

end

@backfill

;Expose.f3dat

;Expose

group backfill range group fill_1 any

Define backfillgroup

local m

loop m(2,NL)

```

numfill='fill_'+string(m)
command
    group backfill range group backfill any group @numfill any
end_command
end_loop
end
@backfillgroup

free x y z range group backfill y=@ymf
fix x y range group rockmass y=@ymf
set large
step 15000

; Master.f3dat
new
call Parameters
call Initial
save Initial
call Excavation
save Excavation
new
restore Excavation
Define fillcohesion
cf=70e3      ;Cohesion of the backfill (Pa). Change it to 69 kPa, 71 kPa and calculate.
end
@fillcohesion
call Fillproperty
call Fill
save Fill_69
call Expose
save Expose_69
step 60000
save Expose_69_5
step 105000
save Expose_69_12

```

C3 The minimum required cohesion for the considered cases

Table C-1 shows the detailed data of the minimum required cohesion obtained by the numerical simulations (FLAC3D) and analytical solutions (the proposed solution, the Smith et al. (1983) solution, the Mitchell (1989) solution, and the Dirige and Souza (2008) solution) for all the cases considered in Chapter 4.

Table C-1: The minimum required cohesion for the cases in Table 4-1

Case	Unit weight γ (kN/m ³)	Height H (m)	Length L (m)	Width B (m)	Inclination β (°)	friction angle ϕ (°)	Minimum required cohesion c (kPa)					
							FLAC3D	Proposed solution	Smith et al. (1983)	Mitchell (1989)	Dirige and De Souza (2008)	
0	18	40	20	10	70	30	61	67.4	97.0	45.1	34.9	
1	18	40	20	10	70	30	50	61	59.9	97.0	36.8	15.0
							60	67	73.3	97.0	41.6	23.9
							65	69	70.4	97.0	43.5	29.1
							70	70	67.4	97.0	45.1	34.9
							75	68	64.3	97.0	46.4	41.0
							80	66	61.1	97.0	47.3	47.4
							85	60	57.9	97.0	47.8	54.0
							90	56	54.6	97.0	48.0	60.6
2	18	45	15	6	70	35	50	50	36.9	90.8	31.0	6.7
							60	59	51.7	90.8	35.1	14.4
							65	62	53.7	90.8	36.7	19.1
							70	62	50.6	90.8	38.1	24.2
							75	59	47.4	90.8	39.1	29.6
							80	53	44.3	90.8	39.9	35.4
							85	50	41.2	90.8	40.3	41.2
							90	50	38.0	90.8	40.5	47.0
3	18	30	20	10	70	30	58	58.6	81.0	40.6	29.3	
		40					70	67.4	97.0	45.1	34.9	
		50					79	70.8	110.2	48.3	38.6	
		60					87	71.3	121.1	50.7	41.4	
		70					95	70.0	130.3	52.6	43.5	
4	18	40	5	10	70	30	21	13.2	43.8	15.0	17.3	
			10				40	34.7	69.1	27.1	26.0	
			20				70	67.4	97.0	45.1	34.9	
			30				95	87.6	112.1	58.0	39.3	
5	18	40	5	20	70	30	77	69.7	97.0	45.1	28.9	
			10				70	67.4	97.0	45.1	34.9	
			15				62	63.7	97.0	45.1	35.6	
			20				63	58.2	97.0	45.1	34.0	
6	18	40	20	10	70	20	86	79.9	97.0	45.1	48.5	
						25	77	73.1	97.0	45.1	41.7	
						30	70	67.4	97.0	45.1	34.9	
						35	63	62.4	97.0	45.1	27.9	
						40	59	57.8	97.0	45.1	20.9	